University of Kentucky Doctoral Dissertations   Graduate School

2010

SPECTROSCOPY AND STRUCTURES OF METAL-CYCLIC HYDROCARBON COMPLEXES

Jung Sup Lee
University of Kentucky, angcc0903@hotmail.com

ABSTRACT OF DISSERTATION

Jung Sup Lee

The Graduate School

University of Kentucky

2010

SPECTROSCOPY AND STRUCTURES OF METAL-CYCLIC HYDROCARBON
COMPLEXES

_____

ABSTRACT OF DISSERTATION
_____

A dissertation submitted in partial fulfillment of the
requirements for the degree of Doctor of Philosophy in the
College of Arts and Sciences
at the University of Kentucky

By
Jung Sup Lee

Lexington, Kentucky

Director: Dr. Dong-Sheng Yang, Professor of Chemistry

Lexington, Kentucky

2010

ABSTRACT OF DISSERTATION

SPECTROSCOPY AND STRUCTURES OF METAL-CYCLIC HYDROCARBON COMPLEXES

Metal-cyclic hydrocarbon complexes were prepared in a laser-vaporization molecular beam source and studied by single-photon zero electron kinetic energy (ZEKE) and IR-UV resonant two-photon ionization (R2PI) spectroscopy. The ionization energies and vibrational frequencies of the metal complexes were measured from the ZEKE spectra. Metal-ligand bonding and low-lying electronic states of the neutral and ionized complexes were analyzed by combining the ZEKE measurements with density functional theory (DFT) calculations. In addition, C-H stretching frequencies were measured from the R2PI spectra.

In this dissertation, metal complexes of 1, 3, 5, 7-cyclo-octatetraene (COT), toluene, *p*-xylene, mesitylene, hexamethylbenzene, biphenyl, naphthalene, pyrene, perylene, and coronene were studied. For each metal-ligand complex, different effects from the metal coordination have been identified. Although free COT is a nonaromatic molecule with a tub-shaped structure, the group III transition metal atoms (Sc, Y, and La) donate two electrons to a partially filled π orbital of COT, making the ligand a dianion. As a result, metal coordination converts COT into a planar, aromatic structure and the resulting complex exhibits a half-sandwich structure. For the Sc(methylbenzene) complexes, the benzene rings of the ligands are bent and the π electrons are localized in a 1, 4-diene fashion due to differential Sc binding with the carbon atoms of the rings. Due to differential metal binding, the degenerate d orbitals split and the Sc-methylbenzene complexes prefer the low-spin ground electronic states. In addition, as the number of methyl group substituents in the ligand increases, the ionization energies (IEs) of the Sc-methylbenzene complexes decrease. However, Ti, V, or Co coordination does not disrupt the delocalized π electron network within the carbon skeleton in the high-spin ground states of the metal complexes. For group VI metal (Cr, Mo, and W)-bis(toluene) complexes, methyl substitution on the benzene ring yields complexes with four rotational conformers of 0°, 60°, 120°, and 180° conformation angles between two methyl groups. In addition, variable-temperature ZEKE spectroscopy using He, Ar, or their mixtures has determined the totally eclipsed 0° rotamer to be the most stable. When there are two equivalent benzene rings, the metal (Ti, Zr or Hf) binds to both the benzene rings of biphenyl, or the metal (Li) binds to one of the benzene rings of naphthalene. On the other

hand, the metal (Li) favors the ring-over binding site of the benzene ring with a higher π electron content and aromaticity in pyrene, perylene, and coronene.

_____

Jung Sup Lee

_____

December 14, 2010

SPECTROSCOPY AND STRUCTURES OF METAL-CYCLIC

HYDROCARBON COMPLEXES

By

Jung Sup Lee

_____
Dr. Dong-Sheng Yang
Director of Dissertation

_____
Dr. John E. Anthony
Director of Graduate Studies

_____
December 14, 2010

RULES FOR THE USE OF DISSERTATIONS

Unpublished dissertations submitted for the Doctor's degree and deposited in the
University of Kentucky Library are as a rule open for inspection, but are to be used only
with due regard to the rights of the authors. Bibliographical references may be noted, but
quotations or summaries of parts may be published only with the permission of the author,
and with the usual scholarly acknowledgements.

Extensive copying or publication of the dissertation in whole or in part also requires the
consent of the Dean of the Graduate School of the University of Kentucky.

A library that borrows this dissertation for use by its patrons is expected to secure the
signature of each user.

Name   Date

_____

_____

_____

_____

_____

_____

_____

_____

DISSERTATION

Jung Sup Lee

The Graduate School

University of Kentucky

2010

SPECTROSCOPY AND STRUCTURES OF METAL-CYCLIC HYDROCARBON
COMPLEXES

———————————————————

DISSERTATION

———————————————————

A dissertation submitted in partial fulfillment of the
requirements for the degree of Doctor of Philosophy in the
College of Arts and Sciences
at the University of Kentucky

By
Jung Sup Lee

Lexington, Kentucky

Director: Dr. Dong-Sheng Yang, Professor of Chemistry

Lexington, Kentucky

2010

Dedicated to my mentor, family, and friends…

Moreover, my family has given me guidance and support to keep me straight to reach for my goal. They were always besides me whenever I needed them. I am very grateful for my grandfather who has always given me support and attention to be a better person. I would also like to thank my mother and father who have supported me all these years. Without their guidance, I could not be who I am today. Also they have given me opportunity and pressured me to study further in US. If they had not done so, I would not have accomplished such work, nor met my wonderful wife. My wife and her family have helped me when I had hard time while separated from my family in South Korea and also treated me such that I would feel right at home. With the presence of all my family members, my life has always been filled with energy and joy. I can not express my gratitude for their support, understanding, and patience.

During my graduate studies, I have learned so much in various aspects that I have never had a chance to do before. With everyone's help, I was able to accomplish what I never dreamed possible. Now, I feel like I can go over any obstacles that lie ahead of me. The experience that I had in University of Kentucky will never be forgotten. This work is dedicated to all of my teachers, friends, and family. Thank you!

TABLE OF CONTENTS

LIST OF TABLES

LIST OF FIGURES

CHAPTER 1. INTRODUCTION

Metal-ligand interactions are crucial in chemical synthesis, catalysis, and molecular biology. For example, the bindings on many metal oxide surfaces are controlled by the ionic metal interactions.[1-3] The film deposition of microelectronic materials are composed of metal-containing plasmas.[1] In biological systems, the particular metal ion transports through cell membrane according to the selectivity governed by metal-ligand electrostatic interactions.[2] In addition, metals are commonly found in the active sites of enzymes, and the structures and functions of the enzymes are influenced by the metal binding sites, strengths, and mechanisms.[3,4]

Among various metal-ligand complexes, the compounds involving transition metal-benzene or aromatic fragments have been recognized as essential reagents in the homogeneous catalysis of organic reactions and have been studied rigorously.[5,6] Two of the most accredited metal-ligand 1:2 sandwich complexes are the ferrocene[7,8] and chromium-bis(benzene)[9] which have exceptional stabilities by satisfying the 18-electron rule. The metal-bis(benzene) complexes have structures such that a metal center is sandwiched by two benzene ligands. In the sandwich structures, metal binding to the ligand by six-fold symmetry (η^6) is quite common and other binding modes (η^2 or η^4) also exist.[6,10] These complexes have gathered extensive attention, and the studies on these complexes have become captivating areas of research in organometallic chemistry. In addition, the metal-benzene complexes have been used as the prototypes to study the interaction between metal and aromatic surfaces, such as polycyclic aromatics, graphite surfaces, and carbon nanotubes.

The systems in this dissertation are designed to investigate the interactions between the metals and various ligands derived from benzene. In current work, the metals from the main and transition groups have been coordinated to the π electron network of the ligands. The ligands vary from non-aromatic cyclo-octatetraene (COT), aromatic toluene, *p*-xylene, mesitylene, and hexamethylbenzene, to polycyclic aromatic hydrocarbons (PAHs) consisting of 2-7 benzene rings fused or connected together by C-C bonds (biphenyl, naphthalene, pyrene, perylene, and coronene). This work investigates how each metal with different identity coordinates to various ligands and how such

interaction can affect the molecular and electronic structures of the resulting complexes. More specific background and motivation to study individual complex is presented in each chapter.

Recently, many studies in organometallic chemistry have expanded into the gas phase systems.[11,12] These systems do not experience the interference from solvents or counterions, hence the fundamental metal-ligand interactions can be illustrated. The structures, interactions, and thermodynamics of metal containing molecules in the gas phase are widely investigated by the spectroscopic techniques. The following section discusses briefly photoelectron and photoionization spectroscopic techniques used in this work.

1.1. Spectroscopy

The photoelectron spectroscopy (PES) measures the energy of electrons emitted from the sample by the photoelectric effect.[13,14] When a neutral molecule absorbs a photon ($h\nu$) with fixed energy greater than or equal to the ionization energy (IE), an electron with kinetic energy (KE) will be ejected.

$$M + h\nu \rightarrow M^+ + e^- \tag{1.1}$$

By energy conservation, the IE of a neutral molecule can be determined by the energy difference of the initial photon and kinetic electron.

$$IE = h\nu - KE \tag{1.2}$$

Therefore, the first IE of the molecule is the minimum energy required to ionize the neutral molecule. Based on the Koopmans' theorem, this IE equals the negative of the molecular orbital energy. Hence, the PES spectrum can provide the information about the bonding character of molecular orbitals. Moreover, the conventional PES method does not require a tunable light source and is quite easy to implement. However,

photoelectrons with small kinetic energy differences are often hard to separate. This limits the practical resolution of the PES method.

To improve the resolution of PES, Muller-Dethlefs, Sander, and Schlag developed zero electron kinetic energy (ZEKE) spectroscopy.[15] In the ZEKE method, only the photoelectrons with near-zero kinetic energies are detected and a tunable light source is used for the experiment. Therefore, the incident photon energy equals the ionization threshold of the molecule. In principle, the spectral resolution of the ZEKE technique is only limited by the bandwidth of the photon source. In practice, the ZEKE spectra of metal complexes have a resolution of a few wavenumbers.[16]

The time-delayed pulsed field ionization (PFI)-ZEKE technique provides high collection efficiency for the ZEKE electrons and is easy to apply. In this technique, neutral molecules are initially photoexcited to high-lying ($n > 150$) and long-lived Rydberg states. After a short time delay, a small electric field is applied to ionize the molecules and the resultant ZEKE signal is then measured. During the delay, electrons from direct photoionization are removed by a small electric field. Since the ZEKE signal is detected from the field ionization of the Rydberg states just below the ionization continuum, the IE from the PFI-ZEKE spectroscopy is slightly red shifted. The ionization energy shift (ΔIE, cm^{-1}) induced by the field can be calculated by the relation

$$\Delta IE = C\, E_F^{1/2}, \tag{1.3}$$

where E_F in Vcm^{-1} is the field strength. The constant C can be determined by plotting the IE values against various ionization fields and extrapolating to zero field strength.

ZEKE spectroscopy can provide very accurate IE measurement of the complex. This measurement can be used to complete the thermodynamic cycle.

$$IE(M) - IE(M\text{-}L) = D_0^+(M^+\text{-}L) - D_0(M\text{-}L), \tag{1.4}$$

where IE(M) and IE(M-L) are ionization energies of metal and metal-ligand complex, and $D_0^+(M^+\text{-}L)$ and $D_0(M\text{-}L)$ are ionic and neutral bond strengths of the complex, respectively. For many unsaturated metal complexes, the metal-ligand bond strength of

the cation is much better characterized than that of the neutral molecule.[17,18] The neutral metal-ligand bond strength can be calculated by using the measured ionic bond strength and known IE of the metal atom.

In addition to accurate measurement of the IE, ZEKE spectroscopy enables the measurement of low frequency metal-ligand vibrations. The vibrationally resolved ZEKE spectrum provides direct evidence of the equilibrium geometry changes upon ionization. Hence, these vibrational modes can be used to understand metal-ligand bonding. The simulation calculated from the quantum chemical calculations in combination with the Franck-Condon principle can be used to compare with the experimental spectrum to analyze and determine the structure of the metal containing complexes.

In addition to the PFI-ZEKE spectroscopy, resonant two-photon ionization (R2PI) spectroscopy using UV and IR has been implemented to measure the high-frequency vibration modes of the neutral complex. In many cases, R2PI provides spectroscopic information that is unavailable to single-photon spectroscopic methods. The R2PI method involves a first photon (IR) absorption to an excited vibrational level followed by a second photon (UV) absorption which ionizes the complex. An ion will result if the two-photon energies exceed the ionization threshold energy of the complex. Since PFI-ZEKE method can provide very accurate IE of the complex, R2PI method can be easily implemented by fixing the UV below the IE. The UV alone does not ionize the complex, and IR plus UV results in the ion signal. The R2PI spectrum is obtained by measuring the mass-selected ion signal as the photoexcitation IR laser is scanned.

Mass analyzed threshold ionization (MATI) spectroscopy is quite similar to the ZEKE technique. Instead of collecting the ZEKE electrons, ions are collected in MATI. The MATI method typically provides similar resolution as ZEKE spectroscopy with the advantage of mass selectivity. However, MATI technique requires much higher electrical field to separate the directly photoionized ion from the MATI ion. Therefore, a larger Stark effect is expected. In Chapter 5, the MATI technique has been used to identify the atomic transitions. Prior to the MATI measurement, the presences of these atomic transitions were suspected from the spectral analysis due to their exceptionally

narrow bandwidths (< 2 cm^{-1} in our experimental setup). In comparison, the typical linewidths of the ZEKE spectrum in Ar carrier gas is about 5 cm^{-1}.

1.2. Quantum Chemical Calculations

The computational studies are used to compare with and analyze the experimental spectrum. From the computational analysis, the isomers can be identified by geometry optimization and characterized through vibrational frequency calculation. Geometry optimization is the process to determine stationary points on a potential energy surface. The stationary point is the geometry when the first derivative of the energy with respect to all displacements of the nuclei is zero. When the change in the displacement of the stationary point leads to an increase in total energy in all the directions, it is a local minimum on the potential energy surface as the function of the coordinates of all the nuclei. The local minimum with the lowest energy is the global minimum which is the most stable isomer. When the coordinate change leads to a decrease in energy along one direction, the stationary point is a transition state. The vibrational frequencies can be predicted by calculating the second derivatives with respect to all atomic coordinates and used to characterize the stationary points. If the frequencies are all positive (real), the stationary point is a local minimum. When there is an imaginary (negative) frequency, the stationary point is a transition state. Many methods are available for these calculations and some of the computational methods will be introduced briefly in following subsections.

1.2.1. Ab Initio Calculations

In quantum mechanics, the total energy (E) of the molecule can be determined with known wavefunction (ψ) by solving for the time-independent Schrödinger equation.

$$\hat{H}\psi = E\psi, \tag{1.5}$$

where $\hat{H}$ is the Hamiltonian operator. The method involves the Born-Oppenheimer approximation which allows the electronic and nuclear motions to be separated by freezing the slowly moving nuclei in place compared to the fast moving electrons during the calculation.[19] This approximation greatly simplifies the underlying Schrödinger equation. The ab initio method has the advantage that the converged result will be the most accurate and precise of all the currently available methods in molecular modeling, when all the approximations are sufficiently small and there are enough set of basis functions. However, in practice, it is feasible only for small and simple chemical systems. For example, the Schrödinger equation can be solved accurately for the hydrogen atom. The results are given in the forms of the wave function for atomic orbitals and the relative energies of the various orbitals. For larger systems, approximations need to be made for practical reasons such as computational time and memory usage.

1.2.1.1. Hartree-Fock Theory

The simplest type of the ab initio electronic structure calculation is the Hartree-Fock (HF) method. In the HF method, the best possible solution is at the HF limit, which is the limit of the HF energy as the basis set approaches completeness. In the quantum calculations for molecules, the molecular orbitals are formed as a linear combination of atomic orbitals (LCAO). The solutions of the HF equation are the atomic orbitals (wavefunction for one-electron in the atom). Since Slater-type orbitals (STOs) are similar to atomic orbitals of the hydrogen atom, they are used as basis function. However, for fast calculation of two electron integral, Gaussian-type orbitals (GTOs) are used. A number of GTOs are summed up with different exponents and coefficients to approximate the shape of STOs.

The solution from the HF method is found by the iterative self-consistent-field (SCF) method. A set of approximate orbitals are used to initialize the calculation for the first cycle. The solution of the first orbital is used to construct a new orbital for the next cycle. The corresponding energies from SCF cycles are compared, and the best solution is determined to have the lowest electronic energy. These HF orbitals are optimized until the change in the electronic energy between two cycles lies below a threshold. The basis

of this method is that all the electrons in the system are treated to be delocalized over an entire molecule with a smooth distribution of negative charge. Since the HF method neglects the electron correlation, it cannot reach to the exact value. Therefore, a number of new approaches have been devised.

1.2.1.2. Møller-Plesset Perturbation Theory

Møller-Plesset perturbation theory (MP)[20] improves the HF method by adding electron correlation effects as a small perturbation, usually to the second (MP2), third (MP3), and fourth (MP4) order. Since the exactly solvable portion of the Schrödinger equation corresponds to the HF Hamiltonian operator, it is known as post-HF ab initio method. In perturbation theory, the total Hamiltonian operator ($\hat{H}$) is expressed in a form

$$\hat{H} = \hat{H}_0 + \lambda\hat{H}_1, \tag{1.6}$$

where $\hat{H}_0$ is the HF Hamiltonian operator, $\hat{H}_1$ is the difference between the exact electronic and HF Hamiltonian operators, and λ is a perturbation parameter. The wavefunction and energy of the system is expressed as power series of λ as

$$\psi = \psi_0 + \lambda\psi_1 + \lambda^2\psi_2 + \ldots + \lambda^n\psi_n \tag{1.7}$$

and

$$E = E_0 + \lambda E_1 + \lambda^2 E_2 + \ldots + \lambda^n E_n, \tag{1.8}$$

where ψ_n and E_n are the nth order corrections to the wavefunction and energy, respectively. The computer time, memory, and disk space increase rapidly with the size of the system being studied increase. This is because large sets of the wavefunctions are involved in the calculation. Therefore, it is hard to tackle the large and complex systems with post-HF methods.

1.2.1.3. Density Functional Theory

Density functional theory (DFT) is a computationally affordable quantum mechanical theory. This is because DFT has simpler equations compared to traditional ab initio methods based on complicated many-electron wavefunctions. In the traditional ab initio methods, the wavefunction depends on the spatial and spin coordinates of all electrons. However in the DFT method, the wavefunction has been simplified through the use of the electron density functional and hence given the name, "density functional theory". In addition, the accuracy of the DFT is quite comparable to some of the post-HF methods, such as the MP perturbation theory. Therefore, DFT is widely used to investigate the electronic structure of many-electron systems and is one of the most popular and versatile methods in computational chemistry.

In DFT, the total energy of the molecular system is expressed as

$$E[\rho(r)] = T[\rho] + E_{ne}[\rho] + E_{ee}[\rho], \qquad (1.9)$$

where $T[\rho]$ is the kinetic energy, and $E_{ne}[\rho]$ and $E_{ee}[\rho]$ are the potential energies from nuclear-electron attraction and electron-electron repulsion, respectively. $\rho(r)$ is the electron density as a function of the three spatial coordinates. The kinetic and electron-electron interaction energies are the same for any N-electron system (universal functionals), however the nuclear-electron attraction energy is system dependent (non-universal functional).

In DFT method based on the Kohn-Sham (KS) formulation,[21] most of the electron kinetic energy (kinetic energy functional of such a system) is calculated and known exactly. On the other hand, the remaining exchange-correlation part of the total-energy functional remains unknown and must be approximated in molecular calculations. These unknown components of the electron energy, which includes the external potential and the effects of the Coulombic interactions between the electrons, are combined into a single term called the exchange-correlation energy. This term is a functional of the electron density. The KS method provides the exact wavefunction of only the non-interacting electron model system. Therefore, even though orbitals and orbital energies

from KS method are typically quite close to those of the real system, the functional of the electron density needs to be calculated.

For chemical applications, many exchange-correlation functionals have been developed. The exchange part of the energy can be expressed as hybrid functionals by including a component of the exact exchange energy calculated from the HF theory. The accuracy of the calculation can greatly improve if the approximations used in the theory are refined to express the exchange and correlation interactions better. In DFT, the combination of the exchange functional from Becke's three parameter hybrid functional (B3)[22] with the gradient-corrected correlation functionals derived by Lee, Yang, and Parr (LYP)[23] and by Perdew (P86)[24,25] are two of the most popular hybrid functionals. The results obtained from these functionals are typically sufficient in accuracy for most molecular systems. The accuracy is roughly comparable to that of the MP2 method at a much lower cost and these methods are used to analyze for the molecular systems studied in this dissertation.

Unfortunately, since the explicit form of the functional is not known exactly, DFT lacks a systematic improvement for this approximate functional. This is quite different from the traditional wavefunction-based methods. Hence, in the current DFT approach, it is not possible to estimate the error of the calculations without comparing them to other methods or experiments. In this dissertation, the calculations from the DFT methods are compared with the experimental values to determine the reliability of the calculations.

1.3. Franck-Condon Spectral Simulations

1.3.1. The Franck-Condon Principle

In ZEKE spectroscopy, the intensities of the vibronic transitions are governed by the Franck-Condon (FC) principle.[26-28] According to the principle, the intensity of a given vibronic transition is proportional to the square of the transition moment integral. The transition moment integral, M_{ev} can be expressed as

$$M_{ev} = \int \psi^*_{e'v'} \, \mu \, \psi_{e''v''} \, d\tau, \qquad (1.10)$$

where $\psi_{e''v''}$ and $\psi^*_{e'v'}$ are vibronic wavefunctions of the initial and final states, respectively, and μ is the molecular dipole moment operator. The dipole moment operator is determined by both charges and locations of the electrons and nuclei and can be expressed as two parts consisting of the electronic μ_e and nuclear μ_N dipole operators.

$$\mu = \mu_e + \mu_N \qquad (1.11)$$

According to the Born-Oppenheimer approximation[19], the nuclei are stationary compared to the movements of the electrons, and the electronic and nuclear dipole moment operators are independent to each other.

$$M_{ev} = \int \psi^*_{e'} \, \psi_{v'} \, (\mu_e + \mu_N) \, \psi_{e''} \, \psi_{v''} \, d\tau$$

$$= \int \psi^*_{e'} \, \mu_e \, \psi_{e''} \, d\tau_e \int \psi^*_{v'} \, \psi_{v''} \, d\tau_N$$

$$+ \int \psi^*_{e'} \, \psi_{e''} \, d\tau_e \int \psi^*_{v'} \, \mu_N \, \psi_{v''} \, d\tau_N \qquad (1.12)$$

Since the electronic wavefunctions of two different states are orthogonal, the last term is zero. Therefore, the transition moment integral equation can be simplified.

$$M_{ev} = \int \psi^*_{e'} \, \mu_e \, \psi_{e''} \, d\tau_e \int \psi^*_{v'} \, \psi_{v''} \, d\tau_N \qquad (1.13)$$

where the first term in the product corresponds to the electronic transition moment integral and the second term is the vibrational overlap integral. The intensity (I) of a vibronic transition is proportional to the square of the transition moment integral.

$$I_{e'v' \leftarrow e''v''} \propto \left| \int \psi^*_{e'} \, \mu_e \, \psi_{e''} \, d\tau_e \right|^2 \left| \int \psi^*_{v'} \, \psi_{v''} \, d\tau_N \right|^2 \qquad (1.14)$$

The essential strengths of an electronic transition are measured by the first term, whereas the second term determines the intensity distribution among the vibrational bands and called Franck-Condon factor (FCF).

During an electronic transition, a change from one vibrational energy level to another will be more likely to happen if two vibrational wavefunctions overlap more significantly. Since electronic transitions are very fast compared to nuclear motions, the largest overlap of the wavefunctions can be achieved when there is a minimal change in the nuclear coordinates. Therefore, the relative intensities of the vibronic transitions can be used as a guide to determine the structural difference between two electronic states (the initial neutral to the final ionic states in the ZEKE experiment). For example, if a ZEKE spectrum contains a strong 0-0 transition and a short vibrational progression, this indicates that the structural change between the neutral and ionic states is small. Conversely, if there is a long vibrational progression with a weak 0-0 band, there is a large structural change upon ionization. The structural comparison can be visualized by comparing the experimental ZEKE and simulated spectra.

1.3.2. Multidimensional Franck-Condon Factors

The simulated spectrum is obtained by the calculations of the multidimensional FCFs of the vibronic transitions from the neutral to the ionic states. The calculations use the theoretical equilibrium geometries and harmonic vibrational frequencies and normal modes of the neutral and ion. The normal modes of the ion may be displaced and rotated from those of the neutral states, known as Duschinsky effect.[29] A linear and orthogonal transformation between the normal coordinates of the neutral and ionic states are assumed in the Duschinsky transformation, however this transformation is typically non-linear and non-orthogonal according to the axis-switching effect.[30-32] Many attempts were made to determine the exact expression for the calculation of the multidimensional FC overlap integrals.[33-50] The FCF program, used in this dissertation, treats the axis-switching effects by applying a zeroth order Eckart matrix, and off-diagonal elements are diminished with each rotation. More mathematical and computational details can be found in Shenggang Li's Ph.D. dissertation.[51] The FCF program (v2.3) used for the

studies is improved by Li and Clouthier[51] from the original version[52,53]. The FCF program has run in MS-DOS command prompt, operated by Windows XP.

The PreFCF program (v2.3) is used to obtain an input file (fcf.inp) which contains the atomic masses, equilibrium geometries, harmonic vibrational frequencies, and normal coordinates of the neutral and ionic complexes. Through the usage of the program, the input parameters including temperatures, vibrational energies, active modes and quanta, spectral range and linewidths, and display threshold of the simulation can be adjusted to compare with the experimental spectrum clearly. A Boltzmann distribution and a Lorentzian line shape are considered to simulate the spectrum at a finite temperature and experimental linewidth, respectively.

1.4. The Scope of the Dissertation

The aim of this dissertation is to determine the structures of the metal-ligand complexes and investigate the interactions between the metals and various types of ligands. The ligands used in this study are aromatic or non-aromatic cyclic hydrocarbons, and the metals include either transition metals or Li. From the experiment, accurate IE of metal-ligand complexes are measured along with metal-ligand and/or ligand-based vibrational frequencies of the neutral and ionic complexes. From the IE of the complex, bond energy differences between the neutral and ionic species can be determined. The vibrational frequencies measured by PFI-ZEKE spectroscopy provide structural information which is used to identify the metal binding modes by comparing with theoretical calculations.

The experimental setup and computational methodologies are presented in Chapter 2. Since various metals and ligands are involved, the methods for preparing the metal complexes are varied. The detailed methods to introduce metal and ligand and how to analyze produced complexes are described in each chapter. For the theoretical part, quantum chemical calculations are performed to simulate the spectrum and compared with the experiment to determine the structures of the complexes. The complexes presented in this dissertation can be categorized into six different groups. Chapter 3 presents the complexes of the group III transition metals (Sc, Y, and La) with a non-

aromatic hydrocarbon molecule, cyclo-octatetraene (COT). The metal coordination effect on the non-aromatic and bent ring of the ligand is investigated in this chapter. In Chapter 4, Sc metal complexes with methylbenzene ligands are studied to identify the methyl substitution effects on the benzene ring. From this study, how the Sc metal coordination can disrupt the delocalized π electrons in the methylbenzene ligands has been investigated. Additionally, methyl substitution effects upon different metal coordination are studied in Chapter 5. This includes Ti, V, and Co complexes of hexamethylbenzene. Chapter 6 discusses the rotational isomers and isomer conversion of group VI transition metal (Cr, Mo, and W)-bis(toluene) sandwich complexes. In Chapter 7, the transition metal group IV (Ti, Zr, and Hf) complexes with the aromatic ligand, biphenyl is considered. This is a continuing study of Sc-biphenyl complex with clamshell structure studied by Bradford R. Sohnlein.[54] In chapter 8, the interactions between the PAHs and Li metal atom are investigated. PAHs have two or more benzene rings fused together linearly or non-linearly (naphthalene, pyrene, perylene, and coronene). The preference of metal binding to the benzene ring with higher aromaticity and π electron density has been determined. Lastly, Chapter 9 summarizes the IEs of the metal complexes and metal-ligand stretching frequencies of the metal- complexes studied in this work. In addition, the accuracy of theoretical data has been determined by comparing with the experimental measurements. The experimental and theoretical studies on these metal-ligand complexes can be used as simple models to refine the understanding of the structures and bonding schemes in metal-ligand systems. Furthermore, this information can be applied to more complex systems that involve multiple metal-ligand interactions that occur throughout chemistry.

CHAPTER 2. METHODOLOGY

2.1. Experimental Procedure

2.1.1. Complex Formation and Detection

Metal-ligand complexes in a supersonic jet are studied by PFI-ZEKE spectroscopy. The schematic diagram of the home-built laser-vaporization cluster beam ZEKE spectrometer is displayed in Figure 2.1. It consists of two vacuum chambers, pumped by two main vacuum pumps backed by several mechanical pumps, and various electronic devices. The metal-ligand complexes are produced by the interaction of metal atoms with the organic ligand of interest in a cubic chamber called source chamber, and the lengths of each sides are fourteen inches. It houses the metal cluster source and is evacuated down to $\sim 10^{-7}$ Torr by an oil diffusion pump (2200 L/s, Edwards Diffstak 250/2000M), backed by a two-stage mechanical rotary pump (40 L/s, Edwards E2M40). The pressures in this chamber and the foreline are measured by an ion gauge (Edwards AIM-S-NW26) and an active pirani gauge (Edwards APGX-L-NW25), respectively, which are controlled by an active gauge controller (Edwards D386-51-800).

The complex mixture is carried by the intense gas pulses, delivered by a homemade piezoelectric pulsed valve.[55] The inert gases, such as He, Ar, (Ultra High Purity, Scott-Gross) or He/ Ar mixtures of appropriate ratio, are used with the backing pressure varying from 20 to 80 psi, depending on the experiments. The metal atoms are generated by laser vaporization of an appropriate rod by a second harmonic output from the pulsed neodymium doped yttrium aluminum garnet (Nd:YAG) laser (Continuum Minilite II, 532 nm, 3 ~ 5 mJ). The metal rod is translated and rotated by a motor-driven mechanism (Micro Motor Electronics 1516E012S) to ensure each laser pulse ablates a clean and fresh surface, and hence stabilizes the metal vapor production throughout the experiment. To increase the production of metal atoms, a 30 cm focal length lens is used to focus the laser beam onto the surface of the metal rod. In addition, the speed of motor rotation is adjusted to maximize the signal, since it can also affect the stability and

amount of the metal vapor. The methods of ligand introduction depend on individual organic compounds. Vapor of a liquid ligand is introduced at room temperature through a stainless-steel capillary (inner diameter of 0.053") to a small collision chamber (~ 1.5 mL) downstream from the ablation source, prior to expansion into the vacuum chamber. The amount of the ligand vapor introduced to the chamber is controlled by a main gas valve and a needle valve. Ligands in the solid state are placed inside a copper oven where they are heated to an appropriate temperature by a heating cartridge with temperature being controlled by a thermo-controller (Omega CN2110). Water circulating copper tubing is bound around the face plate surface of the piezoelectric pulsed valve to protect the valve from overheating. To make metal complexes of PAHs, the rods made of metal and ligand powders are directly vaporized by the ablation laser. Typically, the rods made of soft metal and PAH powders are strong and last long in the laser ablation. The methods to prepare the mixture rods will be discussed in Chapter 8 with more details. The metal complex mixture vapors are expanded through a nozzle (2 cm in length with inner diameter of 2 mm) into the vacuum to form a supersonic jet. The supersonic expansion converts the rotational and vibrational internal energies of the molecular species to translational energy along the molecular beam axis. Consequently, the vibrational temperatures of molecules are reduced, improving the spectral resolution and simplifying the spectrum. The temperature of the molecule can be further reduced by the use of heavier carrier gas, Ar, which can reduce the vibrational temperature to about 50K. The vibrationally cooled molecular beam is collimated and selected at about a few centimeters downstream from the nozzle by a skimmer (inner diameter of 2 mm). The molecular species pass through a pair of deflection plates to remove residual ionic species which are produced by laser vaporization. One of the plates is charged with +500 V from a dc high voltage power supply (Stanford Research Systems PS350), while the other is grounded. Thus, only neutral molecules enter the spectroscopy chamber and are ionized for the detection. The source and spectroscopy chambers are separated by a gate valve (MDC GV-2000V-P). The gate valve is electrically controlled and will close when an unexpected high pressure is detected by the ion gauge in the spectroscopy chamber (i.e. beyond the pressure set point for the ion gauge). This function works as a protection for the detector in the spectroscopy chamber.

The ZEKE spectrometer is housed in the spectroscopy chamber. The chamber consists of a two-field, space-focused, Wiley-McLaren time-of-flight (TOF) mass spectrometer with a 34 cm long flight tube and a dual microchannel plate (MCP) detector (Burle 25/12/12 D EDR 40:1 MS) to detect ions and electrons. The entire spectrometer is encased in a cylindrical, double-walled, μ-metal shield to block any external magnetic fields. The μ-metal contains about 75 % nickel and 15% iron with small amount of copper and molybdenum. This metal alloy is very effective at screening static or low-frequency magnetic field due to its high magnetic permeability. The chamber is evacuated by two turbomolecular pumps (450 L/s, Seiko Seiki STP451), each backed by a two-stage rotary mechanical pump (3.95 L/s [237 L/min], Edwards RV12). The pressure in the chamber reaches to $\sim 10^{-9}$ Torr in standby condition and increases to $10^{-6} \sim 10^{-7}$ Torr, when the molecular beam is introduced. The vibrationally cooled molecular species in the spectroscopy chamber are photoionized by the frequency doubled output from a dye laser (Lumonics HD-500) pumped by the second or third harmonic of a second Nd:YAG laser (Continuum Surelite II). The output of a tunable dye laser is frequency doubled by an angle-tuned BBO (beta-$Ba_2B_2O_4$) crystal in an autotracker (Lumonics HyperTRAK-1000). The frequency of the laser is controlled by a personal computer unit, which is interfaced with the dye laser. The ionized species are extracted and accelerated upwards towards the MCP detector by a dc voltage applied on a pair of cylindrical metal cans. Four one-inch diameter holes are on four perpendicular sides of the outer can, where the molecular beam and the photoionization laser beam pass through the chamber and are perpendicular to the flight tube. For the homogenous electric field, the holes at the bottom of the extraction cans are covered with a gold mesh of 95 % transmittance. Each MCP consists of several million independent channels. If two or more MCPs are operated in series, a single input event will generate a pulse of 10^8 or more electrons at the output. Incident electrons or ions enter and hit a channel wall, emitting secondary electrons. These electrons are accelerated by an electric field applied by a voltage across the ends of the MCP. They in turn strike the channel surface, producing a large amount of tertiary electrons. This process is repeated many times along the channel, producing several thousand electrons emerging from the rear of the plate. The similar electron amplification occurs in the second plate. Higher electron

acceleration induces stronger electron collision to the wall, higher production of secondary electrons, and in turn, higher amplification of the signals. To detect ions, a dc potential of -1950 V is applied to the input of the voltage divider unit by a high voltage power supply (Stanford Research Systems PS350). The voltages on each MCP and anode are measured and indicated in Figure 2.2. From this setup, each of MCP is provided with about -900 V, and the signal amplification of 10^6 to 10^7 is achieved. The augmented analog signal from the detector is further amplified by a preamplifier (Stanford Research Systems SR445), averaged by a boxcar integrator (Stanford Research Systems SR250), and digitally converted by an analog-to-digital converter. The resulting digital output is stored in a personal computer.

2.1.2. Timing Sequence and Ion Characterization (Time-of-Flight Mass Spectrometry)

In a pulsed experimental scheme, the synchronization of each event is crucial. A pulsed delay generator (Stanford Research Systems DG535) is used to control the timing of the gas, two laser, and electronic pulses. First of all, the home-made pulsed valve driver, which controls the piezoelectric disk, is triggered. This driver controls the time, width, and voltage magnitude of the gas pulses. After 10 - 100 μs of delay, the flashlamp of the vaporization Nd:YAG laser (Minilite) is triggered. This delay is due to an operation time of the piezoelectric pulsed valve. The vaporized metal atoms carried in the carrier gas mixes with the vapors of an organic ligand. The mixtures collide with each other to form various products. After the supersonic expansion, the cooled molecular species are photoionized by a frequency doubled UV laser. The second Nd:YAG laser is used to pump the dye laser, which in turn doubles its frequency by a doubler. Therefore, there is almost no time delay between the pump laser beam and frequency doubled UV laser beam. The flashlamp of the second laser is triggered after triggering the flashlamp of the vaporization laser, and the time delay varies depending on the carrier gases (200 - 300 μs with He and 700 - 900 μs with Ar). In the ZEKE experiments, a ~3 μs time delay for the pulsed electric field is applied after the UV photoexcitation. The oscilloscope (Tektronix Digital Phosphor Oscilloscope TDS3000) is

triggered by the same trigger used for the pulsed electric field to monitor the appearance of the various ionized molecular species. The ion signals are displayed as a function of the flight time.

Since a single extraction field is used to extract and accelerate the cations with +1 charge, the kinetic energies of all ions during the flight from the ionization region to the front of MCP are the same. Therefore, the various mass to charge ratios can be determined by their relative flight times (TOF mass spectrometry). For example, an ion peak at 3.66 μs appears in the mass spectrum only when an aluminum rod is ablated in the source chamber. This peak corresponds to the signal of the aluminum cation. The flight time comparison with the aluminum peak can be used to calculate the mass of the molecular cations present in the molecular beam, hence the identification of the species can be achieved. The mass of the molecule can be calculated by the following formula.

$$\text{Mass (1)} = \left[\frac{\text{Time (1)}}{\text{Time (2)}}\right]^2 \times \text{Mass (2)} \tag{2.1}$$

The more reliable way is to use the time of the metal atomic ion as a reference to define the masses of the ion peaks in a particular metal system. Since only the metal and ligand vapors are introduced into the chamber, the identification of molecular species is often straightforward through the mass determination.

2.1.3. PIE Spectroscopy

Prior to ZEKE measurements, the ionization thresholds are estimated by photoionization efficiency (PIE) spectroscopy. When the incident laser energy exceeds the IE of a molecule, the molecule ionizes. A PIE spectrum is obtained by recording the intensity of a mass-selected ion signal, while scanning the photoionization laser wavelength. The onset between the baseline and sharp increase of the ion signal indicates the first ionization threshold of the molecule. Since a dc electric field is applied in the ionization region, the IE value estimated from the PIE spectrum is shifted by the Stark field effect. Usually +2500 V and +1700 V are applied to outer (1) and inner (2) cans,

respectively (can numbering denoted in Figure 2.1). These two cans are separated by an inch. The more positive voltage in the outer pushes the cations into the acceleration region. This field is used for both ionization and extraction of the molecules. Therefore, the ionization threshold estimated from the PIE spectrum is reduced by this electric field. The field induced shift is measured to be 6.1 x $E_F^{1/2}$ where E_F is the electric field strength of 320 Vcm^{-1} (+800 V ÷ 2.5 cm). Therefore, about +110 cm^{-1} correction is applied to the IE value measured from the PIE spectrum. However, a delay between the ionization laser and the extraction field by about 20 μs in He carrier gas (40 μs in Ar) can eliminate the need for the field correction. This pulsed field acts only as an extraction field, and the molecule is ionized by UV. Therefore, the field-free PIE spectrum can be recorded. The PIE spectra of La_3O_2, metal oxide cluster obtained with dc (a) and pulsed (b) extraction fields are presented in Figure 2.3. From the figure, it is clear that the PIE spectrum with the dc field underestimates the ionization threshold by +110 cm^{-1}, as discussed earlier. Since PIE spectroscopy records the total ion signal at each laser wavelength, its spectral resolution is typically low, rarely with resolved vibrational structures. Therefore, the ionization threshold obtained from the PIE spectroscopy is generally used to simplify the search for and correlate with the ZEKE signal.

2.1.4. ZEKE Spectroscopy

In ZEKE spectroscopy, the electrons are detected rather than the cations. The metal complexes are produced and the production is optimized in the same way as for the PIE experiment. However, the polarity of voltages applied to the extraction cans needs to be changed to detect the electron signal. The specific scheme to generate and detect the ZEKE electron is displayed in Figure 2.4. The neutral complexes are photoexcited to high-lying Rydberg states by UV laser. These excited neutral complexes are a few wavenumbers lower in energy than the ionization threshold. Electrons from directly photoionized molecules are repelled by a small dc field of -0.06 Vcm^{-1}, whereas, photoexcited molecules in high-lying Rydberg states remain undisturbed. After about 3 μs of time delay, a pulsed electric field of -1.2 Vcm^{-1} (-3 V ÷ 2.5 cm) is applied to the outer can (1), whereas the inner can (2) is grounded during the experiment. Since a large

proportion of prompt electrons with kinetic energies are collected within about 100 ns from photoexcitation, the short time delay (~3 μs) is enough to distinguish ZEKE electrons from the kinetic electrons. The pulsed field is provided by a pulsed digital delay generator. The energy shift from the small pulsed electric field (~1 V cm^{-1}) has been shown to be much smaller than spectral linewidth.[56] The pulsed field ionizes the photoexcited species to release electrons with near-zero kinetic energy and extracts electrons towards the detector with positive voltage (+2050 V). Voltage divider for electron detection is displayed in Figure 2.5. In order to collect the electrons, the reversed polarity is applied on each MCP and a large positive potential is applied to the anode to attract the amplified electron signal. In addition, small dc voltage of +5 V is applied to the TOF tube to help guide the ZEKE electrons to the detector. To simplify the search and maximize for the ZEKE signal, all experimental parameters are first optimized in the ion detection mode. To obtain a ZEKE spectrum, the ZEKE electron signal is recorded as the wavelength of the photoexcitation laser is scanned from a few hundred wavenumber below the ionization threshold to a higher energy region to find the ZEKE signal. With the identified ZEKE signal, whole range of spectrum is scanned until no further signal is detected. After each experiment, the laser wavelengths are calibrated against vanadium or titanium atomic transitions.[57]

2.1.5. IR-UV R2PI Spectroscopy

In the IR-UV R2PI experiment, an infrared optical parametric oscillator/amplifier (IR OPO/A) laser (LaserVision) is used for vibrational excitation. The schematic diagram of IR OPO/A is shown in Figure 2.6. The IR laser is pumped by a seeding Nd:YAG laser (1064 nm, Continuum Surelite III) and converts the fixed frequency into tunable radiation in the mid-infrared range. First, about 550 mJ of horizontally polarized 1064 nm laser beam (purple color in the figure) is separated by a beamsplitter (M1) into two beams. One of the beams is directed to a KTP crystal (KTiOPO$_4$, potassium titanyl phosphate) for frequency doubling. The resultant 532 nm light is reflected by three mirrors (M2, M3, and M4) and acts as a pump laser (green color) for the OPO stage. The OPO consists of a back mirror, a diffraction grating, and a tuning mirror. The back mirror

reflects both the 532 nm pumping and resonated wave, and permits fine adjustment of the cavity length. The diffraction grating is placed at grazing incidence relative to the cavity axis. The tuning mirror orients to reflect the diffraction of the resonated wave. The angle tuning of a single set of these nonlinear crystals produces continuous generation of a tunable laser (near-IR output ranging from 710 to 880 nm, blue color). The near-IR signal outputs exit the OPO and enter to the OPA stage. The remaining 1064 nm output beam is directed through a 1064 nm attenuator, M5, and M6 until they recombine with the output beam from OPO. The combined beam is then directed into a 1064 nm pumped OPA stage with four KTA crystals (KTiOAsO$_4$, potassium titanyl arsenate) for different frequency mixing. In the OPO stage, the oscillator wavelength is from 710 to 880 nm [λ(Osc)], and the pump wavelength is 532 nm. This makes the idler laser pulse from the OPO [λ(OPO)] to be 2122 to 1345 nm.

$$\lambda(\text{OPO}) = \frac{1}{\dfrac{1}{532} - \dfrac{1}{\lambda(\text{Osc})}} \qquad (2.2)$$

Then, the idler [λ(OPO)] is sent to the OPA and mixes with the 1064 nm pump for differential frequency mixing. This produces the laser wavelength [λ(OPA)] of 2134 to 5089 nm (4686 to 1965 cm^{-1}).

$$\lambda(\text{OPA}) = \frac{1}{\dfrac{1}{1064} - \dfrac{1}{\lambda(\text{OPO})}} \qquad (2.3)$$

All the crystals including OPO and OPA crystals are each controlled by a dc servo motor connected to an integral modular DSP (digital signal processing) controller. The control program, named MDRIVE with the parametric converter, is operated in Microsoft Windows operating system with a Pentium III host computer. Each motor can be calibrated individually to 10th order polynomial expansion of position as a function of wavelength. To turn on the OPO/A laser, the pump laser needs to warm up about 20 minutes to have a constant full power. Then, the 532 nm attenuator needs to be turned

slowly to the optimal angle of 23 degrees on the waveplate. It takes another 20 minutes to warm up the OPO stage before the 1064 nm attenuator is turned to 45 degrees for maximum transmission. During the operation, each motor is controlled individually for the maximum power of mid-IR. To turn it off, the opposite step is applied and both of attenuators need to be turned to zero degree position before the pump laser can be turned off. The IR OPO/A laser provides pulse energies of ~1-26 mJ in the range of 2200-4500 cm^{-1} and linewidths of ~2.0 cm^{-1}. The linewidths of the beam can be reduced as narrow as ~0.2 cm^{-1} when it is pumped with the injection seeder (Continuum FLSE-10-1-1064.175-001). However, the measurements with the injection seeder on or off make no significant difference in the linewidth of the resonant IR-UV photoionization spectra. Since the use of the seeder results a lower mid-IR power output, all of R2PI measurements are carried out without the seeder. Experimental investigations have found that the optimal signal and spectral linewidth for the molecular systems can be achieved with the IR pulse energy of 6–10 mJ. After each experiment, the IR laser wavelengths are calibrated with the photoacoustic spectra of H_2O.[58]

To record the R2PI spectrum, the IR laser beam is introduced from the opposite side of the chamber from the UV laser. The IR beam counterpropagates with the UV beam, and both laser beams are perpendicular to the molecular beam. The general scheme of R2PI spectroscopy is displayed in Figure 2.7. Typically, the IR is fired about 100-120 ns prior to the UV laser. The resultant ion signal is detected in the same time-of-flight spectrometer as that used in the ZEKE experiment. The UV laser wavelength is fixed about 400 cm^{-1} below the IE of the complex in interest, whereas the IR laser wavelength is scanned in the range of 2700- 4500 cm^{-1} to search for a C-H, N-H, or O-H stretching vibration. Since UV laser alone cannot ionize the neutral molecule, only when the IR light is in resonance with an active IR mode of the complex can the neutral complex be ionized and detected. The IR-UV photoionization spectrum provides high-frequency vibrational modes of the neutral complex.

2.2. Theoretical Calculations

In addition to the experiments, quantum chemical calculations have been used to help spectral interpretation. The theoretical calculations are used to predict molecular structures, electronic states, relative energies, and vibrational frequencies. These theoretical results are then compared with the experimental results for spectral and structural analyses. The theoretical calculations also include the geometry and frequencies of the free ligand to evaluate how metal coordination perturbs the ligand geometry. The geometry optimization and frequency calculations are carried out with the GAUSSIAN 03 program package[59] installed on the IBM supercomputer located at the CENTER FOR COMPUTATIONAL SCIENCE in the University of Kentucky. Due to its relatively low computational costs and reasonable predictions, DFT including B3LYP and B3P86 is selected to study the complexes. Typically, Pople's triple-split-valence zeta basis set is used along with diffuse functions on the heavy elements (carbons and metals) and polarization functions on the heavy elements as well as hydrogen [6-311+G(d,p)]. The B3LYP/6-311+G(d,p) method was proven to yield good predictions of IEs, vibrational frequencies, and spectral intensities of metal-aromatic complexes.[56,60,61] The heavier metal elements, for which the triple basis set is unavailable, are treated with a pseudo effective core potential (ECP) basis set, LanL2DZ (Los Alamos National Laboratory 2 double zeta).[62-64] LanL2DZ basis set treats the valence electrons independently and takes into account the influence of the inert, core electrons as a single, uniform potential. The DFT methods often yield good prediction on IEs, vibrational frequencies, and spectral simulations of metal-organic ligand complexes. However, traditional ab-initio calculation (e.g. MP2) is also carried out to compare with DFT.

The theoretical methods of studying metal complexes can be initiated by considering the structures of free ligands. The reliability of the theoretical method can be investigated by comparing the calculated molecular structures of organic ligand with the experiment. From the minimum energy structures of organic ligands, the possible metal binding sites are predicted and examined. As initial structures, the metal atoms or ions are attached to these various binding sites of the ligand and calculated to determine the ground state structures of the complexes. From the geometry optimization output,

various information including equilibrium geometry, molecular symmetry, electronic state, electronic energy, atomic charges, and molecular orbitals can be obtained. In addition, the structural comparison between the metal complex and the free ligand can provide the geometrical perturbation induced by metal coordination.

From the optimized structures of the complexes, the frequency calculations are carried out by taking the second derivatives of the energy with respect to the parameters. The frequency output files provide valuable information about the vibrational frequencies and modes and zero-point energies, which are used for the spectral analysis. If the vibrational mode contains small negative (imaginary) frequency, this indicates that the particular molecular configuration is at a saddle point on the potential energy surface and is not a local minimum. For example, methyl substituted benzene with freely rotating methyl groups may have several transition states from different methyl group angles with respect to the plane of the phenyl ring and each other. In such a case, different initial structures with various methyl torsional angles should be considered in the geometry optimization to determine the lowest energy structure. Similarly, reducing the molecular symmetry or exploring different electronic states by orbital switching may help to find minimum energy structures.

In the theoretical methodology, the complex multiplicities also need to be considered along with the structural investigation. Typically, the IEs of the ligands are much higher than those of metals. Therefore, the molecular multiplicities of the metal complexes depend on the electronic configuration of the metals. Studied systems involved in this dissertation contain both transition and main group metal elements. The main group elements, Li have very simple electronic configuration. On the other hand, the transition metals have the d orbitals, which have similar energy with the s orbitals. Therefore, numerous ways for the electrons to occupy the molecular orbitals are possible, resulting in the various electron spin multiplicities. As a result, the transition metal containing complexes consume more computational time, and the calculations are more complicated. In some cases, previous theoretical or experimental studies related to the molecular system can help the search for the lowest energy complexes.

From the frequency output files, the ZEKE spectrum of the complex can be simulated. For the simulation, the multidimensional Franck-Condon factors are

calculated from the equilibrium geometries, harmonic vibrational frequencies, and normal coordinates of the neutral and ionized complexes.[52,65] The Duschinsky effect[29] is considered to account for normal mode differences between the neutral and ionic complexes in the FC calculations. In addition, a Lorentzian line shape with the experimental linewidth is used to simulate the spectral broadening. Moreover, transitions from excited vibrational levels of the neutral complexes are simulated by assuming thermal excitations at specific temperatures using Boltzmann distribution. The best simulations at specific vibrational temperatures are used to estimate the experimental vibrational temperatures.

In this dissertation, all of the simulated spectra are shifted to the IEs measured from the ZEKE spectra, whereas the vibrational frequencies are not scaled for clear comparison. In addition, the peak intensity in each spectrum is unified by normalizing the most intense peak. Moreover, the IR intensity of each normal mode is calculated from the first derivative of the dipole moment at the equilibrium bond distance, and each IR peak is plotted with the experimental linewidth.
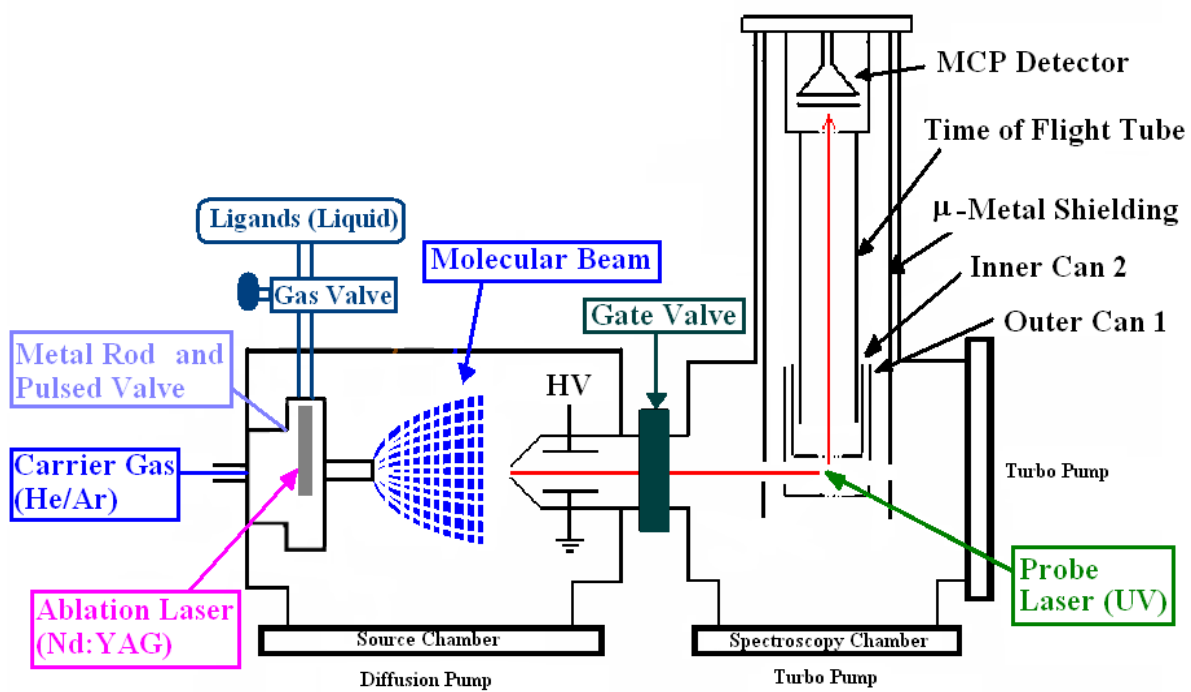
Figure 2. 1. Schematic diagram of the home-built laser-vaporization cluster beam ZEKE spectrometer.
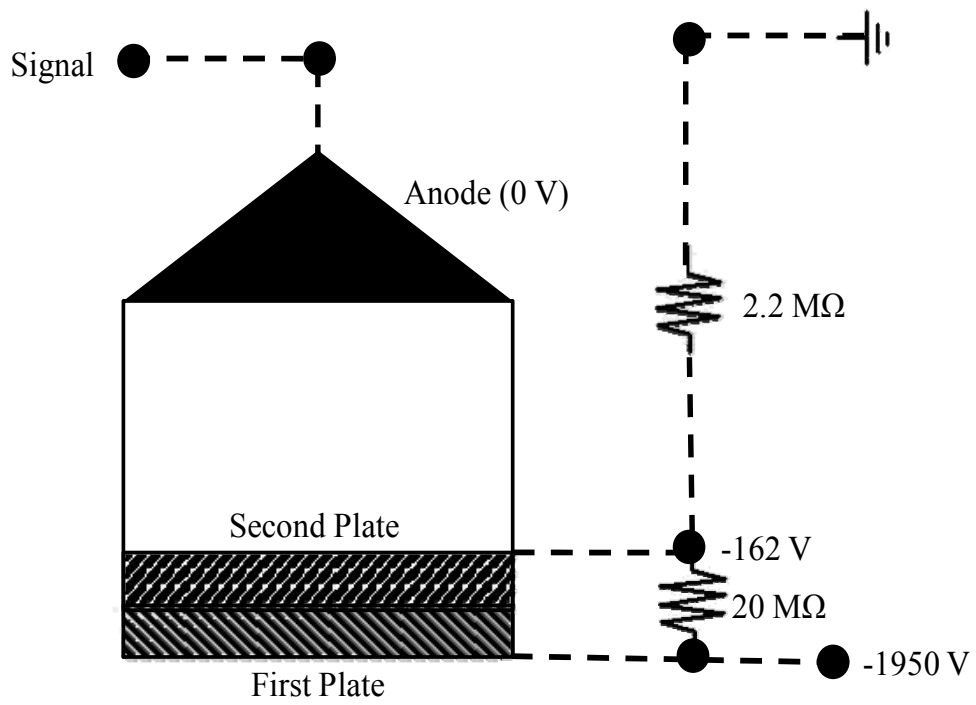
Figure 2. 2. The schematic diagram of the voltage divider used for ion detection.
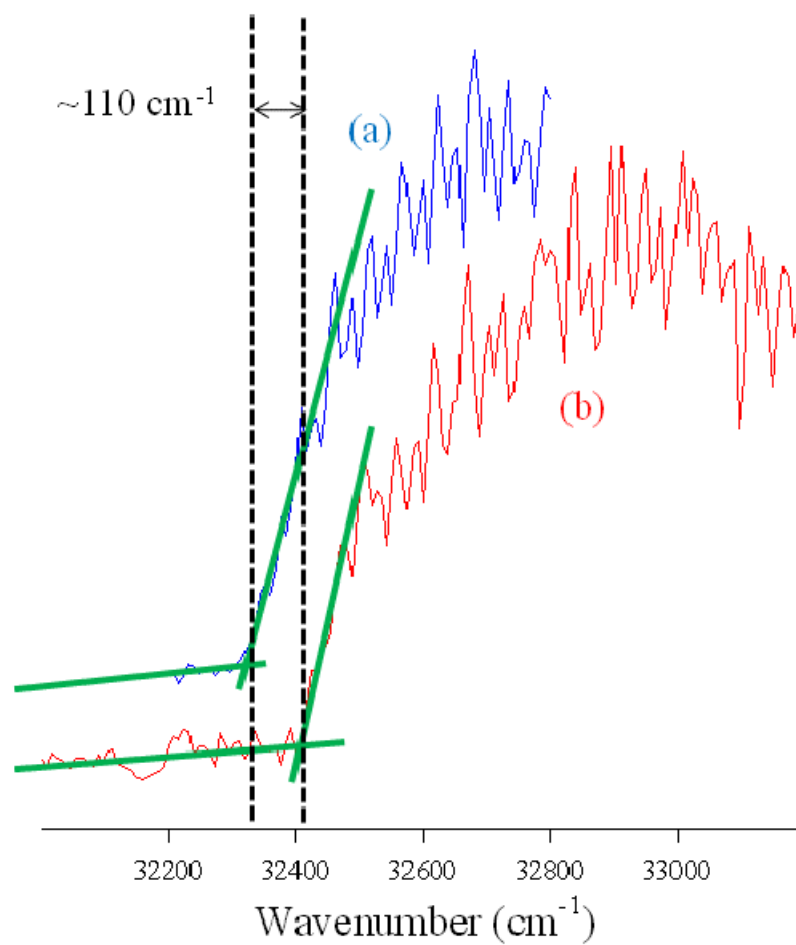
Figure 2. 3. The PIE spectra of La_3O_2 with dc (a) and pulsed (b) extraction fields.
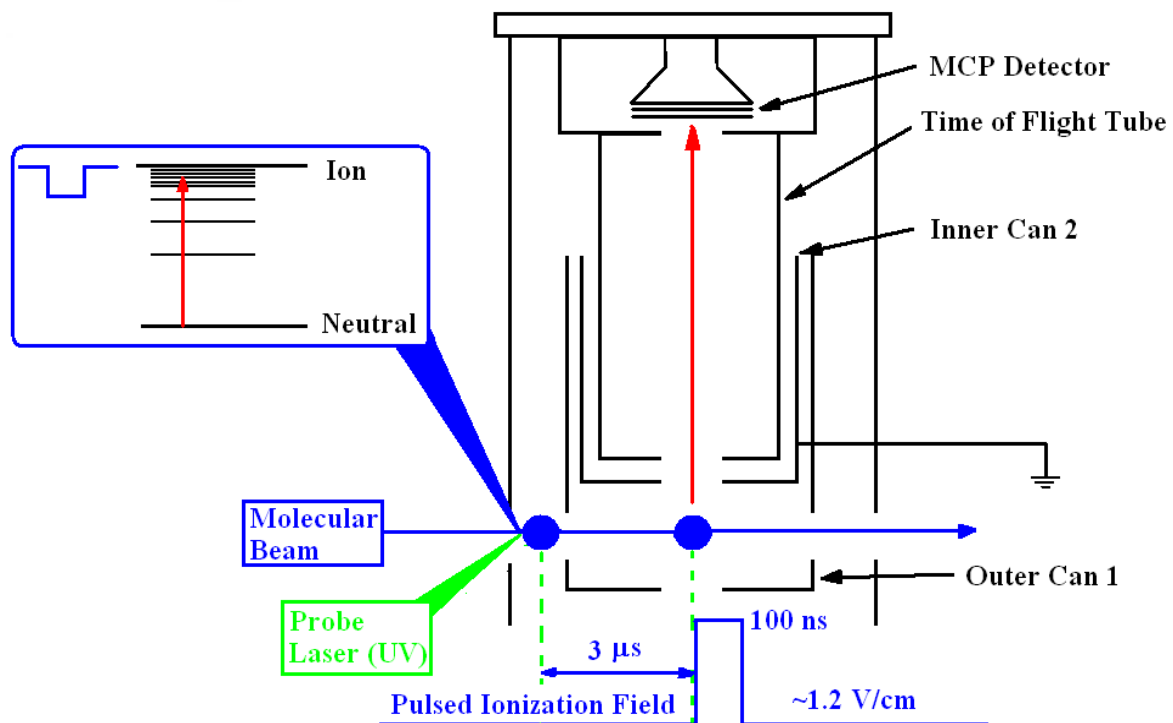
Figure 2. 4. The mechanism of the ZEKE electron production and detection.
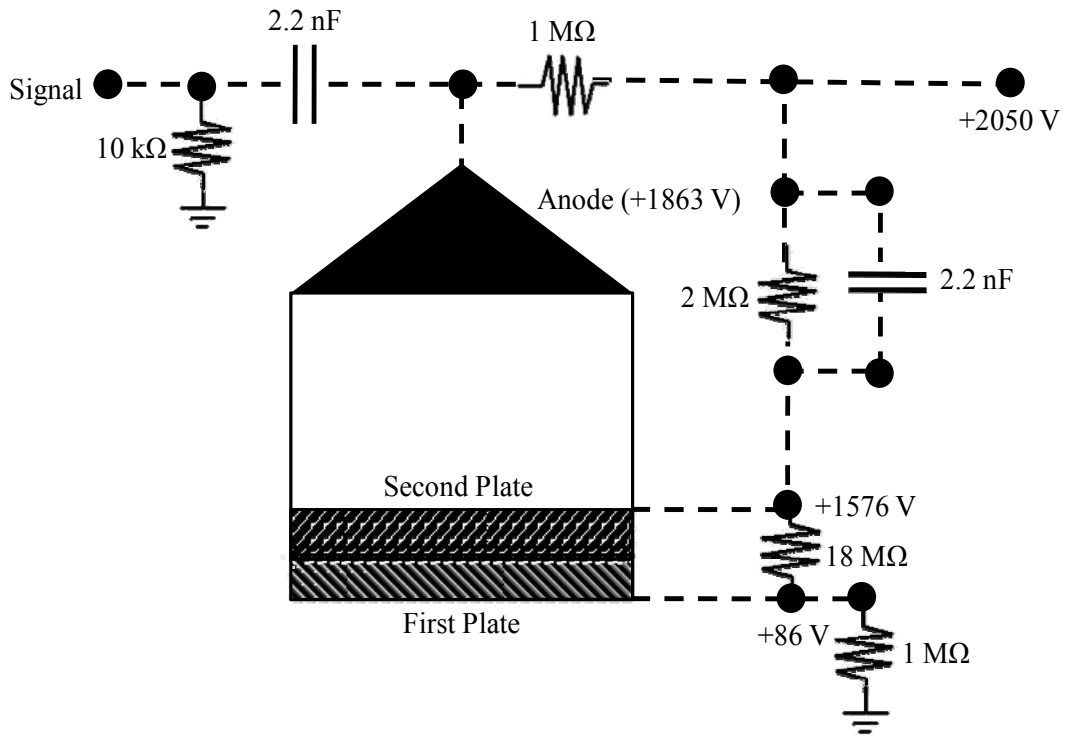
Figure 2. 5. The schematic diagram of the voltage divider used for electron detection.
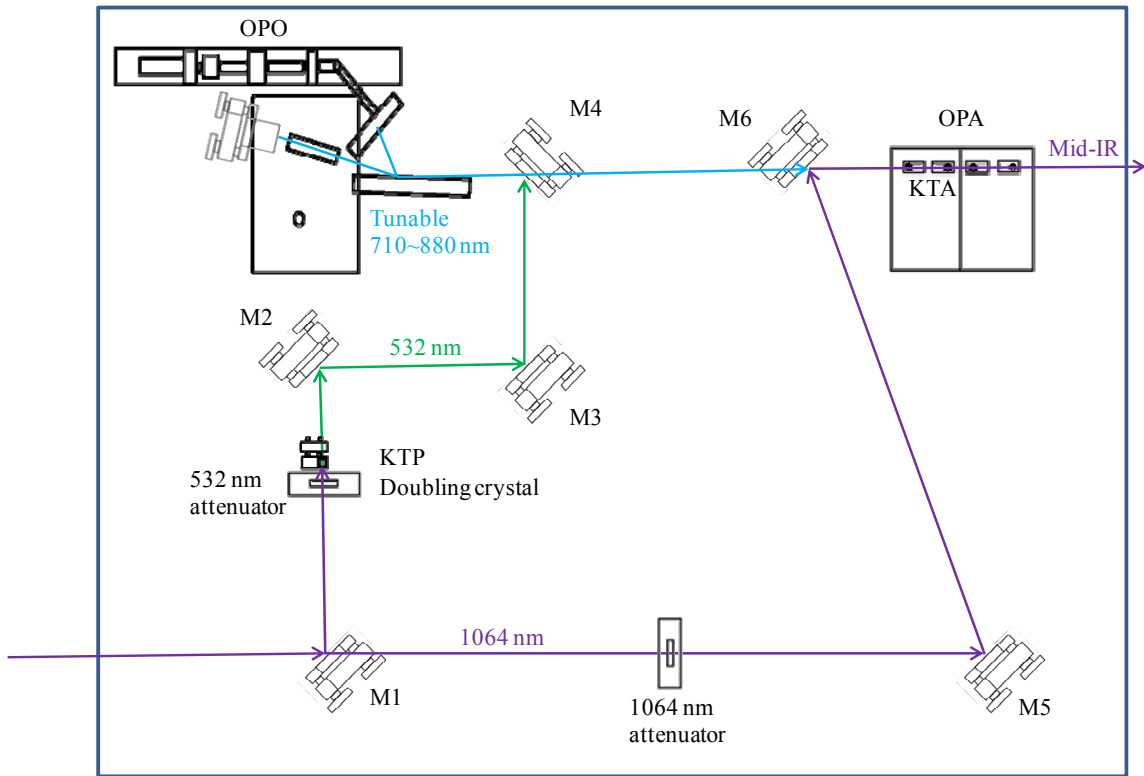
Figure 2. 6. The schematic diagram of an infrared optical parametric oscillator/amplifier (IR OPO/A) laser (LaserVision). The 532, 710~880, and 1064 nm/ mid-IR laser beams are indicated by green, blue, and purple colored lines, respectively.
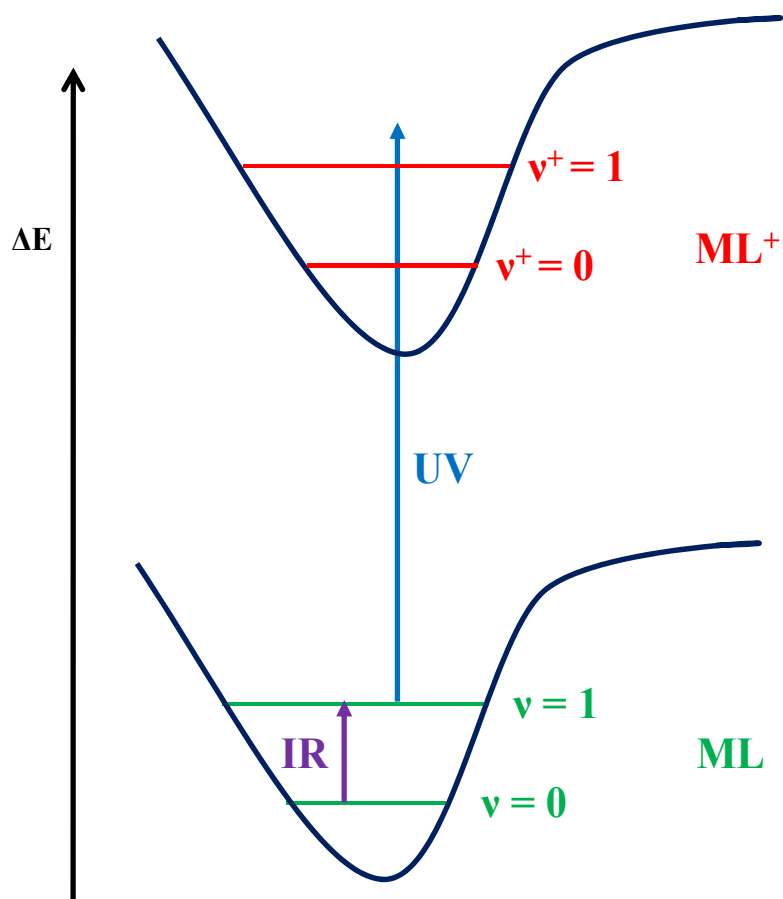
Figure 2. 7. The general scheme of R2PI spectroscopy. The IR laser excites the neutral molecule to an intermediate state and UV ionizes the molecule after 100-120 ns of delay. The resulting ion signal is recorded to find the C-H, N-H, and O-H stretching vibrations.

CHAPTER 3. METAL COORDINATION CONVERTS THE TUB-SHAPED CYCLO-OCTATETRAENE INTO A PLANAR AROMATIC MOLECULE: ELECTRONIC STATES AND HALF-SANDWICH STRUCTURES OF GROUP III METAL-CYCLO-OCTATETRAENE COMPLEXES

3.1. Introduction

Unlike benzene, 1, 3, 5, 7-cyclo-octatetraene (COT) is a nonaromatic molecule and has a tub-shaped structure in its ground electronic state.[66-69] However, one or two-electron attachment to the tub-shaped COT molecule converts it into a planar structure of D_{4h} or D_{8h} symmetry.[70-76] On the other hand, metal coordination may cause a structural change in the tub-shaped molecule as well. For example, the COT molecule has been shown to adopt a planar η^8 binding mode in actinide (Th, U, Np, and Pu) and lanthanide (La, Ce, Pr, Nd, Sm, Gd, and Tb) complexes[77-84] and nonplanar η^2, η^4, or η^6 modes (in addition to the η^8 mode) in transition metal (Ti, V, Cr, Ni, Zr, Ru, and Hf) complexes.[85-91] The diversity of the COT coordination modes has been attributed to the relative small energy barriers for its ring inversion and π-bond shifting.[92]

To investigate fundamental interactions between metal atoms and COT, several gas-phase experimental studies have been reported on the COT complexes of actinide, lanthanide, and transition metals. For actinide metals, Clark and Green reported in an early study He (I) and He (II) photoelectron spectra of [M(COT)$_2$] (M = Th and U) and discussed the major bonding interaction to be between COT π and metal $6d$ orbitals.[93] For lanthanide metals, Kaya and co-workers reported mass, photoionization, and anion photoelectron spectra of [Ln$_n$(COT)$_{n+1}$] (Ln=Ce, Nd, Eu, Ho, and Yb) and suggested that these complexes were in multiple decker sandwich structures, with Ln in +2 or +3 oxidation states and COT in -1, -1.5, or -2 oxidation states.[94-97] The formation mechanism and bonding nature of the lanthanide complexes were further analyzed by using DFT calculations.[98-100] Scott *et al.*[101] reported the mass-selected photodissociation spectra of Sm, Dy, and Nd ionic complexes, and their observations on the Nd complexes were consistent with the mass spectrometry of Kaya and co-workers.[94-97] Miyajima *et al.*[102] reported the magnetic moments of [Ln$_n$(COT)$_m$] (Ln = Eu, Tb, Ho, Tm) obtained

from a Stern-Gerlach magnetic deflection experiment and observed the increase in the magnetic moments with increasing number of lanthanide atoms. For transition metals, Jaeger and Duncan[103] studied $[M(COT)_{1,2}]^+$ (M = V, Fe, Ni, and Ag) ions, again with mass-selected photodissociation spectroscopy, and observed various metal-dependent fragmentation channels. Li *et al.*[104] reported an anion photoelectron study of $[Fe_{1,2}(COT)]^-$ and $[Co(COT)]^-$ complexes. In combination with DFT calculations, they determined the spin multiplicities of the anions and found that the spin magnetic moments of these systems retained those of the bare metal atoms or dimer. Vass *et al.*[105] studied He (I) and He (II) photoelectron spectra of several COT-containing Fe and Cr complexes and proposed an η^4-COT binding mode in the Fe complexes and an η^6-COT mode in the Cr complexes. In addition to the experimental measurements, computational studies have been reported on the sandwich structures of lanthanide and actinide metal complexes,[106-108] half-sandwich structures of alkaline earth metals,[109,110] and fluxional behavior of COT in transition metal complexes.[91]

The previous gas-phase measurements and calculations suggested the conversion of tub-shaped COT into an aromatic molecule upon metal coordination. However, it would be desirable to verify this geometric change by high-resolution spectroscopy with the potential of directly probing the shape of the COT molecule and structures of metal COT complexes. This is the motivation for the current study. In this chapter, we have focused on PFI-ZEKE spectroscopy of group III M(COT) (M = Sc, Y, and La) complexes. By combining the spectroscopic measurements with the molecular orbital treatments and DFT calculations, we have explored the effects of metal coordination on the conformation of COT, the metal-ligand bonding and electronic states of the M(COT) complexes, and the differences between the COT and benzene complexes.[56,60,61]

3.2. Experimental and Computational Methods

The metal-cluster beam ZEKE spectrometer used here was described in Chapter 2. Metal complexes with COT (98%, Aldrich) were prepared in a laser-vaporization cluster beam source. The metal atoms were produced by pulsed-laser vaporization of a metal rod (Sc, 99.9%, Alfa Aesar; Y, 99.9%, Goodfellow; La, 99.9%, Alfa Aesar) in the presence of

He or Ar carrier gas (UHP, Scott-Gross) or a mixture of He and Ar at about 40 psi. These gases were delivered by a home-made piezoelectric pulsed valve.[55] The metal complexes formed in the collision chamber were expanded into the vacuum, collimated by a cone-shaped skimmer (4 mm inner diameter), and passed through a pair of charged deflection plates (+500 V) to remove residual ionic species formed during laser ablation.

The M(COT) complexes in the molecular beams were identified by photoionization time-of-flight mass spectrometry. Ionization thresholds of the complexes were located using PIE spectroscopy by recording the mass-selected ion signal as a function of the ionization laser wavelength. ZEKE electrons were produced by photoexcitation of the neutral complexes to highly excited Rydberg states, followed by photoionization of these Rydberg states with a 3 μs delayed, pulsed-electric field (1.2 Vcm^{-1}, 100 ns). A small dc field (0.06 Vcm^{-1}) was applied to discriminate ZEKE electrons from kinetic electrons produced by direct photoionization. A delay pulse generator was used to generate the pulsed-electric field for ionization. The dc field effects on the ZEKE spectral energies were corrected using the relation of $\Delta IE =$ 6.1 x $E_F^{1/2}$, where E_F in Vcm^{-1} is the field strength.[111] The ion and electron signals were detected by a dual microchannel plate detector, amplified by a preamplifier, averaged by a gated integrator, and stored in a laboratory computer. Laser wavelengths were calibrated against vanadium or titanium atomic transitions.[57]

Molecular geometries and vibrational frequencies were calculated with GAUSSIAN 03 program package.[59] In these calculations, we have used B3LYP method with the triple-split-valence basis set 6-311+G(d,p) for C, H and Sc, and the LanL2DZ basis set for Y and La atoms (for which the triple-split-valence basis was not available). Multidimensional FC factors were calculated from the equilibrium geometries, harmonic vibrational frequencies, and normal coordinates of the neutral and ionized complexes.[52,65] The Duschinsky effect[29] was considered to account for normal mode differences between the neutral and ion complexes in the FC calculations. A Lorentzian line shape with the experimental linewidth was used to simulate spectral broadening. Transitions from excited vibrational levels of the neutral complexes were simulated by assuming thermal excitations at specific temperatures.

3.3. Results and Discussion

3.3.1. PIE and ZEKE Spectra of M(COT)

Figure 3.1 displays the PIE spectra of three M(COT) complexes seeded in He carrier. The wavenumbers were corrected by +110 cm^{-1}, the energy shift induced by the dc extraction field of 320 Vcm^{-1} applied in the ionization region. Each spectrum begins with a small and slowly rising signal, followed by a sharp signal onset. The slowly rising signal originates from ionization of thermally excited vibrational levels of the neutral complexes. The sharp signal onsets, indicated by arrows, corresponds to the first ionization thresholds and are measured to be 42200 (200), 40600 (200) and 36600 (200) cm^{-1} for the Sc, Y, and La complexes, respectively. The ionization thresholds from the PIE measurements were used to simplify the search for and correlate with the ZEKE signal.

The ZEKE spectra of the three complexes seeded in He are shown in Figures 3.2(a), 3.3(a), and 3.4(a). These spectra are similar to each other and display a major progression with intervals ranging from 338 cm^{-1} in Sc(COT), 300 cm^{-1} in Y(COT), and 278 cm^{-1} in La(COT). Superimposed on the high-energy side of each member of the progression are satellite peaks separated by about 20 cm^{-1} from the main peak. Additionally, each spectrum exhibits a weak transition at the low-energy side of the first strong peak, 0-0 transition. The separation of this weak transition from the 0-0 transition is 318 cm^{-1} in Sc(COT), 270 cm^{-1} in Y(COT) and 256 cm^{-1} in La(COT). The intensities of these weak transitions and the satellite peaks depend on the conditions of the molecular beams and decrease with the replacement of He carrier by Ar. Figure 3.2(b) shows the ZEKE spectrum of Sc(COT) with a 1:1 He/Ar mixture. In this spectrum, the intensities of the satellite peaks above the 0-0 band and the weak peak below the 0-0 band decrease due to the reduced vibrational temperatures with the mixture carrier. Therefore, these transitions are attributed to ionization of vibrationally excited neutral complexes.[112-116] The adiabatic ionization energies (AIEs) measured from the 0-0 transition are 42263 (5), 40749 (5), and 36643 (5) cm^{-1} for the Sc, Y, and La complexes, respectively. The AIE value of each complex measured in the ZEKE spectrum corresponds to the

energy position of the sharp onset in the PIE spectrum, but with a much higher precision and accuracy.

The ZEKE spectrum of the Sc(COT) is very similar to that of Sc(benzene).[60] The 42263 cm^{-1} AIE is close to that of the benzene complex (41600 cm^{-1}), the 338 cm^{-1} interval of the main progression is comparable to the Sc$^+$-benzene stretching frequency (375 cm^{-1}) in the ion state, and the 318 cm^{-1} interval is about the same as the Sc-benzene stretching frequency (324 cm^{-1}) in the neutral state. Therefore, it is reasonable to assign the 338 and 318 cm^{-1} intervals to the Sc-COT stretching excitations in the ionized and neutral species. The satellite peaks, separated from the 338 cm^{-1} progression by ~20 cm^{-1}, are likely due to the sequence transitions between the first excited levels of the Sc-COT stretching vibrations in the ionic and neutral states. Similar to Sc(COT), the 300 and 270 cm^{-1} intervals in the ZEKE spectrum of Y(COT) may be attributed to excitations of the Y$^+$/ Y-COT stretching vibrations, and the 278 and 256 cm^{-1} intervals in the spectrum of La(COT) to excitations of the La$^+$/ La-COT stretching vibrations. The decrease of the metal-ligand stretching frequencies from Sc to La is associated with the increase in the metal masses down the group triad. Because of the smaller stretching frequencies of the Y- and La-COT complexes, additional sequence transitions from higher excited vibrational levels are also observed for these two heavier species.

The observation of large AIE variations among the three M(COT) complexes suggests that photoionization removes a metal-based electron, rather than a COT-based one. The AIE values of these complexes decrease down the group triad and are in the same order as the metal atomic IEs. The removal of a metal-based electron by ionization in these systems is understood because the IEs of the group III metal atoms (6.5615 eV for Sc, 6.2173 eV for Y, and 5.5769 eV for La)[117] are lower than that of the COT ligand (8.42 eV).[76,118] Because of the removal of a metal-based electron, ionization should largely affect the coordinates between the metal and ligand, rather than the COT framework. Therefore, a stronger FC activity is expected for the metal-ligand stretching vibrations in these systems. The spectral assignment will be discussed in more details later by comparing the measured spectra with spectral simulations.

3.3.2. Low-Lying Electronic States and Conformation of M(COT)

In this section, we will discuss the electronic states and molecular conformation from the viewpoint of the frontier molecular orbital treatments and using the results from DFT calculations.

3.3.2.1. Qualitative Molecular Orbital Treatment

Like Sc(benzene), M(COT) is expected to be in a π binding mode. Figure 3.5(a) presents a diagram for valence molecular orbital interactions between the $3d/4s$ orbitals of M and occupied π orbitals of COT. In this diagram, the metal $3d/4s$ orbitals are plotted on the right side of the diagram, the ligand π orbitals on the left, and the formed molecular orbitals in the middle. The metal $3d/4s$ orbitals are placed higher in energy than the ligand π orbitals because the IEs of group III metal atom are lower than that of the organic ligand (Koopmans' theorem). As a starting point, M(COT) is assumed to be in C_{8v} point group, the highest possible symmetry for M(COT) in a π conformation. COT is known to be non-planar and is properly described as a conjugated nonaromatic tetraolefin. A molecular orbital treatment of the hypothetical planar COT is useful, however, with respect to the questions of the instability of this configuration for the free molecule and the possible stabilization upon metal coordination.[119,120] Based on the Frost and Musulin energy diagram,[121] five occupied π orbitals of COT are in the energy order of π_1 (a_1, bonding) < π_2, π_3 (e_1, bonding) < π_4, and π_5 (e_2, nonbonding). The five metal atomic d orbitals are split into three sets: d_{z^2} (a_1), $d_{xz, yz}$ (e_1) and d_{xy, x^2-y^2} (e_2) in C_{8v}. Interactions between these M and COT orbitals yield three bonding and antibonding orbitals, respectively, with the ligand π orbitals being stabilized and the atomic d orbitals destabilized. The interaction between the COT π_1 and M d_{z^2} orbitals is the weakest because of their large energy difference and spatial mismatch. The formation of M(COT) results in a two-electron transfer from the metal atom to the COT half-filled e_2 orbital, making COT a dianion. Thus, the metal-coordinated COT satisfies the requirement of 4n + 2 electrons and becomes aromatic.

Since group III metal atoms have three outermost valence electrons, the remaining outermost electron should fill in the metal-based $2a_1$ orbital, the highest occupied molecular orbital (HOMO). Thus, the ground electronic state of M(COT) should be $^2A_1$ under C_{8v} molecular symmetry. First ionization removes the electron from the HOMO and yields the $^1A_1$ ground state for the corresponding ion. From this molecular orbital treatment, the observed ZEKE spectra should be associated with the $^1A_1 \leftarrow {}^2A_1$ transition. Because the $2a_1$ orbital has a weak antibonding character, M(COT) is expected to have a lower IE compared to the metal atom. This qualitative prediction is confirmed by the ZEKE measurement, which shows a red IE shift of 8300 – 10700 cm^{-1} from M to M(COT). The red IE shift indicates that the metal-ligand bonding is stronger in the ion than in the neutral complex.

3.3.2.2. DFT Calculations

The qualitative MO treatment discussed above is consistent with DFT/B3LYP predictions presented below. Table 3.1 lists the electronic states and their energies of the neutral and ionic complexes and transition energies for allowed electronic transitions from a neutral state to an ionic state. Calculations starting with low-symmetry C_{2v} and C_1 structures were also carried out, but converged to either C_{4v} or C_{8v} depending on the electron multiplicities. For each complex, the ground state is predicted to be $^2A_1$ in the C_{8v} structure. In this doublet state, the HOMO has largely a metal-based orbital character: $(n-1)d_{z^2}$ mixed with ns (Figure 3.6). As pointed out in previous section, this doublet state is formed through the two-electron transfer from M to COT, making the ligand a dianion. The argument of the dianionic COT in these complexes is further supported by comparing the C-C bond distances in the ground states of COT, COT$^-$, COT^{2-}, and M(COT). Table 3.2 presents these C-C bond distances obtained from the DFT/B3LYP calculations. It can be seen from the table that C-C bond distances are nearly identical in the M(COT) complexes and the COT^{2-} dianion, while they are quite different between M(COT) and COT or COT$^-$.

Above the $^2A_1$ ground state, a $^4B_1$ state is predicted to be in the range of 20000-30000 cm^{-1} depending on the metal atoms. The $^4B_1$ state is formed through electron

excitation from $1e_2$ to $2e_2$ orbital. Upon the $2e_2 \leftarrow 1e_2$ excitation, the electron configuration is $(1e_2)^3(2a_1)^1(2e_2)^1$, and the electronic symmetries derived from it include $A_1 + A_2 + B_1 + B_2$. In addition to the $^4B_1$ state, we tried to search for the $^4A_1$, $^4A_2$, and $^4B_2$ states, but without success. The $^4B_1$ state is predicted to be a transition state, as frequency calculations show an imaginary frequency [$1228i$ cm^{-1} for Sc(COT), $1027i$ cm^{-1} for Y(COT), and $1015i$ cm^{-1} for La(COT)]. The molecular symmetry of the $^4B_1$ state (C_{4v}) is lower than that of the $^2A_1$ ground state (C_{8v}). The reason why the high-spin state has lower symmetry than the low-spin state is as follows. Upon exciting an electron from the ligand-based $1e_2$ orbital, COT becomes a singly charged anion with $4n + 1$ electrons and thus loses its aromaticity. Although the COT⁻ anion is still planar, the molecular symmetry of its ground state is reduced to D_{4h}.[70,71] Therefore, the maximum symmetry of M(COT) in the high-spin state should be no higher than C_{4v}.

The ground state of the singly-charged M⁺(COT) cation is predicted to be $^1A_1$ in C_{8v} symmetry, and a $^3B_1$ excited ion state in C_{4v} symmetry is located at 13000-17000 cm^{-1}, depending upon the identity of the metal atoms. The $^1A_1$ state arises from the removal of an electron from the HOMO $2a_1$ in the $^2A_1$ neutral ground state, whereas the $^3B_1$ state may result from the removal of an electron from the $1e_2$ orbital of the $^2A_1$ state or the $2e_2$ orbital of the $^4B_1$ state (Figure 3.5). Like the quartet neutral state, the triplet ion state is predicted to be a transition state, because frequency calculations result in an imaginary frequency [$448i$ cm^{-1} for Sc⁺(COT), $343i$ cm^{-1} for Y⁺(COT), and $551i$ cm^{-1} for La⁺(COT)]. The AIEs for the $^1A_1 \leftarrow ^2A_1$ ionization process are predicted to be about 43800, 41200, and 38300 cm^{-1} for M = Sc, Y, and La, respectively. The predicted AIEs for the $^3B_1 \leftarrow ^2A_1$ ionization are much higher (Table 3.1) because ionization removes an electron from the strong bonding, low energy $1e_2$ orbital. On the other hand, the predicted AIE values for the $^3B_1 \leftarrow ^4B_1$ process are much lower, because ionization removes an electron from the antibonding, high energy $2e_2$ orbital.

3.3.2.3. Observed $^1A_1 \leftarrow {}^2A_1$ Transition for the C_{8v} Structure of M(COT)

Among the three ionization processes described in previous section, the $^1A_1 \leftarrow {}^2A_1$ ionization is observed by the ZEKE measurements. Figure 3.2 compares the experimental spectra with the simulations of the $^1A_1 \leftarrow {}^2A_1$ and $^3B_1 \leftarrow {}^2A_1$ processes of Sc(COT). The simulation for the $^3B_1 \leftarrow {}^4B_1$ ionization is not included for the comparison, because the $^4B_1$ neutral state is predicted to be a transition state, which is not expected to survive under the experimental conditions. In these simulations, the calculated vibrational frequencies are not scaled, but the predicted AIE is shifted to the measured value for the sake of simplicity. Clearly, the $^1A_1 \leftarrow {}^2A_1$ simulation matches nicely to the experimental spectra in both vibrational intervals and intensities, while the $^3B_1 \leftarrow {}^2A_1$ simulation exhibits a longer FC progression and smaller vibrational intervals than the measured spectra do. Moreover, the predicted AIE of $^1A_1 \leftarrow {}^2A_1$ (43831 cm^{-1}) is close to the measured value (42263 cm^{-1}), while the predicted AIE of $^3B_1 \leftarrow {}^2A_1$ (56244 cm^{-1}) is too high. Therefore, the comparison between the experimental and theoretical AIEs, vibrational frequencies, and spectral intensities shows that the $^1A_1 \leftarrow {}^2A_1$ ionization is responsible for the observed spectrum. Based on the good agreement between the experiment and theory, the 338 cm^{-1} vibrational progression is assigned to the excitations of the Sc$^+$-COT stretching mode in the $^1A_1$ ionic state. The 318 cm^{-1} interval is assigned to the first-quantum excitation of the Sc-COT stretching mode in the $^2A_1$ neural. The satellite peaks with separations of $\sim$20 cm^{-1} are due to the sequence transitions between the first excited levels of the metal-ligand stretching vibrations in the neutral and ion states. As in Sc(COT), the $^1A_1 \leftarrow {}^2A_1$ ionization is observed for the heavier Y and La analogs, as shown in Figures 3.3 and 3.4. Table 3.3 summarizes the measured and calculated AIEs of the $^2A_1$ state and the M-COT stretching frequencies in the $^2A_1$ and $^1A_1$ states. The excellent agreement between the experiment and theory again confirms the spectral assignment discussed above.

The ground electronic states of the neutral and ionic Sc(benzene) complex have been determined to be $^4A_1$ and $^3A_1$, respectively.[60] The difference in the electron spin multiplicities between the ground states of Sc(COT) and Sc(benzene) is explained as

follows. The degenerate e_2 (π_4, π_5) orbital in benzene is unfilled, and it is at higher energy than the metal d orbitals [see Figure 3.5(b)]. Thus, three Sc valence electrons retain at the metal-based molecular orbitals. Due to the small energy separations between the metal-based $1e_2$ and $2a_1$ orbitals, these electrons prefer the $(1e_2)^2(2a_1)^1$ configuration, resulting in the high-spin quartet ground state. Upon removal of the $2a_1$ electron by ionization, the ion is thus in the triplet ground state.

3.4. Conclusions

In this work, we have obtained the first high-resolution electron spectra of group III metal complexes with a COT molecule and determined metal-ligand bonding and electronic states of these systems by combining the ZEKE measurements with the molecular orbital treatment and DFT calculations. The spectra of these complexes are very similar to each other and show a strong 0-0 transition and a major metal-ligand stretching vibrational progression. The AIEs of the complexes are lower than those of the bare metal atoms are and decrease with increasing metal atomic number. The red AIE shift from M to M(COT) shows the metal-ligand bonding is stronger in the ion than in the neutral species.

Metal coordination converts the tub-shaped structure of the COT molecule to a planar, aromatic structure. This conformational change is due to the two-electron transfer from the metal-based orbitals to a COT partially filled π orbital, making the ligand a dianion. The ground electronic state of the neutral complexes is determined to be $^2A_1$, whereas the ground state of the corresponding ions is $^1A_1$. Both neutral and ionic structures have C_{8v} symmetry in their ground states.

Table 3. 1. Point groups, electronic states, relative energies (E_{rel}, cm^{-1}), and AIEs (cm^{-1}) of M(COT) (M = Sc, Y, and La) complexes from DFT/B3LYP calculations.

Complexes	Symmetry	States[a]	E_{rel} (cm^{-1})	Transitions	AIE (cm^{-1})
Sc(COT)					42263[b]
	C_{4v}	$^3B_1$	56951	$^1A_1$ (C_{8v}) ←$^2A_1$ (C_{8v})	43831
	C_{8v}	$^1A_1$	43575	$^3B_1$ (C_{4v}) ←$^2A_1$ (C_{8v})	56244
	C_{4v}	$^4B_1$	19815	$^3B_1$ (C_{4v}) ←$^4B_1$ (C_{4v})	37475
	C_{8v}	$^2A_1$	0		
Y(COT)					40749[b]
	C_{4v}	$^3B_1$	58066	$^1A_1$ (C_{8v}) ←$^2A_1$ (C_{8v})	41193
	C_{8v}	$^1A_1$	41061	$^3B_1$ (C_{4v}) ←$^2A_1$ (C_{8v})	57488
	C_{4v}	$^4B_1$	31728	$^3B_1$ (C_{4v}) ←$^4B_1$ (C_{4v})	26753
	C_{8v}	$^2A_1$	0		
La(COT)					36643[b]
	C_{4v}	$^3B_1$	53186	$^1A_1$ (C_{8v}) ←$^2A_1$ (C_{8v})	38254
	C_{8v}	$^1A_1$	38075	$^3B_1$ (C_{4v}) ←$^2A_1$ (C_{8v})	52675
	C_{4v}	$^4B_1$	27254	$^3B_1$ (C_{4v}) ←$^4B_1$ (C_{4v})	26416
	C_{8v}	$^2A_1$	0		

[a] The doublet and quartet states refer to the neutral complex, and the singlet and triplet states are for the ion. The $^3B_1$ and $^4B_1$ states of M(COT) are transition states as frequency calculations show an imaginary frequency in each of these high-spin states.
[b] AIE values from ZEKE spectra.

Table 3. 2. Carbon-carbon bond distances (Å) in the ground states of COT, COT^-, COT^{2-}, M(COT), and $M^+(COT)$ (M = Sc, Y, and La) from DFT/B3LYP calculations.

Bond distance	COT	COT^-	COT^{2-}	M(COT)	$M^+(COT)$
C-C	1.472,1.340	1.441, 1.378	1.417	1.416-1.418	1.414-1.417

Table 3. 3. AIEs (cm^{-1}), and metal-ligand stretching frequencies (cm^{-1}) of M(COT) (M = Sc, Y, and La) complexes from pulsed-field-ionization ZEKE spectroscopy and DFT/B3LYP calculations.

	ZEKE[a]	B3LYP
Sc(COT) (C_{8v}, $^1A_1 \leftarrow {}^2A_1$)		
AIE	42263	43831
Sc-COT stretch (v_8)	318	317
Sc$^+$-COT stretch (v_8^+)	338	341
Y(COT) (C_{8v}, $^1A_1 \leftarrow {}^2A_1$)		
AIE	40749	41193
Y-COT stretch (v_8)	270	260
Y$^+$-COT stretch (v_8^+)	300	287
La(COT) (C_{8v}, $^1A_1 \leftarrow {}^2A_1$)		
AIE	36643	38254
La-COT stretch (v_8)	256	243
La$^+$-COT stretch (v_8^+)	278	263

[a]The uncertainty of AIE from the ZEKE measurement is about 5 cm^{-1}.
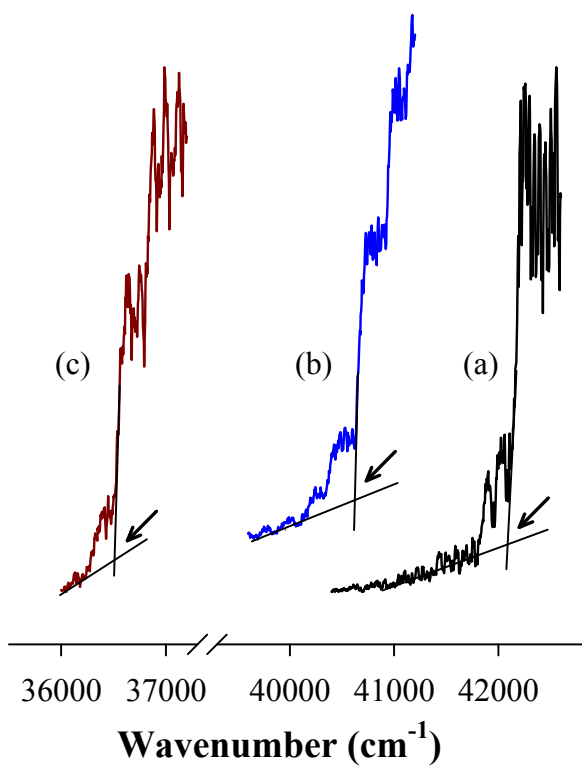
Figure 3. 1. PIE spectra of M(COT) [M = Sc (a), Y (b), and La (c)] seeded in He carrier. The ionization threshold of each complex is located by the intersecting point of two lines as pointed by the arrow.
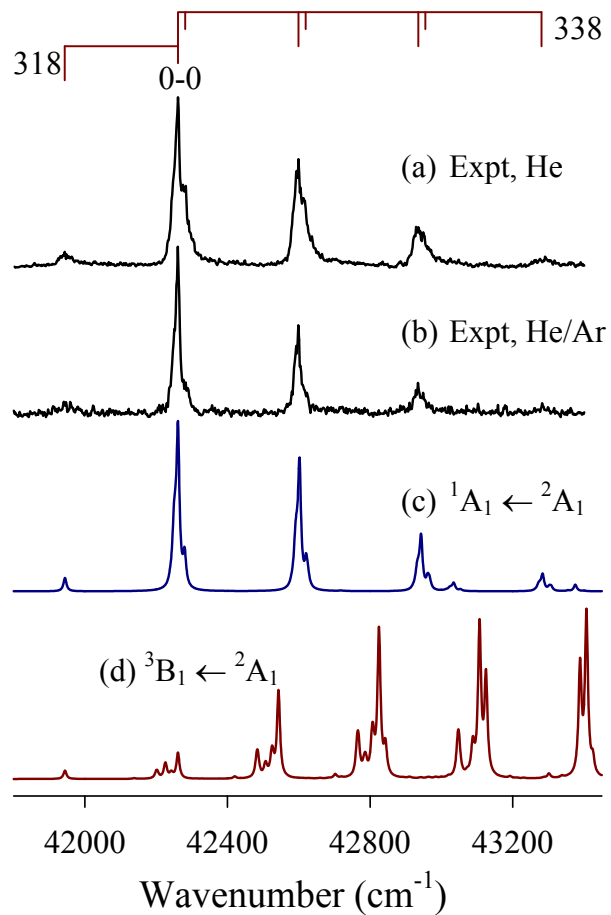
Figure 3. 2. Experimental ZEKE spectra of Sc(COT) seeded in He (a) and 1:1 He/Ar mixture (b) and simulations (200 K) of the $^1A_1 \leftarrow {}^2A_1$ (c) and $^3B_1 \leftarrow {}^2A_1$ (d) transitions.
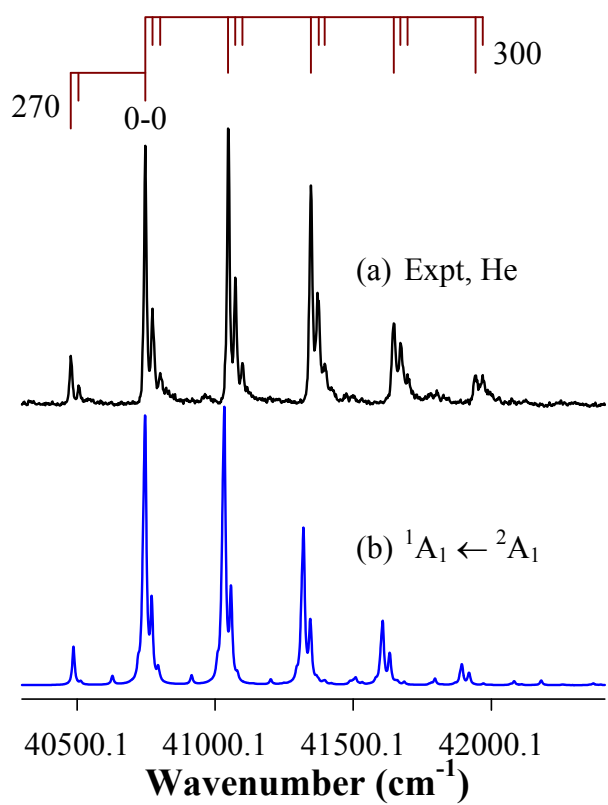
Figure 3. 3. Experimental ZEKE spectrum of Y(COT) seeded in He (a) and simulation (200 K) of the $^1A_1 \leftarrow {}^2A_1$ transition (b).
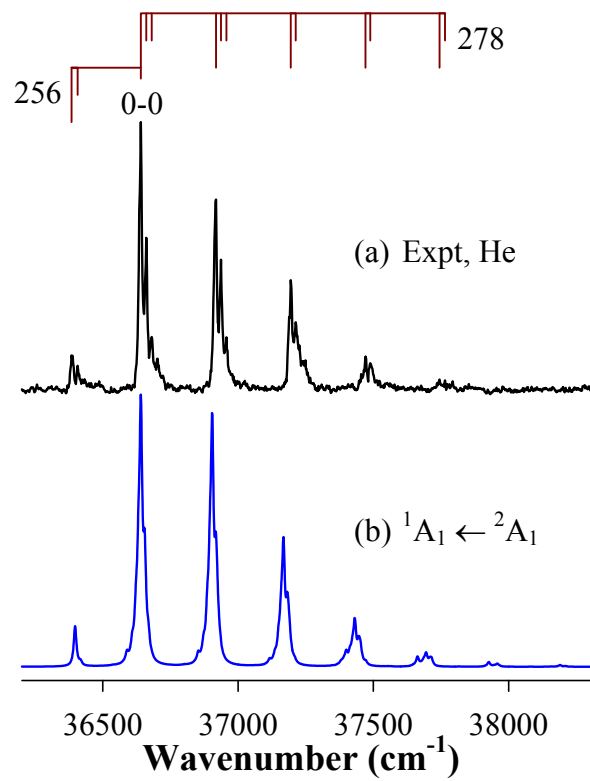
Figure 3. 4. Experimental ZEKE spectrum of La(COT) seeded in He (a) and simulation (200 K) of the $^1A_1 \leftarrow {}^2A_1$ transition (b).
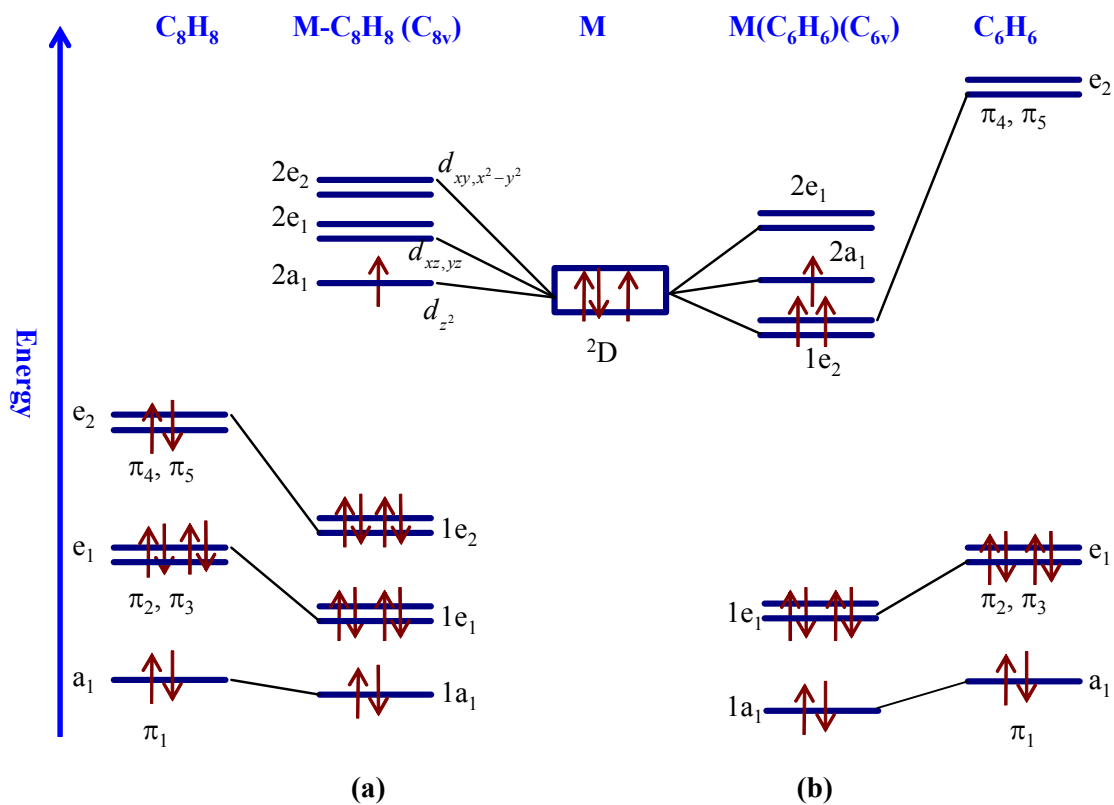
Figure 3. 5. An orbital interaction diagram between the M (M = Sc, Y, and La) and cyclo-octatetraene (a) or benzene (b) fragments.
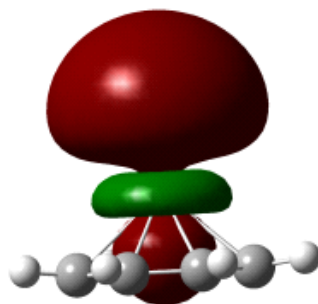
Figure 3. 6. HOMO of the $^2A_1$ ground electronic state of Sc(COT).

CHAPTER 4. RING DEFORMATION AND Π-ELECTRON REDISTRIBUTION OF METHYLBENZENES INDUCED BY METAL COORDINATION

4.1. Introduction

Arene complexes of transition metals are essential to the understanding of homogeneous catalysis involving aromatic C-C and C-H bond activation[122-124] and arene hydrogenation.[125-127] To probe fundamental interactions between transition metals and arene molecules, metal-benzene complexes have been studied by various spectroscopic methods.[128] For early transition metals, it has been reported that in the ground electronic states of monobenzene complexes, M(benzene), the benzene ring remains planar with M = Sc, V, Nb, and Hf,[60,129,130] and is bent with M = Ti, Zr, and Hf.[131] Similarly, the benzene ring in the ground states of the M^+(benzene) cations has been reported to be flat with $M^+ = Ti^+$ and Cr^+, but bent with $M^+ = V^+$.[132] These studies indicate that the degree of the perturbation of the carbon skeleton by metal coordination depends on the identity and charge of metal atoms. The deformation of aromatic rings by metal coordination may be significant for metal mediated chemical reactions, as it modifies the π electron distribution and weakens some of the C-C bonds in the ring, making the C-C bond cleavage more feasible.

Previously, our group reported the ground electronic state and molecular conformation of M(benzene)$_{1,2}$ (M = Sc, Ti, V, Cr, Mo, and W).[56,60,61] For Sc(benzene), we determined a quartet ground state ($^4A_1$) for the neutral species and a low-energy triplet state ($^3A_1$) for the singly charged cation.[60] The benzene ring in these neutral and ionic states is planar. On the other hand, the benzene ring was predicted to be significantly bent in the ion singlet and neutral doublet states, by DFT and the second order perturbation theory.[60,133] To test these predictions, we designed an experiment to probe the doublet and singlet states of several Sc(arene) complexes. The major experimental techniques used in this study are single-photon PFI-ZEKE and IR-UV R2PI spectroscopy. The benzene molecule is modified by methyl substitutions for hydrogen atoms. Although the substitutions induce small variations in the C-C bond distances and C-C-C bond angles, they have no effect on the planarity of the benzene ring in the free ligands.[134-139]

This simple chemical modification has allowed us to observe the low-spin singlet and doublet states of the Sc complexes with methyl-substituted monobenzene molecules.

4.2. Experimental and Computational Methods

4.2.1. Single-Photon ZEKE Spectroscopy

The ZEKE spectrometer used in this work has been described in Chapter 2. The Sc-$C_6(CH_3)_xH_{6-x}$ [x = 2, 3, or 6] complexes were synthesized by the reactions of Sc atoms with ligand vapor (*p*-xylene or 1, 4-dimethylbenzene, 98%, EMD; mesitylene or 1, 3, 5- trimethylbenzene, 98%, Aldrich; and hexamethylbenzene, 99%, TCI America) in a laser-vaporization molecular beam source. The Sc atoms were produced by pulsed laser vaporization of a Sc rod (99.9%, Alfa Aesar) with the second-harmonic output of a pulsed neodymium doped yttrium aluminum garnet (Nd:YAG) laser (Continuum, Minilite II, 532 nm, 3 ~ 4 mJ) in the presence of He or Ar carrier gas (UHP, Scott-Gross) or a mixture of He and Ar. These gases were delivered by a home-made piezoelectric pulsed valve with backing pressure of 40-70 psi.[55] The metal rod was translated and rotated by a motor-driven mechanism to ensure each laser pulse ablated a fresh metal surface. The methylbenzenes were used without further purification, and the complexes were synthesized by two different methods depending on the states of the ligands. To synthesize Sc(*p*-xylene) and Sc(mesitylene), the volatile *p*-xylene and mesitylene liquids were introduced at room temperature to a small stainless-steel collision chamber (~ 1.5 mL) placed downstream of the metal ablation region, from a glass bulb located outside of the source chamber and through a stainless-steel capillary (0.053″ inner diameter). To produce Sc(hexamethylbenzene), the less-volatile ligand (mp, 165-168 °C) was heated to 45 °C in a copper oven also placed downstream of the metal vaporization region to obtain sufficient vapor pressure. The vaporized ligands then interacted with the metal atoms entrained in the carrier gas to form metal(methylbenzene) complexes, which were expanded into the vacuum through a nozzle to form molecular beams. The molecular beams were collimated by a cone-shaped skimmer (4mm inner diameter) and passed

through a pair of charged deflection plates (+500 V) to remove residual ionic species that might have formed by laser vaporization.

Prior to ZEKE measurements, the production of the metal complexes was maximized by optimizing the timing and power of the vaporization and ionization lasers, backing pressure of the carrier gas, and the amount of the ligand. The neutral metal complexes in the molecular beams were ionized by a frequency-doubled dye laser (Lumonics, HD-500) pumped by the third-harmonic output of a second pulsed Nd:YAG laser (Continuum Surelite II, 355 nm) and identified by photoionization time-of-flight mass spectrometry. The linewidth of the frequency-doubled UV laser is 0.08 cm^{-1}. Ionization thresholds of the complexes were located with PIE spectroscopy by recording the mass-selected ion signal as a function of the ionization laser wavelength. The ZEKE electrons were produced at the optimized conditions by photoexcitation of the neutral complexes to highly excited Rydberg states, followed by pulsed-electric field (3 μs in time delay, 1.2 Vcm^{-1} in field strength, and 100 ns in pulse width) ionization of these Rydberg states. A small dc field (0.06 Vcm^{-1}) was applied to discriminate ZEKE electrons from kinetic electrons produced by direct photoionization. A delay pulse generator (Stanford Research Systems, DG535) was used to generate the electric pulses for field ionization. The ion and electron signals were detected by a dual microchannel plate detector (Galileo), amplified by a preamplifier (Stanford Research Systems, SR445), averaged by a gated integrator (Stanford Research Systems, SR250), and stored in a laboratory computer. Laser wavelengths were calibrated against vanadium or titanium atomic transitions.[57] The dc field effects on the PIE and ZEKE spectral energies were corrected using the relation of $\Delta IE = 6.1E_F^{1/2}$, where E_F in Vcm^{-1} is the field strength.[111]

4.2.2. IR-UV Photoionization Spectroscopy

The details of the IR-UV photoionization setup have been described in Chapter 2. An IR optical parametric oscillator/amplifier (OPO/A) laser (LaserVision) was used for vibrational excitation and a frequency-doubled UV dye laser (Lumonics, HD-500) for molecular ionization. The IR OPO/A laser was pumped by an injection-seeded Nd:YAG laser (Continuum, Surelite III) and the dye laser was pumped by a Nd:YAG laser

(Continuum, Surelite II). The IR linewidth is ~ 0.2 cm^{-1} when pumped with the injection seeder on and ~ 2.0 cm^{-1} with the injection seeder off. The IR and UV laser beams were counterpropagated, and both were perpendicular to the molecular beam. The time difference between the IR and UV lasers was 50-200 ns. The UV laser was fixed at 400-500 cm^{-1} below the IE of Sc(hexamethylbenzene), whereas the IR laser was scanned in the C-H stretch region. The resultant ion signal was detected in the same time-of-flight spectrometer as that used in the ZEKE experiment. The IR laser wavelengths were calibrated with the photoacoustic spectra of H_2O.[140] The effect of IR pulse energies was studied, and the energy of 8-10 mJ/ pulse was found to give the optimal signal and spectral linewidth for this molecule. Measurements with the injection seeder on or off were also carried out, and no significant difference was observed on the linewidth of the photoionization spectra.

4.2.3. Computation

Molecular geometry optimization, vibrational frequencies, and IR intensities were obtained with B3LYP method and the 6-311+G(d,p) basis set implemented in GAUSSIAN 03 program package.[59] To simulate the ZEKE spectrum, multidimensional Franck-Condon (FC) factors were calculated from the equilibrium geometries, harmonic vibrational frequencies, and normal coordinates of the neutral and ionized complexes.[52,65] The Duschinsky effect[29] was considered to account for normal mode differences between the neutral and ionic complexes in the FC calculations. A Lorentzian line shape with the experimental linewidth was used to simulate the spectral broadening. Transitions from excited vibrational levels of the neutral complexes were simulated by assuming thermal excitations at specific temperatures. The IR intensities of C-H stretches were calculated from the first derivative of the dipole moment at the equilibrium bond distance, and each IR band was plotted with the experimental bandwidth.

4.3. Results and Discussion

4.3.1. Low-Energy Electronic States and Possible Conformations

Table 4.1 summarizes the low-energy electronic states and molecular point groups of the neutral and singly charged cationic Sc(methylbenzene) complexes predicted by DFT calculations. Because a Sc atom has three valence electrons, we have considered electron spin multiplicities of 2 and 4 for the neutral species and of 1 and 3 for the singly charged cations. In the ground electronic state of the free ligands, p-xylene has a C_{2h} geometry with two methyl groups in the eclipsed form,[134] mesitylene a C_{3h} geometry also with eclipsed methyl groups,[135] and hexamethylbenzene a D_{3d} geometry with staggered para-methyl groups.[136-138] With Sc binding above the benzene ring, the maximum molecular symmetries should be no higher than C_{2v} for Sc(p-xylene) and C_{3v} for Sc(mesitylene) and Sc(hexamethylbenzene), respectively, as the metal coordination removes the inversion center. Through an extensive search with various relative methyl orientations in each complex, the molecular geometry of the high-spin quartet state is predicted to be in C_{2v}, C_{3v}, and C_I point groups and that of the low-spin doublet in C_2, C_s, and C_{2v} for the p-xylene, mesitylene, and hexamethylbenzene complexes, respectively. The methyl group orientations in the complexes are different from those in the free ligands, as shown in Figure 4.1.

For the neutral complexes, the doublet state is predicted to be the ground electronic state, and the quartet state is located at a slightly higher energy (2-6 kcal mol^{-1} depending on the number of methyl groups) In contrast, a quartet state was determined to be the ground state of Sc(benzene),[60] with a doublet state at about 3.5 kcal mol^{-1}. Although the energy difference between the doublet and quartet states is relatively small, their geometric variation is quite large, as shown in Table 4.2. First, although the benzene ring remains almost planar in the quartet state, it is bent by as much as 26.5 degrees in the doublet state (Figure 4.2). The ring deformation in the low-spin state is caused by Sc differential binding with the ring carbon atoms. The differential binding is reflected by the two sets of Sc-C distances, which average 2.250/ 2.469 Å in Sc(p-xylene), 2.255/ 2.470 Å in Sc(mesitylene), and 2.237/ 2.484 Å in Sc(hexamethylbenzene).

Second, although the six C-C distances in the benzene ring are essentially the same in the quartet states, they are different by as much as 0.1 Å in the doublet state. The shorter/ longer C-C bond distances in the doublet states are predicted to be 1.376/ 1.460, 1.376/ 1.462, and 1.384/ 1.476 Å in the p-xylene, mesitylene, and hexamethylbenzene complexes, respectively. These C-C bond distances are very close to the averaged ring C-C double (two double bonds in 1,4-positions) and single bond distances (1.375/ 1.462 Å) in the transition metal-arene compounds[141] and also comparable to those (1.340/ 1.504 Å) in 1,4-cylcohexadiene.[142-144] Therefore, the π electrons in the benzene ring of these Sc complexes may be considered in an 1,4-diene fashion (Figure 4.2), and the π electron redistribution is due to the ring folding caused by metal coordination. Third, the relative methyl group orientations are different between the quartet and doublet states. In the quartet state, the methyl groups of Sc(p-xylene) and Sc(mesitylene) are in the eclipsed conformation, while the para methyl groups of Sc(hexamethylbenzene) are in the staggered form. In the doublet state, the two methyl groups of Sc(p-xylene) are staggered; among the three methyl groups of Sc(mesitylene), two pairs are staggered and the third is eclipsed; for Sc(hexamethylbenzene), two pairs of para methyl groups are staggered and the third pair is eclipsed.

Ionization of the doublet and quartet neutral states produces the singlet and triplet ions. For Sc(p-xylene) and Sc(mesitylene), the low-spin singlet ion is slightly more stable than the high-spin triplet ion. On the other hand, the energies of the singlet and triplet ions of Sc(hexamethylbenzene) are about the same (Table 4.1). The geometries of the singlet and triplet ions are similar to those of the doublet and quartet neutral complexes.

4.3.2. Spectroscopy, Electronic Transition, and Molecular Conformation

Figure 4.3 presents the PIE spectra of the Sc(methylbenzene) complexes seeded in supersonic molecular beams. The ionization thresholds estimated from the onsets of the ion signals are 40770 (50), 40500 (100), and 39500 (150) cm^{-1} for the p-xylene (a), mesitylene (b), and hexamethylbenzene (c) complexes, respectively. The ion onsets are located by intersecting two lines drawn through a baseline and a sharp rise of the ion

signals as indicated by the arrows. The threshold values are corrected by adding the energy shift of +110 cm^{-1} to the laser wavenumbers to account for the Stark effect induced by the dc extraction field (320 Vcm^{-1}) applied in the ionization region.[111] The measurement of the ionization thresholds obtained from the PIE spectra is used to simplify the search for and correlate with the ZEKE electron signals.

4.3.2.1. Sc(*p*-xylene)

Figure 4.4(a) shows the ZEKE spectrum of Sc(*p*-xylene) seeded in He. The origin of the spectrum lies at 40770 (5) cm^{-1} and exhibits transitions involving six vibrational intervals (116, 136, 290, 378, 446, and 544 cm^{-1}) on the high energy side and two intervals (116 and 142 cm^{-1}) on the low energy side of the band origin. In addition, weaker peaks appear at ~ 18 cm^{-1} to the higher energy side of the 378 cm^{-1} progression. Transitions at these vibrational intervals are denoted by the vertical lines in the figure, and others are combinations involving two or more vibrational modes. Table 4.3 summarizes the ZEKE peak positions, which are field corrected by adding +1.5 cm^{-1} to laser wavenumbers. The 40770 cm^{-1} position of the strongest peak correlates with the ionization threshold (40770 cm^{-1}) estimated from the PIE spectrum [Figure 4.3(a)] and corresponds to the adiabatic IE of the complex. The IE of the complex is 12152 cm^{-1} lower than that of the Sc atom (52922 cm^{-1}).[117] From the thermodynamic cycle [IE(Sc) - IE[Sc(*p*-xylene)] = D_0^+[Sc(*p*-xylene)] - D_0(Sc(*p*-xylene)], where D_0^+ and D_0 are bond energies of the ionized and neutral complexes), the IE shift equals to the bond energy difference between the ion and neutral species. The stronger metal-ligand bonding in the cation is largely due to additional charge-electric multipole interactions between the metal ion and the ligand. The intensities of the 18, 116, and 142 cm^{-1} peaks are reduced when the complex is seeded in a 1:1 He/Ar mixture [Figure 4.4(b)], suggesting that these are transitions from excited vibrational levels of the neutral complex.

Most of the observed vibrational intervals can be assigned by comparing with the ZEKE spectra of Sc(benzene)[60] and Sc(toluene)[145] or with the fluorescence excitation,[146] resonance enhanced multiphoton ionization,[147,148] ZEKE,[149] and mass-analyzed threshold photoionization spectra[150,151] of the free ligand. The 378 cm^{-1} interval is very close to the

Sc[+]-benzene (375 cm^{-1}) and Sc[+]-toluene (378 cm^{-1}) stretching frequencies and thus assigned to the Sc[+]-(p-xylene) stretch for the complex. The very short Sc[+]-(p-xylene) stretching progression suggests only a small change in the metal-ligand bond distance upon molecular ionization. The 116 and 136 cm^{-1} intervals are similar to the CH_3 anticlockwise (112 or 113 cm^{-1}) and clockwise (144 cm^{-1}) torsional motions of the singly charged p-xylene cation[146-151] and thus assigned to the same vibrational mode in the Sc[+](p-xylene) ion. Similarly, the 116 and 142 cm^{-1} transitions below the 0-0 transition can be attributed to the CH_3 anticlockwise and clockwise torsional frequencies in the neutral complex. The 446 and 544 cm^{-1} intervals are consistent with the frequencies of an in-plane benzene ring breathing mode (440, 425, or 424 cm^{-1})[147,148,150,151] and an out-of-plane ring bending along the methyl group (553 cm^{-1})[146-148] of the free ligand. The remaining 290 cm^{-1} interval is likely due to ligand-based vibrational excitation and will be discussed in combination with DFT calculations and spectral simulations.

Because the IE, metal-ligand stretching frequency, and spectral profile of Sc(p-xylene) resemble those of Sc(benzene), it is tempting to assume that the observed transitions in these two complexes should involve electronic states with the same spin multiplicities, and the ejected electron should have similar characteristics. For Sc(benzene), the initial state was determined to be a quartet state, and the final state was a triplet state; the electron removed from the quartet ground state was of predominantly Sc (4s3d4p$_z$) character. For Sc(p-xylene), however, the theory predicts that the quartet state, [4]A_2 (C_{2v}), is at higher energy than the doublet state, [2]A (C_2), and that the [3]$A_2 \leftarrow$ [4]A_2 and [1]A $\leftarrow$ [2]A transitions have similar energies. To identify the transition probed by the ZEKE spectra, we simulated the spectra for transitions from the [4]A_2 and [2]A states, which are shown in Figure 4.4(c)-(e). In these simulations, the vibrational frequencies are not scaled, but the 0-0 transition energies are shifted to the experimental value to simplify the spectral comparison. A vibrational temperature of 50 K is found to be the best to reproduce the experimental spectrum with 1:1 He/Ar mixture [Figure 4.4(b)] and 150 K to reproduce the spectrum with He carrier (not shown). The simulation of the [3]$A_2 \leftarrow$ [2]A transition exhibits a much longer FC profile than the experimental spectrum due to a large structural change from the neutral [2]A state to the ionic [3]A_2 state. Although the simulation of the [3]$A_2 \leftarrow$ [4]A_2 transition reproduces the metal-ligand stretching progression,

it fails to give other observed vibrational intervals. The best match to the experimental spectrum is the $^1A \leftarrow ^2A$ simulation, where both frequencies and intensities are in nice agreement. On the basis of the excellent agreement between the $^1A \leftarrow ^2A$ simulation and the experimental spectrum, all ZEKE peaks (except for a small peak at 40998 cm^{-1} marked by a question mark) are assigned (Table 4.3), and frequencies are obtained for several vibrational modes (Table 4.4). The 290 cm^{-1} interval, which is not assignable by comparing with the spectra of the free ligand, is now assigned to an out-of-plane benzene ring bending. In this vibration, the bending motion is largely from two C-H bonds. The assignments for other vibrational intervals from the simulation are consistent with those from the comparison with the spectra of the free ligand and other Sc complexes discussed above. As shown in Table 4.4, the theoretical vibrational frequencies agree well with the measured values, providing further support for the spectral assignments.

The ZEKE spectra of Sc(p-xylene) are attributed to the electronic transition between the ground states of the neutral complex (^2A) and cation (^1A). In these states, the benzene ring is bent with two carbon atoms towards Sc, and the π electrons are redistributed in an 1,4-diene fashion. On the other hand, the ground states of the neutral and cationic Sc(benzene) complexes were determined to be $^4A_1$ and $^3A_1$ in C_{6v}, with a planar benzene ring.[60] The valence electron configuration of the neutral $^4A_1$ ground state is $e_2^2 a_1^1$, largely Sc $(3d_{x^2-y^2,xy})^2 (4s4p_z3d_z^2)^1$, where the z-axis is collinear with the six-fold rotational axis. The substitution of two H atoms by the CH_3 groups reduces the molecular symmetry of the Sc half-sandwich complex from C_{6v} to C_{2v} for the $^4A_2$ state with a flat benzene ring or to C_2 for the ^2A state with a bent ring. In either case, the doubly degenerate Sc $3d_{x^2-y^2,xy}$ orbital is split into two non-degenerate orbitals $3d_{x^2-y^2}$ and $3d_{xy}$. The electron configuration of the $^4A_2$ state is $(3d_{xy})^1 (3d_{x^2-y^2})^1 (4s4p_z4d_z^2)^1$ and that of the ^2A state is $(3d_{xy})^2 (4s4p_z3d_z^2)^1$, with Sc $(4s4p_z3d_z^2)^1$ being the highest occupied molecular orbitals (HOMOs) of the two states. The Sc $3d_{x^2-y^2}$-based orbital becomes less stable in the ^2A state than in the $^4A_2$ state, because of the differential Sc binding to the ligand π orbital of the boat-like ring in the low-spin state.   Because of the comparable HOMO characters in the Sc(p-xylene) ^2A and Sc(benzene) $^4A_1$ states, the ZEKE spectra of these two complexes share a very similar profile even though the electron spin multiplicities are different in their ground electronic states.

60

4.3.2.2. Sc(mesitylene)

The ZEKE spectra of Sc(mesitylene) [Figure 4.5(a) and (b)] display a rather similar spectral profile to those of the p-xylene complex. The first strong band at 40505 (5) cm^{-1} correlates well with the ion-signal onset at 40500 cm^{-1} in the PIE spectrum [Figure 4.3(b)] and is assigned to the 0-0 transition. The IE of the mesitylene complex is 265 cm^{-1} lower than that of the p-xylene complex. The spectra exhibit a 378 cm^{-1} vibrational progression, 136, 172, 242, and 452 cm^{-1} intervals above the 0-0 transition, and a 154 cm^{-1} interval below. By comparing with Sc(p-xylene), we can easily assign the 136, 378, and 452 cm^{-1} intervals to the clockwise CH_3 torsion, Sc^+-mesitylene stretch, and in-plane benzene ring breathing mode in the ion, respectively, and the 154 cm^{-1} interval to the clockwise CH_3 torsion in the neutral species. As expected, these vibrational modes have very similar frequencies to the corresponding modes in the p-xylene complex. The 154 cm^{-1} peak in the He spectrum [Figure 4.5(a)] disappears in the spectrum with 1:1 He/Ar mixture [Figure 4.5(b)], as the vibrational cooling is more efficient with the heavier carrier. Like Sc(p-xylene), the simulation of the $^1A' \leftarrow \, ^2A'$ transition (among the three possible transitions in spectra (c)-(e) in Figure 4.5) has the best match with the experimental spectrum. The excellent agreement between the experimental spectrum and the $^1A' \leftarrow \, ^2A'$ simulation supports the spectral assignments for the 136, 154, 378, and 452 vibrational intervals discussed above and attributes the 172 and 242 cm^{-1} intervals to methyl bending and rocking modes, respectively (Tables 4.3 and 4.4).

4.3.2.3. Sc(hexamethylbenzene)

The ZEKE spectrum of Sc(hexamethylbenzene) seeded in 1:1 He/Ar mixture [Figure 4.6(a)] is rather different from those of the partially methyl substituted species. It exhibits three broad peaks separated by ~ 400 cm^{-1}. These peaks have a spectral linewidth up to ~ 120 cm^{-1}, compared to 7 or 8 cm^{-1} for the spectra of Sc(p-xylene) and Sc(mesitylene). We tried to narrow down the spectral linewidth by using pure Ar, however, the attempt was unsuccessful because of extremely weak ZEKE signals with the

heavier carrier. The broad spectral linewidth may be caused by a larger number of rotational and vibrational degrees of freedom and transitions from rotational isomers with different methyl orientations. Unfortunately, in addition to the minimum energy structures presented in Figure 4.1, we did not find any other local minima. The first peak appears at 39535 (5) cm^{-1}, which corresponds to the ion signal onset (39500 cm^{-1}) in the PIE spectrum, and corresponds to the origin bands. The 400 cm^{-1} interval is comparable with the Sc^+-(p-xylene) and Sc^+-mesitylene stretching frequencies and thus assigned to the corresponding Sc^+-hexamethylbenzene stretching motion in the cation. The 400 cm^{-1} progression is reproduced by the simulation of the $^1A_1 \leftarrow {}^2A_1$ transition [Figure 4.6(b)], but not shown in the others [Figure 4.6(c) and (d)]. Like the di- and trimethylbenzene complexes, the ground states of the neutral and ionized Sc(hexamethylbenzene) are doublet and singlet, respectively.

Since bands in the ZEKE spectrum of Sc(hexamethylbenzene) are broad, we have also recorded the IR-UV R2PI spectrum in the C-H stretching region [Figure 4.7(a)]. The IR-UV ion spectrum was obtained by fixing the UV laser at 39000 cm^{-1} (535 cm^{-1} below the IE of the complex) and scanning the IR laser in the 2700-3000 cm^{-1} region. The spectrum with a linewidth of ~ 15 cm^{-1} exhibits a very strong peak at 2850 cm^{-1}, followed by some weak, broad signals. The predicted IR spectra in the C-H stretching region of the $^2A_1$ and ^4A state are shown in Figure 4.7(b) and (c). The theoretical C-H frequencies are scaled by a factor of 0.9670, the averaged ratio of the measured to predicted frequencies of these stretching modes in the free hexamethylbenzene molecule.[152] As shown in Figure 4.7, the predicted IR spectrum of the $^2A_1$ state matches much better to the experimental spectrum than that of the ^4A state in energy positions and spectral profile, consistent with the conclusion obtained from the ZEKE spectra. The strong peak at 2850 cm^{-1} is attributed to the nearly degenerate symmetric and asymmetric C-H stretches of the two methyl groups attached to the carbon atoms strongly bound to Sc, i.e., $Sc-C_1(CH_3)$ and $Sc-C_4(CH_3)$ in Figure 4.2. The predicted frequencies for these stretching vibrations are 2861 and 2862 cm^{-1}. Compared to the corresponding degenerate mode of the free ligand (2890 cm^{-1})[152], the C-H stretch is red shifted by 40 cm^{-1}. The relatively large shift is surprising at first glance, because metal coordination should have little effect on the C-H coordinates. As predicted by the DFT calculations, the C-H bond distances in

these two methyl groups are only 0.001 Å different between the free ligand (1.093 Å) and the complex (1.094 Å). Moreover, the frequency red shift is in contrast to the blue shift observed for the ring C-H stretches in metal benzene ions.[153-155] The major reason for the red shift is the charge redistribution of the $C_{1,4}$ upon Sc coordination. An atomic charge analysis shows that the charges on the carbon atoms of the methyl groups are reduced from -0.79e in the free ligand to -0.03e in the complex, whereas the charges on the hydrogen atoms remain essentially unchanged (0.15e). This charge redistribution makes the C-H bonds in the methyl groups significantly less polarized in the complex and thus reduces the C-H bond strength.

4.3.2.4. Methyl Substitution Effects

Table 4.4 summarizes the IEs and vibrational frequencies of the Sc(methylbenzene) complexes measured from the ZEKE and IR-UV spectra, along with those from the DFT calculations. The table also includes the IEs and vibrational frequencies of Sc(benzene) and Sc(toluene) obtained previously by our group.[60,145] Several observations can be made from the data in Table 4.4. First, methyl substitution reduces the IE of the Sc complexes by 345 ± 88 cm^{-1} (or 0.0428 ± 0.0109 eV) with each methyl group. Larger IE reductions by the methyl substitutions (0.14-0.41 eV) were observed previously for the free ligands[117] and this finding is explained by hyperconjugation and charge transfer from the methyl radical to the benzene ring, which stabilizes the molecular ion more than the neutral molecule. Such stabilization clearly exists in the metal complexes, but to a lesser degree, because a large fraction of the positive charge in the complexes is located on the metal atom rather than the benzene ring. Second, although the Sc$^+$-ligand stretching frequencies do not change significantly with methylation, the stretching force constants are expected to increase because of the increase in the reduced masses with methyl substitutions. Except for Sc(benzene), there has been no report on the experimental bond energies for these half-sandwich species. However, if theoretical bond energies are used for comparison, a significant increase is found from benzene to *p*-xylene, and smaller change from further methylation. Third, the number of vibrational modes observed for the ion is increased from benzene to

methylbenzene species, due to additional methyl torsional motions and lower molecular symmetries of the methyl substituted species. Finally, although the spectral linewidths are comparable for all partially methylated species, much broader spectra are observed as a result of permethylation.

4.4. Conclusions

We obtained the first-high resolution electron spectra of $Sc[C_6H_{6-x}(CH_3)_x]$ ($x = 2$, 3, and 6) and IR-UV ion spectra of $Sc[C_6(CH_3)_6]$. From these spectra, we determined adiabatic IEs and several vibrational frequencies of these complexes. The IEs decrease with increasing number of the methyl groups, although this effect is much smaller than that in the free methylbenzene molecules. Sc coordination to these methylbenzene molecules causes the benzene ring to fold into a boat-like shape and π electrons to redistribute in a 1, 4-diene fashion. This is different from Sc(benzene), where Sc complexation does not affect the planarity and aromaticity of the carbon ring in the ground state of the complex. Moreover, these methylated metal complexes have a lower electron spin multiplicity in their ground states than, but a similar HOMO character to the corresponding benzene-scandium complex.

Table 4. 1. Electronic states, relative electronic energies (E_{rel}, cm^{-1}), and IEs (cm^{-1}) of Sc(methylbenzene) complexes from B3LYP/6-311+G(d,p) calculations.

	Symmetry	State	E_{rel} (cm^{-1})	Transition	IE (cm^{-1})
Sc(*p*-xylene)					40770[a]
	C_{2v}	$^3A_2$	41802	$^1A \leftarrow {}^2A$	40253
	C_2	^1A	40075	$^3A_2 \leftarrow {}^2A$	41993
	C_{2v}	$^4A_2$	1543	$^3A_2 \leftarrow {}^4A_2$	40444
	C_2	^2A	0		
Sc(mesitylene)					40505[a]
	C_{3v}	$^3A_1$	40634	$^1A' \leftarrow {}^2A'$	39998
	C_s	$^1A'$	39754	$^3A_1 \leftarrow {}^2A'$	40818
	C_{3v}	$^4A_1$	878	$^3A_1 \leftarrow {}^4A_1$	39921
	C_s	$^2A'$	0		
Sc(hexamethylbenzene)					39535[a]
	C_1	^3A	38672	$^1A_1 \leftarrow {}^2A_1$	38931
	C_{2v}	$^1A_1$	38712	$^3A \leftarrow {}^2A_1$	38965
	C_1	^4A	1996	$^3A \leftarrow {}^4A$	36992
	C_{2v}	$^2A_1$	0		

[a] From ZEKE spectroscopy.

Table 4. 2. Bond distances (R, Å), conformation angles ($\angle$, degrees) of methylbenzenes, 1, 4-cyclohexadiene, and Sc-methylbenzene complexes from the B3LYP/6-311+G(d,p) calculations.

State	Point group	R(Sc-C)	R(C-C)	$\angle$ (C-C-C-C)
p-xylene				
^1A_g	C_{2h}		1.393 / 1.398	-0.2 / 0.2
mesitylene				
$^1A'$	C_{3h}		1.393 / 1.402	0.0
hexamethylbenzene				
$^1A_{1g}$	D_{3d}		1.406	-3.0 / 3.0
1, 4-cyclohexadiene				
^1A_g	D_{2h}		1.332 / 1.505	0.0
Sc(toluene)				
^2A	C_1	2.247 / 2.252 / 2.455 / 2.460 / 2.473 / 2.485	1.373 / 1.375 / 1.450 / 1.461 / 1.462 / 1.465	-25.4 / -24.3 / 1.1 / 22.9 / 24.1
$^4A''$	C_s	2.430 / 2.432 / 2.436 / 2.446	1.416 / 1.419 / 1.421	±0.1 / ±0.2
^1A	C_1	2.192 / 2.203 / 2.366 / 2.383 / 2.399 / 2.424	1.380 / 1.384 / 1.447 / 1.459 / 1.461 / 1.466	-24.2 / -22.1 / 2.1 / 19.1 / 21.4
$^3A''$	C_s	2.373 / 2.374 / 2.378 / 2.402	1.418 / 1.420 / 1.424	±0.1 / ±0.2 / 0.0
Sc(p-xylene)				
^2A	C_2	2.250 / 2.445 / 2.492	1.376 / 1.454 / 1.465	-25.0 / 3.2 / 22.2
$^4A_2$	C_{2v}	2.428 / 2.448	1.420	±0.1 / 0.0
^1A	C_2	2.199 / 2.359 / 2.426	1.386 / 1.450 / 1.467	-23.4 / 5.3 / 18.4
$^3A_2$	C_{2v}	2.369 / 2.399	1.421 / 1.423	±0.9 / 0.0
Sc(mesitylene)				
$^2A'$	C_s	2.241 / 2.268 / 2.452 / 2.488	1.376 / 1.460 / 1.463	±0.3 / ±23.4 / ±25.0
$^4A''$	C_s	2.426 / 2.439	1.421	±0.1 / ±0.2 / ±0.3
$^1A'$	C_s	2.189 / 2.212 / 2.371 / 2.416	1.384 / 1.460 / 1.462	±1.3 / ±20.1 / ±23.5
$^3A''$	C_s	2.369 / 2.390	1.423	±1.3 / ±1.4

Table 4.2 (continued).

Sc(hexamethylbenzene)				
$^2A_1$	C_{2v}	2.237 / 2.484	1.384 / 1.476	0.0 / $\pm$26.5
^4A	C_1	2.419 / 2.422/ 2.424/ 2.437 / 2.438/ 2.448	1.430 / 1.431 / 1.432 / 1.433	-3.9 / -3.6 / -2.1 / 2.5 / 2.9 / 4.3
$^1A_1$	C_{2v}	2.181 / 2.405	1.393 / 1.478	0.0 / $\pm$24.2
^3A	C_1	2.529 / 2.545 / 2.547 / 2.561 / 2.570 / 2.596 /	1.413 / 1.416/ 1.420 / 1.422/ 1.430 / 1.432	-6.3 / -4.9 / 0.0 / 1.5 / 1.7 / 8.0

Table 4. 3. Peak position (cm^{-1}) and assignment of the ZEKE spectra of the Sc(methylbenzene) complexes.

(a) Sc(p-xylene) $^1A \leftarrow {}^2A$		(b) Sc(mesitylene) $^1A' \leftarrow {}^2A'$		(c) Sc(hexamethylbenzene) $^1A_1 \leftarrow {}^2A_1$	
Position	Assignment	Position	Assignment	Position	Assignment
40628	25_1^0	40351	32_1^0	39535	0_0^0
40654	26_1^0	40505	0_0^0	39935	21_0^1
40770	0_0^0	40641	32_0^1	40335	21_0^2
40788	$25_0^1 26_1^0$	40677	31_0^1		
40886	26_0^1	40747	30_0^1		
40906	25_0^1	40883	28_0^1		
40988	?	40957	27_0^1		
41008	$22_0^1 25_1^0$	41017	$28_0^1 32_0^1$		
41034	$22_0^1 26_1^0$	41053	$28_0^1 31_0^1$		
41060	24_0^1	41255	28_0^2		
41148	22_0^1	41331	$27_0^1 28_0^1$		
41168	$22_0^1 25_0^1 26_1^0$	41627	28_0^3		
41216	21_0^1	41709	$27_0^1 28_0^2$		
41266	$22_0^1 26_0^1$				
41286	$22_0^1 25_0^1$				
41314	20_0^1				
41402	$22_0^2 26_1^0$				
41422	$22_0^1 25_0^2$				
41432	$20_0^1 26_0^1$				
41524	22_0^2				
41546	$22_0^2 25_0^1 26_1^0$				
41596	$21_0^1 22_0^1$				
41642	$22_0^2 26_0^1$				
41682	$22_0^2 25_0^2 26_0^1$				
41694	$20_0^1 22_0^1$				
41898	22_0^3				
41920	$22_0^3 25_0^1 26_1^0$				

Table 4. 4. IEs (cm^{-1}), bond energies (D$_0^+$/D$_0$, kcal mol^{-1}), and vibrational frequencies (cm^{-1}) of Sc(benzene) and Sc(methylbenzene) complexes from ZEKE and IR-UV R2PI spectroscopy and DFT/B3LYP calculations.

		ZEKE	B3LYP
Sc(benzene)[a]	IE	41600	41618
(C_{6v}, $^3A_1 \leftarrow$ $^4A_1$)	D$_0^+$/D$_0$	48.4/ 16.1	48.9/ 16.4
	Sc$^+$/Sc -benzene stretch	375/324	336/320
Sc(toluene)[b]	IE	41167	40802
(C_1, $^1A \leftarrow$ ^2A)	D$_0^+$/D$_0$		53.5/ 18.9
	CH$_3$ clockwise torsion, ν_{42}^+	134	144
	Sc$^+$-toluene stretch, ν_{36}^+	378	378
	Phenyl ring o.p. deformation, ν_{35}^+	476	495
Sc(p-xylene)	IE	40770	40253
(C_2, $^1A \leftarrow$ ^2A)	D$_0^+$/D$_0$		57.2 / 21.0
	CH$_3$ anticlockwise torsion, ν_{26}^+/ν_{26}	116/ 116	116 / 122
	CH$_3$ clockwise torsion, ν_{25}^+/ν_{25}	136/ 142	140 / 163
	Ring o.p. bend along C-H bonds, ν_{24}^+	290	304
	Sc$^+$-(p-xylene) stretch, ν_{22}^+	378	379
	Ring breathing, ν_{21}^+	446	452
	Ring o.p.bend along C(CH$_3$) groups, ν_{20}^+	544	555
Sc(mesitylene)	IE	40505	39998
(C_s, $^1A' \leftarrow$ $^2A'$)	D$_0^+$/D$_0$		56.2/ 19.2
	CH$_3$ clockwise torsion, ν_{32}^+/ν_{32}	136/ 154	153/ 151
	CH$_3$ bend towards Sc, ν_{31}^+	172	177
	CH$_3$ rock, ν_{30}^+	242	272
	Sc$^+$-mesitylene stretch, ν_{28}^+	378	375
	Ring breathing, ν_{27}^+	452	482
Sc(hexamethylbenzene)	IE	39535	38931
(C_{2v}, $^1A_1 \leftarrow$ $^2A_1$)	D$_0^+$/D$_0$		59.5/ 19.4
	Sc$^+$-hexamethylbenzene stretch, ν_{21}^+	400	366
	Symmetric and asymmetric C-H stretch, ν_5 & ν_{69}	2850[c]	2861/ 2862[d]

[a] From reference[60].
[b] From reference[145].
[c] From IR-UV ion spectrum.
[d] Scaled by a factor of 0.9670.

(a) *p*-xylene and Sc(*p*-xylene)

Symm	C_{2h}	C_2	C_{2v}
State	^1A_g	$^2A/^1A$	$^4A_2/^3A_2$
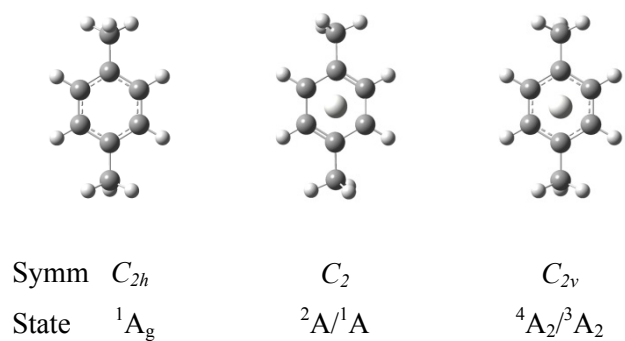
(b) mesitylene and Sc(mesitylene)

Symm	C_{3h}	C_s	C_{3v}
State	$^1A'$	$^2A'/^1A'$	$^4A_1/^3A_1$

(c) hexamethylbenzene and Sc(hexamethylbenzene)

Symm	D_{3d}	C_{2v}	C_1
State	$^1A_{1g}$	$^2A_1/^1A_1$	$^4A/^3A$
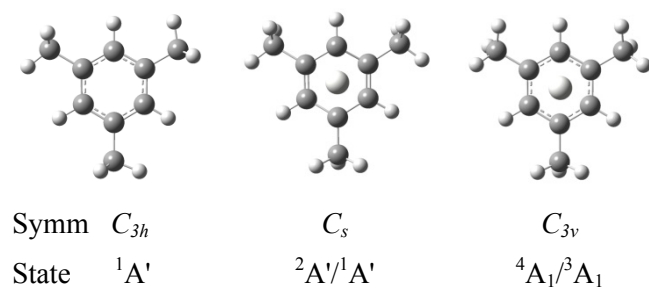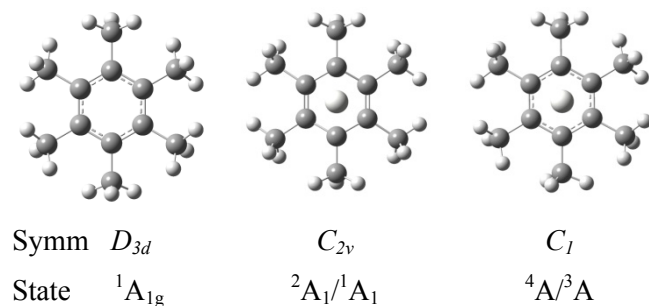
Figure 4. 1. The minimum-energy conformers of methylbenzene molecules in the ground electronic state and of Sc(methylbenzene) complexes in various electron spin states. The Sc(methylbenzene) complexes have doublet and quartet states in the neutral molecule and singlet and triplet states in the cation.   Methyl group orientations are different between the free ligand and complex.

Top view   Side view
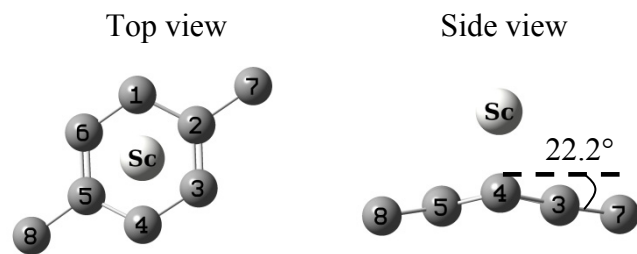
(a) Sc(*p*-xylene), ^{2}A/^{1}A (C_2)
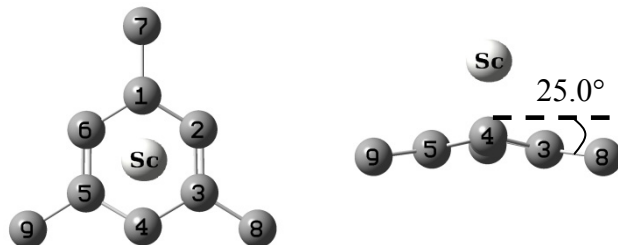
(b) Sc(mesitylene), ^{2}A'/^{1}A' (C_s)
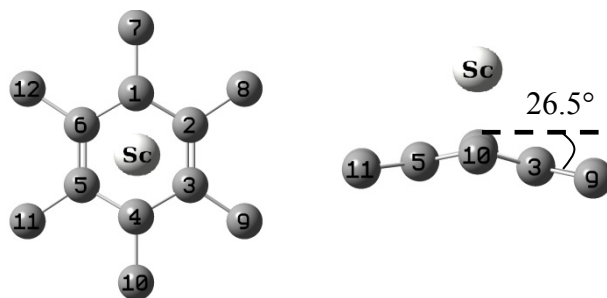
(c) Sc(hexamethylbenzene), ^{2}A$_1$/^{1}A$_1$ (C_{2v})

Figure 4. 2. The conformations of the neutral doublet and cation singlet states of Sc(methylbenzene) complexes. The phenyl ring is bent with C_1 and C_4 atoms towards Sc, and conformation angles are for $\angle C_2$-C_3-C_4-C_5. Hydrogen atoms are not shown in the figure.
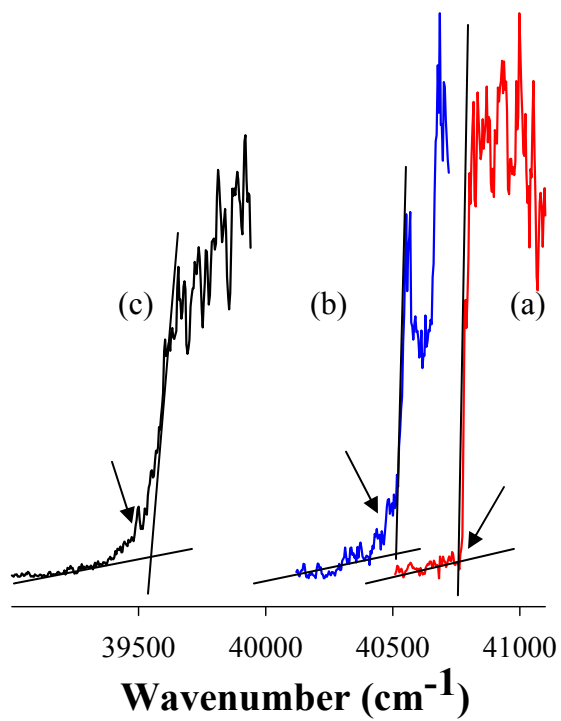
Figure 4. 3. PIE spectra of Sc(*p*-xylene) (a), Sc(mesitylene) (b), and Sc(hexamethylbenzene) (c) complexes. The ionization threshold of each complex is estimated from the intersection point of the baseline and ion signal rising onset as indicated by the arrows.

544
446
378
290
136
116
116
142
? x15

(a) Expt, He

(b) Expt, 1:1 He/Ar

(c) $^{1}A \leftarrow {}^{2}A$

(d) $^{3}A_2 \leftarrow {}^{2}A$

(e) $^{3}A_2 \leftarrow {}^{4}A_2$

40500   41000   41500   42000

Wavenumber (cm^{-1})
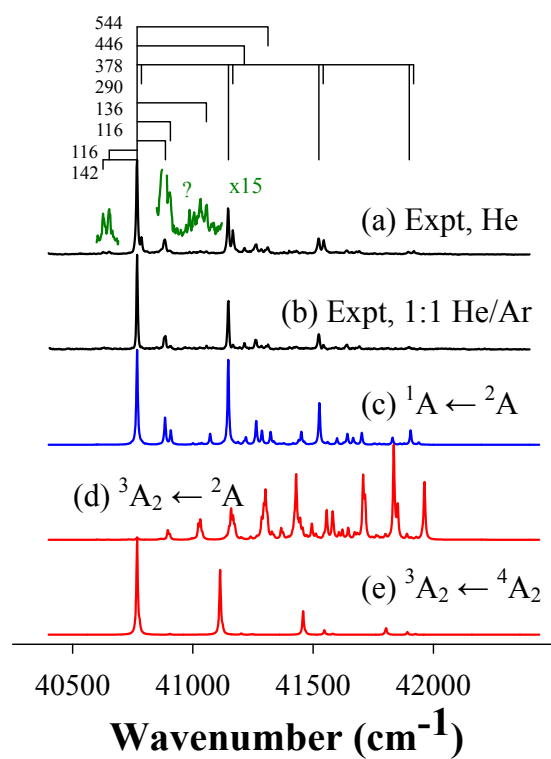
Figure 4. 4. Experimental ZEKE spectra of Sc(*p*-xylene) seeded in He (a) and 1:1 He/Ar (b), and simulations of $^{1}A \leftarrow {}^{2}A$ (c), $^{3}A_2 \leftarrow {}^{2}A$ (d), and $^{3}A_2 \leftarrow {}^{4}A_2$ (e) transitions at 50K.
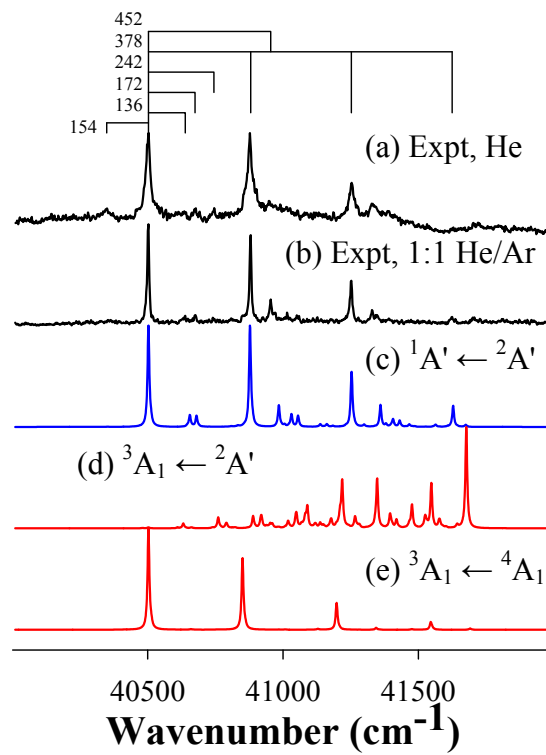
Figure 4. 5. Experimental ZEKE spectra of Sc(mesitylene) seeded in He (a) and 1:1 He/Ar (b) and simulations of $^1A' \leftarrow {}^2A'$ (c), $^3A_1 \leftarrow {}^2A'$ (d), and $^3A_1 \leftarrow {}^4A_1$ (e) transitions at 50K.
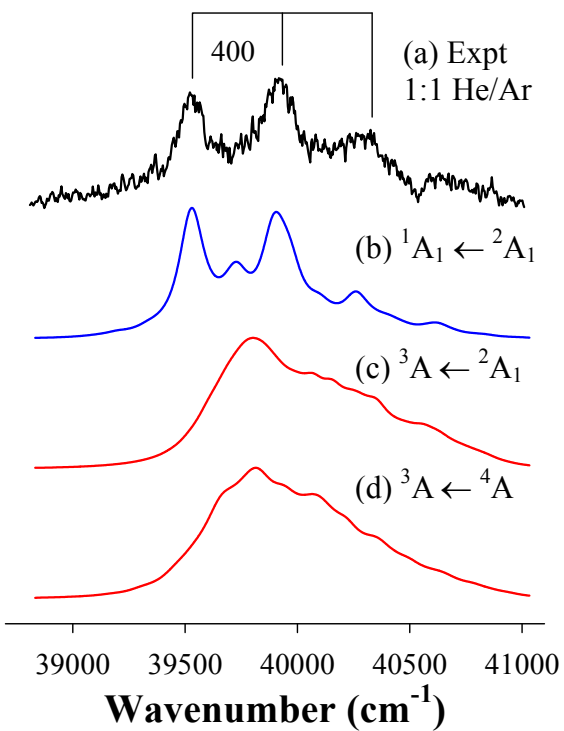
Figure 4. 6. Experimental ZEKE spectrum of Sc(hexamethylbenzene) seeded in 1:1 He/Ar (a) and simulations of $^1A_1 \leftarrow {}^2A_1$ (b), $^3A \leftarrow {}^2A_1$ (c), and $^3A \leftarrow {}^4A$ (d) transitions at 50 K.
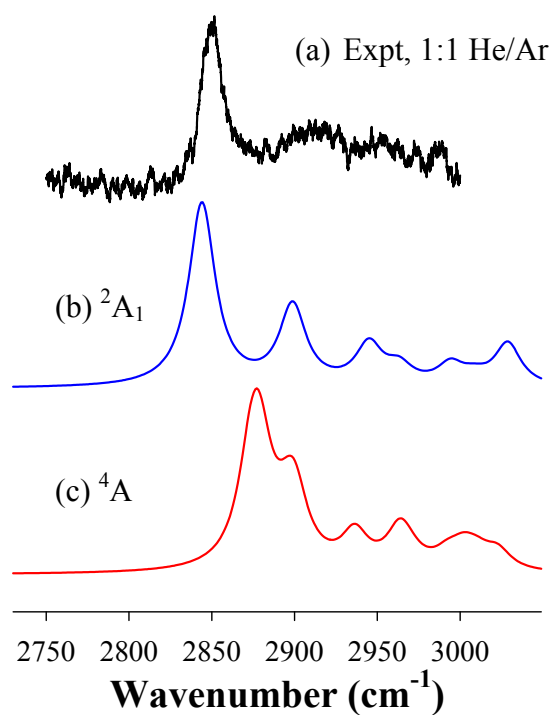
Figure 4. 7. Experimental IR-UV ion spectrum of Sc(hexamethylbenzene) seeded in 1:1 He/Ar (a) and simulated IR spectra of the $^2A_1$ (b) and ^4A (c) states of the complex in the C-H stretching region. The calculated C-H frequencies are scaled by 0.9670, the averaged ratio of the experimental to calculated C-H stretching frequencies of the free ligand.

CHAPTER 5. PULSED-FIELD IONIZATION ELECTRON SPECTROSCOPY OF TITANIUM, VANADIUM, AND COBALT HEXAMETHYLBENZENE COMPLEXES

5.1. Introduction

Metal-arene interaction is of fundamental importance in homogeneous catalysis involving aromatic C-C and C-H bond activation[122-124] and arene hydrogenation.[125-127] Benzene is the simplest arene molecule and its interactions with metal ions have been studied by numerous spectroscopic measurements.[128] The molecular structures of early transition metal benzene complexes have been reported previously.[129,132,156,157] The metal-benzene complexes can have planar benzene ring with (Ti/ V)[129,156] and (Ti$^+$/ Cr$^+$/ Mn$^+$/ Cu$^+$)[132] metal atom binding. However, a planar benzene ring may deform with metal coordination of a different identity and charge on the metal atom. For example, (Zr/ Hf)[157] and (V$^+$/ Fe$^+$/ Co$^+$/ Ni$^+$)[132] metal coordination have been reported to disrupt the delocalized π electrons in the carbon network and bend the benzene ring. Previously, our group has identified a planar benzene ring of gaseous Sc(monobenzene) complex in the neutral quartet and ionic triplet states.[60] In addition, the electron multiplicities of other early transition metal-benzene complexes were explored by experimental[129,132,153,156,158-160] and theoretical[161-168] means. However, these data have shown much discrepancy in the results. DFT methods have predicted the quintet ground state of the neutral Ti(benzene) complex, and the triplet state is located ~ 0.2 eV higher in energy.[156,161,162] However, the electronically excited Ti atoms (^{5}F or ^{1}D) in the supersonic beam are likely to experience collisional relaxation and a triplet state of the complex has been proposed to be favored in the experimental supersonic beam.[156] For the cationic Ti(benzene) complex, the quartet ground state of either ^{4}A$_1$ or ^{4}A$_2$ states has been predicted by DFT and HF calculations.[162-166] Such theoretical results were later tested and ^{4}A$_1$ state of the cationic complex has been determined by the infrared resonance enhanced multiple-photon dissociation (IR-REMPD) spectroscopy.[132] The electronic multiplicities of the neutral and ionic V(monobenzene) complexes exhibit more deviations. Either doublet[129,158,159,161,167], quartet[167], or sextet[162] electronic ground states for the neutral complex and quintet[162,163,165,166] or triplet[166] for the ion are predicted from theory. In

addition, the electronic state of the V(benzene) complex is determined to be $^2A_1$[129] and that of V^+(benzene) is either $^5E_1$[163] or $^5B_2$[165,166]. Moreover, the IR-REMPD spectra of V^+(benzene) shows the possibility of either $^5B_2$[160] or $^3A_2$[132] ground state, and infrared laser photodissociation technique has determined $^5B_1$[153] ground state for the complex. Furthermore, theoretical studies have predicted a triplet ($^3A_1$ or $^3A_2$) ground electronic state for Co^+(benzene)[163,165,166] and a doublet ground state for Co(benzene) complex.[162,168]

Uncoordinated hexamethylbenzene has a planar ring structure with D_{3d} point group.[136-138] However, similar to benzene, the metal coordination may retain or perturb the carbon plane of the benzene ring. The crystal structure of the ruthenium-bis(hexamethylbenzene) complex has shown one of the hexamethylbenzene ligands bent by 42.8°, whereas the other one remains planar.[169-171] This X-ray analysis has determined that the planar ligand is coordinated to the metal by six-fold and the bent ring has distorted cyclic π electron conjugation with four-fold binding ("butadiene" moiety) to the metal. Such deviations of the planarity of the rings are explained by the planar and bent rings donating six and four π electrons to the metal center, respectively. As a result, the ruthenium reaches the inert gas 18 electron configuration. In Ta(hexamethylbenzene), the ligand is bent and ligand π electrons are localized in a 1,4-diene fashion.[141,172] Niobium[173,174], rhodium[175], or ruthenium[176] metal coordination causes similar bending of the arene ring but the degrees of ring distortion are less. On the other hand, for other transition metal complexes, a different prediction has been made. For $[TiCl_3-C_6(CH_3)_6]^+$ complex, the Ti metal retains six-fold binding and the bond distance from the Ti metal to the centroid of hexamethylbenzene is determined to be 2.059 (12) Å.[177] In addition, Fischer et al have synthesized paramagnetic $Co-[C_6(CH_3)_6]_2^+PF_6^-$ and $Co[C_6(CH_3)_6]_2$ complexes.[178,179] The $Co-[C_6(CH_3)_6]_2^+$ fragment was proposed to be triplet with six paired electrons in d_{xy}, d_{x2-y2}, and d_{z2} and two unpaired electrons in d_{yz} and d_{xz} orbitals.[180] The X-ray diffraction study shows that there are three distinct Co-C bond lengths of 2.235 (2), 2.257 (2), and 2.278 (2) Å.[181] Additionally, nuclear magnetic resonance contact shifts have been observed for cationic V- and Co-bis(hexamethylbenzene) complexes.[182] From the study, the ground $^3A_{1g}$ state of [Co-bis(hexamethylbenzene)]$^+$ complex is determined under the assumption of the electron delocalization and D_{6h}

symmetry. Unfortunately, there has not been any structural determination on the early transition metal-mono(hexamethylbenzene) complex except the studies from our group. Previously, we have determined the Sc(*p*-xylene), Sc(mesitylene), and Sc(hexamethylbenzene) complexes to be in the low-spin doublet ground state with a bent benzene ring in 1,4-diene fashion (Chapter 4). This study has shown that the Sc metal binds to the benzene ring differently when one or more hydrogen is substituted by methyl groups. Current work is designed to investigate the metal binding mode and ligand perturbation caused by other metal coordination. In the present study, the structures of the M(hexamethylbenzene) (M = Ti, V, and Co) complexes are studied by the PFI-ZEKE spectroscopy. The structures of the complexes are determined by comparing the experimental spectra with the simulations from the DFT calculations. In addition, IR-UV R2PI spectroscopy is applied to characterize the neutral Co(hexamethylbenzene) complex.

5.2. Experimental and Computational Methods

5.2.1. UV PFI-ZEKE spectroscopy

The PFI- ZEKE spectrometer used in this work was described in Chapter 2. The $M[C_6(CH_3)_6]$ (M = Ti, V, and Co) complexes were synthesized by the reactions of metal atom vapors with ligand vapor (hexamethylbenzene, 99%, TCI America) in a laser-vaporization cluster beam source. The metal atoms were produced by laser ablation of a metal rod [Ti (99.7%), V (99.7%), and Co (99.95%), Aldrich] with the second-harmonic output of a pulsed neodymium doped yttrium aluminum garnet (Nd:YAG) laser (Continuum Minilite II, 532 nm, 3-5 mJ) in the presence of He or Ar carrier gas (UHP, Scott-Gross) or the mixture. These gases were delivered by a home-made piezoelectric pulsed valve with backing pressure of 40-70 psi.[55] The metal rod was translated and rotated by a motor-driven mechanism to ensure each laser pulse ablated a fresh metal surface. The hexamethylbenzene ligand is a solid (mp, 165-168 °C) and has relatively low vapor pressure at room temperature. To obtain sufficient ligand vapor, the ligand was placed inside a copper oven and was heated if necessary to maximize the ion signals.

For the Ti and V complexes, the ligand was heated up to 37 °C by a heating cartridge and the temperature was maintained by a thermo-controller (Omega CN2110). On the other hand, Co(hexamethylbenzene) did not require the ligand to be heated and was able to obtain good intensity of ion (~ 2 V) and electron (~ 100 mV) signals. The ligand was used with no further purifications. The vaporized ligands interacted with the metal atoms entrained in the carrier gas. The metal complexes were expanded into the vacuum through the pulsed valve nozzle. The molecular beam was collimated by a cone-shaped skimmer (4mm inner diameter) and passed through a pair of charged deflection plates (+500 V) to remove residual ionic species which might have formed during metal ablation.

The production of the metal complexes was maximized by optimizing the timing and power of the vaporization and ionization lasers, backing pressure of the carrier gas, and by adjusting the temperature to regulate the amount of the ligand introduced. The neutral metal complexes in molecular beams were ionized by a frequency-doubled dye laser (Lumonics HD-500) pumped by third-harmonic output of a second pulsed Nd:YAG laser (Continuum Surelite II, 355 nm) and identified by photoionization time-of-flight mass spectrometry. Ionization thresholds of the complexes were located using PIE spectroscopy by recording the mass-selected ion signal as a function of the ionization laser wavelength. The ZEKE electrons were produced at the optimized conditions of the molecular ions. The neutral complexes were photoexcited to highly excited Rydberg states, followed by pulsed field-ionization of these Rydberg states with a 3 μs delayed, pulsed-electric field (1.2 Vcm^{-1} in height and 100 ns in width). A small dc field (0.06 Vcm^{-1}) was applied to discriminate ZEKE electrons from kinetic electrons produced by direct photoionization. A delay pulse generator (Stanford Research Systems DG535) was used to generate the pulsed-electric field for ionization. The ion and electron signals were detected by a dual microchannel plate detector (Galileo), amplified by a preamplifier (Stanford Research Systems SR445), averaged by a gated integrator (Stanford Research Systems SR250), and stored in a laboratory computer. Laser wavelengths were calibrated against vanadium or titanium atomic transitions.[57] The dc field effects on the PIE and ZEKE spectral energies were corrected using the relation of $\Delta IE = 6.1 E_F^{1/2}$, where E_F in Vcm^{-1} is the field strength.[111]

5.2.2. IR-UV Photoionization Spectroscopy

Details of two-photon IR-UV ionization spectroscopy have been described in Chapter 2. The Co(hexamethylbenzene) complex was synthesized by the method described earlier and vibrationally excited by an IR optical parametric oscillator/amplifier (OPO/A) laser (LaserVision). The IR OPO/A laser was pumped by an injection seeding Nd:YAG laser (Continuum, Surelite III). The system provides tunable mid-IR output range from 2200 – 4500 cm^{-1} using a single KTP and four KTA crystals in the oscillator and amplifier stages, respectively. The IR laser wavelength was scanned in the ranges of 2700 – 3500 cm^{-1} to photoexcite the molecule to intermediate state, whereas the UV laser wavelength was fixed at 150-200 cm^{-1} below the IE after a time delay of 50 - 200 ns. The frequency doubled UV dye laser (Lumonics, HD-500) and IR lights were counterpropagated with each other and perpendicular to the molecular beam. When the IR laser was resonance with the C-H vibrations, the ion signal was produced, and the C-H stretching frequencies of the neutral complex were determined. The spectrum recorded with the injection seeder (laser linewidth, ~ 0.2 cm^{-1}) did not improve the spectral resolution, and the IR spectra were recorded without the injection seeder (~ 2.0 cm^{-1}) to provide higher pulse energies of ~ 10 mJ in the range of C-H stretch bands. The resultant ion signal was detected in the same time-of-flight spectrometer as that used in the ZEKE experiment. The IR laser wavelengths were calibrated with the photoacoustic spectra of H$_2$O.[58]

5.2.3. Computation

The molecular geometry optimization, vibrational frequency, and IR intensity calculations were carried out using B3LYP with 6-311+G(d,p) basis set implemented in GAUSSIAN 03 program package.[59] To simulate the ZEKE spectrum, multidimensional FC factors were calculated from the equilibrium geometries, harmonic vibrational frequencies, and normal coordinates of the neutral and ionized complexes.[52,65] The Duschinsky effect[29] was considered to account for normal mode differences between the neutral and ionic complexes in the FC calculations. A Lorentzian line shape with the

experimental linewidth was used to simulate the spectral broadening. Transitions from excited vibrational levels of the neutral to ionic complexes were calculated by considering Boltzmann distributions. The IR intensity of each normal mode was calculated from the first derivative of the dipole moment at the equilibrium bond distance. The theoretical C-H stretching frequencies are scaled by a factor of 0.9670, the average ratio of the measured to predicted frequencies of the C-H stretching modes in the free hexamethylbenzene molecule.[183] The theoretical IR spectra were calculated with GAUSSIAN 03 and plotted with the experimental linewidth.

5.3. Results and Discussion

5.3.1. Low-Energy Electronic States and Possible Conformations

Table 5.1 summarizes the low-energy electronic states, the IEs of the possible electronic transitions, and molecular symmetries of the neutral and ionic M(hexamethylbenzene) (M = Ti, V, and Co) complexes from the B3LYP/6-311+G(d,p) calculations. The Ti, V, and Co atoms have four, five, and nine outermost valence electrons, respectively. Hence, the electron spin multiplicities that need to be considered are singlet, triplet, qunitet; doublet, quartet, sextet; and doublet, quartet for the neutral and 2, 4; 1, 3, 5; and 1, 3 for the Ti^+, V^+, and Co^+ ion complexes, respectively. Hexamethylbenzene has D_{3d} symmetry in which the para-substituted methyl groups are all staggered.[136-138] In order to search for a local minimum structure of the metal complex, various metal-carbon bond distances and relative methyl orientations in each complex are explored. With the metal binding above the ring, the metal coordination removes the inversion center and the highest possible symmetry of the metal complex is C_{3v}. However, for each complex in each state, the methyl group orientation determines the symmetry of the complex (Figure 5.1). For example, the triplet and quintet states of the Ti-hexamethylbenzene complex have C_{2v} and C_1 point groups, respectively (Table 5.2). This is quite surprising as the quintet state of the complex has a less puckered benzene ring with smaller conformation angle [$\angle$(C-C-C-C) < 4.2°] than that of the triplet state

(the conformation angle reaches up to 11.7°). Due to the methyl orientation, the molecular symmetry of the high-spin states of the complexes are predicted to be C_1 for the quintet/ quartet and sextet/ quintet states of neutral/ ionic Ti and V complexes, respectively. For Co(hexamethylbenzene), the structures of both quartet and triplet states have C_s point group, and the neutral and ionic ground states are 4A" and 3A".

For the neutral transition metal complexes, the high-spin states are predicted to be the ground electronic states. The lower spin states are predicted to have significantly higher energies (3.6-18.9 kcal mol^{-1}, depending on the metal atoms). This trend follows the previous studies on the Sc(benzene) complex, for which the high-spin quartet ground state has a planar benzene ring, and the doublet state with bent ring is located ~ 3.5 kcal mol^{-1} higher in energy.[60] On the other hand, the low-spin doublet ground state of the Sc(hexamethylbenzene) complex with bent ring has been observed (Chapter 4). In Table 5.2, the geometries of the three complexes with possible electron spin multiplicity are presented and compared with those of the Sc(hexamethylbenzene) complex. The degrees of the ring bending are displayed in Figure 5.2 for clear comparison. In the figure, the hydrogen atoms are omitted for simplicity. The major structural differences between each electron spin state are the degrees of bending of the benzene ring. For M(hexamethylbenzene) (M = Ti, V, and Co), the high-spin states have nearly planar rings with bent conformation angles of 2.7-10.3°. The ionic states have slightly less bent ring with the conformation angles of 0.5-9.0°. The high-spin states of the neutral and ionic Ti, V, and Co complexes have similar M-C and C-C bond distances [R(M-C) and R(C-C)]. The M-C and C-C bond distances range in the average values of 2.4 ± 0.1 and 1.43 ± 0.01 Å, respectively. In contrast, the low-spin states have more highly bent ring structures with conformation angles up to 23.8°. From the bent ring structure, two sets of M-C distances are predicted and the differences reach up to 0.2 Å.

The indices of the aromaticities have been calculated to investigate how much the aromaticity of the ring changes by metal coordination. In this work, the structure-based harmonic oscillator model of aromaticity (HOMA),[184,185] which is known as one of the most effective structural aromaticity indicators,[186,187] has been used.

$$\text{HOMA} = 1 - \frac{\alpha}{n}\Sigma(R_{opt} - R_i)^2 \qquad\qquad (5.1)$$

where α is an empirical constant chosen to give HOMA values equal to zero and one for a model system of non-aromatic and aromatic molecules, respectively and n is the total number of bonds taken into an account. For C-C bonds, α_{C-C} is 257.7, and R_{opt} (1.394 Å) and R_i are the bond distances in the benzene molecule and the ring of the hexamethylbenzene from the B3LYP calculations, respectively. Table 5.5 displays the HOMA values of each electronic states of M(hexamethylbenzene) (M = Ti, V, and Co) complexes studied here. As shown in the table, the HOMA values of the high-spin states are higher than those of the low-spin states of the metal complexes. The higher the HOMA value, the higher the aromaticity the ring has and the less perturbation of the delocalized π electron network upon metal coordination. More structural comparison of each complex will be carried out with the individual spectral analysis.

5.3.2. Spectroscopy

5.3.2.1. PIE Spectra of M(hexamethylbenzene) (M = Ti, V, and Co) Complexes

Figure 5.3 presents the PIE spectra of the M(hexamethylbenzene) (M = Ti, V, and Co) complexes. The ion onsets are located by intersecting two lines drawn through a baseline and a sharp rise of the ion signals and indicated by the arrows in the figure. The ionization thresholds are estimated to be 38220 (50), 40300 (100), and 40770 (50) cm^{-1} for the Ti (a), V (b), and Co (c) complexes, respectively. These values are obtained by adding the energy shift of +110 cm^{-1} to the wavenumbers to correct for the dc extraction field effect (320 Vcm^{-1}) in the ionization region.[111] The ionization thresholds obtained from the PIE spectra are used to simplify the search for and correlate with the electron signals in the high resolution ZEKE spectroscopy.

5.3.2.2. ZEKE Spectra of Ti and V(hexamethylbenzene)

Figures 5.4(a) and 5.5(a) show the ZEKE spectra of Ti and V(hexamethylbenzene) complexes seeded in He, respectively. The peaks in both Ti and V(hexamethylbenzene) spectra have quite broad linewidths of about 50 and 150 cm^{-1}, respectively. The attempt to narrow down the spectral linewidths by using heavier Ar carrier gas was unsuccessful due to a weak ZEKE signal. Similarly, a broad spectral linewidth (~ 120 cm^{-1}) is observed in the ZEKE spectrum of the Sc(hexamethylbenzene) complex (Chapter 4). This can be due to a large number of rotational and vibrational degrees of freedom. However, the possibility of having additional transitions from rotational isomers with different methyl orientations is neglected since no other local minima with different methyl orientations are found except for the minimum energy structure presented in Figure 5.1.

The Ti(hexamethylbenzene) spectrum originates at 38248 (5) cm^{-1} and exhibits only one interval of 356 cm^{-1}. Similarly, V(hexamethylbenzene) spectrum originates at 40364 (5) cm^{-1} with one interval of 392 cm^{-1} as well. These vibrational intervals are denoted by the vertical lines in each figure. The strongest peaks at 38248 and 40364 cm^{-1} in the ZEKE spectra of Ti and V(hexamethylbenzene) correlate to the ionization thresholds of the complexes estimated by the PIE spectra [38220 (50) and 40300 (100) cm^{-1}] in Figure 5.3(a) and (b), respectively. These peaks are assigned to the IE of each complex. The IEs of the Ti and V complexes are 16824 and 14047 cm^{-1} lower than those of the Ti and V atoms (55072 and 54411 cm^{-1})[188], respectively. From the thermodynamic cycle [IE(M) – IE(M-ligand) = D_0^+(M^+-ligand) - D_0(M-ligand), where M = Ti or V, ligand = hexamethylbenzene, and D_0^+ and D_0 = bond energies of the ionic and neutral complexes], the IE shift equals to the bond energy difference between the ionic and neutral species. The positive bond energy differences between ionic and neutral species indicate stronger cationic metal-ligand bonding than the neutral. This is because of additional electrostatic interactions between the metal ion and the ligand. From the band origin, the 356 and 392 cm^{-1} intervals in the ZEKE spectra are quite comparable to the Sc^+-benzene (375 cm^{-1}) and Sc^+-hexamethylbenzene (400 cm^{-1}) stretching frequencies and thus assigned to the Ti^+- and V^+-hexamethylbenzene stretching frequencies,

respectively. To confirm such assignments and determine the electronic transition probed in the ZEKE spectra, the theoretical calculations were made.

5.3.2.2.1. Ti(hexamethylbenzene)

In Figure 5.4, the ZEKE spectrum of the Ti(hexamethylbenzene) complex is compared with the simulated spectra of all the possible transitions from the neutral ^{1}A', ^{3}A$_2$, and ^{5}A to the ionic ^{2}A" and ^{4}A states.   In these simulations, the vibrational frequencies are not scaled, but the 0-0 transition energies are shifted to the experimental value for clear comparison. The simulations of the ^{4}A ← ^{3}A$_2$ [Figure 5.4(c)], ^{2}A" ← ^{3}A$_2$ (d), and ^{2}A" ← ^{1}A' (e) transitions exhibit much longer FC profiles than the experimental spectrum due to larger structural changes as predicted by the geometry calculations (Table 5.2). The simulation of the ^{4}A ← ^{5}A transition [Figure 5.4(b)] matches the best with the experimental spectrum in the spectral profile. In addition, the theory predicts that the neutral quintet state has the lowest energy, while the singlet and triplet states are located about 5 and 19 kcal mol^{-1} higher in energy, respectively. Due to the supersonic cooling, the productions of these higher energy states are likely to be quenched, and the transitions from these lower spin states are unlikely to contribute to the ZEKE spectrum. Moreover, the predicted IE from the quintet to quartet state transition (37244 cm^{-1}) resembles the experimental value (38248 cm^{-1}) closely (Table 5.1). The theoretical vibrational frequency (347 cm^{-1}) agrees well with the measured value (356 cm^{-1}), confirming the assignment of the Ti$^+$-hexamethylbenzene stretching frequency. The simple spectrum with no other observed vibrational transitions indicates that ionization removes a weakly-bound metal-based electron and the geometry of the ligand is less affected by the electron removal. According to the DFT calculations, there is significant deviation in the M-C bond distances of the neutral quintet (2.384-2.408 Å) and ionic quartet states (2.346-2.370 Å). On the other hand, the C-C bond distances of the neutral and ionic complex differ only by 0.001 Å. In addition, the conformation angles [∠(C-C-C-C)] of the neutral and ionic complex range less than 4.2° [Table 5.2 and Figure 5.2(a)]. The observed ZEKE peak positions in the Ti(hexamethylbenzene) spectrum, with the dc field correction of +1.5 cm^{-1}, are listed in Table 5.3.

5.3.2.2.2. V(hexamethylbenzene)

As in the Ti(hexamethylbenzene) complex, the high-spin neutral state (^{6}A) of the V(hexamethylbenzene) complex has the lowest energy among all the neutral states (Table 5.1). The low-spin states (^{2}A$_1$ and ^{4}B$_2$) have bent benzene ring structures with conformation angles up to 21.7° [Table 5.2 and Figure 5.2(b)]. In comparison, the conformation angles of the high-spin states are much smaller. The simulations of possible transitions are displayed in Figure 5.5 with narrow linewidths for more evident identification of major progressions contributing to the simulations and comparison with the experimental spectrum. The simulations of the ^{5}A ← ^{4}B$_2$ [Figure 5.5(c)], and ^{3}A" ← ^{2}A$_1$ (e) transitions display long progressions. In addition, the simulations of the ^{3}A" ← ^{4}B$_2$ [Figure 5.5(d)] and ^{1}A' ← ^{2}A$_1$ (f) transitions exhibit combinations of the methyl group rotation (130 cm^{-1})/ out-of-plane (o.p.) bending (186 cm^{-1}) modes and soft mix of these two modes (124 cm^{-1}), respectively. These simulations show quite different spectral profiles from the ZEKE spectrum, which exhibits a major progression of 392 cm^{-1}. On the other hand, the simulation of the high-spin state transition [^{5}A ← ^{6}A, Figure 5.5(b)] reproduces the major progression of the experimental spectrum much better than the others. The simulation exhibits V$^+$-hexamethylbenzene stretching progression (294 cm^{-1}) and methyl group torsional frequencies (72 and 177 cm^{-1}). These small frequency torsional modes and their combinational peaks are unresolved and embedded by the broad peaks of the metal-ligand stretching progression in the experimental spectrum. Therefore, the spectrum in Figure 5.5(b) is simulated with the experimental linewidths. The simulated spectrum resembles the recorded ZEKE spectrum very well. On the other hand, the theory severely underestimates the metal-ligand stretching frequencies, so another theoretical approach is considered to improve the calculated frequency. Unfortunately, both B3P86 and MP2 methods result in similar frequency values around 300 cm^{-1} and more investigation is needed to improve the theoretical predictions. In addition, there is an intense peak at 40556 cm^{-1} denoted by the asterisks in Figure 5.5(a). This peak has very narrow linewidth and is due to vanadium atomic transition by multi-photon processes.[57]

5.3.2.3. ZEKE and R2PI Spectra of Co(hexamethylbenzene)

Figure 5.6 shows the ZEKE spectra of Co(hexamethylbenzene) seeded in He (a), He/Ar mixture (b), and pure Ar (c) carrier gases. The linewidth of the peaks in He carrier gas is about 80 cm^{-1}, which is quite broad like those of M(hexamethylbenzene) (M = Sc, Ti, and V) complexes. As the concentration of Ar gas increases, the cooling effect of the supersonic jet increases and the spectral linewidth reduces to 4 cm^{-1} in the Ar spectrum [Figure 5.6(c)]. Well-resolved Ar spectrum is compared with the simulations in Figure 5.7 for spectral analysis. The ZEKE spectrum originates at 40807 (5) cm^{-1}, which correlates with the ion signal onset [40770 (50) cm^{-1}] from the PIE curve and is assigned to the vibrationless transition. In the experimental spectrum, there are four vibrational intervals above the band origin (17, 43, 359, 416 cm^{-1}) and a 20 cm^{-1} interval is located at low energy side. In addition, there are two intense peaks (41645 and 41785 cm^{-1}) denoted by the asterisks in Figure 5.7(a). These two peaks are much narrower than others, and their intensities depend strongly on the excitation laser power. As in the case in the V(hexamethylbenzene) complex [Figure 5.5(a)], these peaks are likely to be atomic transitions from multiphoton processes. In order to confirm that these peaks do not result from the transitions of the complex, the MATI spectroscopy is applied. The MATI technique has an advantage of mass selectivity and only specific complex [Co(hexamethylbenzene)] can contribute to the spectrum. Indeed, these two peaks do not appear in the MATI spectrum (not shown), and they are assigned to atomic transitions. A sharp line at 41645 cm^{-1} corresponds to a multi-photon ionization of Co metal atom.[57] Unfortunately, the MATI signals in Ar carrier gas were too small to record the whole-range spectrum. In addition, the linewidths of the MATI spectra in He (~ 100 cm^{-1}) and Ar (50 cm^{-1}) were broader than those of the ZEKE spectra (80 cm^{-1} in He and 4 cm^{-1} in Ar). Therefore, the spectral analysis was carried out solely from the well-resolved ZEKE spectrum recorded in Ar carrier.

In the ZEKE spectra of Ti and V complexes, transitions from the high-spin ground states were observed. Similarly, in the case of Co(hexamethylbenzene), the doublet state is more than 9 kcal mol^{-1} higher in energy than the quartet ground state. In addition, the IE of the transition from the quartet to triplet states is predicted to be very close to the

experiment with only 3.7% deviation. Therefore, it is reasonable to assume that the quartet to triplet transition will contribute to the experimental ZEKE spectrum of the Co(hexamethylbenzene) complex. The molecular structure of the complex follows in a similar manner to the previous two species [Ti and V(hexamethylbenzene)]. High-spin quartet and triplet states have nearly planar ring structure [Figure 5.2(c)] with quite equivalent C-C bond lengths (Table 5.2). On the other hand, the neutral doublet and ionic singlet states have diverse C-C bond distances within the ring and bent ring (up to 19.0°) structures, respectively. Therefore, the transitions from doublet states will result in long Franck-Condon profiles due to large structure changes. The experimental spectrum in Ar is compared with the simulated spectra in Figure 5.7. The high-spin state transition [^{3}A" ← ^{4}A", Figure 5.7(b)] clearly resembles the experimental ZEKE spectrum. On the other hand, two transitions from the doublet state (^{3}A" ← ^{2}B and ^{1}A ← ^{2}B) show long progressions [Figure 5.7(c) and (d)] as predicted from the structural comparison. In the simulation of quartet to triplet transition, two intervals of 156 and 170 cm^{-1} above the band origin appear with significant intensities. These peaks in the experimental spectrum are unresolved and the calculations have overestimated the intensities of these transitions. These peaks are related to 1, 3, 5- and 2, 4, 6-methyl group out-of-plane bending modes from the DFT calculations (carbon numbering is denoted in Figure 5.1).

The observed vibrational intervals from the Co(hexamethylbenzene) spectrum can be assigned by comparing with the ZEKE spectra of the M(hexamethylbenzene) (M = Sc, Ti, and V) complexes. The major progression of 359 cm^{-1} is very close to M$^+$-hexamethylbenzene stretching frequencies of Sc (400 cm^{-1}), Ti (356 cm^{-1}), and V (392 cm^{-1}) complexes. The theory predicts the Co$^+$-hexamethylbenzene stretching frequency to be 341 cm^{-1} which confirms such assignment. Unfortunately, all of the Sc, Ti, and V(hexamethylbenzene) spectra do not exhibit other vibrations due to broad linewidths. Therefore, from the comparison between the experiment and the simulation of the ^{3}A" ← ^{4}A" transition, all the vibrational modes from the Co(hexamethylbenzene) spectrum are listed and assigned in Tables 5.3 and 5.4, respectively. Small frequencies located below (20 cm^{-1}) and above (17 and 43 cm^{-1}) the band origin are neutral and ionic vibrational modes, respectively. According to the DFT calculations, these frequencies are assigned to two different methyl group torsional modes and these intervals are well

reproduced in the simulation [Figure 5.7(b)]. In addition, according to previous inelastic neutron-scattering studies, uncoordinated hexamethylbenzene ligand contains three vibrational modes ranging in 400-450 cm^{-1} frequencies.[189] These modes are C-CH$_3$ bends with frequencies of 406, 411, and 451 cm^{-1}. Among these, only a C-CH$_3$ bending vibration mode of 411 cm^{-1} is totally symmetric in the metal complex. Therefore, the remaining 416 cm^{-1} interval can be easily assigned to C-CH$_3$ bending vibration mode of hexamethylbenzene. The DFT calculated frequency for this mode is 412 cm^{-1}.

Unlike the Ti and V complexes, the Co(hexamethylbenzene) complex exhibits strong ion and electron signals, which makes it possible to carry out further investigation using the R2PI spectroscopy. In this method, the UV laser wavelength was fixed at 40600 cm^{-1} which is below the IE, while the IR laser wavelength was scanned in the ranges of 2700-3200 cm^{-1} to find the C-H stretching vibrations of the neutral Co(hexamethylbenzene) complex. The recorded R2PI spectrum is displayed in Figure 5.8(a). The predicted IR spectra of the $^4A''$ and ^2B states in the C-H stretching region are displayed in Figure 5.8(b) and (c), respectively for comparison. The theoretical C-H frequencies are scaled by an average ratio of the measured to calculated frequencies of the hexamethylbenzene C-H stretching modes (0.9670).[183] As shown by the figure, the simulated IR spectrum of the $^4A''$ state matches with the experiment better than that of the ^2B state in energy positions and spectral profile. It is consistent with the result obtained from the ZEKE experiment.

The IR spectrum of Co(hexamethylbenzene) complex is quite different from that of Sc complex (Chapter 4). In the Sc(hexamethylbenzene) complex, only one IR active frequency of 2850 cm^{-1} was identified due to weak intensity of the signal. For the Co complex, several peaks are resolved, and Ar carrier gas narrowed the peak linewidths such that more thorough spectral analysis can be carried out. The experimental spectrum exhibits four intense peaks located at 2916, 2928, 2981, and 3005 cm^{-1}, and two additional peaks at 2874 and 2890 cm^{-1}. Four intense peaks are well estimated by the theory with close in frequency values of 2915/2916, 2927, 2994, and 3021/3022 cm^{-1}, respectively [Figure 5.8(b) and Table 5.4]. In the experimental spectrum, two additional weak bands (2874 and 2890 cm^{-1}) appear around the strong peaks. However, these weak peaks are estimated to have frequencies of 2915 cm^{-1} from the calculation, which is very

similar to and embedded by the intense 2916 cm^{-1} peak. The predicted C-H stretching frequencies are listed and compared with the experimental values in Table 5.4.

The first three peaks (2874, 2890, and 2916 cm^{-1}) are attributed to the near degenerate symmetric and asymmetric C-H [C(1)-(CH$_3$), C(3)-(CH$_3$), and C(5)-(CH$_3$)] stretching modes (carbon numbering is denoted in Figure 5.1). Similarly, asymmetric C-H stretch of C(2,4,6) is present at 2928 cm^{-1}. The calculation predicts these modes to have very close frequencies: 2915 (v_{10}/ v_{55}), 2916 (v_9), and 2927 (v_8/ v_{54}) cm^{-1}, respectively. Compare to the symmetric and asymmetric C-H stretching frequencies in the Sc(hexamethylbenzene) complex observed as one broad peak (2850 cm^{-1}, Chapter 4), these observed frequencies are separated and blue-shifted by more than 24 and to 78 cm^{-1}, respectively. In addition, the range of these values is quite similar to that of the free ligand (2890 cm^{-1}).[183] This is because the Co metal coordination to the hexamethylbenzene has less effect on the C-H coordinates, but Sc coordination causes the charge redistribution on the C(1,4) of the ligand and the red-shift on the C-H stretch frequencies (Chapter 4). Indeed, an atomic charge analysis shows that the charges on the carbon atoms of the methyl groups in the Co complex (-0.77e) are similar to those of free ligand (-0.79e), whereas the charges are much smaller in the Sc(hexamethylbenzene) complex (-0.12e). For these molecules, the charges on the hydrogen atoms are similar [0.15e for hexamethylbenzene and Sc(hexamethylbenzene), and 0.17e for Co(hexamethylbenzene)]. Therefore, C-H bonds in the methyl groups are more polarized upon Co metal coordination than Sc, and larger C-H stretching frequencies are observed for the Co(hexamethylbenzene) complex.

The C-H bonds in the CH$_3$ methyl group can be separated into two groups; hydrogen paired C-H$_2$ and unpaired C-H bonds. These hydrogen paired C-H$_2$ bond groups point to the same direction, whereas they point to the opposite direction from the unpaired C-H bond groups. In addition, the Co metal coordination differentiates six unpaired C-H groups into two. They are carbon groups pointing away from [C(1,3,5)-(CH)] and towards [C(2,4,6)-(CH)] the metal atom (Figure 5.1). Such differentiation results in richer transitions in the Co(hexamethylbenzene) spectrum than that of free ligand. Remaining two peaks (2981 and 3005 cm^{-1}) are assigned to the symmetric and asymmetric hydrogen paired C-CH$_2$ bond stretches, respectively. The

theory predicts three peaks in this region with 2994 (ν_6) and 3021 (ν_{50})/ 3022 (ν_2) cm^{-1} frequencies, respectively. These peaks correspond to the same modes in the free ligand with 2938 and 3018 cm^{-1} of energies.[183]

5.3.3. Trends of Metal Binding Modes, Ground Electronic States, and Ionization and Binding Energies

Table 5.4 summarizes the electronic transitions, IEs, neutral and ionic bond energies (D_0, D_0^+), and the vibrational frequencies of the M(hexamethylbenzene) complexes where M = Sc, Ti, V, and Co. From the table, the trends of the IEs and electronic transitions of the complexes can be easily determined. The IE reduction from the metals to the metal complexes follows the sequence of Sc < V < Ti < Co, which is parallel to the IEs of the metals [Sc (6.5615 eV) < V (6.7462 eV) < Ti (6.8281 eV) < Co (7.8810 eV)].[188] The electronic transitions of the metal-hexamethylbenzene complexes differ with different metals. The ground state of the Sc(hexamethylbenzene) complex is the low-spin doublet state with a bent benzene ring due to differential binding of Sc to the ring carbon atoms (Chapter 4). On the other hand, the high-spin ground states of Ti, V, and Co complexes with nearly planar ring structures are observed.

The relationship between the ring bending and the electron spin multiplicities can be explained by investigating an orbital interaction diagram between the 3d/4s orbitals of the transition metal and occupied π orbitals of ligand. As an example, the orbital interaction between Ti metal and hexamethylbenzene ligand is displayed in Figure 5.9. In the diagram, the metal 3d/4s orbitals are located on the right side, the ligand π orbitals on the left, and the formed molecular orbitals with different electron spin states in the middle. Since the IE of Ti metal atom is lower than that of the hexamethylbenzene, the metal 3d/4s orbitals are placed higher in energy than the highest occupied molecular orbitals (HOMO) of the ligand. In the ^{1}A' and ^{3}A$_2$ states, the benzene ring is bent with two carbon atoms away and towards Ti, respectively and the π electrons are redistributed in 1, 4-diene fashion (Figure 5.2). Similar conformation has been previously observed for the doublet state of Sc(hexamethylbenzene) complex (Chapter 4). On the other hand, the ^{5}A state retains a nearly planar benzene ring but has no symmetry due to methyl

orientations. In the ^{5}A state, the orbital energy gap between (d_{z^2}), (d_{xy}), ($d_{x^2-y^2}$), and (sd_{z^2}) is small because the complex possesses a nearly planar benzene ring, which is similar to the quartet state of the Sc(benzene) complex.[60] Therefore, two doubly degenerate d_{xz}, d_{yz} and $d_{x^2-y^2}$, d_{xy} orbitals are predicted for the quintet state, whereas these orbitals are split into four non-degenerate orbitals in the singlet state. The split of the degenerate orbitals lead to perturbations of π electron network and severe puckering of the benzene ring. As a result, the electron configuration of the neutral ^{5}A state of Ti(hexamethylbenzene) is $(d_{z^2})^1(d_{xy})^1(d_{x^2-y^2})^1(sd_{z^2})^1$. On the other hand, the Ti (sd_{z^2}) based orbital becomes less stable in the triplet state and the electron configuration of ^{3}A$_2$ state is $(d_{z^2})^2(d_{xy})^1(d_{x^2-y^2})^1$.

The high-spin ground states of Ti, V, and Co(hexamethylbenzene) complexes can be justified by considering the energy required to pair up or promote the electrons in the metal atoms. The electron pairing and $3d$-$4s$ orbital promotion energies have been estimated by considering the atomic energy levels of Ti, V, and Co metal atoms. For example, Ti has $3d^24s^2$ (^{3}F) electronic configuration in the ground state and an excited level of $3d^24s^2$ (^{1}D) which has one of the electrons in $3d$ orbital paired up with another. This energy difference can be thought of the energy required to pair up the electrons, resulting in the low-spin state.[190] Similarly, $3d^34s^1$ (^{5}F) configuration is another excited state and the energy difference from the ground state is an energy estimation of orbital energy difference between $3d$ and $4s$ orbitals (energy required to promote one electron from $4s$ to $3d$ orbitals). This electron promotion results in the high-spin state. Based on this consideration, the electron pairing and $3d$-$4s$ orbital promotion energies are estimated for Ti, V, and Co atoms. For these metals, less energy is required to promote electron from $4s$ to $3d$ orbitals (77.7, 23.8, and 40.0 kJ mol^{-1} for Ti, V, and Co atoms, respectively) than to pair up electrons in $3d$ orbitals (84.6, 75.4, and 43.1 kJ mol^{-1} for each metal). This estimation supports the observation of the high-spin states of the Ti, V, and Co(hexamethylbenzene) complexes.

Despite the different structures and the spin states of the M(hexamethylbenzene) (M = Sc, Ti, V, and Co) complexes, the spectra of these species exhibit mainly metal-ligand stretching vibrations. To explain this, the highest occupied molecular orbitals (HOMOs) of the individual complexes need to be considered. The electron configuration of the neutral ^{5}A and ^{6}A states of Ti and V(hexamethylbenzene) are

$(d_{z^2})^1(d_{xy})^1(d_{x^2-y^2})^1(sd_{z^2})^1$ and $(d_{z^2})^1(d_{x^2-y^2})^1(d_{z^2}d_{xy})^1(d_{xz})^1(sd_{z^2})^1$, respectively. That of the quartet Co(hexamethylbenzene) is $(d_{xy})^1(d_{yz})^1(sd_{z^2})^1$. The HOMO of these states has the same sd_{z^2} character. Since the HOMOs of the quartet Sc(benzene)[60], the doublet Sc(methylbenzene) (Chapter 4), and the high-spin states of the M(hexamethylbenzene) (M = Ti, V, and Co) have similar character, the ZEKE spectra of these complexes show similar spectral profiles with the major progression of cationic metal-ligand stretching vibrations.

In Table 5.4, the ionic and neutral bond strength differences of the complexes are compared with the experimental IE shift from the metal atom to the complex to determine the accuracy of the theory. The calculated values have errors of 5, 15, 10, and 1 % for the Sc, Ti, V, and Co(hexamethylbenzene) complexes, respectively. The B3LYP calculation underestimates the relative energy difference of the neutral triplet and ionic quartet states or the IE of Ti metal atom. The IE determined from the experiment (6.8281 eV)[188] and calculated by the theory (6.3985 eV) differ by more than 0.4 eV. To examine the calculated value, a different DFT method (B3P86) with 6-311+G(d,p) basis set is used. The B3P86 calculated IE of the Ti metal is much better (IE = 6.6654 eV) and close to the experimental value. In addition, the B3P86 calculation gives much better prediction on the bond strength difference (48.8 kcal mol^{-1}) of the neutral and ionic Ti(hexamethylbenzene) complexes (48.1 kcal mol^{-1} from the experiment). However, the good prediction from B3P86 is coincidental, since it has been determined that the B3P86 calculation overestimates the IE of the transition metal-aromatic hydrocarbon complexes by an average of about 10%.[191]

5.4. Conclusions

The high-resolution ZEKE spectra of the M(hexamethylbenzene) (M = Ti, V, and Co) complexes and R2PI spectrum of the Co(hexamethylbenzene) complexes have been recorded and analyzed. From the comparison between the experiment and theory, the molecular and electronic structures of the complexes have been determined. The transition metals (Ti, V, and Co) bind to the near planar benzene ring in near six-fold. The resulting complexes exhibit transitions from the high-spin states in the ZEKE spectra.

This finding is different from the Sc(methylbenzene) complexes, where the Sc complex has been observed to be in the low-spin ground state and the benzene ring is bent with π electrons localized in 1, 4-diene fashion (Chapter 4). The electron spectra of the transition metal-hexamethylbenzene complexes show strong transitions from the zero vibration levels of the neutral ground electronic states to the ion and a short progression of the cationic metal-ligand stretch vibration excitations. This is because the HOMOs of the high-spin states of the Ti, V, and Co(hexamethylbenzene) complexes (sd_{z^2}) have a weak binding character.

Table 5. 1. Point groups, electronic states, relative energies (E_{rel}, cm^{-1}), IEs (cm^{-1}) of the M(hexamethylbenzene) (M = Ti, V, and Co) complexes from the B3LYP/6-311+G(d,p) calculations.

Complexes	Symmetry	States	E_{rel} (cm^{-1})	Transitions	IE (cm^{-1})
Ti(hexamethylbenzene)					38248[a]
	C_s	^{2}A"	44184	^{2}A" ← ^{1}A'	37766
	C_1	^{4}A	36939	^{2}A" ← ^{3}A$_2$	42573
	C_s	^{1}A'	6596	^{4}A ← ^{3}A$_2$	35654
	C_{2v}	^{3}A$_2$	1761	^{4}A ← ^{5}A	37244
	C_1	^{5}A	0		
V(hexamethylbenzene)					40364[a]
	C_s	^{1}A'	46754	^{1}A' ← ^{2}A$_1$	44848
	C_s	^{3}A"	39228	^{3}A" ← ^{2}A$_1$	37406
	C_1	^{5}A	37087	^{3}A" ← ^{4}B$_2$	38202
	C_{2v}	^{2}A$_1$	2139	^{5}A ← ^{4}B$_2$	36104
	C_{2v}	^{4}B$_2$	1273	^{5}A ← ^{6}A	37402
	C_1	^{6}A	0		
Co(hexamethylbenzene)					40807[a]
	C_2	^{1}A	51802	^{1}A ← ^{2}B	48829
	C_s	^{3}A"	38979	^{3}A" ← ^{2}B	36093
	C_2	^{2}B	3397	^{3}A" ← ^{4}A"	39290
	C_s	^{4}A"	0		

[a] From ZEKE measurements.

Table 5. 2. Bond distances (R, Å), conformation angles (∠, degrees) of the M(hexamethylbenzene) (M = Sc, Ti, V, and Co) complexes from the B3LYP/6-311+G(d,p) calculations.

State	Point group	R(M-C)	R(C-C)	∠ (C-C-C-C)
Hexamethylbenzene				
--	D_{3d}		1.406	±3.0
Sc(hexamethylbenzene)				
$^2A_1$	C_{2v}	2.237 / 2.484	1.384 / 1.476	0.0 / ±26.5
^4A	C_1	2.419 / 2.422 / 2.424 / 2.437 / 2.438 / 2.448	1.430 / 1.431 / 1.432 / 1.433	-3.9 / -3.6 / -2.1 / 2.5 / 2.9 / 4.3
$^1A_1$	C_{2v}	2.181 / 2.405	1.393 / 1.478	0.0/ ±24.2
^3A	C_1	2.529 / 2.545 / 2.547 / 2.561 / 2.570 / 2.596	1.413 / 1.416 / 1.420 / 1.422 / 1.430 / 1.432	-6.3 / -4.9 / 0.0 / 1.5 / 1.7 / 8.0
Ti(hexamethylbenzene)				
$^1A'$	C_s	2.232 / 2.233 / 2.421 / 2.422	1.416 / 1.476	±23.8 / 0.0
$^3A_2$	C_{2v}	2.282 / 2.388	1.409 / 1.445	±11.7 / 0.0
^5A	C_1	2.384 / 2.385 / 2.387 / 2.404 / 2.405 / 2.408	1.426 / 1.427 / 1.428	-4.2 / -3.3 / -2.8 / 2.7 / 3.6 / 4.0
$^2A''$	C_s	2.131 / 2.143 / 2.275 / 2.290	1.407 / 1.461 / 1.463	±17.9 / ±13.8 / ±2.0
^4A	C_1	2.346 / 2.348 / 2.351 / 2.366 / 2.367 / 2.370	1.427 / 1.428 / 1.429	-4.2 / -3.0 / -2.7 / 2.4 / 3.6 / 3.9

Table 5.2 (continued).

V(hexamethylbenzene)				
$^2A_1$	C_{2v}	2.180 / 2.320	1.421 / 1.469	$\pm$17.4 / 0.0
$^4B_2$	C_{2v}	2.135 / 2.334	1.396 / 1.471	$\pm$21.7 / 0.0
^6A	C_1	2.438 / 2.439 / 2.490 / 2.495 / 2.514 / 2.533	1.411 / 1.416 / 1.426 / 1.427	-10.3 / -4.0 / -3.3 / 3.0 / 3.8 / 10.8
$^1A'$	C_s	2.183 / 2.346	2.418 / 1.468	$\pm$20.1 / 0.0
$^3A''$	C_s	2.112 / 2.114 / 2.250 / 2.264	1.407 / 1.455 / 1.458	$\pm$17.8 / $\pm$14.4 / $\pm$1.7
^5A	C_1	2.368 / 2.376 / 2.400 / 2.416 / 2.444	1.420 / 1.422 / 1.427 / 1.430	-9.0 / -3.1 / -0.5 / 0.6 / 5.4 / 6.6
Co(hexamethylbenzene)				
^2B	C_2	2.078 / 2.101 / 2.108	1.433 / 1.440	-1.9 / -0.3 / 2.2
$^4A''$	C_s	2.259 / 2.263 / 2.285 / 2.286	1.422	$\pm$4.3 / $\pm$4.2 / $\pm$4.1
^1A	C_2	2.016 / 2.182 / 2.209	1.407 / 1.445 / 1.449	-19.0 / 3.4 / 15.5
$^3A''$	C_s	2.176 / 2.178 / 2.197 / 2.198	1.430 / 1.431	$\pm$3.9 / $\pm$3.5 / $\pm$3.2

Table 5. 3. ZEKE peak position (cm^{-1}) and assignment of the M(hexamethylbenzene) (M=Ti, V, and Co) complexes.

(a) Ti(hexamethylbenzene) $^4A \leftarrow {}^5A$		(c) Co(hexamethylbenzene) $^3A'' \leftarrow {}^4A''$	
Position	Assignment	Position	Assignment
38248	0_0^0	40787	86_1^1
38604	74_0^1	40807	0_0^0
		40824	47_0^1
(b) V(hexamethylbenzene) $^5A \leftarrow {}^6A$		40837	47_0^2
		40850	86_0^2
40364	0_0^0	41146	$41_0^1 86_1^1$
40756	75_0^1	41166	41_0^1
		41182	$41_0^1 47_0^1$
		41196	$41_0^1 47_0^2$
		41209	$41_0^1 86_0^2$
		41223	38_0^1
		41520	41_0^2
		41534	$41_0^2 47_0^1$
		41551	$41_0^2 47_0^2$
		41564	$41_0^2 86_0^2$
		41580	$38_0^1 41_0^1$
		41887	41_0^3
		41904	$41_0^3 47_0^1$

Table 5. 4. IEs (cm^{-1}), ionic and neutral bond energies (D$_0^+$/D$_0$, kcal mol^{-1}), vibrational frequencies (cm^{-1}) of the M(hexamethylbenzene) (M = Sc, Ti, V, and Co) complexes from ZEKE spectroscopy and DFT/B3LYP calculations.

		ZEKE	B3LYP
Sc(hexamethylbenzene)	IE	39535	38931
(C_{2v}, $^1A_1 \leftarrow {}^2A_1$)[a]	D$_0^+$-D$_0$ (D$_0^+$/D$_0$)	38.3	40.1 (59.5/19.4)
	M-L stretch (ν_{21}^+)	400	366
	C-H stretch (ν_{69})	2850[b]	2861[c]
Ti(hexamethylbenzene)	IE	38248	37244
(C_1, $^4A \leftarrow {}^5A$)	D$_0^+$-D$_0$ (D$_0^+$/D$_0$)	48.1	41.1 (66.4/25.3)
	M-L stretch (ν_{74}^+)	356	347
V(hexamethylbenzene)	IE	40364	37402
(C_1, $^5A \leftarrow {}^6A$)	D$_0^+$-D$_0$ (D$_0^+$/D$_0$)	40.2	44.0 (59.3/15.3)
	M-L stretch (ν_{75}^+)	392	294
Co(hexamethylbenzene)	IE	40807	39290
(C_s, $^3A'' \leftarrow {}^4A''$)	D$_0^+$-D$_0$ (D$_0^+$/D$_0$)	65.1	65.6 (72.7/7.1)
	CH$_3$ asymmetric torsion (ν_{86}^+/ ν_{86})	22/42	42/57
	CH$_3$ symmetric torsion (ν_{47}^+)	17	29
	M-L stretch (ν_{41}^+)	359	341
	C-CH$_3$ bend (ν_{38}^+)	416	412
	Symmetric and asymmetric C-H stretch [C(1,3,5)-CH]	2874[b], 2890[b], 2916[b]	2915[c] (ν_{10} / ν_{55}), 2916[c] (ν_9)
	Asymmetric C-H stretch [C(2,4,6)-CH]	2928[b]	2927[c] (ν_8 / ν_{54})
	Symmetric C-H$_2$ stretch	2981[b]	2994[c] (ν_6)
	Asymmetric C-H$_2$ stretch	3005[b]	3021[c] (ν_{50}) 3022[c] (ν_2)

[a] Results from the Sc(methylbenzene) studies (Chapter 4).
[b] From IR-UV ion spectrum.
[c] Scaled by a factor of 0.9670.

Table 5. 5. Aromatic indices from the structure-based harmonic oscillator model of aromaticity (HOMA) of M(hexamethylbenzene) (M = Ti, V, and Co) in different electronic states.

benzene					
States	$^1A_{1g}$				
Aromatic index[a]	1				

hexamethylbenzene					
States	--				
Aromatic index[a]	0.96				

Ti(hexamethylbenzene)					
States	$^1A'$	$^2A''$	$^3A_2$	^4A	^5A
Aromatic index[a]	0.34	0.19	0.53	0.70	0.72

V(hexamethylbenzene)						
States	$^1A'$	$^2A_1$	$^3A''$	$^4B_2$	^5A	^6A
Aromatic index[a]	0.43	0.39	0.31	0.02	0.73	0.79

Co(hexamethylbenzene)				
States	^1A	^2B	$^3A''$	$^4A''$
Aromatic index[a]	0.50	0.51	0.65	0.80

[a]The aromatic index of each state metal-hexamethylbenzene complexes are calculated by using the C-C bond lengths calculated from the B3LYP/6-311+G(d,p) calculations (refer to text).

(a) Ti(hexamethylbenzene)
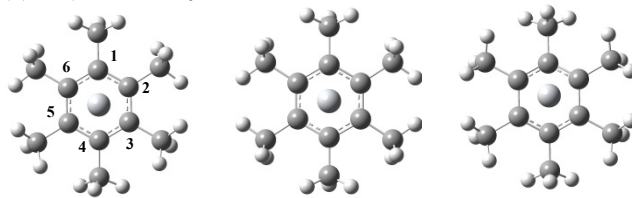
Symm	C_1	C_{2v}	C_s
State	$^5A/\,^4A$	$^3A_2$	$^1A'/\,^2A''$

(b) V(hexamethylbenzene)
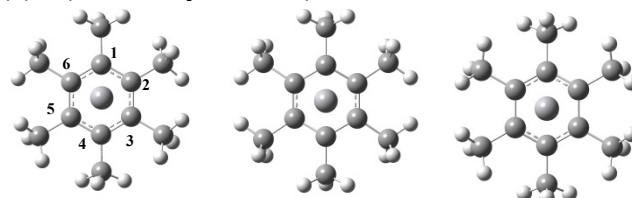
Symm	C_1	C_{2v}/C_s	C_{2v}/C_s
State	$^6A/\,^5A$	$^4B_2/\,^3A''$	$^2A_1/\,^1A'$

(c) Co(hexamethylbenzene)
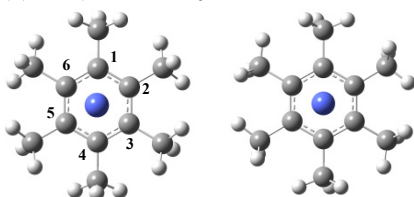
Symm	C_s	C_2
State	$^4A''/\,^3A''$	$^2B/\,^1A$

Figure 5. 1. The minimum-energy conformers of the M(hexamethylbenzene) (M = Ti, V, and Co) complexes in various electron spin states.

(a)Ti(hexamethylbenzene)

^{5}A (C_1) ^{3}A$_2$ (C_{2v}) ^{1}A' (C_s)

< 4.2° 11.7° 23.8°

(b) V(hexamethylbenzene)

^{6}A (C_1) ^{4}B$_2$ (C_{2v}) ^{2}A$_1$ (C_{2v})

< 10.8° 21.7° 17.4°

(c) Co(hexamethylbenzene)

^{4}A" (C_s) ^{2}B (C_2)

< 4.3° < 2.2°
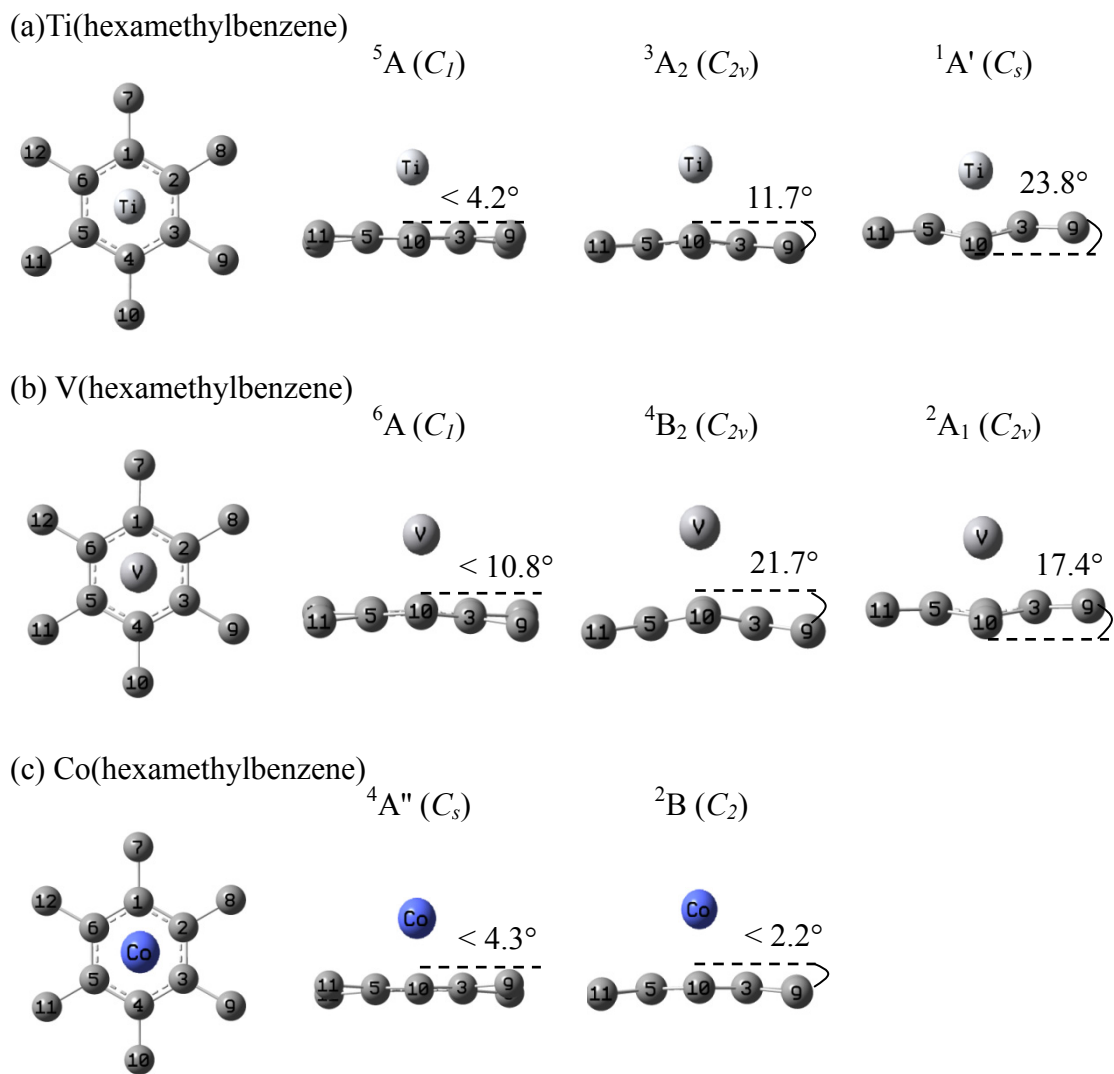
Figure 5. 2. The conformations of the M(hexamethylbenzene) (M = Ti, V, and Co) complexes in various electron spin states. The conformation angles are for ∠(C$_2$-C$_3$-C$_4$-C$_5$). Hydrogen atoms are omitted in the figure.

103
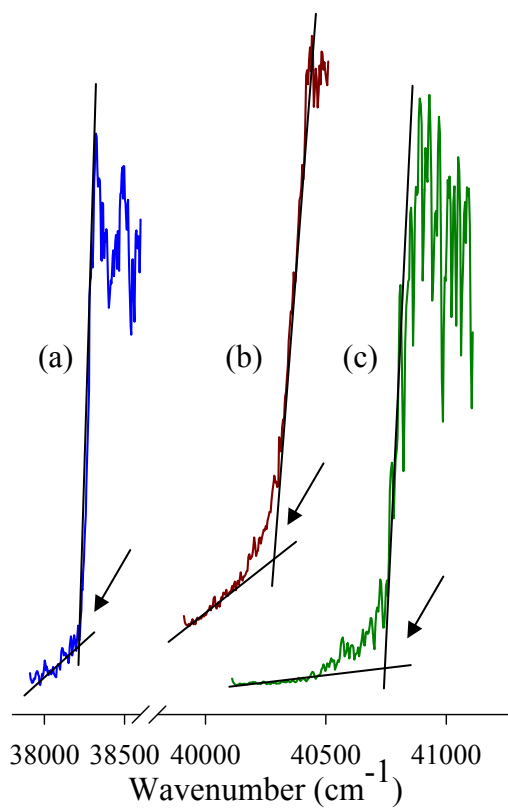
Figure 5. 3. PIE spectra of Ti (a), V (b), and Co(hexamethylbenzene) (c) seeded in He carrier. The ionization threshold of each complex is located by the intersecting two lines from baseline and rising ion signal as pointed by the arrows.
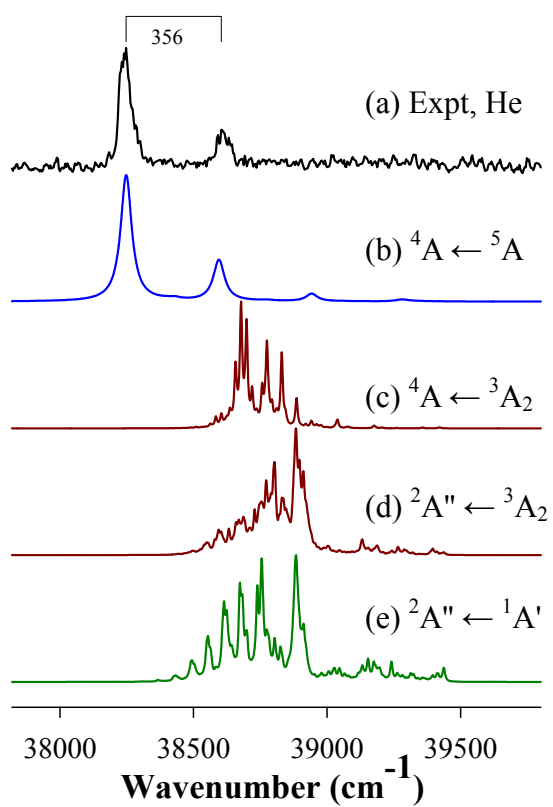
Figure 5. 4. Experimental ZEKE spectra of Ti(hexamethylbenzene) seeded in He (a) and the simulations of $^4A \leftarrow {}^5A$ (b), $^4A \leftarrow {}^3A_2$ (c), $^2A'' \leftarrow {}^3A_2$ (d), and $^2A'' \leftarrow {}^1A'$ (e) transitions at 10K.
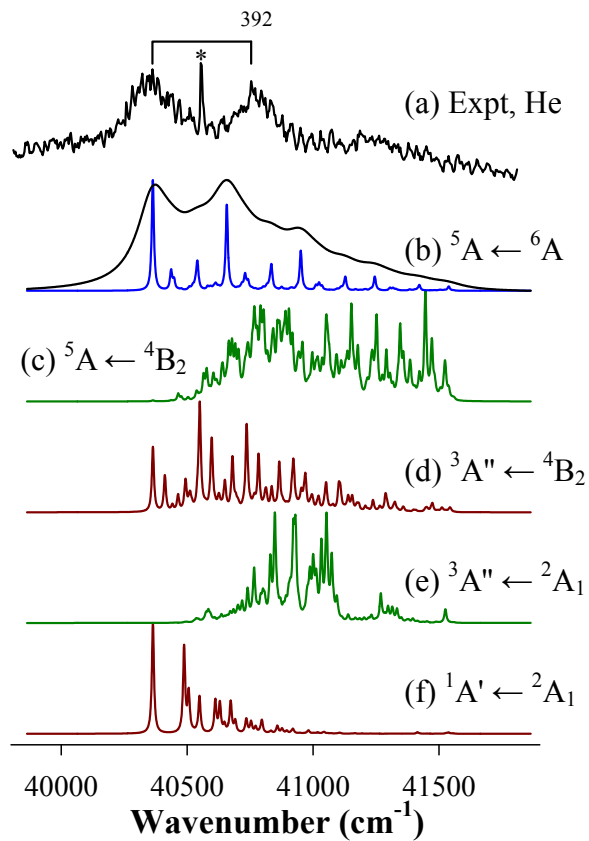
Figure 5. 5. ZEKE spectra of V(hexamethylbenzene) seeded in He (a) and the simulations of $^5A \leftarrow {}^6A$ (b), $^5A \leftarrow {}^4B_2$ (c), $^3A'' \leftarrow {}^4B_2$ (d), $^3A'' \leftarrow {}^2A_1$ (e), and $^1A' \leftarrow {}^2A_1$ (f) transitions at 10K.
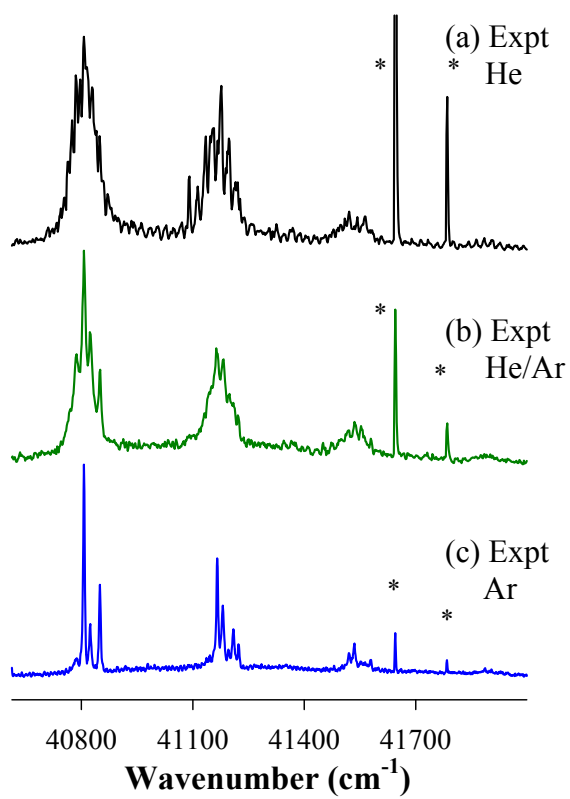
Figure 5. 6. Experimental ZEKE spectrum of Co(hexamethylbenzene) seeded in He (a), He/Ar 1:1 mixture (b), and Ar (c) carrier gas.
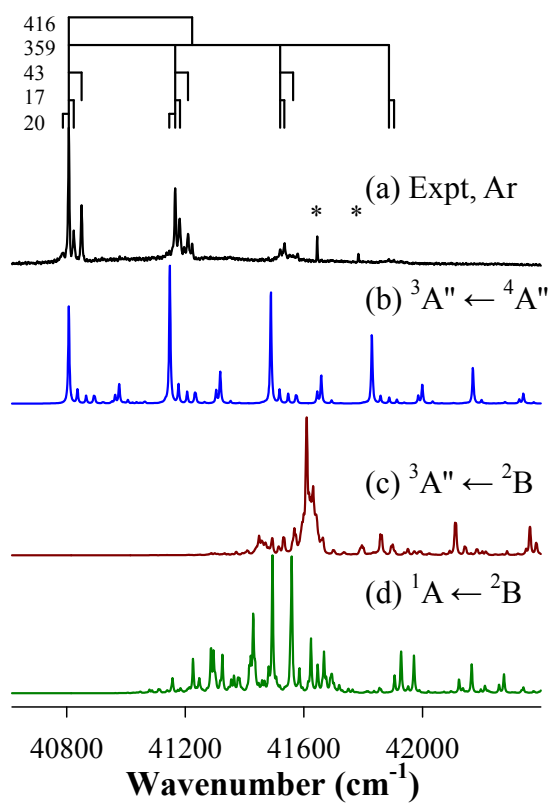
Figure 5. 7. ZEKE spectra of Co(hexamethylbenzene) seeded in Ar (a) and the simulations of ^{3}A" $\leftarrow$ ^{4}A" (b), ^{3}A" $\leftarrow$ ^{2}B (c), and ^{1}A $\leftarrow$ ^{2}B (d) transitions at 10K.
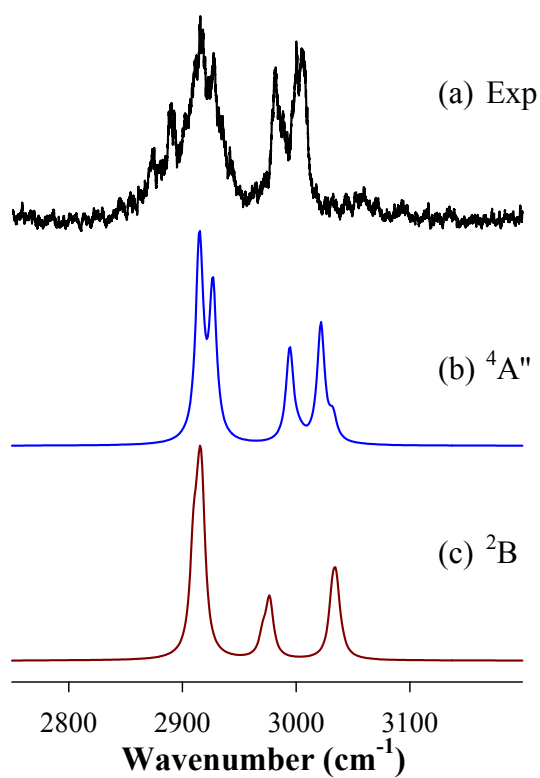
Figure 5. 8. Experimental R2PI spectrum of Co(hexamethylbenzene) seeded in Ar carrier (a) and simulated IR spectra of ^{4}A" (b) and ^{2}B (c) states of the complex in the C-H stretching region. The calculated C-H frequencies are scaled by 0.9670, the average ratio of the experimental and calculated C-H stretching frequencies of the free ligand.
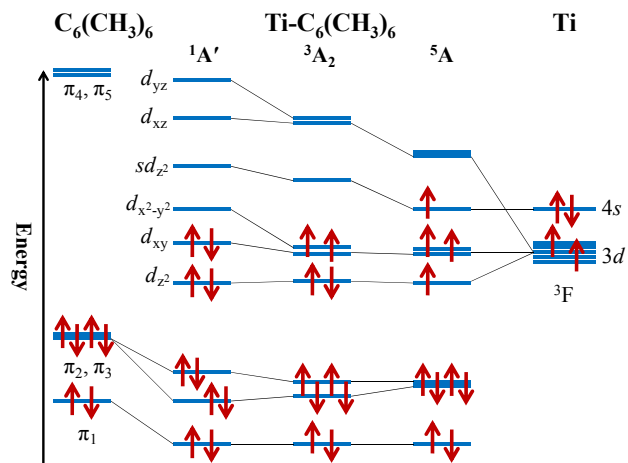
Figure 5. 9. An orbital interaction diagram between the Ti metal and hexamethylbenzene fragments in the ^{1}A' (C_s), ^{3}A$_2$ (C_{2v}), and ^{5}A (C_1) electronic states.

Copyright © Jung Sup Lee 2010

CHAPTER 6. CONFORMATIONAL ISOMERS AND ISOMERIZATION OF GROUP VI TRANSITION METAL-BIS(TOLUENE) SANDWICH COMPLEXES PROBED BY VARIABLE-TEMPERATURE ELECTRON SPECTROSCOPY

6.1. Introduction

Transition metal-arene complexes are true classics among organometallic compounds, and many of them have been identified as key intermediates in homogeneous catalysis.[5,6] These systems are extensively studied in solution-phase chemistry and recently in the gas phase.[17,128,192] Group VI metal-bis(benzene) complexes have received most attention among the metal sandwiches in gas-phase chemistry and spectroscopy, partly because they are 18-electron, coordinatively saturated compounds and can be used as stable precursors for gas-phase measurements. Most of the early studies investigated IEs through photoelectron spectroscopy or mass spectrometry.[193-202] More recently, the gas phase measurements were extended to, for example, collision-induced dissociation,[203] radiative association kinetics,[204] ultraviolet photoabsorption,[205-208] photoionization efficiency,[209] resonance enhanced two photoionization,[210,211] threshold photoelectron-photoion coincidence,[212] MATI,[213-216] and PFI-ZEKE spectroscopy.[56]

Substitution of one or more hydrogen atoms in benzene with functional groups yields benzene derivatives with distinct chemical properties,[217-220] because the substitution modifies the electronic and steric environments around the phenyl ring, provides competing sites for metal coordination, or yields multiple conformers for a metal complex. For example, we have recently found that C_6H_5X prefers the phenyl-ring π binding with X = H, F, CH_3, and OH, but nitrile coordination with X = CN.[60,145] Among the phenyl-ring π complexes, a single conformer was identified for X = H, F, and CH_3, and two were detected for X = OH in supersonic molecular beams.[145] The formation of two distinct $Sc(C_6H_5OH)$ rotational conformers is due to a relatively high energy barrier of the OH group rotation[221-224] and to the unequal Sc-binding with six carbon atoms in the phenyl ring.[145]

Although only a single conformer with methyl group orientation was identified in the mono-toluene complex, four stable rotamers of Cr-bis(toluene) were predicted by

DFT.[225] These rotamers are in an eclipsed phenyl-ring configuration, with methyl-group conformation angles of 0°, 60°, 120°, and 180° (Figure 6.1). The predicted energy differences among these rotational isomers were less than 0.2 kcal mol^{-1}, and energy barriers for isomer conversions were less than 1 kcal mol^{-1}. Since the predicted energy differences among these isomers are so small that the theoretical identification of the most stable conformation becomes problematic. The vapor-phase electronic absorption spectrum of the chromium-bis(toluene) complex was measured in an evacuated heated sample cell and assigned to the 0° and 60° conformers.[226] The MATI spectrum of the complex seeded in a supersonic jet displayed two strong, distinct band origins and several weak vibronic transitions.[227] The energies of the two origins were attributed to the IEs of two sets of rotamers, 0° and 60°/120°/180°, and the weak vibronic transitions were assigned to chromium-toluene vibrational excitations. However, the relative stability of these conformers has not been determined from these measurements, and the IEs of the 60°/120°/180° rotamers remain to be resolved. In condensed phases, phenyl rings in chromium-bis(toluene) cations are essentially free to rotate in isotropic solutions, but they are locked in place by the surrounding anions in the solid state and adopt the conformation dictated by the energetics of the lattice formation.[228] Thus, both eclipsed and staggered conformers have been identified for chromium-bis(toluene) cations in the solid state.[228-232]

   This work aims to probe the rotational conformers, conformer relative stability, and possible conformational isomerization of group VI metal (Cr, Mo, and W)-bis(toluene) sandwich complexes using variable-temperature (variation of the carrier gas) pulsed-field-ionization ZEKE spectroscopy. By studying the three metals in the same group of the periodic table, we hope to investigate metal size effects on the conformational stability and relaxation of these metal-bis(arene) complexes.

6.2. Experimental and Computational Methods

   The molecular beam ZEKE spectrometer used in this work has been described previously in Chapter 2. The group VI transition metal-bis(toluene) sandwich complexes were prepared by reactions of gaseous metal atoms with toluene vapor ($C_6H_5CH_3$, 99.9%,

Aldrich) in a laser-vaporization cluster beam source. The metal atoms were produced by pulsed laser vaporization of a metal rod (Cr, 99.7%, Goodfellow; Mo, 99.95%, Aldrich; W, 99.95%, Goodfellow) with the second-harmonic output of a pulsed Nd:YAG laser (Continuum Minilite II, 532 nm, 3-4 mJ) in the presence of He or Ar carrier gas (UHP, Scott-Gross) or a mixture of He and Ar.   These gases were delivered by a home-made piezoelectric pulsed valve with backing pressure of 40-70 psi.[55]   The metal rod was translated and rotated by a motor-driven mechanism to ensure each laser pulse ablated a fresh metal surface. The ligand was used without further purification, and the complexes were synthesized by two different methods depending on the metal. To synthesize W-bis(toluene), the ligand was delivered at room temperature through a stainless-steel capillary (0.053″ inner diameter) to a small collision chamber (~1.5 mL) placed downstream of the ablation, where the ligand interacted with metal atoms entrained in the carrier gas. For Cr- and Mo-bis(toluene), the toluene vapor was mixed with the carrier gas at a ratio of $(5\text{-}7) \times 10^{-4}$ and expanded through the pulsed valve nozzle. The metal complexes formed in the collision chamber were expanded into the vacuum, collimated by a cone-shaped skimmer (4 mm inner diameter), and passed through a pair of charged deflection plates (+ 500 V) to remove residual ionic species produced by laser ablation.

The metal-bis(toluene) complexes in the molecular beams were identified by photoionization time-of-flight mass spectrometry. A frequency-doubled dye laser (Lumonics HD-500) pumped by the third-harmonic output of a second pulsed Nd:YAG laser (Continuum Surelite II, 355 nm) was used to ionize the neutral complexes. The production of the metal complexes was maximized by optimizing the timing and power of the vaporization and ionization lasers, backing pressure of the carrier gas, and by adjusting the amount of the toluene vapor. Ionization thresholds of the metal-bis(toluene) complexes were located using photoionization efficiency spectroscopy by recording the mass-selected ion signal as a function of the ionization laser wavelength. The ZEKE electrons were produced at the optimized conditions by photoexcitation of the neutral complexes to highly excited Rydberg states, followed by field ionization of these Rydberg states with a 3 μs delayed, pulsed-electric field (1.2 Vcm^{-1}, 100 ns). A small dc field (0.06 Vcm^{-1}) was applied to discriminate ZEKE electrons from kinetic electrons produced by direct photoionization. A delay pulse generator (Stanford Research Systems

DG535) was used to generate the pulsed-electric field for ionization. The ion and electron signals were detected by a dual microchannel plate detector (Galileo), amplified by a preamplifier (Stanford Research Systems SR445), averaged by a gated integrator (Stanford Research Systems SR250), and stored in a laboratory computer. Laser wavelengths were calibrated against vanadium or titanium atomic transitions.[57] The dc field effects on the ZEKE peak positions were corrected using the relation of $\Delta IE = 6.1 E_F^{1/2}$, where E_F in Vcm^{-1} is the field strength.[111]

Molecular geometry optimization and vibrational frequency calculations were carried out with GAUSSIAN 03 program.[59] In these calculations, B3LYP methods with 6-311+G(d,p) basis set was used for H, C, and Cr atoms, and the LanL2DZ basis set for the heavier Mo and W atoms for which the triple-split valence basis set is not available. Additionally, the pseudo-core-potential basis set was applied to Cr metal atoms to compare with Mo and W atoms. Multidimensional FC factors were calculated from the equilibrium geometries, harmonic vibrational frequencies, and normal coordinates of the neutral and ionized complexes.[52,65] The Duschinsky effect[29] was considered to account for normal mode differences between the neutral and ion complexes in the FC calculations. A Lorentzian line shape with the experimental linewidth was used to simulate the spectral broadening. Transitions from excited vibrational levels of the neutral complexes were simulated by assuming thermal excitations at specific temperatures.

6.3. Results and Discussion

6.3.1. Theoretical Conformers

Figure 6.2 presents relative electronic energies as a function of the rotational angle between the two methyl groups of Cr-bis(toluene) predicted by B3LYP/DFT calculations. As shown by the figure, the staggered conformers with conformation angles of 30°, 90°, and 150° are transition states located about 200-300 cm^{-1} higher in energy than the eclipsed conformers of 0°, 60°, 120°, and 180°. The conformational preference

of the Cr-bis(toluene) complex is predicted to be similar to that of M-bis(benzene) (M =

Cr, Mo, and W), where the staggered conformer is also a non-local minimum energy

structure.[56] This finding seems contradictory to the classical textbook assumption that

steric considerations play the leading role in deciding the stability of staggered and

eclipsed conformers. However, it is now clear that the steric effects are not the only

factors that drive the conformations and that hyperconjugation is often a dominating

one.[233-235]

Table 6.1 lists the ground electronic states and relative energies of the four

eclipsed conformers for the three M-bis(toluene) complexes in the neutral and cationic

forms, respectively. For neutral Cr-bis(toluene) complex, the $0°$ and $180°$ rotamers are

essentially energetically degenerate and slightly more stable than the $60°$ and $120°$ ones.

The relative stability from the B3LYP/DFT is somewhat different from a previous

PBE/DFT calculation, where $120°$ and $180°$ rotamers were predicted to be 40-80 cm^{-1}

more stable than the $0°$ and $60°$ ones.[225] Nevertheless, the energy differences among the

four conformers are so small that the theory alone is doubtful in determining which one

of the conformers is the true global energy minimum. For neutral Mo- and W-bis(toluene)

complexes, the energies of the four conformers are predicted to be in the order of $0° <$

$120° < 180° < 60°$. The stability order is different from that of the corresponding Cr

species, but the energy differences are again very small.

The neutral ground electronic states of all conformers are singlet, as the group VI

metal-bis(toluene) complexes contain 18 valence electrons (6 from the metal atom and 12

from the two toluene molecules). However, their molecular symmetries are different and

range from C_2 ($60°$ and $120°$) to C_{2v} ($0°$) to C_{2h} ($180°$) (Figure 6.1). Metal coordination

elongates the carbon-carbon bond distances by 0.02 – 0.03 Å, and the extent of the

elongation increases slightly down the metal triad. The increase of the C-C bond

distances upon metal coordination is due to electron back donation from the filled metal d

orbitals to the empty toluene orbitals. Metal-carbon distances in the M-bis(toluene)

complexes can be divided into two groups, M-C(CH$_3$) and M-C(H), with the former

being about 0.02-0.03 Å longer than the latter. The metal-carbon bond distances increase

in the order of Cr < W < Mo. The W-C distances are shorter than expected because of the

well-known relativistic effect on the heavier element, which shrinks the metal s orbitals

and thus enhances the metal-ligand interactions. Ionization of the neutral singlet state yields a cationic doublet state. Upon ionization, the M-C distances increase by 0.01-0.02 Å, while the C-C distances remain essentially the same. The small increase in the cationic M-C distances is due to the removal of a weakly-bound, metal-based electron from the highest occupied molecular orbital of the neutral molecule. Since the ejected electron is metal-based, ionization is expected not to have a significant effect on the C-C bond distances. In both neutral and ionic states, the six-member phenyl plane is only slightly distorted, with $\angle$(C-C-C-C) conformation angles being smaller than 1.0° in the neutral molecule and 2.5° in the cation. The bond distances and angles of the M-bis(toluene) conformers are summarized in Table 6.5. The C-C and M-C(H) bond distances in these M-bis(toluene) sandwiches are nearly identical to those in the M-bis(benzene) species.[56]

6.3.2. Spectroscopy and Observed Conformers

6.3.2.1. Cr-bis(toluene)

Figure 6.3(a, b, c) presents the ZEKE spectra of Cr-bis(toluene) seeded in He, 2:1 He/Ar, and Ar carrier gases, with the peak positions listed in Table 6.2. The spectrum with He carrier [Figure 6.3(a)] exhibits the strongest transition (A) at 42744 (5) cm^{-1}, with the full width at half maximum (FWHM) of about 20 cm^{-1}. The second strongest transition (B) is observed at ~ 63 cm^{-1} higher in energy. Following these two transitions, several weaker transitions appear in three groups: the first group consists of peaks C-E (42907, 42923, and 42939 cm^{-1}), the second F-I (43003, 43015, 43021, and 43030 cm^{-1}) and the third J (43098 cm^{-1}). When the complex is seeded in a 2:1 He/Ar mixture, peak A is resolved into two components A1 (42741 cm^{-1}) and A2 (42747 cm^{-1}) because of the reduced spectral linewidth; the intensity of peak B increases dramatically so that it becomes stronger than A, and its FWHM is narrowed down to ~ 7 cm^{-1} [Figure 6.3 (b)]. Moreover, intensities of peaks I and J are increased compared to those in the He spectrum. With pure Ar, intensities of peaks A1, A2, and C-H are further reduced, whereas those of

peaks B, I, and J become even stronger [Figure 6.3 (c)]. The linewidth of the strongest peak B is reduced to ~ 5 cm^{-1}.

Previously, we observed that inert-gas carriers affected the internal temperatures of metal complexes in supersonic jets and vibrational cooling was more efficient with heavier gases.[56,113,116] However, the strongest transition with He carrier [peak A in Figure 6.3 (a)] is not a vibrational hot band. This is because if it were from the transition of the first excited vibrational level of a neutral mode, at least an additional, weaker transition from the 2nd excited level would be expected from the standpoint of Boltzmann distribution. Furthermore, peak A is unlikely due to the transition from an excited electronic state of the neutral complex, because no excited state is expected to be so close in energy to the singlet ground state. Instead, peaks A and B correspond to (0,0) transitions of different conformers, as suggested by the previous MATI study.[227] The intensity variations of A and B with different gas carriers are due to the interconversion of the conformational rotamers. Such conformational relaxation has been observed for numerous organic molecules in supersonic jets,[236-242] but much less is known about organometallic complexes. In cases of single internal rotational degree of freedom, conformers with relative energies within 1 kcal mol^{-1} (350 cm^{-1}) of the global minimum were observed in supersonic expansions, and the interconversion of the conformers with an energy barrier of 1 kcal mol^{-1} or less was found to depend on carrier gases. For example, in studying the conformational conversion of organic molecules with a barrier height of less than 1 kcal mol^{-1}, Ruoff et al.[236] found that no conformer relaxation was observed with He carrier, and the relative conformer concentrations remained the same before and after the supersonic expansion. On the other hand, they found that all high energy conformers were effectively removed by the Ar expansion. For Cr-bis(toluene), the relative energies of the eclipsed conformers (0°, 60°, 120°, and 180°) are predicted to be within 100 cm^{-1} (0.29 kcal mol^{-1}), and energy barriers for their conversion are within 300 cm^{-1} (0.86 kcal mol^{-1}). Therefore, the observation of the conformational isomerization should not be surprising for this metal species.

By comparing the ZEKE spectra with the three carrier gases, peak B is assigned to the (0,0) transition of the lowest-energy conformer, and A1/A2 to the (0,0) transitions of higher energy ones. Since the relative intensities of peaks I and J increase and those of

peaks (C-H) decrease from He to Ar carrier, I and J should be associated with the most stable conformer and (C-H) with the less stable ones. The energy separation of peak J from B is 291 cm^{-1}, and those of F-H from A1/A2 are in the range of 260-280 cm^{-1}. These intervals are comparable to the Cr$^+$-bis(benzene) stretching frequency (264 cm^{-1}) reported previously.[56,213,215] Thus, peak J is assigned to the transition from the neutral ground vibronic state of the most stable conformer to the first Cr$^+$-bis(toluene) stretching level of the corresponding ion. Similarly, peaks F, G, and H are attributed to the first Cr$^+$-bis(toluene) stretching excitations of the three less stable conformers. Other observed transitions include peak I at 223 cm^{-1} from B and peaks C-E at 166-192 cm^{-1} from A1/A2. The assignment of these transitions is discussed below in combination with theoretical predictions.

According to the theory, there are four minimum-energy rotational conformers (0°, 60°, 120°, and 180°) for Cr-bis(toluene). Experimentally, three (0,0) transitions (A1, A2, and B) are resolved. From the DFT calculations, the 0° rotamer has the highest IE, with the largest IE difference from the other rotamers; the 180° rotamer has the lowest IE; and the IEs of the 60° and 120° rotamers are in between and close to each other. Based on this predicted IE sequence, peak A1 is assigned to the (0,0) transition of the 180° conformer, A2 to 60° and 120°, and B to 0°. The (0,0) transitions of the 60° and 120° are not resolved because of their IE proximity. The theoretical IE differences among the 0°, 60°/ 120°, and 180° conformers are 35 and 11 cm^{-1}, in qualitative agreement with the measured differences of 60 and 6 cm^{-1}. The Cr$^+$-bis(toluene) stretching frequencies of the 0°, 60°, 120°, and 180° conformers are predicted to be 281, 265, 257, and 258 cm^{-1}, which match nicely to the measured frequencies of 291, 274, 268, and 262 cm^{-1}, respectively. The Cr$^+$-bis(toluene) bending frequencies of the 0°, 60°, 120°, and 180° conformers are calculated to be 220, 199, 169, and 148 cm^{-1}. The 220 cm^{-1} bending frequency of the 0° rotamer matches the energy interval between peaks B and I transitions (223 cm^{-1}), the 199/ 169 cm^{-1} frequencies of the 60°/ 120° rotamers correspond to the observed energy separations between A2 and E/ D (192/ 176 cm^{-1}), and the 148 cm^{-1} frequency of the 180° rotamer is comparable to the energy difference between A1 and C (166 cm^{-1}). Thus, peaks I, E, D, and C can be assigned to the Cr$^+$-bis(toluene) bending excitations of the 0°, 60°, 120°, and 180° conformers,

respectively. On the basis of this assignment, the most stable conformer is identified as having the completely eclipsed configuration (0°). If the spectral intensities are used to estimate the relative populations, the 0° rotamer is ~ 20% in He, ~ 50% in He/Ar, and ~ 80% in Ar. The higher intensity of peak A than B with He carrier [Figure 6.3(a)] is because peak A corresponds to ionization of multiple rotamers (60°/ 300°, 120°/ 240°, and 180°, where 300° and 240° rotamers are energetically equivalent to 60° and 120°, respectively), where peak B is from ionization of a single conformer (0°).

As an additional support for the above spectral assignment, we have calculated the spectrum for each rotamer and combined the individual spectra together to produce an overall simulation to compare with the experimental spectra. Figure 6.3(d, e, f) presents the simulations at 250, 55, and 35 K to compare with the experimental spectra with He, He/Ar, and Ar carriers, respectively. The theoretical (0,0) transition energy of the 0° conformer is shifted to the experimental values, the (0,0) transition energies of the other three rotamers are referenced to that of the 0° rotamer, and the vibrational frequencies of all four conformers are not scaled in these simulations. Even at a temperature as low as 55 K, transitions from excited vibrational levels are visible at low energy side of the (0,0) transitions [Figure 6.3(e)]. These are sequence transitions of low-frequency modes with small frequency differences between the neutral and ion modes. At 250 K, the excited vibrational transitions become more pronounced, resulting in much broader spectra linewidth. However, the vibrational hot band transitions are not well-resolved in the experimental spectra. The increased linewidth with increasing temperatures in these simulations reproduce nicely the linewidth change of the measured spectra from Ar to He/Ar and to He carrier. The overall good agreement between the simulations and measured spectra are consistent with the spectral assignments discussed above.

Table 6.2 summarizes the assignment for the observed ZEKE transitions, and Table 6.3 lists the measured IEs and vibrational frequencies, along with those from the DFT calculations and previous MATI study.[227] The predicted IEs are several hundreds of wavenumbers higher than the measured values, whereas the errors on the vibrational frequencies are up to about twenty wavenumbers. Our assignment on the rotational conformers is consistent with the previous MATI study. However, the current work identifies for the first time the most stable conformer (0°) and shows conformational

isomerization of these complexes. There are also other new observations in this study. First, the IEs from the MATI spectra are about 20 cm^{-1} lower than the values obtained from this work (Table 6.3). The lower IE values from the previous study are likely caused by the electric field used to separate MATI from prompt ions. Although the strength of the field was not indicated in the previous paper, a much stronger field is generally required to separate ions in the MATI experiment than is needed to separate electrons in the ZEKE experiment. Second, the IEs of the three conformers (60°/ 120°/ 180°) were not separated previously, whereas they are now resolved for the 60°/ 120° and 180° rotamers, respectively. Finally, although the metal-ligand stretching modes were not resolved previously, three distinctive frequencies are determined for the 60°/ 120°/ 180° conformers in this work.

6.3.2.2. Mo- and W-bis(toluene)

Like Cr-bis(toluene), the spectra of the heavier metal-bis(toluene) complexes show two well-separated 0-0 bands, A and B, and several weaker transitions (Figures 6.4 and 6.5). In the case of Mo-bis(toluene), A is partially resolved into A1 and A2. On the other hand, at least two differences are visible between the spectra of the Mo/ W and Cr complexes. With He carrier, the relative intensity of peak B in the spectra of the Mo and W complexes is much stronger and the spectral linewidths of these heavier species are broader than that of Cr-bis(toluene). The line broadening is largely due to increased unresolved rotational and vibrational excitations in the heavier metal species. Because of the line broadening, vibronic transitions are less resolved in the heavier species. With Ar, peak A almost completely disappears in the spectra of the Mo/ W species, while it can easily be seen in the spectrum of the Cr complex. This observation indicates that the conformational conversion is more efficient for the heavier species.

By comparing with the spectra of Cr-bis(toluene) and theoretical calculations, A (A1/ A2) and B transitions are easily attributed to the band origin of 60°/ 120°/ 180° and 0° rotamers, respectively. Peaks C-F are ascribed to the metal-ligand vibrations, whereas G and H are assigned to ligand-based ones. The population of the 0° conformer of the Mo and W sandwiches is about 50% in He and almost 100% in Ar, as shown by the

relative spectral intensities of 0° to 60°/ 120°/ 180° conformers. The spectral assignments and spectroscopic constants are summarized in Tables 6.2 and 6.3, respectively. From these tables, several observations can be made for the three metal complexes. Among the four conformers of each metal complex, the 0° rotamer has a significantly higher IE and metal-ligand stretching frequency than the other conformers (Table 6.3). These measurements are consistent with the observation that the 0° rotamer is the most stable one among the four conformers. Among the three metals, the rotational conformers of W-bis(toluene) have the lowest IE values but highest metal-ligand stretching frequencies, even though the W atom has the highest IE and atomic masses. The large IE shift from W to W-bis(toluene) arises from the large metal-ligand bonding difference between the cationic and neutral forms. The high W-ligand stretching frequency is indicative of the strong metal-ligand bonding at the bottom of the potential energy surface along the metal-ligand bond coordinates. Although distinctive metal-toluene stretching and bending frequencies are determined for each of the four Cr-bis(toluene) conformers, only three frequencies are resolved for Mo-bis(toluene), and two for W-bis(toluene).   On the other hand, phenyl-ring deformation frequencies of 418, 402, and 410 cm^{-1} are observed for the 0°, 60°/ 120°, and 180° conformers of Mo-bis(toluene), and C-C in-plane bending frequencies of 684 and 798 cm^{-1} are measured for the 0° and 60°/ 120°/ 180° conformers of W-bis(toluene) (Table 6.2).

It is noted from Table 6.3 that the predicted IEs for the conformers of all three metal complexes are in very good agreement with the measured values, with absolute errors of a few hundreds of wavenumbers or relative errors of about 1-2 %. Similarly, the predicted metal-ligand stretching and bending frequencies compare well with the experimental values for the Cr and Mo complexes. However, the calculated W^+-toluene stretching frequencies are too small compared to the measured values. In a previous study of the M-bis(benzene) complex, we investigated the basis set effect on the W-benzene stretching frequency.[56] Among all effective core potential basis sets we tried, the CRENBS basis[243] with averaged effective potentials and spin-orbit operators appears to yield the best W^+-benzene stretching frequency. Unfortunately, calculations of W-bis(toluene) with the CRENBS basis ended up with a large negative frequency, indicative of a transition state, rather than a minimum-energy structure.

6.3.2.3. Comparison with M-bis(benzene) (M= Cr, Mo, and W) Complexes

Table 6.4 summarizes the IEs, metal-ligand stretching frequencies, and metal-ligand bond dissociation energies of M-bis(toluene) and -bis(benzene) complexes. For M-bis(benzene) sandwiches, the most stable conformer is also the eclipsed form, and the staggered form is a transition state.[56] The M^+-benzene stretching frequencies (264, 277, and 370 cm^{-1} down the metal triad) are lower than those of the M^+-toluene stretches of the 0° rotamer (291, 294, and 432 cm^{-1}). This may suggest that the metal-ligand binding at the bottom of the potential energy surface is strengthened by the methyl substitution of hydrogen in phenyl rings. The methyl substitution also reduces the IEs of the sandwich complexes by 1000 - 1200 cm^{-1}. However, the bond dissociation energies of the Cr- and W-bis(toluene) complexes are not significantly affected by the methyl substitution with considerations of the measurement uncertainties. For these two complexes, the bond energies of Cr^+- and W-bis(toluene) are taken from previous measurements,[244,245] and those of Cr- and W^+-bis(toluene) are calculated from the thermodynamic cycle, $D_o^+[M\text{-bis(toluene)}] - D_o[M\text{-bis(toluene)}] = IE\,(M) - IE\,[M\text{-bis(toluene)}]$. For Mo-bis(toluene), the bond dissociation energies are not included in the table, because the experimental bond energy of either neutral or cationic form is not available to complete the thermodynamic cycle. Ionization increases the metal-ligand bond strength, consistent with the IE red shift from the metal atom to the complex.

6.4. Conclusions

We have determined IEs, vibrational frequencies, and the relative stability of the rotational conformers and observed the conformational isomerization of group VI metal-bis(toluene) complexes in supersonic expansions through variable-temperature ZEKE spectroscopy. Among the four eclipsed conformers with methyl-group conformation angles of 0°, 60°, 120°, and 180°, the 0° rotamer is the most stable one and has the highest IE for all three metal sandwiches. For Cr-bis(toluene), distinctive metal-ligand stretching and bending frequencies are determined for each of the four conformers, while IEs are resolved for the 0°, 60°/ 120°, and 180° rotamers. For Mo-bis(toluene), the four

conformers are separated into three groups; and for W-bis(toluene), they are separated into two groups. Further work to improve the spectral resolution is in progress to better resolve the four individual conformers of the Mo and W sandwiches. The population of the 0° rotamer is determined to be 20% in He and 80% in Ar for Cr-bis(toluene) and about 50% in He and almost 100% in Ar for the Mo and W species.

Table 6. 1. Molecular point groups, electronic states, and relative electronic energies (ΔE_e) of neutral and cationic M-bis(toluene) (M = Cr, Mo, and W) complexes from the B3LYP calculations with 6-311+G(d,p) basis set on C and H and LanL2DZ on the metal atoms.

Rotamer	Point group	Electronic state (neutral / ion)	ΔE_e / cm^{-1} (neutral / ion)
Cr-bis(toluene)			
0°	C_{2v}	$^2A_1$ / $^1A_1$	1 / 37
60°	C_2	^2A / ^1A	43 / 35
120°	C_2	^2A / ^1A	47 / 42
180°	C_{2h}	^2A_g / ^1A_g	0 / 0
Mo-bis(toluene)			
0°	C_{2v}	$^2A_1$ / $^1A_1$	0 / 17
60°	C_2	^2A / ^1A	83 / 36
120°	C_2	^2A / ^1A	34 / 0
180°	C_{2h}	^2A_g / ^1A_g	58 / 24
W-bis(toluene)			
0°	C_{2v}	$^2A_1$ / $^1A_1$	0 / 4
60°	C_2	^2A / ^1A	109 / 36
120°	C_2	^2A / ^1A	60 / 0
180°	C_{2h}	^2A_g / ^1A_g	83 / 21

Table 6. 2. ZEKE peak positions (cm^{-1}) and assignments of M-bis(toluene) (M = Cr, Mo, and W) complexes.

Cr-bis(toluene)[a]		Mo-bis(toluene)[a]		W-bis(toluene)[a]	
Position	Assignment (rotamer)	Position	Assignment (rotamer)	Position	Assignment (rotamer)
42741	0_0^0(180°)	43440	0_0^0(180°)	42567	0_0^0 (60, 120, 180°)
42747	0_0^0(60, 120°)	43448	0_0^0(60, 120°)	42655	0_0^0 (0°)
42807	0_0^0(0°)	43522	0_0^0(0°)	42723	ν_b^+ (60, 120, 180°)
42907	ν_b^+(180°)	43606	ν_b^+(60, 120, 180°)	42847	ν_b^+ (0°)
42923	ν_b^+(120°)	43708	ν_s^+(60, 120, 180°)	42953	ν_s^+ (60, 120, 180°)
42939	ν_b^+(60°)	43730	ν_b^+(0°)	43087	ν_s^+ (0°)
43003	ν_s^+(180°)	43816	ν_s^+(0°)	43251	$\nu_{c\text{-}c}^+$ (60, 120, 180°)
43015	ν_s^+ (120°)	43850	ν_d^+ (60, 120, 180°)	43453	$\nu_{c\text{-}c}^+$ (0°)
43021	ν_s^+(60°)	43910	?		
43030	ν_b^+(0°)	43940	ν_d^+ (0°)		
43098	ν_s^+(0°)				

[a] ν_b^+ and ν_s^+: metal-toluene bend and stretch in the ion, respectively, ν_d^+: phenyl ring deformation combined with metal-carbon stretch in the ion, $\nu_{c\text{-}c}^+$ and $\nu_{c\text{-}c}$: C-C in plane bend in the ion and neutral molecule.

Table 6. 3. IEs and vibrational frequencies of M-bis(toluene) (M = Cr, Mo, and W) complexes from ZEKE spectroscopy and DFT/B3LYP calculations with 6-311+G(d,p) basis set on C and H and LanL2DZ on the metal atoms.[a]

Rotamer	Transition	IE (cm^{-1})		ν_b^+ / cm^{-1}		ν_s^+ / cm^{-1}	
		ZEKE (MATI)[b]	B3LYP	ZEKE (MATI)[b]	B3LYP	ZEKE (MATI)[b]	B3LYP
Cr-bis(toluene)							
0°	$^2A_1 \leftarrow {}^1A_1$	42807 (42786)	43221	223 (228)	220	291 (295)	281
60°	$^2A \leftarrow {}^1A$	42747 (42723)	43189	192 (200)	199	274 (291)	265
120°	$^2A \leftarrow {}^1A$	42747 (42723)	43183	176 (184)	169	268 (291)	257
180°	$^2A_g \leftarrow {}^1A_g$	42741 (42723)	43175	166 (159)	148	262 (291)	258
Mo-bis(toluene)							
0°	$^2A_1 \leftarrow {}^1A_1$	43522	43309	208	192	294	277
60°	$^2A \leftarrow {}^1A$	43448	43268	158	179	260	269
120°	$^2A \leftarrow {}^1A$	43448	43271	158	155	260	266
180°	$^2A_g \leftarrow {}^1A_g$	43440	43259	166	145	268	266
W–bis(toluene)							
0°	$^2A_1 \leftarrow {}^1A_1$	42655	42193	192	190	432	296
60°	$^2A \leftarrow {}^1A$	42567	42107	156	174	386	288
120°	$^2A \leftarrow {}^1A$	42567	42105	156	152	386	288
180°	$^2A_g \leftarrow {}^1A_g$	42567	42117	156	155	386	288

[a]The uncertainty of IE values from the ZEKE measurements is about 5 cm^{-1}. ν_b^+ and ν_s^+ are metal-toluene bending and stretching modes in the ion, respectively.
[b]From reference[227].

Table 6. 4. Metal-ligand stretching frequencies (ν_s^+), IEs, and bond dissociation energies (D_0, D_0^+) of M-bis(benzene) and M-bis(toluene) (M = Cr, Mo, and W).

Complex[a]	ν_s^+ (cm^{-1})	IE (cm^{-1})	D_0 (kcal mol^{-1})	D_0^+ (kcal mol^{-1})
Cr-bis(benzene)	264	44081	66	96
Mo-bis(benzene)	277	44581	118	154
W-bis(benzene)	370	43634	145	202
Cr-bis(toluene)	291	42807	62	95[b]
Mo-bis(toluene)	294	43522		
W-bis(toluene)	432	42655	145[c]	204

[a] ν_s^+, AIE, D_0, and D_0^+ of M-bis(benzene) are taken from reference[56] and references therein, and those of M-bis(toluene) are for the 0° conformer.
[b] From radiative association kinetics, reference[245], with an uncertainty of 9 kcal mol^{-1}.
[c] From microcalorimetry, reference[244], with an uncertainty of 1.4 kcal mol^{-1}.

Table 6. 5. M-C bond distances (R, Å) and conformation angles ($\angle$, degrees) of toluene and M/ M^+-bis(toluene) complexes (M = Cr, Mo, and W) from the B3LYP calculations with 6-311+G(d,p) basis set on C and H, and LanL2DZ on metal atoms. $R(C_1-C_1)$: distance of C-C bonds within the ring; $R(C_1-C_2)$: distance of C-C bonds between phenyl rings.

Rotamer	Point group	State	R(M-C)	$R(C_1-C_1)$	R(C-H)	$R(C-CH_3)$	$R(C_1-C_2)$	$\angle$ (C-C-C-C)
Toluene								
	Cs	$^1A'$		1.394	1.084	1.510		±0.32
				1.399	1.085			±0.13
					1.086			±0.10
Cr-bis(toluene)								
0°	C_{2v}	$^1A_1$	2.175	1.415	1.083	1.506	3.261	±0.09
			2.176	1.419	1.084		3.290	±0.01
			2.181				3.347	0.00
			2.202				3.380	0.19
		$^2A_1$	2.188	1.414	1.081	1.504	3.301	±1.28
			2.189	1.415	1.082		3.328	±0.65
			2.194	1.420			3.381	±0.02
			2.228				3.436	
60°	C_2	^1A	2.174	1.414	1.083	1.508	3.297	-0.46
			2.176	1.415	1.084		3.300	-0.34
			2.178	1.416			3.321	0.06
			2.180	1.418			3.334	0.19
			2.196	1.420				0.21
								0.33
		^2A	2.187	1.413	1.081	1.504	3.339	-1.06
			2.188	1.414	1.082		3.355	-1.03
			2.189	1.416			3.373	-0.04
			2.193	1.419				0.03
			2.223	1.421				0.53
								1.56
120°	C_2	^1A	2.173	1.414	1.083	1.507	3.322	-0.49
			2.177	1.416	1.084		3.300	-0.21
			2.180	1.419			3.307	-0.16
			2.182	1.420			3.322	0.13
			2.195				3.337	0.20
								0.54
		^2A	2.186	1.413	1.081	1.504	3.339	-1.53
			2.187	1.414	1.082		3.343	-0.73
			2.189	1.416			3.367	0.09
			2.193	1.420			3.368	0.23
			2.195	1.421				0.92
			2.223					1.03
180°	C_{2h}	^1A_g	2.178	1.415	1.083	1.507	3.311	±0.44
			2.179	1.420	1.084		3.320	±0.31
			2.180					±0.07
			2.191					
		^2A_g	2.190	1.414	1.081	1.504	3.353	±0.70
			2.191	1.415	1.082		3.358	±0.53
			2.192	1.421				±0.33
			2.219					

Table 6.5 (continued).

Mo-bis(toluene)								
0°	C_{2v}	$^1A_1$	2.319	1.419	1.083	1.507	3.657	±0.43
			2.320	1.424	1.084		3.671	±0.20
			2.335				3.679	±0.03
							3.683	
		$^2A_1$	2.326	1.419	1.082	1.504	3.677	±0.78
			2.327	1.425	1.083		3.691	±0.59
			2.328				3.703	±0.38
			2.356				3.726	
60°	C_2	^1A	2.316	1.417	1.083	1.507	3.665	-0.47
			2.318	1.419	1.084		3.679	-0.46
			2.320	1.420			3.688	-0.20
			2.321	1.421				-0.18
			2.325	1.422				0.65
			2.339	1.424				0.66
		^2A	2.322	1.417	1.082	1.505	3.681	-1.17
			2.326	1.419	1.083		3.701	-1.04
			2.328	1.420			3.726	-0.32
			2.330	1.421				-0.14
			2.332	1.423				0.90
			2.362	1.425				1.76
120°	C_2	^1A	2.314	1.417	1.083	1.507	3.666	-0.65
			2.320	1.418	1.084		3.670	-0.62
			2.321	1.420			3.682	0.21
			2.327	1.421			3.690	0.24
			2.337	1.422				0.39
				1.424				0.43
		^2A	2.323	1.416	1.082	1.505	3.688	-1.88
			2.325	1.418	1.083		3.691	-0.86
			2.327	1.421			3.712	0.02
			2.329	1.423			3.715	0.32
			2.335	1.425				1.08
			2.360					1.33
180°	C_{2h}	^1A_g	2.319	1.418	1.083	1.507	3.671	±0.39
			2.322	1.419	1.084		3.679	±0.31
			2.323	1.424				±0.04
			2.331					
		^2A_g	2.328	1.418	1.082	1.505	3.700	±0.60
			2.330	1.419	1.083		3.703	±0.46
			2.353	1.425				±0.30

Table 6.5 (continued).

W-bis(toluene)								
0°	C_{2v}	$^1A_1$	2.306	1.421	1.083	1.506	3.614	±0.47
			2.308	1.425	1.084		3.634	±0.16
			2.323				3.653	±0.14
							3.660	
		$^2A_1$	2.305	1.422	1.081	1.505	3.614	±0.67
			2.306	1.428	1.082		3.632	±0.61
			2.307		1.083		3.646	±0.53
			2.333				3.668	
60°	C_2	^1A	2.302	1.418	1.083	1.507	3.625	±0.79
			2.305	1.421	1.084		3.649	-0.61
			2.310	1.422			3.663	-0.27
			2.314	1.423				-0.09
			2.328	1.425				0.96
		^2A	2.298	1.419	1.082	1.505	3.622	-1.47
			2.300	1.422			3.643	-1.24
			2.307	1.425			3.662	-0.64
			2.309	1.428				-0.47
			2.314					1.51
			2.341					2.30
120°	C_2	^1A	2.300	1.417	1.083	1.507	3.641	-1.31
			2.306	1.420	1.084		3.642	-1.21
			2.309	1.422			3.648	0.41
			2.310	1.423			3.655	0.52
			2.319	1.424				0.76
			2.327	1.426				0.85
		^2A	2.298	1.419	1.082	1.505	3.630	-2.47
			2.300	1.421			3.631	-1.44
			2.307	1.425			3.652	0.42
			2.316	1.428			3.654	0.51
			2.340					1.49
								1.52
180°	C_{2h}	^1A_g	2.307	1.422	1.081	1.505	3.640	±0.48
			2.308	1.428	1.082		3.641	±0.43
			2.329					±0.36
		^2A_g	2.308	1.420	1.083	1.507	3.634	±0.49
			2.311	1.425	1.084		3.638	±0.45
			2.318				3.648	±0.02

| 0° (*C₂ᵥ*) | 60° (*C₂*) | 120° (*C₂*) | 180° (*C₂ₕ*) |
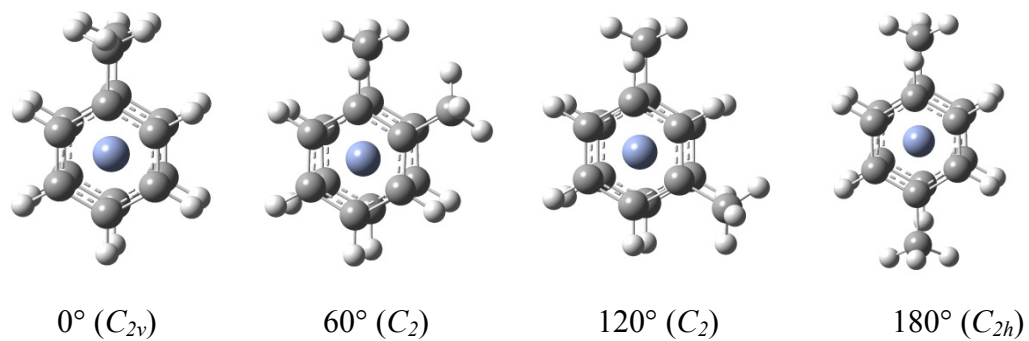
Figure 6. 1. Possible rotational conformers and their molecular point groups of M-bis(toluene) (M = Cr, Mo, and W) complexes with methyl-group conformation angles of 0°, 60°, 120°, and 180°.
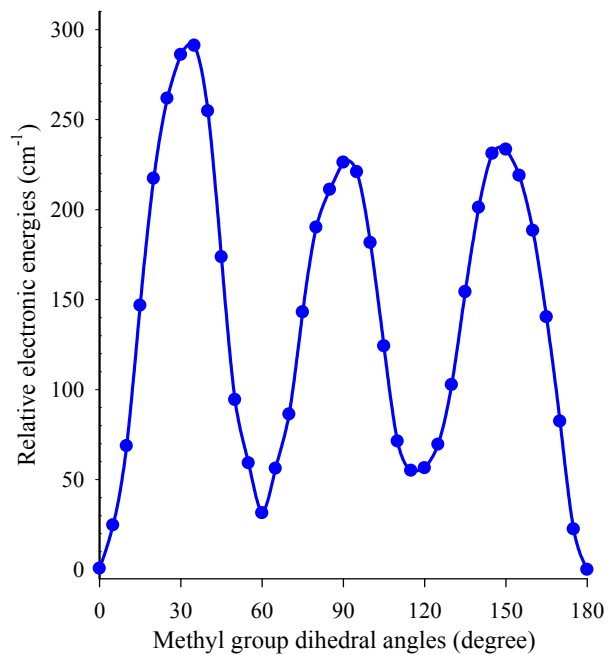
Figure 6. 2. Relative electronic energies of Cr-bis(toluene) as a function of the conformation angles between the methyl-groups from B3LYP/DFT calculations.
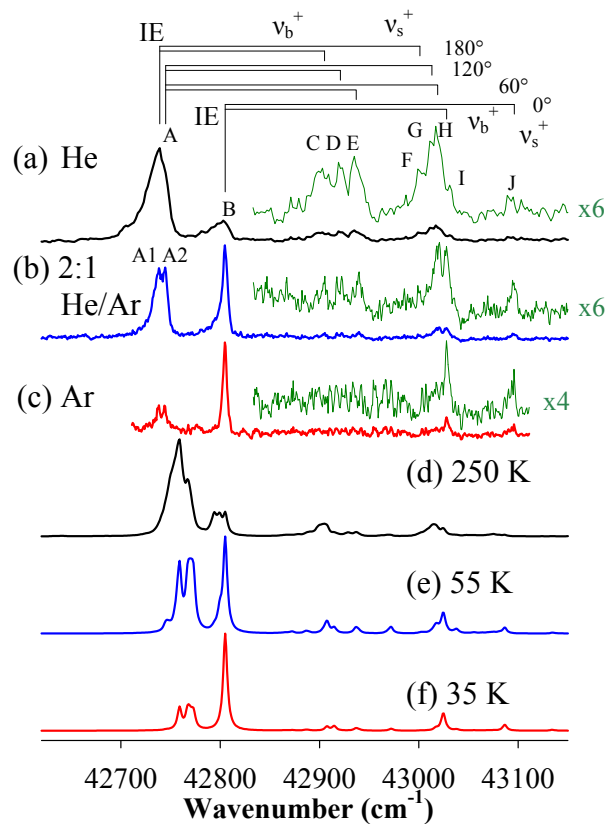
Figure 6. 3. Experimental ZEKE spectrum of Cr-bis(toluene) seeded in He (a), 2:1 He/Ar (b), and Ar (c), in comparison with the sum of simulations of $^2A_1 \leftarrow {}^1A_1$, $^2A \leftarrow {}^1A$, $^2A \leftarrow {}^1A$, and $^2A_g \leftarrow {}^1A_g$ transitions of 0°, 60°, 120°, and 180° rotamers at 250 K (d), 55 K (e), and 35 K (f).
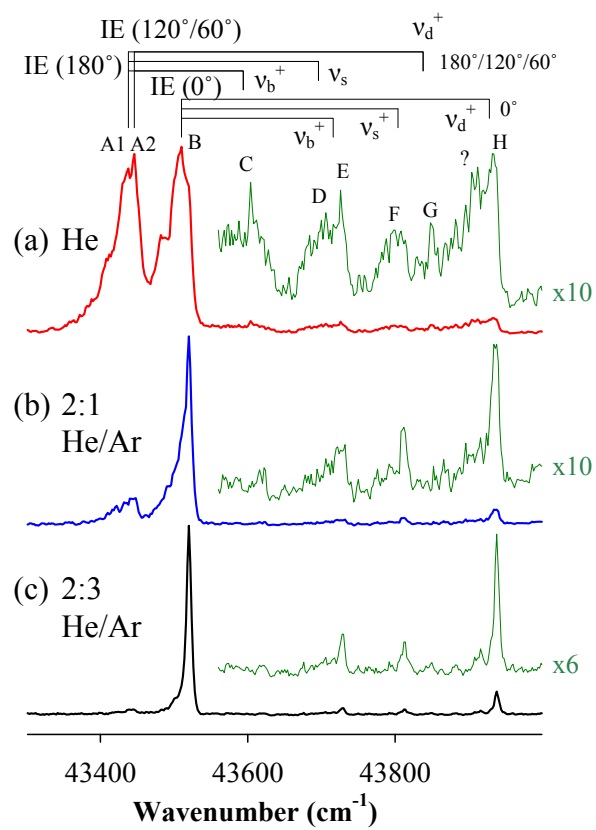
Figure 6. 4. Experimental ZEKE spectrum of Mo-bis(toluene) seeded in He (a), 2:1 He/Ar (b), and 2:3 He/Ar (c).
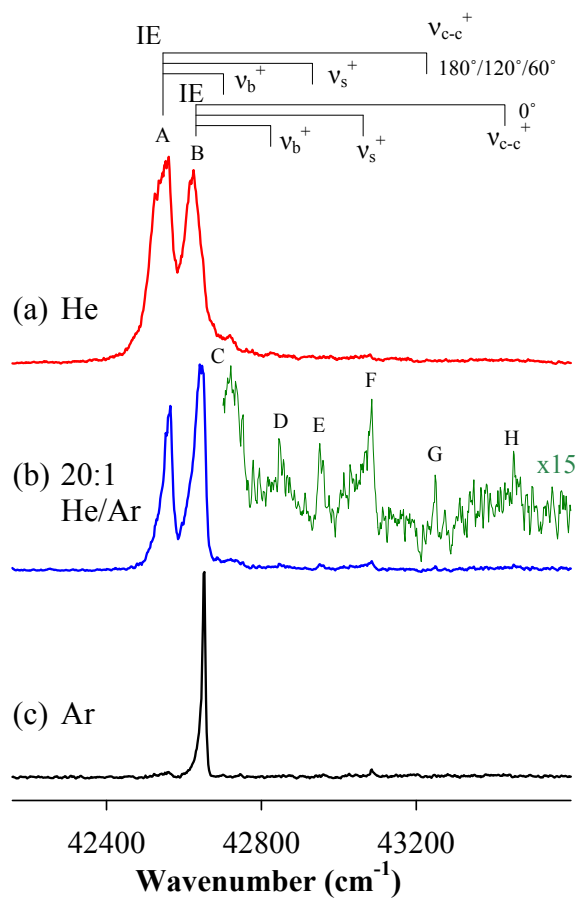
Figure 6. 5. Experimental ZEKE spectrum of W-bis(toluene) seeded in He (a), 20:1 He/Ar (b), and Ar (c).

CHAPTER 7. PULSED-FIELD IONIZATION ZERO-ELECTRON-KINETIC-ENERGY PHOTOELECTRON SPECTROSCOPY OF GROUP IV TRANSITION METAL BIPHENYL CLAMSHELL STRUCTURE COMPLEXES

7.1. Introduction

This chapter is a continuation of the work by Bradford R. Sohnlein. In his dissertation, the Ti-biphenyl complex was studied by photoelectron spectroscopy.[191] In this work, two-photon ionization spectroscopy has been used to further characterize the Ti complex. In addition, the first spectroscopic investigation of the Zr- and Hf-biphenyl complexes is reported.

Biphenyl ($C_{12}H_{10}$) is an aromatic hydrocarbon, of which two phenyl rings are joined by a single C-C bond. There is a low barrier energy for the rotation about the central C-C bond.[246] Therefore, many theoretical[247-253] and experimental[246,254-263] attempts have been made to determine the conformation angle between the two phenyl rings and their respective energies. In the solid state, the average structure of biphenyl is planar.[254] However, electronic absorption and emission[255] and x-ray analysis[256] have determined that a twisted structure is also possible with the temperature variation. This finding is further confirmed by Brillouin[257] and neutron[258] scattering and electron paramagnetic resonance (EPR) spectroscopy[259]. In addition, Raman scattering study has verified that pressure affects crystalline biphenyl in a similar manner.[260] In the solution and melt states, non-planar structures of biphenyl have also been determined.[261] In the gas phase, the dihedral angle of biphenyl, the angle between the planes of two phenyl rings, is determined to be about 40 ~ 44° by electron diffraction[246,262] and electronic absorption[263]. The near 45° twist angle is explained by the competition between π electron delocalization, favoring co-planar structure, and proximate hydrogen steric repulsion, which prefers non-planar arrangement.[251-253]

X-ray crystallography has determined that the metal-biphenyl 1:2 complex prefers 6-fold binding of metal to each phenyl ring in two different biphenyls.[264] Similarly, the cationic metal and biphenyl 2:2 complex has the structure such that two biphenyls stack on top of each other.[265] Each metal ion is positioned in-between these biphenyls and

binds to π electrons of two individual phenyl rings and forms a double-sandwich complex. Theoretical determination of the metal-biphenyl 2:2 complex has been carried out with DFT calculations.[266] The electronic and geometric structural analysis confirms the formation of a doubly stacked sandwich structure of diatomic bis(biphenyl) complex. Unfortunately, there is limited information on the metal-biphenyl 1:1 complex in the gas phase. In a previous publication, our group has determined that the gaseous Sc-biphenyl complex has a clamshell structure, where Sc is clamped between two phenyl rings.[54] In this work, we report the PFI-ZEKE spectra of Ti-, Zr-, and Hf-biphenyl complexes in the gas phase, where interferences from counter-ions or solvents are removed. In addition, IR-UV R2PI spectra of these metal-biphenyl complexes have been recorded and compared with the theory for further confirmation of the molecular structures and electronic states. The group IV metal-biphenyl complexes have been investigated to study the difference in effects of the electronic configuration and metal size in binding with biphenyl. The comparison between the experimental and simulated spectra confirms that, similar to the Sc-biphenyl complex, Ti, Zr, and Hf metal atoms form clamshell structures with biphenyl ligand. The larger atomic size and one more valence electron do not hinder the clamshell structure formation. The IEs and metal-ligand and ligand-based vibrational frequencies are measured from the ZEKE spectra. Additionally, C-H stretching frequencies are determined from R2PI spectroscopy.

7.2. Experimental and Computational Methods

7.2.1. UV PFI-ZEKE Spectroscopy

Details of our ZEKE spectrometer setup have been described in Chapter 2. Group IV transition metal-biphenyl complexes were formed in the molecular beam source chamber by reactions of gaseous metal atoms with biphenyl vapor ($C_{12}H_{10}$, 99.5 %, Sigma-Aldrich). The metal rods (Ti, 99.7%, Aldrich; Zr, $\geq$ 99%, Aldrich; and Hf, 99.9%, Alfa Aesar) were ablated by the second harmonic (532 nm) Nd:YAG laser (Continuum, minilite II, 3~4 mJ) in the presence of He with 40 psi backing pressure (UHP, Scott-Gross)

and delivered by a home-made piezoelectric pulsed valve.[55] To ensure that each laser pulse ablates a fresh metal surface, the rod was translated and rotated by a micro motor (1516 series 012S type, Faulhaber). Biphenyl vapor was introduced at room temperature through a stainless steel capillary. The vapor was carried to a small collision chamber (~1.5mL) by the carrier gas, downstream from the ablation region, where the metal atom and ligand were interacted to form metal-biphenyl complexes. The metal complexes were expanded into the vacuum through a nozzle to form molecular beams. The molecular beams were collimated by a cone-shaped skimmer (4 mm inner diameter) and passed through a pair of charged deflection plates (+ 500 V) to remove residual ionic species formed during laser ablation.

The masses of the complexes of the interest were determined by photoionization time-of-flight mass spectrometry in the spectroscopy chamber. Ionization was carried out by a frequency-doubled dye laser (Lumonics, HD-500), pumped by second Nd:YAG laser (Continuum, Surelite II, 355 nm). The production of the metal-biphenyl 1:1 complexes was maximized by adjusting the time and power of the vaporization and ionization lasers and the backing pressure of the carrier gas. Ionization thresholds were located by recording mass-selected ion signal as a function of laser wavelength. ZEKE electrons were generated by photoexcitation of the neutral complexes to high-lying Rydberg states, which were ionized after 3μs of time delay by a pulsed electric field (1.2 Vcm^{-1}). This field was applied for 100 ns and the delay was generated by a delay pulse generator (Stanford Research Systems DG535). A small dc field (0.08 Vcm^{-1}) was used to separate ZEKE electrons from kinetic electrons produced by photoionization. The ion and electron signals were detected by a dual microchannel plate detector (Galileo), amplified by a preamplifier (Stanford Research System, SR445), averaged by a gated integrator (Stanford Research System, SR250), and stored in a laboratory computer. Laser wavelengths were calibrated against titanium atomic transitions in the range of ZEKE spectra.[57]

7.2.2. IR-UV Photoionization Spectroscopy

One-color ZEKE spectroscopy yields information about metal-ligand and low-frequency ligand vibrations. On the other hand, two-color R2PI of the metal-biphenyl complexes can be used to measure high-frequency ligand-based vibrations. The details of two photon IR-UV ionization spectroscopy have been described in Chapter 2. The IR laser was scanned in the range of 2700 – 3500 cm^{-1} to photoexcite the molecule to an intermediate state, whereas the UV laser wavelength was fixed at about 300 – 600 cm^{-1} below the IE of the complex after a time delay of 50 – 200 ns. The IR laser was produced by an IR optical parametric oscillator (OPO) and amplifier (OPA) laser (LaserVision), with the use of a KTP and four KTA crystals, respectively. The IR OPO/A laser was pumped by an injection seeding Nd:YAG laser (Continuum, Surelite III). The frequency doubled UV dye laser (Lumonics, HD-500) and IR laser were introduced in such a way that they were counterpropagated with each other and perpendicular to the molecular beam. Only when the scanned IR laser was resonance with C-H stretching vibrations, the ion signal was produced. The use of the injection seeding pump narrows the IR laser linewidth to about 0.2 cm^{-1}, but does not improve the spectral resolution. Therefore, the pump laser without seeder (with IR laser linewidth ~ 2.0 cm^{-1}) was used to improve the ion signal. The resultant ion signal was detected by the same time-of-flight spectrometer used in the ZEKE spectroscopy. The IR laser wavelengths were calibrated with the photoacoustic spectra of H_2O.[58]

7.2.3. Computation

DFT calculations were performed to predict the geometries and vibrational frequencies of the ground electronic state. The DFT methods include the Becke's exchange functional[267] with Perdew and Wang's gradient-corrected correlation functional 91 (BPW91)[268], and the B3P86 or B3LYP. In these calculations, the 6-311+G(d,p) basis was used for hydrogen and carbon atoms. On the other hand, the LanL2DZ basis set was applied for Zr and Hf atoms, since the triple-split-valence basis was not available. In addition, Ti atom was calculated with both the 6-311+G(d,p) and the pseudo core

potential basis sets to compare with the Zr and Hf complexes. All calculations were carried out with the GAUSSIAN 03 program.[269] Multidimensional FC factors were computed from the theoretical equilibrium geometries, harmonic frequencies, and normal coordinates of the neutral and ionic complexes.[52] The Duschinsky effect[29] was considered to account for normal mode differences between the neutral and ionic molecules. A Lorenztian line shape with the experimental linewidth was used to simulate the spectral broadening. Transitions from excited vibrational levels of the neutral complexes were simulated by assuming thermal excitations at specific temperatures. The theoretical IR spectra were calculated with GAUSSIAN 03 and plotted with the experimental linewidth.

7.3. Results and Discussion

7.3.1. Equilibrium Structures of M-biphenyl (M = Ti, Zr, and Hf)

The group IV transition metals have four outermost valence electrons, $(n-1)d^2ns^2$ in the ground state. Therefore, electron-spin multiplicities of neutral M-biphenyl (M = Ti, Zr, and Hf) complexes can be singlet/ triplet/ quintet, and those of M^+-biphenyl are doublet/ quartet. Based on the B3P86 calculations, the triplet and quintet states of M-biphenyl complexes are predicted to be 2274 and 16762 cm^{-1} (Ti-biphenyl), 5191 and 21121 cm^{-1} (Zr-biphenyl), and 3593 and 19210 cm^{-1} (Hf-biphenyl) higher in energy than singlet states, respectively. The DFT calculation predicts the ground electronic states are singlet and doublet for the neutral and ionic complexes, respectively. Therefore, the geometrical analysis has been limited to the neutral singlet and ionic doublet states of M-biphenyl (M = Ti, Zr, and Hf) complexes. The bond lengths and angles of the metal complexes are listed and compared with those of the free ligand in Table 7.2.

In the case of Sc-monobenzene complex, benzene binds to Sc metal and the resulting complex has a half-sandwich structure.[60] Comparatively, the metal-bis(benzene) complex forms a sandwich structure with equal binding from the metal to two benzenes.[56,61] Similar to the metal-bis(benzene) complex, two π networks from two

individual phenyl rings in biphenyl bind to metal center by orienting equally towards the metal and donating π electrons. Unlike two benzene rings however, biphenyl has additional C_4-C_5 bond joining the two phenyl rings together (carbon numbering is denoted in Figure 7.1). Therefore upon complexation, the two phenyl groups bend towards and wrap the metal core, whereas C_4-C_5 bond stays relatively steady in the original position, forming a clamshell structure with C_{2v} symmetry. Such structural conformation is also observed for the Sc-biphenyl complex.[54] Figure 7.1 shows the geometry of the M-biphenyl complex, optimized by the B3P86 with 6-311+G(d,p) basis set applied on C, H, and Ti and LanL2DZ on Zr and Hf.

Upon metal complex formation, biphenyl undergoes various geometrical changes. The DFT calculation predicts the C-C bond distance in phenyl rings to increase by more than 0.02 Å from the free ligand (Table 7.2). This is due to electron back donation from the filled metal d orbital to the empty orbital of phenyl ring, which strengthens the M-C bonds and weakens the C-C bonds. The M-C bond distances decrease in the order of M-C_2 > M-C_1 > M-C_3 > M-C_4 for the M-biphenyl (M = Ti, Zr, and Hf) complexes. In addition, the length of C-C bond increases in the order of R(C_1-C_2) < R(C_2-C_3) < R(C_3-C_4). The strength of electron back donation from the metal appears more significant for heavier atoms with more available electrons, as the C-C bond length increases in the order of Ti-biphenyl < Zr-biphenyl < Hf-biphenyl. This trend is consistent with previous ab-initio relativistic core potential calculations of Ti-, Zr-, and Hf-bis(arene) sandwich complexes.[270] When the metal coordinates to the free ligand, two phenyl rings bind to the metal and the resulting metal complex exhibits twelve fold binding between the metal and the carbon atoms. However, the C_4 and C_5 atoms are forced to approach closer towards each other to wrap the metal center and the resulting complex exhibits the clamshell structure (carbon numbering denoted in Figure 7.1). The calculation shows that the C_4-C_5 bond distance shrinks by more than 0.1 Å.

By considering the geometric changes of ligand upon metal insertion, the binding strength of the metal to the phenyl ring can be estimated. In the free ligand, the angle between the plane of phenyl ring and that of the C_4-C_5 bond [$\angle$(C_1-C_4-C_5)] is 180°, indicating the C_4-C_5 bond is in the plane of the phenyl ring. By taking the difference of these angles in the absence and presence of the metals, the binding strength of each metal

can be estimated. This angle difference follows the order of Zr-biphenyl (180°-129.1° = 50.9°) < Hf-biphenyl (180°-127.1° = 52.9°) < Ti-biphenyl (180°-123.1° = 56.9°), indicating the strongest binding of Ti to biphenyl. Ti has the least number of electrons; hence there is the weakest repulsion for π electrons donated from phenyl rings. However, the stronger binding strength of the Hf-biphenyl complex compared to the Zr complex is astonishing. This can be explained by the lanthanide contraction.[270] The heavier Hf atom shrinks spatial extension of the orbitals, reducing the atomic radius, and enhancing the metal-ligand interaction and causing greater phenyl ring bend in biphenyl. Moreover, the M-C bond lengths, R(M-C) decrease in the order of Zr > Hf > Ti. This trend is parallel to that of the binding strength estimated by the $[\angle(C_1\text{-}C_4\text{-}C_5)]$ angle comparison of the M-biphenyl complex and free ligand.

7.3.2. PIE Spectra of M-biphenyl complexes (M = Ti, Zr, and Hf)

Figure 7.2 shows the PIE spectra of the M-biphenyl (M = Ti, Zr, and Hf) complexes seeded in He carrier gas. The ionization thresholds can be measured by finding the intersection of lines drawn through the baseline and the sharp increase of the ion signal. These values are shifted by +110 cm^{-1} to correct for the dc extraction field effect (320 Vcm^{-1}) applied in the ionization region. The ionization thresholds are determined to be 43800 (100), 43350 (50), and 43700 (100) cm^{-1} for Ti- (a), Zr- (b), and Hf-biphenyl (c) complexes, respectively. These values are used to simplify the search for and correlate with the ZEKE signals.

7.3.3. ZEKE Spectrum of Zr-biphenyl

Figure 7.3(a) presents the ZEKE spectrum of Zr-biphenyl complex seeded in He carrier gas. The first intense peak is positioned at 43343 (5) cm^{-1} with full widths at half maximum (FWHM) of about 12 cm^{-1}. This peak correlates to the ionization threshold obtained in the PIE spectrum [Figure 7.2 (b)] and is assigned to the IE of the Zr-biphenyl complex. Below this 0-0 band, three distinct peaks are observed with 210, 346, and

413 cm^{-1} intervals. These peaks are assigned to the transitions from the vibrationally excited neutral complex to the ion. There are three intervals of 208, 331, and 398 cm^{-1} intervals above the IE. These peaks correspond to excitations of three vibrational modes of the ionic complex. All others can be assigned to the combinational bands of these vibrational frequencies and listed in Table 7.3.

The comparison with the ZEKE spectrum of Sc-biphenyl can help the assignment of many of the vibrational frequencies.[54] Two of the three neutral/ ionic vibrational intervals in the Zr-biphenyl spectrum (331/ 346 and 398/ 413 cm^{-1}) are quite comparable to the Sc-biphenyl ionic frequencies of 336 and 378 cm^{-1}. These frequencies are assigned to the metal-biphenyl stretching and symmetric out-of-plane phenyl ring waving vibrations, respectively. Unfortunately, the remaining 208/ 210 cm^{-1} energy intervals do not match with any of the Sc-biphenyl vibrational frequencies. To assign the remaining vibrational intervals in the Zr-biphenyl spectrum, the DFT calculation is used.

Based on the B3P86 calculation, the neutral singlet, triplet, and quintet and ionic doublet states of the Zr-biphenyl complex have clamshell structures, where Zr is clamped between two phenyl rings (Figure 7.1). However, the structure of the ionic quartet state is quite different. The structure of biphenyl in the quartet state is less affected by the metal coordination, and the metal complex exhibits a more open clamshell than the other states. Therefore, the simulations of the transitions from the neutral triplet and quintet to the ionic quartet states are predicted to have very long FC profiles with weak band origin. This is quite different from the experimental spectrum which exhibits strong 0-0 transition. Therefore, for the spectral comparison between the simulations and the experiment, only the transitions from the singlet and triplet to the doublet states are considered. In addition, the triplet and quintet states are about 6.5 and 47.9 kcal mol^{-1} (0.3 and 2.1 eV) higher in energy than singlet (Table 7.1). Hence, most likely transition is from the singlet to the doublet states. The simulations of the transitions from the singlet and triplet to the doublet states at 300K are displayed in Figure 7.3(b) and (c), respectively. In these simulations, the vibrational frequencies are not scaled, but the 0-0 band transition energies are shifted to the experimental value for clear comparison. The simulation of the transition from $^1A_1$ to $^2B_1$ shows very good match with the experimental spectrum as expected. In contrast, the simulation of the $^2B_1 \leftarrow {}^3B_1$ transition shows poor

agreement; the overall intensity profile does not match and the simulation predicts many more peaks than the experiment. Based on the good agreement between the $^2B_1 \leftarrow {}^1A_1$ simulation and the experimental spectrum, the remaining unidentified intervals are assigned. The remaining 208/ 210 cm^{-1} intervals are assigned to excitations of a phenyl ring bending towards metal (v_{18}^+/ v_{18}). This vibrational mode is characterized by small but significant changes in [$\angle$(C$_1$-C$_4$-C$_5$)] angles from the neutral to ionic complexes and in the formation of the clamshell structure. The assignments of metal-biphenyl stretching (v_{17}^+/ v_{17} = 331/ 346 cm^{-1}) and symmetric out-of-plane phenyl ring waving (v_{16}^+/ v_{16} = 398/ 413 cm^{-1}) vibrations are confirmed as well. In addition, there are peaks marked by asterisks which are separated by ~ 17 cm^{-1} and superimposed below the intense peaks. Since the 331 and 346 cm^{-1} intervals are associated with the ionic and neutral metal-ligand stretching vibrational modes (v_{17}^+/ v_{17}), the neutral mode is then about 15 cm^{-1} larger than the ionic mode. The peaks marked with asterisks can be assigned to the sequence transitions from the excited levels of the 346 cm^{-1} neutral mode to the levels of the 331 cm^{-1} ion mode. The DFT calculation supports such assignment. The ZEKE peak positions, which are field corrected by adding +1.5 cm^{-1} to laser wavenumbers are listed in Table 7.3 (b). In addition, Table 7.4 summarizes the vibrational frequencies and their corresponding assignments.

7.3.4. ZEKE Spectrum of Hf-biphenyl

As shown in Figure 7.4 (a), the ZEKE spectrum of Hf-biphenyl, seeded in He carrier gas, originates at 43752 (5) cm^{-1} with a FWHM of 30 cm^{-1}. The first intense peak corresponds to the onset of the ion signal observed in the PIE spectrum in Figure 7.2 (c). Therefore, it can be assigned to vibrationless transition of Hf-biphenyl. Similar to the Zr-biphenyl complex, the triplet and quintet states of Hf-biphenyl are 3593 and 19210 cm^{-1} higher in energy than the singlet, respectively. In addition, the simulation from the triplet to doublet transition contains many peaks that are not present in the experimental spectrum [Figure 7.4 (c)]. In contrast, the simulation of the singlet to doublet transition [Figure 7.4 (b)] predicts the vibrational frequencies and relative peak intensities very close to the experimental values. Based on the good agreement between

144

the experiment and theory, the ZEKE spectrum of Hf-biphenyl complex has been analyzed.

Similar to the spectrum of Zr-biphenyl complex, that of Hf-biphenyl also contains six intervals. These intervals are positioned at 210, 300, 404 cm^{-1} above and 208, 314, 422 cm^{-1} below the 0-0 band. According to the vibrational frequencies obtained from the Zr-biphenyl spectrum, these intervals can be easily assigned. The 210/ 208 cm^{-1} intervals are assigned to the frequencies of a phenyl ring bending towards metal (ν_{18}^{+}/ ν_{18}) in the ionic and neutral states. The remaining intervals at 300/ 314 and 404/ 422 cm^{-1} are due to the vibrations of metal-biphenyl stretching (ν_{17}^{+}/ ν_{17}) and symmetric out-of-plane phenyl ring waving (ν_{16}^{+}/ ν_{16}), respectively. Observed ZEKE peak positions are listed and summarized in Tables 7.3 (c) and 7.4, respectively. Similar to the ZEKE spectrum of Zr-biphenyl complex, that of Hf-biphenyl also exhibits broad bands denoted by asterisks in Figure 7.4(a). These bands are likely to be the sequence transitions in the excitation of the vibrational modes. However, the spectral linewidth of Hf-biphenyl complex was much too broad, and locating these sequence bands was not possible. These hot bands can be reduced or removed from the spectrum by using Ar or Ar/He mixture carrier gases, which cool down the molecular beam more efficiently than He.[113] Unfortunately, the electron signals in the He/Ar mixture or Ar carrier gases were too weak to obtain an useful spectrum.

7.3.5. ZEKE Spectrum of Ti-biphenyl

The ZEKE spectrum of the Ti-biphenyl complex is displayed in Figure 7.5 (a). The most intense peak at 43845 (5) cm^{-1} (FWHM of ~14 cm^{-1}) lies on the IE threshold measured in the PIE spectrum [Figure 7.2 (a)] and is assigned to the 0-0 transition of the complex. Three (194, 352, and 985 cm^{-1}) and five (207, 324, 447, 596, and 658 cm^{-1}) vibrational intervals are located above and below the band origin, respectively. The former belongs to the vibrational frequencies of the ionic complex, whereas the latter belongs to those of the neutral. These intervals can be assigned to specific vibrational modes by comparing with the Zr- and Hf-biphenyl ZEKE spectra. The 194 and 207 cm^{-1} progressions above and below the 0-0 transition are assigned to phenyl ring bending

towards metal (v_{18}^+/ v_{18}) vibrational modes of Ti^+ and Ti-biphenyl complexes, respectively. The 352 and 324 cm^{-1} intervals are due to the ionic and neutral Ti-biphenyl stretching (v_{17}^+/ v_{17}) vibrations, respectively. The 447 cm^{-1} interval below the 0-0 transition is assigned to symmetric ring wave vibration (v_{16}) of the Ti-biphenyl complex. Moreover, the ZEKE spectrum of the Ti-biphenyl complex presents vibrational frequencies that are not present in those of the Zr- and Hf-biphenyl complexes. Therefore, theory was used to assign the remaining vibrational intervals.

Figure 7.5 presents the experimental ZEKE spectrum (a) and the B3P86 simulations from $^1A_1$ (b) and $^3B_1$ (c) to $^2B_1$ transitions. Similar to Zr- and Hf-biphenyl, the triplet and quintet states of Ti-biphenyl are 2274 and 16762 cm^{-1} higher in energy than the singlet state, respectively. In addition, the simulation of the transition from the triplet to the doublet states shows some peaks that are not present in the experimental spectrum. On the other hand, the simulation of the transition from the $^1A_1$ to $^2B_1$ states of the Ti-biphenyl complex exhibits relatively good prediction on the vibrational frequencies. Based on the B3P86 method, the remaining vibrational intervals of 596 and 658 cm^{-1} below the 0-0 transition are assigned to out-of-plane ring distortion (v_{15}) and biphenyl ring breathing (v_{14}) vibrational modes, respectively. The 985 cm^{-1} interval above the band origin is due to in-plane ring distortion vibration (v_{10}^+).

For the experimental ZEKE spectra of the Ti-, Zr-, and Hf-biphenyl complexes, the 0-0 band transition is the most intense peak and each spectrum possesses three or more distinctive neutral and ionic vibrational frequencies. On the other hand, only the simulated spectrum of the Ti-biphenyl complex severely underestimates the 0-0 band transition and displays a long progression [Figure 7.5 (b)]. This indicates that the calculation estimates larger geometry changes upon the ionization of the Ti-biphenyl complex, compared to those of the Zr- and Hf-biphenyl complexes. To improve the theoretical results, different calculation methods are investigated. Figure 7.6 displays and compares the simulations from the DFT [(b) through (f)] and MP2 (g) calculations with the experimental ZEKE spectrum (a). The MP2 simulation (g) can be eliminated since it has poor correspondence with the experimental spectrum in both intensity and position of the vibrational peaks. Further investigation shows that both B3P86 (b) and B3LYP (c) methods with 6-311+G(d,p) basis set show better prediction on the sequence frequencies

of vibrational modes than the BPW91 (d) calculations. For the Zr- and Hf-biphenyl complexes, the calculations using 6-311+G(d,p) basis set on C and H, and effective core potential (ECP) LanL2DZ basis set on each metal atom show quite good predictions on both frequencies and spectral profiles, as displayed in Figure 7.3 and 7.4, respectively. Therefore, the B3P86 and B3LYP methods with LanL2DZ basis set applied on Ti atom [Figure 7.6 (e) and (f)] are simulated and compared. Such calculations do not improve the spectral profile of the spectrum. The frequency analysis shows that both calculations are not far off from the experimental value; however, many frequencies are in better agreement with the calculations using the 6-311+G(d,p) basis set. In B3LYP simulation [Figure 7.6 (c)], many of the frequency intervals are well reproduced, however some of the combination and sequence transitions are better simulated by the B3P86 method [Figure 7.6 (b)]. Table 7.4 displays the comparison of the experimental and the B3P86 predicted frequencies with 6-311+G(d,p) basis set for the Ti-biphenyl complex. In addition, the calculated frequencies from various DFT and MP2 methods are included in the table. Many of the vibrational frequencies are well reproduced by DFT methods; they have 0 - 4 % of error. This provides further support for the spectral assignments.

7.3.6. R2PI Spectra of M-biphenyl (M = Ti, Zr, and Hf)

To further investigate the molecular structure and characterize the electronic states of the M-biphenyl (M=Ti, Zr, and Hf) complexes, R2PI measurements have been carried out. The R2PI spectra of the Zr-, Ti-, and Hf-biphenyl complexes are displayed in Figures 7.7 (a), 7.8 (a), and 7.9 (a), respectively. As described earlier, the UV laser wavelength was fixed below IE at 43200, 42800, and 43400 cm^{-1} for the Ti-, Zr-, and Hf-biphenyl complexes, respectively. The IR laser was scanned in the range of 3000 – 3200 cm^{-1} to find the C-H stretching vibrations of the neutral complexes. Both Ti- and Zr-biphenyl complexes have two intense peaks located at 3078/ 3093 and 3074/ 3096 cm^{-1}, respectively. Unfortunately, the R2PI spectrum of Hf-biphenyl has too much noise to locate the precise peak positions for the C-H stretching frequencies. Thus, the two most intense peak regions (3082/ 3098 cm^{-1}) have been picked to compare with those of the Ti- and Zr-biphenyl complexes. To determine the identity of these peaks, the IR simulations

of three neutral states $^1A_1$ (b), $^3B_1$(c), and $^5A_2$ (d) are compared with the experimental spectra of the Zr-, Ti-, and Hf-biphenyl complexes in Figures 7.7, 7.8, and 7.9, respectively. The simulated spectra of the neutral states are scaled by a factor of 0.957, the average ratio between the experimental and the B3P86 calculated C-H stretching frequencies.[183]

The quintet and triplet states of the Zr- and Ti-biphenyl complexes (Figures 7.7 and 7.8, respectively) can be easily eliminated, since the spectral profiles and frequencies are different from those of the experimental spectra. On the other hand, the simulations of the singlet states reproduce the experimental spectra very well with two peak regions above 3070 cm^{-1}. It is consistent with the results obtained from the ZEKE spectroscopy. For the R2PI spectrum of the Hf-biphenyl complex (Figure 7.9), the noise level is so high that the comparison between the experimental and simulated spectra is not obvious as in the previous two cases. However, it is possible to determine that the calculated frequencies of the singlet state are closer to the measured values than other spin states. Therefore, it is reasonable to confirm that the electronic transitions of group IV metal-biphenyl complexes in ZEKE spectra are most likely to arise from the neutral $^1A_1$ states. With the results from R2PI spectroscopy, the ambiguity of the Ti-biphenyl ZEKE spectral assignment has been resolved and the ZEKE spectrum should be from the $^2B_1 \leftarrow {}^1A_1$ transition.

The experimental C-H stretching frequencies are assigned by the comparison with the DFT calculations and displayed in Table 7.5. Both B3P86 and B3LYP calculated frequencies are scaled by the ratio of the experimental to calculated IR frequencies of free ligand (0.957 and 0.962, respectively).[183] These calculated frequencies, which are scaled by the conversion factors, match well with the experimental values. Two peak regions at 3074-3082 cm^{-1} and 3093-3098 cm^{-1} in the M-biphenyl complexes (M = Ti, Zr, and Hf) are assigned to symmetric and asymmetric C-H stretching frequencies, respectively. Compared to the corresponding C-H stretching modes of the free ligand, those of the metal complexes are blue shifted by more than 20 cm^{-1}.[183] Similar blue shifts were also observed for the C-H stretches in metal-benzene complexes[153-155] and in the Co-hexamethylbenzene complex (Chapter 5). An atomic charge analysis shows that the charges on the carbon atoms of biphenyl increase from -0.17/ -0.31e in the free ligand

to -0.23/ -0.37e in the metal complex. On the other hand, the charges on the hydrogen atoms remain essentially unchanged (0.13e in the free ligand and 0.14e in the metal complex). The metal coordination makes the C-H bonds in the phenyl ring to be significantly more polarized and increases the C-H bond strength.

7.3.7. IEs, Bond Energies, and DFT Calculations

Table 7.6 lists and summarizes the IEs and bond energies of M-biphenyl (M = Ti, Zr, and Hf) complexes. As it does for the other metal containing molecules studied, the B3P86 method shows ~10 % overestimation of the IE values.[52,191,271-273] On the other hand, the B3LYP method predicts the IEs with less than 5 % error. Several observations can be made from the data in the table. The IEs of the metal-biphenyl complexes increase in the order of the IEs of the metal atoms [IE(Zr) = 53506 cm^{-1} < IE(Hf) = 55048 cm^{-1} < IE(Ti) = 55072 cm^{-1}].[188] The parallel order indicates that the ionization of the complex removes the electron from the metal atoms. Unfortunately, the experimental bond strengths of neutral and ionic species have not yet been determined. Therefore, the DFT calculations have been used to compare the bond dissociation energies between three metal complexes. Based on the thermochemical cycle: IE (M) – IE (M-biphenyl) = D_0^+ (M-biphenyl) - D_0 (M-biphenyl), the IE difference from the metal to the metal complex equals the bond energy difference from the ionic to neutral complex. Therefore, the differences between the calculated neutral and ionic bond energies are compared with the IE differences from the experiment to determine the accuracy of the calculations. Similar to previous IE comparisons, the B3LYP method shows much closer bond energy differences to the experimental IE differences. The changes in the neutral and ionic bond energies increase as that of the metal complex IEs, and the B3LYP method follows this trend. The trend of the B3LYP calculated dissociation energies follow the order of D_0^+ (Hf-biphenyl) < D_0^+ (Zr-biphenyl) < D_0^+ (Ti-biphenyl). This order correlates with that of the M-biphenyl stretching frequencies, $[v_{17}^+$ (Hf-biphenyl) = 300 cm^{-1}] < $[v_{17}^+$ (Zr-biphenyl) = 331 cm^{-1}] < $[v_{17}^+$ (Ti-biphenyl) = 352 cm^{-1}]. Similarly, the order in D_0 of the complexes correlates with that of the neutral M-biphenyl stretching frequencies.

7.4. Conclusions

In this work, ZEKE and R2PI spectroscopy in combination with the DFT calculations have been used to determine the clamshell structure of the group IV metal (Ti, Zr, and Hf)-biphenyl complexes. The electronic states of the neutral and ionic metal-biphenyl complexes are determined to be $^1A_1$ and $^2B_1$, respectively. The ZEKE spectra of the Ti-, Zr-, and Hf-biphenyl complexes display very strong 0-0 transitions at 43845 (5), 43343 (5), and 43752 (5) cm^{-1}, respectively. In addition, various metal and ligand-based vibrational frequencies have been observed for these species. The R2PI spectroscopy is used to further determine the neutral ground state of the M-biphenyl complexes, and symmetric and asymmetric C-H stretching frequencies of neutral $^1A_1$ states have been observed.

Table 7. 1. Point groups, electronic states, relative energies (E_{rel}, cm^{-1}), IEs (cm^{-1}) of the M-biphenyl (M = Ti, Zr, and Hf) complexes from the DFT calculations (6-311+G(d,p) basis set for C and H and LanL2DZ basis set for Ti, Zr, and Hf).

Complexes	Point group	States	E_{rel} (cm^{-1})[a]	Transitions	IE (cm^{-1})[a]
Ti-biphenyl					43845[b]
	C_{2v}	$^4B_1$	51740 (42431)	$^2B_1 \leftarrow {}^1A_1$	47339 (41919)
	C_{2v}	$^2B_1$	46801 (41368)	$^2B_1 \leftarrow {}^3B_1$	45057 (40871)
	C_{2v}	$^5A_2$	16762 (15347)	$^4B_1 \leftarrow {}^3B_1$	49817 (41637)
	C_{2v}	$^3B_1$	2274 (1083)	$^4B_1 \leftarrow {}^5A_2$	35995 (28055)
	C_{2v}	$^1A_1$	0 (0)		
Zr-biphenyl					43343[b]
	C_{2v}	$^4B_1$	58209 (49697)	$^2B_1 \leftarrow {}^1A_1$	46956 (41874)
	C_{2v}	$^2B_1$	46489 (41378)	$^2B_1 \leftarrow {}^3B_1$	41802 (34370)
	C_{2v}	$^5A_2$	21121 (20256)	$^4B_1 \leftarrow {}^3B_1$	53513 (42764)
	C_{2v}	$^3B_1$	5191 (7954)	$^4B_1 \leftarrow {}^5A_2$	38212 (30725)
	C_{2v}	$^1A_1$	0 (0)		
Hf-biphenyl					43752[b]
	C_{2v}	$^4B_1$	60176 (54063)	$^2B_1 \leftarrow {}^1A_1$	47346 (42294)
	C_{2v}	$^2B_1$	46860 (41791)	$^2B_1 \leftarrow {}^3B_1$	43702 (39408)
	C_{2v}	$^5A_2$	19210 (18434)	$^4B_1 \leftarrow {}^3B_1$	56755 (51419)
	C_{2v}	$^3B_1$	3593 (2846)	$^4B_1 \leftarrow {}^5A_2$	41680 (36405)
	C_{2v}	$^1A_1$	0 (0)		

[a] The energy values are calculated by B3P86 (B3LYP) methods.
[b] From ZEKE measurements.

Table 7. 2. Bond distance (R, Å) and angle ($\angle$, ˚) comparisons of Ti-, Zr-, and Hf-biphenyl clamshell structures with free biphenyl ligand from B3P86 calculations (6-311+G(d,p) basis set for C and H and LanL2DZ basis set for Ti, Zr, and Hf).

	biphenyl (D_2)		Ti-biphenyl (C_{2v})		Zr-biphenyl (C_{2v})		Hf-biphenyl (C_{2v})	
	^1A	Expt.[a]	$^1A_1$	$^2B_1$	$^1A_1$	$^2B_1$	$^1A_1$	$^2B_1$
$R(M\text{-}C_1)$			2.335	2.321	2.536	2.517	2.473	2.449
$R(M\text{-}C_2)$			2.371	2.435	2.553	2.591	2.493	2.531
$R(M\text{-}C_3)$			2.253	2.341	2.389	2.455	2.353	2.414
$R(M\text{-}C_4)$			2.044	2.067	2.187	2.198	2.161	2.168
$R(C_1\text{-}C_2)$	1.391	1.390 1.379	1.411	1.418	1.412	1.417	1.415	1.419
$R(C_2\text{-}C_3)$	1.389	1.385 1.391	1.411	1.387	1.416	1.396	1.420	1.398
$R(C_3\text{-}C_4)$	1.399	1.399 1.394	1.456	1.458	1.461	1.460	1.463	1.463
$R(C_4\text{-}C_5)$	1.478	1.496	1.466	1.445	1.464	1.452	1.467	1.452
$\angle(C_1\text{-}C_4\text{-}C_5)$	180.0	180.0	123.1	124.1	129.1	129.3	127.1	127.3

[a] The bond distances and angles of biphenyl in solid state from reference[254].

Table 7. 3. ZEKE peak positions (cm^{-1}) and assignments of M-biphenyl (M = Ti, Zr, and Hf) complexes.

(a) Ti-biphenyl		(b) Zr-biphenyl		(c) Hf-biphenyl	
ZEKE	Assignment	ZEKE	Assignment	ZEKE	Assignment
43187	14_1^0	42930	16_1^0	43330	16_1^0
43249	15_1^0	42997	17_1^0	43438	17_1^0
43398	16_1^0	43133	18_1^0	43544	18_1^0
43433	18_2^0	43326	17_1^1	43634	$16_1^0 17_0^1$
43521	17_1^0	43343	0_0^0	43752	0_0^0
43638	18_1^0	43374	$16_0^1 17_1^0$	43824	$16_0^1 17_1^0$
43784	$17_0^1 18_2^0$	43463	$17_0^1 18_1^0$	43840	$17_0^1 18_1^0$
43845	0_0^0	43534	$17_1^1 18_1^0$	43962	18_0^1
43991	$17_0^1 18_1^0$	43551	18_0^1	44052	17_0^1
44039	18_0^1	43653	17_1^2	44156	16_0^1
44197	17_0^1	43674	17_0^1	44262	$17_0^1 18_0^1$
44236	18_0^2	43727	$16_0^1 17_1^1$	44348	17_0^2
44395	$17_0^1 18_0^1$	43741	16_0^1	44368	$16_0^1 18_0^1$
44436	18_0^3	43792	$17_0^2 18_1^0$	44454	$16_0^1 17_0^1$
44549	17_0^2	43877	$17_0^1 18_0^1$	44538	$17_0^2 18_0^1$
44592	$17_0^1 18_0^2$	43948	$16_0^1 18_0^1$	44562	16_0^2
44624	18_0^4	43999	17_0^2	44644	17_0^3
44744	$17_0^2 18_0^1$	44070	$16_0^1 17_0^1$	44662	$16_0^1 17_0^1 18_0^1$
44784	$17_0^1 18_0^3$	44140	16_0^2	44762	$16_0^1 17_0^2$
44830	10_0^1	44275	$16_0^1 17_0^1 18_0^1$	44862	$16_0^2 17_0^1$
44903	17_0^3	44326	17_0^3		
44940	$17_0^2 18_0^2$	44468	$16_0^2 17_0^1$		
44983	$17_0^1 18_0^4$				
45092	$17_0^3 18_0^1$				
45135	$17_0^2 18_0^3$				

Table 7. 4. Vibrational frequencies (cm^{-1}) and assignments for Ti-, Zr-, and Hf-biphenyl complexes.

Mode	Expt.	B3P86[a,b]	B3LYP[a]	MP2[a]	Description
Ti-biphenyl					
ν_{10}^{+}	985	963 (970)	969	976	In-plane ring distortion
ν_{14}	658	660 (661)	655	655	Ring breathing
ν_{15}	596	564 (594)	562	555	Out-of-plane ring distortion
ν_{16}	447	416 (419)	412	487	Symmetric ring wave
ν_{17}^{+}/ ν_{17}	352/ 324	345/ 399 (351/ 409)	321/ 378	324/ 402	Metal-ligand stretch
ν_{18}^{+}/ ν_{18}	194/ 207	201/ 204 (198/ 204)	187/ 189	232/ 224	Phenyl ring bend towards M
Zr-biphenyl					
ν_{16}^{+}/ ν_{16}	398/ 413	395/ 414	389/ 407	385/ 397	Symmetric ring wave
ν_{17}^{+}/ ν_{17}	331/ 346	326/ 353	309/ 338	359/ 328	Metal-ligand stretch
ν_{18}^{+}/ ν_{18}	208/ 210	200/ 203	185/ 190	250/ 207	Phenyl ring bend towards M
Hf-biphenyl					
ν_{16}^{+}/ ν_{16}	404/ 422	404/ 420	399/ 414	380/ 379	Symmetric ring wave
ν_{17}^{+}/ ν_{17}	300/ 314	295/ 318	280/ 305	322/ 321	Metal-ligand stretch
ν_{18}^{+}/ ν_{18}	210/ 208	209/ 209	197/ 198	229/ 214	Phenyl ring bend towards M

[a]All the frequency values are calculated by using LanL2DZ basis set on metals and 6-311+G(d,p) basis set on C and H.
[b]The vibrational frequencies of Ti-biphenyl in parenthesis are calculated by using 6-311+G(d,p) basis set on all the atoms.

Table 7. 5. Experimental R2PI and calculated IR active C-H stretching frequencies (cm^{-1}) of the M-biphenyl complexes (M=Ti, Zr, and Hf). Experimental IR frequencies of free ligand, biphenyl is included for the comparison.

	Expt.	B3P86[b]	B3LYP[b]	Assignments
biphenyl				
	3041[a]			Symmetric C-H stretching
	3075[a]			Asymmetric C-H stretching
Ti-biphenyl				
	3078	3080	3081	Symmetric C-H stretching
	3093	3098	3100	Asymmetric C-H stretching
Zr-biphenyl				
	3074	3079	3079	Symmetric C-H stretching
	3096	3098	3102	Asymmetric C-H stretching
Hf-biphenyl				
	3082[c]	3081	3082	Symmetric C-H stretching
	3098[c]	3101	3104	Asymmetric C-H stretching

[a] From the reference[183]
[b] All the frequencies are calculated by using LanL2DZ basis set on metals and 6-311+G(d,p) basis set on C and H and the calculated frequencies are multiplied by conversion factor of 0.957 for B3P86 and 0.962 for B3LYP, the average ratios of the experimental and calculated C-H stretching frequencies of the free ligand.
[c] Due to the noise level, these peaks are assigned by taking the most intense peak within the range of calculated C-H frequencies.

Table 7. 6. The IEs (cm^{-1}) and bond energies (kcal mol^{-1}) of the M-biphenyl (M = Ti, Zr, and Hf) complexes

		Ti-biphenyl	Zr-biphenyl	Hf-biphenyl
Electronic transition		$^2B_1 \leftarrow {}^1A_1$	$^2B_1 \leftarrow {}^1A_1$	$^2B_1 \leftarrow {}^1A_1$
IE[a,b]	ZEKE	43845	43343	43752
	B3P86	47339 (46613)	46956	47346
	B3LYP	41919	41874	42294
$\Delta(D_0^+ - D_0)$, (D_0^+/ D_0)[a]	ZEKE	32	29	32
	B3P86	22 (106/ 84)	19 (109/ 90)	22 (109/ 87)
	B3LYP	38 (87/ 49)	33 (86/ 53)	36 (83/ 47)

[a] The IEs and bond strengths of the complexes are calculated by using LanL2DZ basis set on metals and 6-311+G(d,p) basis set on C and H, unless noted otherwise.
[b] The IE of Ti-biphenyl in parenthesis is calculated by using 6-311+G(d,p) basis set on all the atoms.
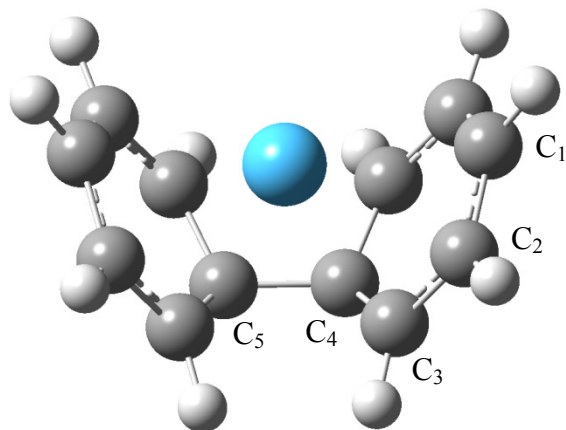
Figure 7. 1. M-biphenyl (M=Ti, Zr, and Hf) clamshell structure complexes, optimized by the B3P86 method with 6-311+G(d,p) basis set on C and H, and LanL2DZ on metal atoms. The figure is shown with the corresponding carbon numberings used in the text.
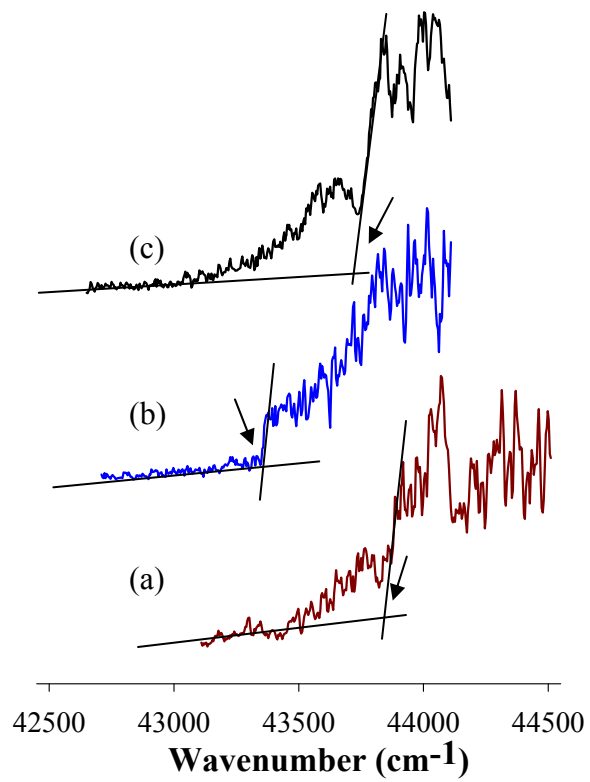
Figure 7. 2. PIE spectra of Ti- (a), Zr- (b), and Hf-biphenyl (c) complexes. The ionization thresholds are indicated by the arrows.
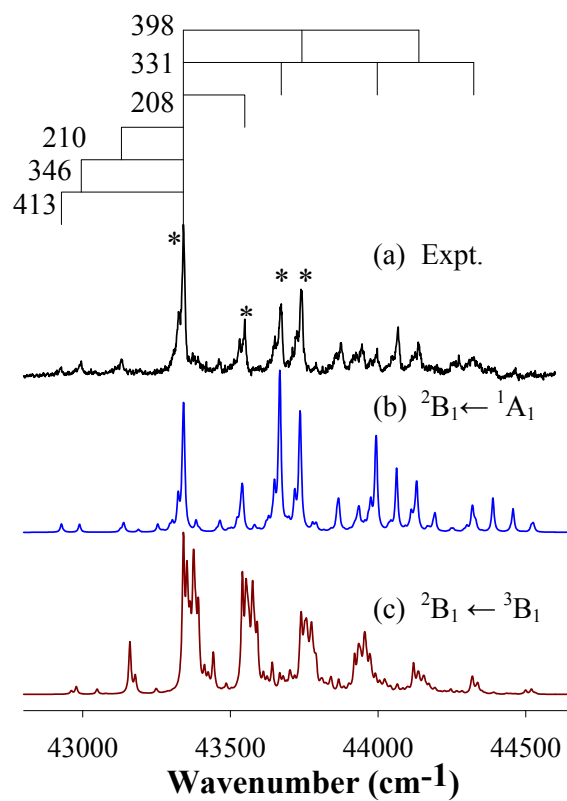
Figure 7. 3. Experimental ZEKE spectra of Zr-biphenyl complex seeded in He (a) and simulations of $^2B_1 \leftarrow {}^1A_1$ (b) and $^2B_1 \leftarrow {}^3B_1$ (c) transitions.
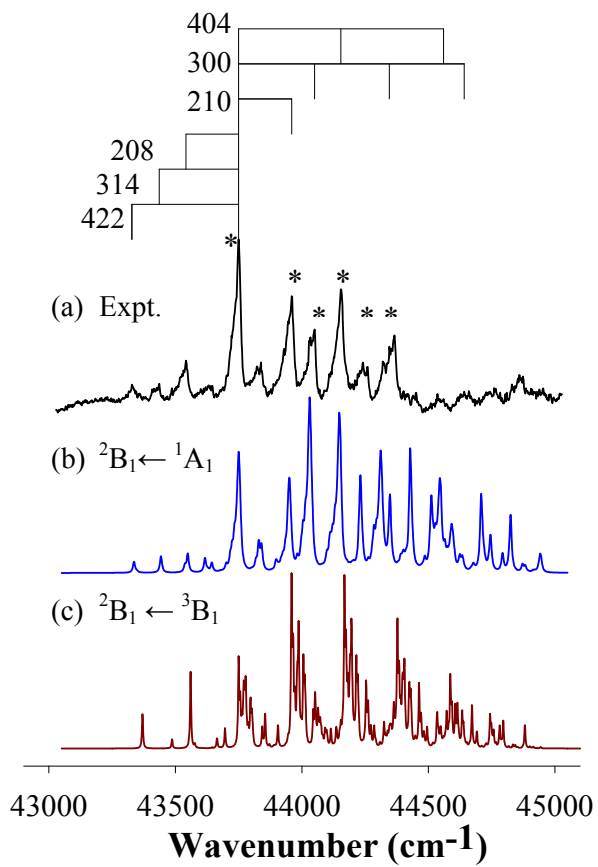
Figure 7. 4. Experimental ZEKE spectra of Hf-biphenyl complex seeded in He (a) and simulations of $^2B_1 \leftarrow {^1}A_1$ (b) and $^2B_1 \leftarrow {^3}B_1$ (c) transitions.
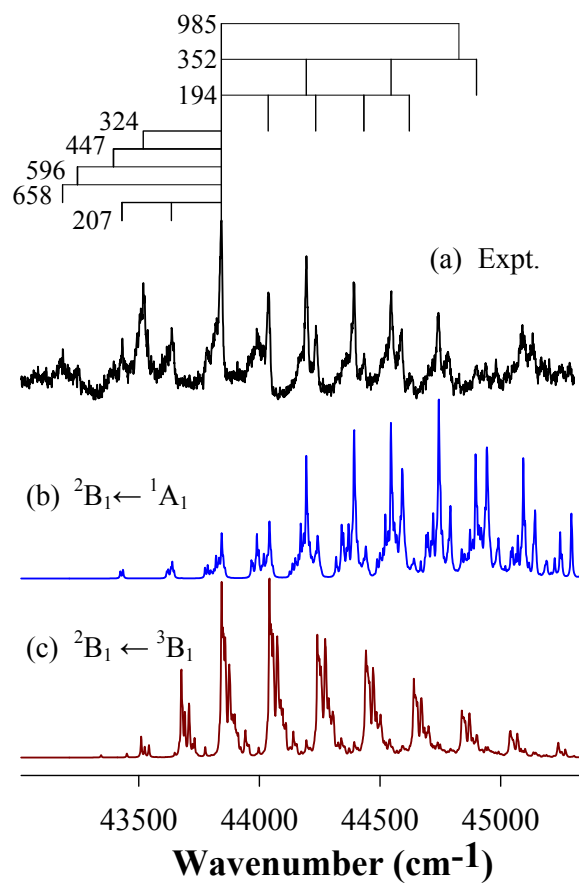
Figure 7. 5. Experimental ZEKE spectra of Ti-biphenyl complex seeded in He (a) and simulations of $^2B_1 \leftarrow {}^1A_1$ (b) and $^2B_1 \leftarrow {}^3B_1$ (c) transitions.
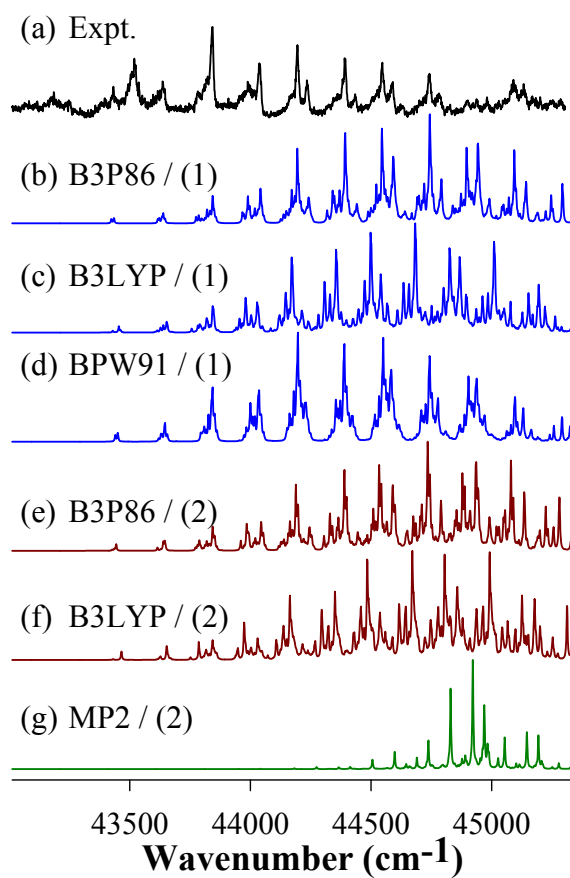
Figure 7. 6. Experimental ZEKE spectra of Ti-biphenyl complex seeded in He (a) and simulations of $^2B_1 \leftarrow {}^1A_1$ transition using DFT and MP2 methods and basis sets (1) 6-311+G(d,p) on all atoms and (2) 6-311+G(d,p) on C and H, and LanL2DZ on Ti.
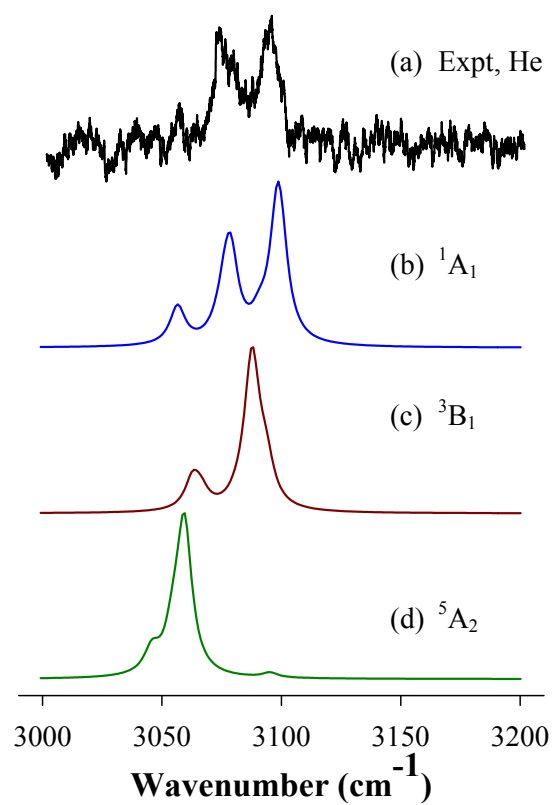
Figure 7. 7. Experimental R2PI spectrum of Zr-biphenyl seeded in He gas (a) and simulated IR spectra of $^1A_1$ (b), $^3B_1$ (c), and $^5A_2$ (d) states of Zr-biphenyl in the C-H stretching region.
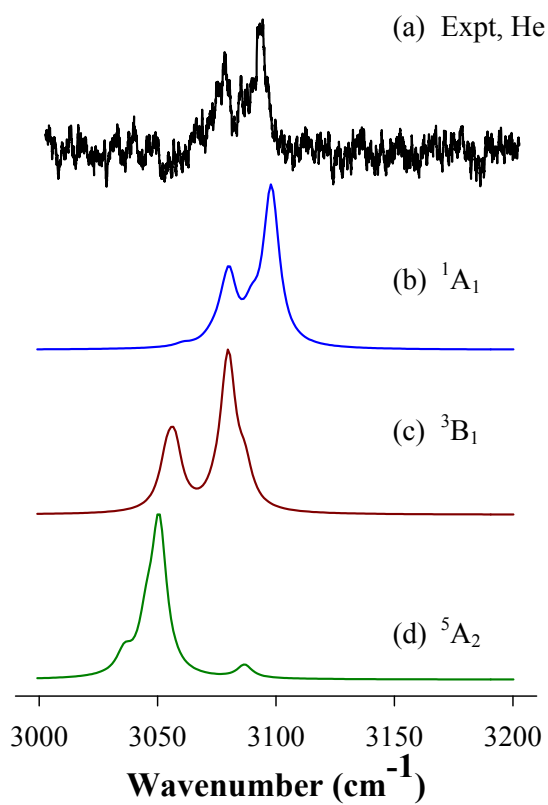
Figure 7. 8. Experimental R2PI spectrum of Ti-biphenyl seeded in He gas (a) and simulated IR spectra of $^1A_1$ (b), $^3B_1$ (c), and $^5A_2$ (d) states of Ti-biphenyl in the C-H stretching region.
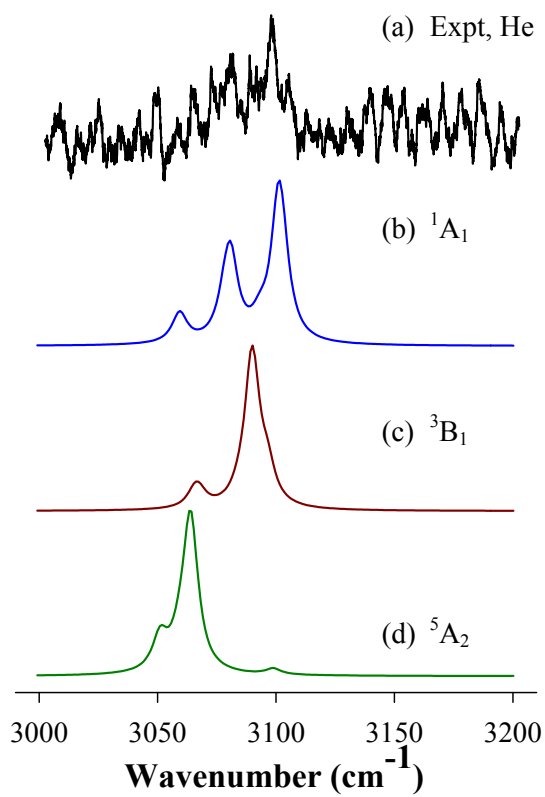
Figure 7. 9. Experimental R2PI spectrum of Hf-biphenyl seeded in He gas (a) and simulated IR spectra of $^1A_1$ (b), $^3B_1$ (c), and $^5A_2$ (d) states of Hf-biphenyl in the C-H stretching region.

CHAPTER 8. HIGH-RESOLUTION ELECTRON SPECTRA, PREFERENTIAL
METAL-BINDING SITES, AND THERMOCHEMISTRY OF LITHIUM COMPLEXES
OF POLYCYCLIC AROMATIC HYDROCARBONS

8.1. Introduction

Mechanisms of lithium (Li) storage in carbonaceous materials have received
considerable attention because of their importance in developing high-density Li
rechargeable batteries.[274-277] The physical mechanisms depend on the type of carbon-
based material: Li can be inserted reversibly into layered graphite structures or adsorb on
the surfaces of single-layered graphenes.

PAH molecules are model systems that can provide new insight into the precise Li
binding site and thermochemistry of carbon-based materials. Interactions between Li/ Li$^+$
and PAH molecules have been studied by many computational calculations.[278-292] For Li-
PAH neutral complexes, semiempirical computer simulations by Papanek et al. showed
that the high capacity of Li uptake by PAH molecules (Li atomic percent with respect to
the number of carbon atoms) is partially attributable to Li binding at the hydrogen-
terminated edges of pyrene, coronene, and several other PAH molecules, with local
geometries analogous to the stable isomer of the organolithium molecule $C_2H_2Li_2$.[278]
Using the ab initio Hartree-Fock method and DFT, Ago et al.[279] and Ishikawa et al.[280]
examined ring-edge and ring-over binding sites of phenanthrene, anthracene, and pyrene
for two Li atoms and found that the Li complexes with ring-over binding are more stable
than those with edge binding. However, the energy barrier for a Li atom migrating from
one site to the other is so small that both ring-edge and ring-over sites are possible at
room temperature. Similarly, Zhu and Lu's DFT calculations predicted the ring-over
binding to be more stable than the edge binding in several Li complexes of graphite
models.[281] Additionally, Martinez et al. reported a weakly-bound Li-coronene structure
with Li binding above the center ring of the ligand.[282] On the other hand, in their
theoretical studies of alkali metal binding with PAHs Baker and Head-Gordon reported Li
binding with the external ring of the nonlinear PAH molecules, including coronene.[283]
For Li$^+$-PAH cations, Gal et al. examined the effect of increasing the number of fused

rings from naphthalene ($C_{10}H_8$) to circumcoronene ($C_{54}H_{18}$).[284] Their DFT calculations showed that the strength of the binding to a given aromatic ring decreases as the number of the cycles directly fused to it increases and the energy gap between and the activation barrier connecting the local minima decreases as the number of the fused rings in the system increases. Guell et al. investigated the effect of Li^+ on the aromaticity of the PAH molecules at the DFT level of theory and found that the ring directly interacting with Li^+ suffers a significant reduction of aromaticity, while the reduction of the local aromaticity of the adjacent rings is minor.[285] In contrast to the computational studies, there has been very little experimental work on these systems, except for a Fourier-transform-ion-cyclotron-resonance mass spectrometric study of the Li^+ cation basicities of naphthalene, azulene, anthracene, and phenathrene[284] and a threshold collision-induced dissociation measurement of the Li^+ binding energy of naphthalene.[293]

Although the two benzene rings are equivalent in naphthalene, two types (outer ring I and inner ring II) of the six-member carbon rings exist in PAH molecules (Figure 8.1). These two-type rings are different because they contain different number of C-H bonds and share different number of fused C-C bonds. In this paper, we report high-resolution electron spectra of Li complexes of naphthalene, pyrene, perylene, and coronene measured by PFI-ZEKE spectroscopy. From these spectra, we have identified the preferential metal binding sites and determined AIEs, metal-ligand bond dissociation energies, and vibrational frequencies of the Li complexes. The work provides the first spectroscopic evidence about the bonding and structures of these Li complexes.

8.2. Experimental and Computational Methods

The experimental setup has been described in Chapter 2. Li complexes of PAHs were prepared by interactions of Li atoms with PAH molecules in a pulsed molecular beam source. The Li-PAH complexes were synthesized by two different methods. To synthesize Li-naphthalene, solid naphthalene (Aldrich, 99%) was introduced at room temperature to a small stainless-steel collision chamber (~ 1.5mL), placed downstream of the metal ablation region. The ligand was located inside a glass bulb and entered through a stainless-steel capillary (0.053″ inner diameter) into the source chamber. The metal

atom was produced by pulsed laser vaporization (Quanta Ray, GCR-3 Nd:YAG, 532 nm) of Li metal rod (Aldrich, 99%). To produce Li atoms and larger PAH molecules, a cylindrical rod made of Li and PAH (Aldrich or TCI America: pyrene, 98%; perylene, 99%; or coronene, 95%) powders in 1:1 volume ratio was vaporized by laser. The vaporized metal atoms and organic ligands were entrained in the pulsed flow of ultrahigh-purity inert gas (He, Ar, or He/Ar mixture) delivered by a home-made piezoelectric pulsed valve.[55] The ablation rod was translated and rotated by a motor-driven mechanism to ensure that each laser pulse ablated a fresh rod surface.

The Li-PAH complexes were identified by photoionization time-of-flight mass spectrometry. ZEKE electrons were generated by photoexcitation of the neutral complexes to highly excited Rydberg states, followed by time-delayed (3 μs) pulsed-electric-field ionization of these states. The pulsed field used for ionization was 1.2 Vcm^{-1} in height and 100 ns in width. A small dc electric field of 0.08 Vcm^{-1} was applied to remove the kinetic electrons produced by direct photoionization. Photoexcitation was carried out with a frequency-doubled dye laser (Lumonics, HD-500), pumped by the third harmonic output of a second Nd:YAG laser (Continuum, Surelite II, 355 nm). The pulsed electric field was generated by a delay pulse generator (Stanford Research System, DG535). The ion and electron signals were detected by a dual microchannel plate detector (Galileo), amplified by a preamplifier (Stanford Research System, SR445), averaged by a gated integrator (Stanford Research System, SR250), and stored in a laboratory computer. Laser wavelengths were calibrated against vanadium or titanium atomic transitions in the range of the ZEKE spectra.[57] The dc field effects on the ZEKE spectral energies were corrected using the relation of $\Delta IE = 6.1 E_f^{1/2}$, where E_f in Vcm^{-1} is the field strength.[111]

Molecular geometries and vibrational frequencies of the neutral and singly charged cations were obtained using the DFT and 6-311+G(d, p) basis set implemented in the GAUSSIAN 03 software.[269] The DFT methods included B3P86 and B3LYP methods. Since both B3P86 and B3LYP yielded similar predictions, only the results from the B3LYP calculations are presented in this report unless otherwise noted. Multidimensional FC factors were computed from the theoretical equilibrium geometries, harmonic vibrational frequencies, and normal coordinates of the neutral and ionic

complexes.[65,294] The Duschinsky effect[29] was considered to account for normal mode differences between the neutral and ionic molecules. A Lorentzian line shape with the experimental linewidth was used to simulate the spectral broadening. Possible transitions from excited vibrational levels of the neutral complexes were considered by assuming thermal excitation at specific temperatures.

8.3. Results and Discussion

8.3.1. ZEKE Spectra

Each of the spectra (Figures 8.2a, 8.3a, 8.4a, and 8.5a) recorded with argon as the carrier gas exhibits a strong origin band and rich vibronic transitions from the neutral complex to the singly charged cation. The origin of the spectrum corresponds to the transition between the ground vibrational levels of the neutral and cationic states, and its transition energy is referred to the adiabatic IE of the neutral complex. The IEs of the Li-PAH complexes are measured to be 35491, 35481, 37530, and 33467 cm^{-1} for PAH = naphthalene, pyrene, perylene, and coronene, respectively. The uncertainty of the IE values is about 5 cm^{-1} or 6 x 10^{-4} eV. The ZEKE bands marked in the figures arise from single vibrational modes, and others are transitions to combinations of two or more vibrational modes. A complete list of the ZEKE band positions is given in Table 8.4. The observed vibrational intervals are 148, 252, 362, 388, 510, 818, and 1376 cm^{-1} for Li-naphthalene; 76, 226, 374, 408, 430, 588, and 740 cm^{-1} for Li-pyrene; 28, 86, 308, 352, 376, 544, 574, and 1564 cm^{-1} for Li-perylene; and 84, 222, 236, 316, 344, 366, 386, 446, and 480 cm^{-1} for Li-coronene. Among these vibrational excitations, the most active mode (with more than one-quantum excitation) has a frequency of 375 ± 13 cm^{-1} (i.e., 362, 374, 376, and 386 cm^{-1} for Li-naphthalene, Li-pyrene, Li-perylene, and Li-coronene, respectively).

8.3.2. Spectral Analysis and Preferred Li Binding Site

The measured energy intervals correspond to the vibrational frequencies of the cations and can be divided into two groups: Li-PAH and PAH-based vibrations. PAH-based vibrations may be identified by comparing the energy spacings and the vibrational frequencies of the normal modes with appropriate symmetry species in the free ligands. The maximum molecular symmetries of the free PAH molecules are D_{2h} for naphthalene, pyrene, and perylene and D_{6h} for coronene (Figure 8.1). Upon metal coordination, the molecular symmetry of the complex depends on the Li binding sites. For example, the optimal symmetry of Li-naphthalene is C_{2v} if a Li atom binds with the fused C-C bond, and C_s if it is above the center of a benzene ring or bound to a non-fused C-C bond that is parallel to the unique fused C-C bond. Although there are a large number of vibrational modes for these PAH molecules, it is possible to correlate some of the measured energy intervals to likely vibrational modes of the free ligands on the basis of symmetry and frequency considerations. The 148 and 818 cm^{-1} intervals in the ZEKE spectrum of Li-naphthalene correspond to the frequencies of an out-of-plane (o.p.) ring bend (b_{3u}, 167 cm^{-1})[295] and an o.p. C-H bend (b_{3u}, 788 cm^{-1})[296] of naphthalene measured by IR spectroscopy. The 510 and 1376 cm^{-1} transitions are comparable to the frequencies of a ring breathing mode (a_g, 510 cm^{-1})[297] and a C-C stretch (a_g, 1380 cm^{-1})[298] of the free ligand from electronic spectroscopy. The vibrational frequencies of the o.p. C-H bend (818 cm^{-1}) and the C-C stretch (1376 cm^{-1}) Li$^+$-naphthalene are also comparable to those of the corresponding modes in Fe$^+$-naphthalene.[299] The b_{3u} and a_g modes of naphthalene (D_{2h}) are transformed into a_1 modes in the C_{2v} structure or a′ modes in the C_s structure of Li-naphthalene. Both a_1 and a′ excitations are symmetry-allowed in photoelectron spectroscopy. Using similar symmetry and frequency arguments, we were able to assign several ZEKE vibrational intervals of the other Li$^+$-PAH complexes to vibrational modes of the corresponding PAH molecules (Table 8.1). These preliminary vibrational assignments, along with other observed vibrational intervals, are discussed below by comparing the ZEKE spectra with theoretical predictions.

In the search for structural isomers for each Li-PAH complex, we considered binding configurations with Li above a ring and a C-C bond and found that the ring-over

binding forms the minimum-energy structures. In these ring-over binding structures, the PAH molecules remain planar. This prediction is consistent with the most recent calculations on some Li-PAH complexes,[283,284] but different from the earlier calculations on 2Li-PAH or larger systems,[279,280] where the PAH ring is no longer planar. Table 8.2 summarizes the electronic states and relative energies of the neutral and ionized ring-over binding structures predicted at B3LYP/6-311+G(d,p) level of theory. The electronic energies of various states are referenced to the most stable doublet state of the neutral complex. Except for Li-naphthalene, two minimum-energy isomers (I and II) are predicted for each complex, with Li binding over ring I or ring II. The ring-I isomer is more stable than the ring-II isomer by 7-18 kJ mol^{-1} (1 kJ mol^{-1} = 83.6 cm^{-1}) in the neutral doublet neutral state and by 9-15 kJ mol^{-1} in the singlet cation. The stability difference between the neutral isomers increases as the size of the PAH molecules increases. However, this trend does not hold for the cations, as the energy difference between the I and II isomers of Li^{+}-coronene (10 kJ mol^{-1}) is smaller than that between those of Li^{+}-perylene (15 kJ mol^{-1}). Nevertheless, the energy differences between the ring-I and ring-II isomers are relatively small, and the theoretical identification of the preferential binding site is less straightforward. The determination of the preferred binding site is achieved by combining the theoretical predictions and vibrationally resolved ZEKE spectra.

Figures 8.2, 8.3, 8.4, and 8.5 compare the experimental and theoretical spectra of the Li-PAH complexes. In the simulations, the harmonic vibrational frequencies are not scaled, while the 0-0 transition energies are shifted to the experimental values for the sake of simplicity. We calculated the spectra in the temperature range of 10-300 K in an attempt to identify possible transitions from excited vibrational levels of the neutral complexes and found that the best temperatures under which the calculated and measured spectra have the best match were up to about 50 K. By comparing the experimental spectra and simulations at different temperatures, all observed vibrational bands are determined to be cold bands arising from the ground vibrational level of the neutral complexes. This is similar to the previous observations for other metal-organic complexes.[56,113,116,145]

The simulation of Li-naphthalene (Figure 8.2) reproduces nicely the observed vibrational bands. The simulations of the ring-I isomers of Li-pyrene, Li-perylene, and Li-coronene (Figures 8.3, 8.4, and 8.5) show much better agreement with the experimental spectra than those of the ring-II isomers, suggesting that spectral carriers for the three complexes are the ring-I isomers. The ring-II isomers are not likely contributors to the measured spectra, as they have different IE values, and their contributions would have shown a second origin band in the ZEKE spectra. This is consistent with the theoretical prediction that the ring-I isomer is more stable than ring-II. On the basis of the good agreement between the measured and calculated vibrational frequencies and transition intensities, vibrational modes are identified from the measured energy intervals (Table 8.1). From the table, several common vibrational modes are probed for these Li^+-PAH complexes. They are a Li^+-ring stretching, a Li^+ rocking, an o.p ring bending, and a ring breathing mode. The Li^+-ring stretching frequencies display a small increase with increasing the size of the PAH molecules and are averaged around 375 ± 13 cm^{-1}. The Li^+ rocking vibration shows a larger frequency range (222 - 308 cm^{-1}), which is associated with the mixing of an o.p. ring bending motion. The ligand-based ring-breathing frequencies (510, 588, 544, and 480 cm^{-1}) in the complexes are very close to those in the free ligands. On the other hand, the frequencies of the soft o.p. bending vibrations (148, 76, 86, and 84) are significantly reduced ($\geq$ ~10%) by metal coordination. In addition to these common vibrational modes, several other ligand-based vibrations are observed for each Li^+-PAH complex. These additional modes of Li^+-naphthalene include an asymmetric ring o.p. bend mixed with a Li^+-ring stretch (388 cm^{-1}), an o.p. C-H bend (818 cm^{-1}), and a C-C stretch combined with an i.p. C-H bend (1376 cm^{-1}). The additional modes of Li^+-pyrene are ring i.p. and o.p. bends (408 and 430 cm^{-1}) and a C-H bend (740 cm^{-1}). For Li^+-perylene, they are a ring-I twist (28 cm^{-1}), two i.p. ring bends (352 and 574 cm^{-1}), and a C-C stretch combined with an i.p. C-H bend (1564 cm^{-1}). For Li-coronene, they include three o.p ring bends (236, 316, and 446 cm^{-1}) and two i.p ring bends (344 and 366 cm^{-1}). Again, all these individual ligand-based vibrations have similar frequencies to those of the corresponding modes of the respective free ligands (Table 8.1).

172

The preferential Li and Li$^+$ binding with ring I is correlated with a higher π electron content and aromaticity of the ring. From the viewpoint of atomic contributions,[300] a carbon atom shared by single, two, and three rings contributes 1, 1/2, and 1/3 π electron to each ring, respectively. Ring I of pyrene consists of three unshared carbon atoms, two carbons shared with another ring, and one shared with two other rings; thus, the total number of the π electrons for type-I ring is 3 + 2/2 + 1/3 = 4.33. On the other hand, ring II of pyrene contains two unshared carbon atoms, two shared by two rings, and the other two shared by three rings; thus, a type-II ring possesses 2 + 2/2 + 2/3 = 3.67 π electrons. The number of the π electrons of the free ligands estimated using this simple method is listed in Table 8.3 and is in reasonable agreement with that from a more refined method based on the number of Kekule structures in a PAH molecule.[301,302] For the local aromaticity, we have calculated the aromatic indices (Table 8.3) of ring I and ring II in these PAH molecules using the structure-based harmonic oscillator model of aromaticity (HOMA),[184,185]

$$\text{HOMA} = 1 - \frac{\alpha}{n}\Sigma(R_{opt} - R_i)^2 \qquad (8.1)$$

where n is the total number of bonds taken into the summation and α is an empirical constant chosen to give HOMA = 0 for a model nonaromatic molecule and HOMA = 1 for a model aromatic molecule with all bonds equal to an optimal R_{opt}. For C-C bonds, α_{C-C} is 257.7, R_{opt} (1.394 Å) and R_i are the bond distances in benzene and the PAH molecules from the B3LYP calculations. The higher the HOMA value, the more aromatic the ring in question. The HOMA index is known as one of the most effective structural indicators of aromaticity.[186,303] As shown in Table 8.3, the HOMA value of ring I is higher than that of ring II for each of the PAH molecules.

The higher π-electron content and aromaticity of ring I enhances the charge transfer from the PAH molecules to the metal atom. Figure 8.6 presents a valence orbital interaction diagram between the Li $2s/2p$ and pyrene HOMO/LUMO (highest occupied molecular orbital/lowest unoccupied molecular orbital). The ring-I complex is in C_s point group with the symmetric plane overlapping with the Cartesian xy plane. The HOMO

energies are taken as the negatives of the experimental IEs of the metal atom, ligand, and complex, respectively. Other orbitals are referenced to the HOMO by the energy difference between the HOMO and relevant orbitals predicted by B3LYP for the ligand and complex, or measured for the Li atom.[117] The HOMO (b_{1g}) and LUMO (a_u) of pyrene (D_{2h}) are converted to a'' orbitals in Li-pyrene (C_s), which have the same symmetry as one ($2p_z$) of the Li $2p$ orbitals. The HOMO of Li-pyrene is formed by the interaction between the pyrene LUMO and Li $2p_z$ and is half filled by an electron from the metal atom. The ligand to metal charge transfer is largely facilitated by the electron donation from the pyrene HOMO to the Li $2p_z$ orbital, and the higher π-electron content of ring I enhances such a charge transfer and makes ring I more favorable for the metal binding.

8.3.3. Ionization and Bond Energies and Extended π-Electron Network

Table 8.1 summarizes the IEs and bond energies (D_0) of the neutral Li-PAH and Li-benzene complexes and the bond energies (D_0^+) of the cations. The inclusion of the Li-benzene complex aids in the discussion about the influence of the extended π network. The experimental bond energies (D_0^+) of Li^+-benzene and Li^+-naphthalene are taken from previous threshold collision-induced dissociation measurements.[293,304] The "experimental" bond energies of the other Li^+-PAH ions are obtained from the calibrated DFT/B3LYP values. This correction adds the difference (22 kJ mol^{-1}) between the measured and calculated D_0^+ values of Li^+-naphthalene to the calculated values of the other three Li^+-PAH ions. The bond energies (D_0) of the neutral complexes are obtained from the thermodynamic circle: D_0 (Li-L) = D_0^+ (Li^+-L) − IE (Li) + IE (L), where L is a PAH ligand.

The IEs of the Li complexes show no clear correlation with those of the free ligands.[117] This observation suggests that the ejected electron is not from the HOMO of the ligand. Because the IE of the Li atom is lower than those of the aromatic ligands, ionization is expected to remove a Li $2s$-based electron. As shown by the orbital interaction diagram (Figure 8.6), the Li $2s$ electron is transferred into the HOMO of the

174

complex formed by the interaction between the pyrene LUMO and Li $2p_z$ orbital. The IEs of the complexes are in a similar trend to the negative LUMO energies of the free ligands (Tables 8.1 and 8.3).

The metal-ligand bond energies of the neutral complexes increase from benzene to perylene, then decrease from perylene to coronene. Unlike for a given PAH molecule where the ring with a higher π-electron content and aromaticity is preferred for Li binding, the bond energies of the complexes have no correlations with the π-electron content or the aromaticity of the benzene ring that is attached to the metal atom (i.e., ring I). For example, although benzene has the most π-electrons and highest aromaticity compared to ring I of the PAH molecules, the Li-benzene binding energy is the smallest among the five Li complexes. For the neutral complexes, the strength of the metal-ligand interaction is enhanced by the ligand-to-metal and metal-to-ligand charge transfer. As shown by the orbital interaction diagram in Figure 8.6, the increase of the HOMO energy of the ligand improves the electron donation from the ligand to the metal (Li $2p_z$), whereas the decrease of the LUMO energy of the ligand increases the charge transfer from the metal (Li $2s$) to the ligand LUMO. The overall result of this two-way charge transfer is a net charge transfer from Li to the ligand (by about 0.3e, from Mulliken population analysis). In a conventional wisdom, one would think that the LUMO-HOMO energy gap will decrease as the π-electron network of the aromatic molecules expands. Indeed, the LUMO-HOMO gaps predicted by the theory confirm this trend from benzene to perylene. However, the trend is reversed from perylene to coronene (Table 8.3). The change in the HOMO-LUMO gaps of the ligands is correlated with the increase of the bond energies of the Li complexes from benzene to perylene, then the decreases from perylene to coronene.

The ion bond energies follow a similar trend to those of the neutral complexes, but the changes are much smaller, especially among the three larger complexes. Although the metal-to-ligand electron donation is lost in the cations, the ligand-to-metal charge transfer remains, and additional electrostatic and polarization interactions enhance the metal-ligand binding.[305-307] These electrostatic and polarization interactions over compensate the loss of the metal-to-ligand charge transfer, making the Li$^+$ ion binding 2-3 times stronger than the Li atom binding. In the electrostatic binding, it is the first

non-zero electrical moment that dominants the metal ion interaction. Because the dipole moment in these aromatic molecules is zero, interaction between the metal ion and the quadrupole moment is the dominant one in these ions. Among the three components of the quadrupole moments in benzene and PAH molecules, the out-of-plane component (that is perpendicular to the aromatic ring) is negative and two in-plane components are positive because the electronegativity of the carbon atom is larger than that of hydrogen. Thus, the cation-π interaction is attractive with the out-of-plane quadrupole moment, while it is repulsive with the in-plane ones. However, because Li^+ is above the aromatic ring, the repulsive interaction should be very small and can be neglected. Thus, we will consider only the out-of-plane quadrupole moments in the following discussion. The quadrupole moments of benzene and naphthalene were measured to be -8.69 ± 0.50 and -13.49 ± 1.50 DÅ, respectively.[308,309] The quadrupole moments of the other ligands have not been measured, but are predicted to increase with increasing size of the aromatic network. To examine the ion-quadrupole interactions in these systems, however, it is more reasonable to consider the local quadrupole moments of ring I that is attached to the metal than the total values of the whole molecule. The quadrupole moments of ring I are proportional to the number of the CH group within the ring,[309] and they can be estimated by considering the number of the CH groups in ring I and the total number of the CH groups in the PAH molecule. For example, the ring-I quadrupole moment of pyrene is estimated as 18.83 x (3/10) = 5.64 DÅ, where 18.83 DÅ is the total quadrupole moment of the molecule, 3 is the number of the CH groups in a type-I ring, and 10 is the total number of the CH groups in the pyrene molecule. The local quadrupole moments estimated with this method (Table 8.3) decrease gradually with increasing the size of the aromatic molecules, except for perylene. Thus, the ion-quadrupole interactions should follow the same trend. On the other hand, because the polarizability of the ligands increases with the extended π-network, the ion-induced dipole interaction should be enhanced with increasing the size of the aromatic molecules. Therefore, the Li^+ binding strengths are collectively determined by the three factors: the ligand-to-metal charge transfer, the ion-quadrupole interaction, and ion-induced dipole interaction. From Tables 8.1 and 8.3, the Li^+ binding energies increase with the decrease of the HOMO energies and the increase of the polarizabilities of the ligands.

8.4. Conclusions

In this work, we obtained the first high-resolution electron spectra of the Li-PAH (PAH = naphthalene, pyrene, perylene, and coronene) complexes and determined preferential binding sites and ionization and bond energies of these molecular systems. Among these complexes, Li and Li^+ favor the ring-over binding site of the benzene ring with a higher electron content and aromaticity, and the metal coordination does not affect the planarity of the PAH molecules. The adiabatic IEs show no clear correlation with the extension of the π network of the aromatic molecules. The metal-ligand bond energies of the neutral and ionized complexes increase from benzene to perylene, then decrease from perylene to coronene, and the variation is larger in the neutral species than in the cations. The ion binding is about 2-3 times stronger than the neutral binding. The metal-ligand binding in the neutral species are largely due to the two-way charge transfer between the metal atom and ligand, whereas those in the ions are due to ion-quadrupole and ion-induced dipole interactions, in addition to the ligand-to-metal charge transfer.

The PAH ligands used in this study (pyrene, perylene, and coronene) are made of nonlinearly fused benzene rings, where there are carbon atoms common to three benzene rings. It would be interesting to study the Li binding with polyacenes in which no carbon atom is common to more than two rings. It is expected that structural isomers of a Li-polyacene complex should have a smaller energy difference than those of a Li complex formed with a nonlinear PAH molecule. Thus, the observation of more than one isomer may be possible for Li-polyacene complexes.

Table 8. 1. AIEs (eV), metal-ligand bond energies (D_0/D_0^+, kJ mol^{-1}), and vibrational frequencies (v_i^+, cm^{-1}) of Li-aromatic complexes from ZEKE spectra and B3LYP/6-311+G(d,p) calculations.

	ZEKE[a]	B3LYP	Ligand[b]
Li-benzene, C_{6v}			
IE		4.24	
D_0	50	20	
D_0^+	161	153	
Li-naphthalene, C_s			
IE	4.4003	4.54	
D_0	91	61	
D_0^+	187	165	
Ring o.p. bend, v_{26}^+	148	154	167.0 (b$_{3u}$)[c]
Li$^+$ rock, v_{25}^+	252	261	
Li$^+$-ligand stretch, v_{24}^+	362	382	
Ring o.p. bend, v_{23}^+	388	402	
Ring breath, v_{21}^+	510	519	501(a$_g$)[d]
C-H o.p. bend, v_{17}^+	818	837	822 (b$_{3u}$)[e], 788(b$_{3u}$)[f]
C-C stretch with C-H i.p. bend, v_9^+	1376	1374	1350 (a$_g$)[e], 1380(a$_g$)[g]
Li-pyrene, C_s			
IE	4.3991	4.52	
D_0	106	74	
D_0^+	202	180	
Ring o.p. bend, v_{41}^+	76	93	95.0 (b$_{3u}$)[c]
Li$^+$ rock, v_{39}^+	226	230	214.2(b$_{3u}$)[c]
Li$^+$-ligand stretch, v_{37}^+	374	399	
Ring i.p. bend, v_{36}^+	408	417	407(a$_g$)[h]
Ring o.p. bend, v_{35}^+	430	496	498 (b$_{3u}$)[f,i]
Ring breath, v_{32}^+	588	583	593(a$_g$)[h]
C-H o.p. bend, v_{29}^+	740	714	745 (b$_{3u}$)[f,i], 740(b$_{3u}$)[j]
Li-perylene, C_1			
IE	4.6532	4.76	
D_0	137	103	
D_0^+	208	186	
Ring twist, v_{93}^+	28	32	24.5 (a$_u$)[k], 25.1(a$_u$)[l]
Ring o.p. bend, v_{92}^+	86	89	94 (a$_u$)[k,l]
Li$^+$ rock, v_{84}^+	308	317	
Ring i.p. bend, v_{83}^+	352	358	353 (a$_g$)[k,l]
Li$^+$-ligand stretch v_{81}^+	376	404	
Ring breath, v_{71}^+	544	557	547 (a$_g$)[k,l]
Ring i.p. bend, v_{70}^+	574	588	573(b$_{1u}$)[k]
C-C stretch with C-H i.p. bend, v_{18}^+	1564	1588	1551 (a$_g$)[m], 1580 (a$_g$)[k,l]

Table 8.1 (continued).

Li-coronene, C_s			
IE	4.1494	4.24	
D_0	84	49	
D_0^+	204	182	
Ring o.p. bend, ν_{53}^+	84	85	
Li^+ rock, ν_{50}^+	222	228	$225(b_{2g})^n$
Ring o.p. bend, ν_{49}^+	236	295	
Ring o.p. bend, ν_{48}^+	316	322	
Ring i.p. bend, ν_{47}^+	344	373	
Ring i.p. bend, ν_{46}^+	366	386	$365(e_{2g})^n$, $363.0 (e_{2g})^o$
Li^+-ligand stretch ν_{45}^+	386	402	
Ring o.p. bend, ν_{44}^+	446	453	$435(e_{1g})^n$
Ring breath, ν_{42}^+	480	484	$485(a_{1g})^n$

[a]From this work unless otherwise noted. The uncertainty of IE is 6 x 10^{-4} eV. D_0 values are obtained from the thermodynamic cycle: D_0 (Li-PAH) = D_0^+(Li^+-PAH) – IE(Li) + IE (Li-PAH), where D_0^+ values of Li^+-benzene and Li^+-naphthalene are taken from previous threshold collision-dissociation measurements, with uncertainties of ± 14 and ± 16 kJ mol^{-1}, respectively,[293,304] and D_0^+ values of the other Li-PAH complexes are from calibrated theoretical calculations (see text), IE(Li) = 5.3917 eV, and IE (Li-PAH) from ZEKE spectra. The measured vibrational modes are all totally symmetric, that is, a$'$ for Li-naphthalene, Li-pyrene, and Li-coronene. For Li-perylene (C_1), all vibrational modes are symmetry-allowed.
[b]These values are for free aromatic molecules unless otherwise noted, with vibrational symmetry species in parentheses.
[c]From gas-phase IR emission spectra, reference[295].
[d]From gas-phase fluorescence excitation spectra, reference[297].
[e]From IR spectra of Fe^+-pyrene, reference[299].
[f]From Ar matrix IR spectra, reference[296].
[g]From gas-phase fluorescence spectra, reference[298].
[h]From resonant Raman spectra, reference[310].
[i]From Ar matrix IR spectra, reference[311].
[j]From gas-phase IR spectra, reference[312].
[k]From gas-phase IR fluorescence spectra, reference[313].
[l]From gas-phase cavity ring-down spectra, reference[314].
[m]From reference[315].
[n]From vibrational spectra, references[316-318].
[o]From gas-phase fluorescence spectra, reference[319].

Table 8. 2. Molecular symmetries, electronic states, and relative electronic energies (E_{rel}, cm^{-1}) of ring-I and ring-II isomers of the Li-PAH complexes from B3LYP/6-311+G(d,p) calculations.

Complex	Ring type	Sym.	State	E_{rel} (cm^{-1})
Li-naphthalene				
		C_s	$^1A'$	35727
		C_s	$^2A'$	0
Li-pyrene				
	II	C_s	$^1A'$	36366
	II	C_s	$^2A''$	592
	I	C_s	$^1A'$	35565
	I	C_s	$^2A''$	0
Li-perylene				
	II	C_{2v}	$^1A_1$	38988
	II	C_{2v}	$^2B_1$	849
	I	C_1	^1A	37669
	I	C_1	^2A	0
Li-coronene				
	II	C_{2v}	$^1A_1$	33908
	II	C_{2v}	$^2B_1$	1554
	I	C_s	$^1A'$	33063
	I	C_s	$^2A''$	0

Table 8. 3. Properties of several aromatic molecules.

	benzene	Naphthalene	pyrene	perylene	coronene
IE (eV)[a]	9.24378	8.1442	7.4256	6.960	7.29
HOMO (eV)[b]	-7.08	-6.15	-5.67	-5.29	-5.78
LUMO (eV)[b]	-0.48	-1.40	-1.86	-2.31	-1.78
Polarizability (10^{-24} cm^3)[a]	10.0-10.74	16.5-17.48	28.22	35.5[c]	42.5
Ring-I quadrupole moment (DÅ, 3.3356 x 10^{40} C m^2)[d]	-8.18	-6.31	-5.64	-5.91	-4.48
# of π-electrons[e]					
Ring I	6	5	4.33	4.33	3.67
Ring II			3.67	2.67	2.00
Aromatic index[f]					
Ring I	1	0.83	0.90	0.82	0.81
Ring II			0.65	0.19	0.74

[a]From reference[117] unless otherwise noted.
[b]Highest occupied and lowest unoccupied molecular orbital energies from B3LYP/6-311+G(d,p) calculations.
[c]From reference[320].
[d]The ring I local out-of-plane (o.p.) quadrupole moments are calculated by multiplying the molecular o.p. quadrupole moments by the ratio of the number of the C-H bonds in a type-I ring to the number of the C-H group in the molecule (see text). The molecular o.p. quadrupole moment is defined $Q_{o.p.} = x^2 - \frac{1}{2}(z^2 + y^2)$ (reference[321]), where x^2, y^2, and z^2 are three components of the quadrupole moments from B3LYP/6-311+G(d,p) calculations and x-axis is perpendicular to the ring plane.
[e]The number of π-electrons in ring I and ring II are calculated from atomic carbon contributions (see text).
[f]The aromatic index of ring I and ring II are calculated using the C-C bond distances calculated from the B3LYP/6-311+G(d,p) calculations (see text).

Table 8. 4. The ZEKE band positions (cm^{-1}) and assignments for Li-PAH (PAH = naphthalene, pyrene, perylene, and coronene) complexes.

Li-naphthalene		Li-pyrene		Li-perylene		Li-coronene	
Pos.	Assig.	Pos.	Assig.	Pos.	Assig.	Pos.	Assig.
35491	0_0^0	35481	0_0^0	37530	0_0^0	33467	0_0^0
35639	26_0^1	35557	41_0^1	37558	93_0^1	33551	53_0^1
35743	25_0^1	35707	39_0^1	37588	93_0^2	33689	50_0^1
35785	26_0^2	35855	37_0^1	37616	92_0^1	33703	49_0^1
35853	24_0^1	35889	36_0^1	37644	$92_0^1 93_0^1$	33783	48_0^1
35879	23_0^1	35911	35_0^1	37674	$92_0^1 93_0^2$	33811	47_0^1
36001	21_0^1	35965	$36_0^1 41_0^1$	37838	84_0^1	33833	46_0^1
36025	$23_0^1 26_0^1$	36069	32_0^1	37882	83_0^1	33853	45_0^1
36131	$23_0^1 25_0^1$	36221	29_0^1	37906	81_0^1	33913	44_0^1
36151	$21_0^1 26_0^1$	36231	37_0^2	37936	$81_0^1 93_0^1$	33947	42_0^1
36245	$23_0^1 24_0^1$	36263	$36_0^1 37_0^1$	38074	71_0^1	34095	48_0^2
36271	23_0^2	36287	$35_0^1 37_0^1$	38104	70_0^1	34121	$47_0^1 48_0^1$
36309	17_0^1			38258	$81_0^1 83_0^1$	34143	$46_0^1 48_0^1$
36391	$21_0^1 23_0^1$			38280	81_0^2	34165	$45_0^1 48_0^1$
36415	$23_0^2 26_0^1$			38426	$71_0^1 83_0^1$	34293	$42_0^1 47_0^1$
36517	21_0^2			38454	$71_0^1 81_0^1$	34311	$42_0^1 46_0^1$
36629	$23_0^2 24_0^1$			38486	$70_0^1 81_0^1$	34331	$42_0^1 45_0^1$
36657	23_0^3			38508	$70_0^1 81_0^1 93_0^1$	34423	42_0^2
36779	$21_0^1 23_0^2$			38660	81_0^3	34437	$47_0^1 48_0^2$
36867	9_0^1			38826	$71_0^1 81_0^2$	34457	$46_0^1 48_0^2$
				38852	$70_0^1 81_0^2$	34573	$44_0^1 47_0^1 48_0^1$
				38880	$70_0^1 81_0^2 93_0^1$	34587	$44_0^1 46_0^1 48_0^1$
				39094	18_0^1	34605	$42_0^1 47_0^1 48_0^1$
				39120	$18_0^1 93_0^1$	34629	$42_0^1 46_0^1 48_0^1$
				39242	$18_0^1 92_0^1 93_0^2$		

(a) naphthalene   (b) pyrene

(c) perylene   (d) coronene
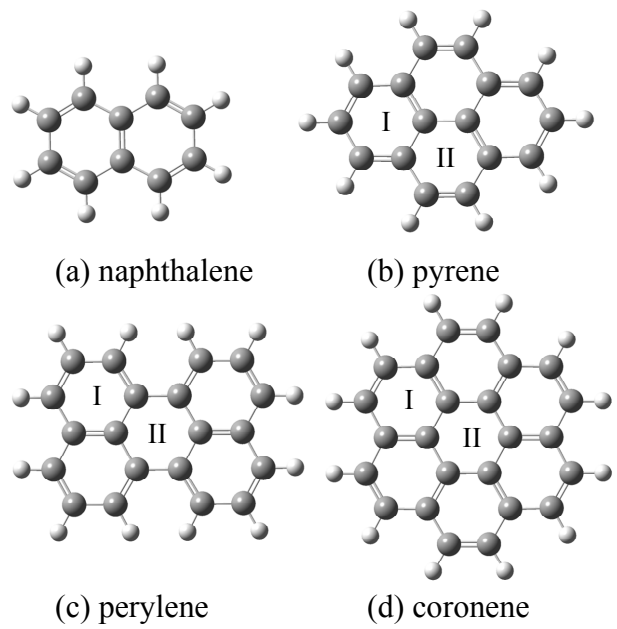
Figure 8. 1. Polycyclic aromatic hydrocarbons with two types of benzene rings (I and II) in pyrene, perylene, and coronene.
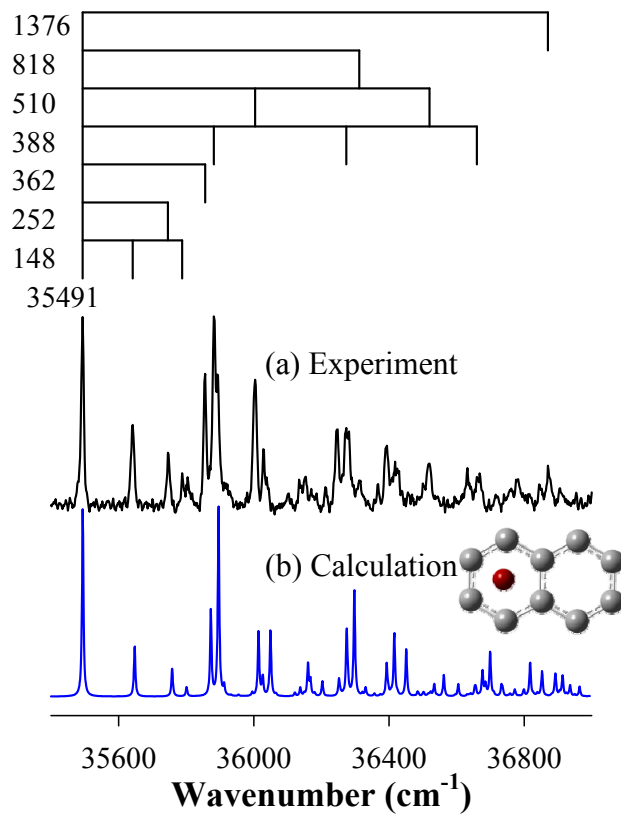
Figure 8. 2. The experimental spectrum (a) and simulation (b) of Li-naphthalene.

740
588
430
408
374
226
76
35481

(a) Experiment

x5

(b) Ring I

(c) Ring II

35600   35800   36000   36200

Wavenumber (cm^{-1})

Figure 8. 3. The experimental spectrum (a) and simulations of the ring-I (b) and ring-II (c) structures of Li-pyrene.
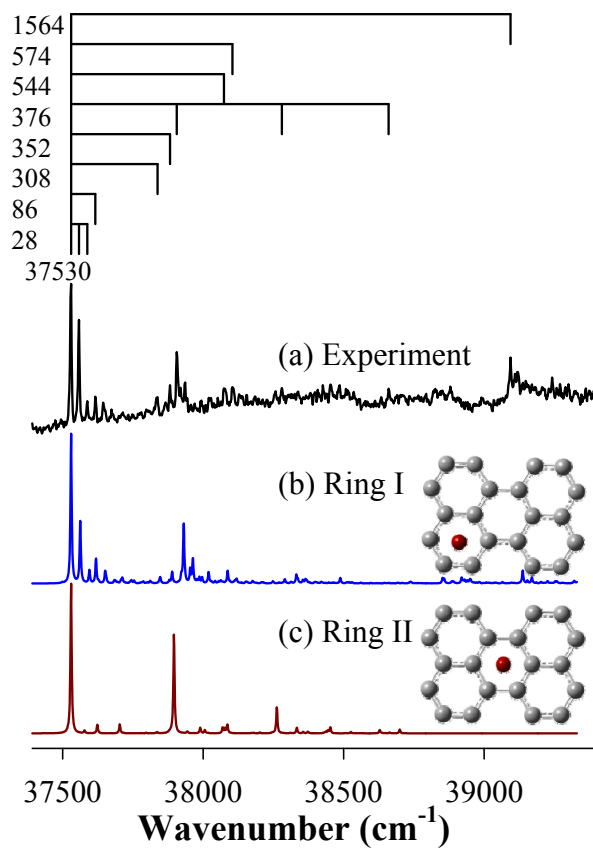
Figure 8. 4. The experimental spectrum (a) and simulations of the ring-I (b) and ring-II (c) structures of Li-perylene.
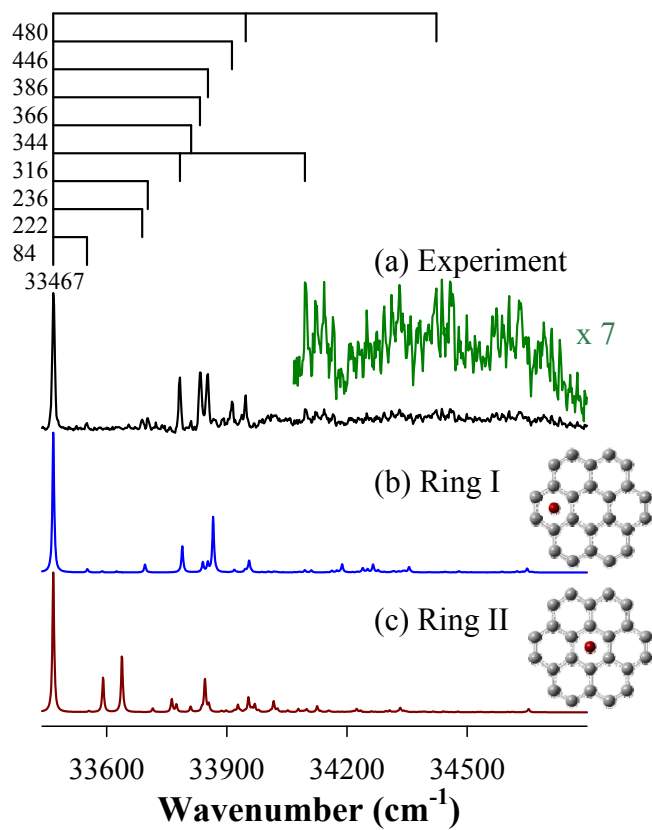
Figure 8. 5. The experimental spectrum (a) and simulations of the ring-I (b) and ring-II (c) structures of Li-coronene.
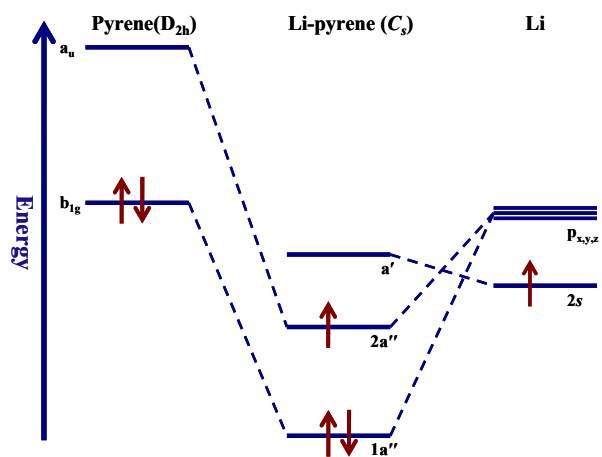
Figure 8. 6. An orbital interaction diagram between Li and pyrene.

CHAPTER 9. SUMMARY OF DISSERTATION

In this dissertation, the spectroscopic and computational studies of 19 different metal-aromatic and non-aromatic hydrocarbon complexes have been reported. From ZEKE spectroscopy, the IEs and metal-ligand stretching frequencies of these complexes were measured. The experimental spectra of the complexes were compared with the simulated spectra, and molecular structures and electronic states were determined. Based on the current study, different effects of metal coordination have been identified. In addition, several trends in the variation of the molecular structures, IEs, and electron spin multiplicities of metal-ligand complexes have been determined.

The COT molecule is a nonaromatic molecule and has a tub-shaped structure. However, group III transition metal (Sc, Y, or La) coordination converts the structure of COT to a planar, aromatic structure. This conversion is induced by two electron donation from the metal to the COT partially filled π orbitals, making the ligand a dianion. The resulting metal complexes have low-spin doublet ground states. On the other hand, methylbenzene molecules (*p*-xylene, mesitylene, hexamethylbenzene) with a planar benzene ring fold into a boat-like shape due to differential Sc metal binding. Upon Sc coordination, π electrons are redistributed in a 1,4-diene fashion and the five degenerate *d* atomic orbitals spl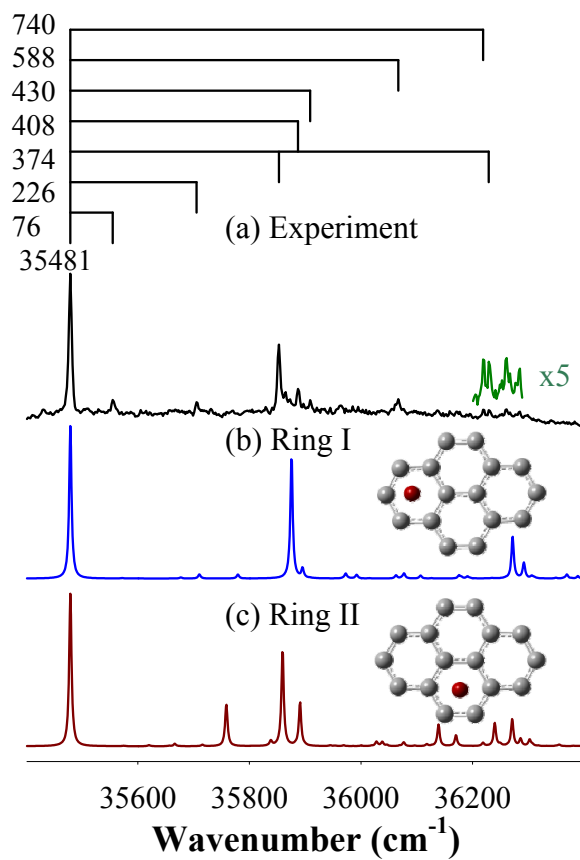it into nondegenerate orbitals. Therefore, the Sc-methylbenzene complexes exhibit low-spin doublet states, although Sc-benzene favors a high-spin quartet state. In addition, the IEs of these Sc complexes decrease with increasing number of the methyl groups on the benzene ring, and each methyl group decreases the IE by about 345 ± 88 cm^{-1}. In contrast, Ti, V, or Co coordination retains the delocalized π-electron network of the hexamethylbenzene ring and the metal complexes have high-spin electronic states. Group VI transition metal (Cr, Mo, or W)-bis(toluene) complexes exhibit four different rotational conformers with 0°, 60°, 120°, and 180° rotational angles between two methyl groups, and the 0° rotamer is the most stable one. For the biphenyl ligand, which has two equivalent benzene rings connected by a single C-C bond, the metal atom (Ti, Zr, or Hf) binds to both rings and the metal-biphenyl complexes adopt a clamshell structure. In addition, when two benzene rings are fused linearly (naphthalene), the metal binds to only one of the benzene rings. However, when the benzene rings are

fused nonlinearly as in pyrene, perylene, and coronene, metal favors the ring-over binding site of the benzene ring with a higher π electron content and aromaticity.

The electronic transitions, molecular symmetries, IEs, and metal-ligand stretching frequencies of the metal-cyclic hydrocarbon complexes reported in this dissertation are summarized in Table 9.1. The experimental IEs from ZEKE spectroscopy have an uncertainty of 5 cm^{-1}. The theoretical IEs are calculated by taking the energy difference between the ground electronic states of the neutral and ionic complexes with zero-point vibrational energy corrections. The calculated IE errors are about 7% for V-hexamethylbenzene complex and 0.4-4.4% for all other complexes. Overall, the B3LYP method provides quite good IE predictions on the metal-cyclic hydrocarbon complexes. More detailed trends of the molecular and electronic structures of the complexes have been described and discussed in each chapter.

Table 9. 1. Electronic transitions, molecular symmetries, the IEs (cm^{-1}) from the experiment and calculations, and metal-ligand stretching frequencies of the ionic complex (cm^{-1}) for the metal-cyclic hydrocarbon complexes presented in the dissertation.

Complex	Rotamer	Transition	Sym.	IE ZEKE[a]	IE Calc.[b]	M$^+$-L stretch ZEKE[a]	M$^+$-L stretch Calc.[b]
Sc-COT		$^1A_1 \leftarrow {}^2A_1$	C_{8v}	42263	43831	338	341
Y-COT[c]		$^1A_1 \leftarrow {}^2A_1$	C_{8v}	40749	41193	300	287
La-COT[c]		$^1A_1 \leftarrow {}^2A_1$	C_{8v}	36643	38254	278	263
Sc-benzene[d]		$^3A_1 \leftarrow {}^4A_1$	C_{6v}	41600	41618	375	336
Sc-toluene[e]		$^1A \leftarrow {}^2A$	C_1	41167	40802	378	378
Sc-(p-xylene)		$^1A \leftarrow {}^2A$	C_2	40770	40253	378	379
Sc-mesitylene		$^1A' \leftarrow {}^2A'$	C_s	40505	39998	378	375
Sc-hexamethylbenzene		$^1A_1 \leftarrow {}^2A_1$	C_{2v}	39535	38931	400	366
Ti-hexamethylbenzene		$^4A \leftarrow {}^5A$	C_1	38248	37244	356	347
V-hexamethylbenzene		$^5A \leftarrow {}^6A$	C_1	40364	37402	392	294
Co-hexamethylbenzene		$^3A'' \leftarrow {}^4A''$	C_s	40807	39290	359	341
Cr-bis(toluene)[c]	0°	$^2A_1 \leftarrow {}^1A_1$	C_{2v}	42807	43221	291	281
	60°	$^2A \leftarrow {}^1A$	C_2	42747	43189	274	265
	120°	$^2A \leftarrow {}^1A$	C_2	42747	43183	268	257
	180°	$^2A_g \leftarrow {}^1A_g$	C_{2h}	42741	43175	262	258
Mo-bis(toluene)[c]	0°	$^2A_1 \leftarrow {}^1A_1$	C_{2v}	43522	43309	294	277
	60°	$^2A \leftarrow {}^1A$	C_2	43448	43268	260	269
	120°	$^2A \leftarrow {}^1A$	C_2	43448	43271	260	266
	180°	$^2A_g \leftarrow {}^1A_g$	C_{2h}	43440	43259	268	266
W-bis(toluene)[c]	0°	$^2A_1 \leftarrow {}^1A_1$	C_{2v}	42655	42193	432	296
	60°	$^2A \leftarrow {}^1A$	C_2	42567	42107	386	288
	120°	$^2A \leftarrow {}^1A$	C_2	42567	42105	386	288
	180°	$^2A_g \leftarrow {}^1A_g$	C_{2h}	42567	42117	386	288
Ti-biphenyl[c]		$^2B_1 \leftarrow {}^1A_1$	C_{2v}	43845	41919	352	321
Zr-biphenyl[c]		$^2B_1 \leftarrow {}^1A_1$	C_{2v}	43343	41874	331	309
Hf-biphenyl[c]		$^2B_1 \leftarrow {}^1A_1$	C_{2v}	43752	42294	300	280
Li-naphthalene		$^1A' \leftarrow {}^2A'$	C_s	35491	36609	362	382
Li-pyrene		$^1A' \leftarrow {}^2A''$	C_s	35481	36457	374	399
Li-perylene		$^1A \leftarrow {}^2A$	C_1	37530	38409	376	404
Li-coronene		$^1A' \leftarrow {}^2A''$	C_s	33467	34193	386	402

[a]The uncertainty of IE values from the ZEKE measurements is about 5 cm^{-1}.
[b]The calculated values are carried out with B3LYP method with 6-311+G(d,p) basis set unless noted otherwise.
[c]The calculated values are carried out with B3LYP method with LanL2DZ basis set on metals and 6-311+G(d,p) basis set on C and H.
[d]From reference[60].
[e]From reference[145].

REFERENCES

(1)   Andres, R. P.; Averback, R. S.; Brown, W. L.; Brus, L. E.; Goddard, W. A.; Kaldor, A.; Louie, S. G.; Moscovits, M.; Peercy, P. S.; Riley, S. J.; Siegel, R. W.; Spaepen, F.; Wang, Y. *J. Mater. Res.* **1989**, *4*, 704.

(2)   Kumpf, R. A.; Dougherty, D. A. *Science* **1993**, *261*, 1708.

(3)   Ma, J. C.; Dougherty, D. A. *Chem. Rev.* **1997**, *97*, 1303.

(4)   Dougherty, D. A. *Science* **1996**, *271*, 163.

(5)   Cornils, B.; Herrmann, W. A. *Applied Homogeneous Catalysis with Organometallic Compounds*, 2nd ed.; Wiley-VCH: Weinheinm, 2002.

(6)   Collman, J. P.; Hegedus, L. S.; Norton, J. R.; Finke, R. G. *Principles and Applications of Organotransition Metal Chemistry*; University Science: Mill Valley, CA, 1987.

(7)   Kealy, T. J.; Pauson, P. L. *Nature* **1951**, *168*, 1039.

(8)   Miller, S. A.; Tebboth, J. A.; Tremaine, J. F. *J. Chem. Soc.* **1952**, 632.

(9)   Fischer, E. O.; Hafner, W. *Z. Naturforsch. B* **1955**, *10*, 665.

(10)   Timms, P. L.; King, R. B. *J. Chem. Soc. Chem. Comm.* **1978**, 898.

(11)   Eller, K.; Schwarz, H. *Chem. Rev.* **1991**, *91*, 1121.

(12)   Leary, J. A.; Armentrout, P. B. *Int. J. Mass Spectrom.* **2001**, *204*, Ix.

(13)   Turner, D. W.; Al-Jobory, M. I. *J. Chem. Phys.* **1962**, *37*, 3007.

(14)   Turner, D. W.; Baker, C.; Baker, A. D.; Brundle, C. R. *Molecular Photoelectron Spectroscopy*; Wiley Interscience: London, 1970.

(15)   Mueller-Dethlefs, K.; Sander, M.; Schlag, E. W. *Chem. Phys. Lett.* **1984**, *112*, 291.

(16)   Yang, D. S. *Coord. Chem. Rev.* **2001**, *214*, 187.

(17)   Freiser, B. S., Ed. *Organometallic Ion Chemistry*; Kluwer: Dordrecht, 1996.

(18)   Armentrout, P. B. *Int. J. Mass Spectrum* **2003**, *227*, 289.

(19)   Born, M.; Oppenheimer, J. R. *Ann. Phys.* **1927**, *79*, 361.

(20)   Moller, C.; Plesset, M. S. *Phys Rev* **1934**, *46*, 0618.

(21)   Kohn, W.; Sham, L. J. *Phys Rev* **1965**, *140*, 1133.

(22)   Becke, A. D. *J. Chem. Phys.* **1993**, *98*, 5648.

(23)   Lee, C.; Yang, W.; Parr, R. G. *Phys. Rev. B* **1988**, *37*, 785.

(24)   Perdew, J. P. *Phys. Rev. B* **1986**, *33*, 8822.

(25)   Perdew, J. P. *Phys. Rev. B* **1986**, *34*, 7406.

(26)   Franck, J. *Trans. Faraday Soc.* **1925**, *21*, 536.

(27)   Condon, E. *Phys. Rev.* **1926**, *28*, 1182.

(28)   Condon, E. *Phys. Rev.* **1928**, *32*, 858.

(29)   Duschinsky, F. *Acta Physicochimica URSS* **1937**, *7*, 551.

(30)   Sando, G. M.; Spears, K. G. *J. Phys. Chem. A* **2001**, *105*, 5326.

(31)   Hougen, J. T.; Watson, J. K. G. *Can. J. Chem.* **1965**, *43*, 298.

(32)   Eckart, C. *Phys. Rev.* **1935**, *47*, 552.

(33)   Sharp, T. E.; Rosenstock, H. M. *J. Chem. Phys.* **1964**, *41*, 3453.

(34)   Doktorov, E. V.; Malkin, I. A.; Man'ko, V. I. *J. Mol. Spectrosc.* **1977**, *64*, 302.

(35)   Hazra, A.; Nooijen, M. *Int. J. Quantum Chem.* **2003**, *95*, 643.

(36)   Faulkner, T. R.; Richardson, F. S. *J. Chem. Phys.* **1979**, *70*, 1201.

(37)   Kulander, K. C. *J. Chem. Phys.* **1979**, *71*, 2736.

(38)   Faulkner, T. R. *J. Chem. Phys.* **1979**, *71*, 2737.

(39)   Kupka, H.; Cribb, P. H. *J. Chem. Phys.* **1986**, *85*, 1303.

(40)   Subbi, J. *Chem. Phys.* **1988**, *122*, 157.

(41)   Roche, M. *Chem. Phys. Lett.* **1990**, *168*, 556.

(42)   Lerme, J. *Chem. Phys.* **1990**, *145*, 67.

(43)   Chen, P. *Unimolecular and Bimolecular Reaction Dynamics*; John Wiley & Sons: Chichester, 1994.

(44)   Ruhoff, P. T. *Chem. Phys.* **1994**, *186*, 355.

(45)   Mebel, A. M.; Chen, Y.-T.; Lin, S.-H. *J. Chem. Phys.* **1996**, *105*, 9007.

(46)   Malmqvist, P.-A.; Forsberg, N. *Chem. Phys.* **1998**, *228*, 227.

(47)   Islampour, R.; Dehestani, M.; Lin, S. H. *J. Mol. Spectrosc.* **1999**, *194*, 179.

(48)   Ruhoff, P. T.; Ratner, M. A. *Int. J. Quantum Chem.* **2000**, *77*, 383.

(49)   Toniolo, A.; Persico, M. *J. Comput. Chem.* **2001**, *22*, 968.

(50)   Kikuchi, H.; Kubo, M.; Watanabe, N.; Suzuki, H. *J. Chem. Phys.* **2003**, *119*, 729.

(51)   Shenggang, L. Threshold Photoionization and ZEKE Photoelectron Spectroscopy of Metal Complexes, University of Kentucky, 2004.

(52)   Yang, D. S.; Zgierski, M. Z.; Rayner, D. M.; Hackett, P. A.; Martinez, A.; Salahub, D. R.; Roy, P. N.; Carrington, T. *J. Chem. Phys.* **1995**, *103*, 5335.

(53)   Berces, A.; Zgierski, M. Z.; Yang, D. S. *Computational Molecular Spectroscopy*; Wiley: New York City, 2000.

(54)   Sohnlein, B. R.; Fuller, J. F.; Yang, D. S. *J. Am. Chem. Soc.* **2006**, *128*, 10692.

(55)   Proch, D.; Trickl, T. *Rev. Sci. Instrum.* **1989**, *60*, 713.

(56)   Sohnlein, B. R.; Yang, D. S. *J. Chem. Phys.* **2006**, *124*, 134305.

(57)   Moore, C. E. *Atomic Energy Levels*; National Bureau of Standards: Washington, DC, 1971.

(58)   Rothman, L. S.; Jacquemart, D.; Barbe, A.; Benner, D. C.; Birk, M.; Brown, L. R.; Carleer, M. R.; Chackerian, C.; Chance, K.; Coudert, L. H.; Dana, V.; Devi, V. M.; Flaud, J. M.; Gamache, R. R.; Goldman, A.; Hartmann, J. M.; Jucks, K. W.; Maki, A. G.; Mandin, J. Y.; Massie, S. T.; Orphal, J.; Perrin, A.; Rinsland, C. P.; Smith, M. A. H.; Tennyson, J.; Tolchenov, R. N.; Toth, R. A.; Vander Auwera, J.; Varanasi, P.; Wagner, G. *J. Quant. Spectrosc. Ra.* **2005**, *96*, 139.

(59)   Frisch, M. J.; Trucks, G. W.; Schlegel, H. B.; Scuseria, G. E.; Robb, M. A.; Cheeseman, J. R.; Montgomery, J., J. A.; Vreven, T.; Kudin, K. N.; Burant, J. C.; Millam, J. M.; Iyengar, S. S.; Tomasi, J.; Barone, V.; Mennucci, B.; Cossi, M.; Scalmani, G.; Rega, N.; Petersson, G. A.; Nakatsuji, H.; Hada, M.; Ehara, M.; Toyota, K.; Fukuda, R.; Hasegawa, J.; Ishida, M.; Nakajima, T.; Honda, Y.; Kitao, O.; Nakai, H.; Klene, M.; Li, X.; Knox, J. E.; Hratchian, H. P.; Cross, J. B.; Bakken, V.; Adamo, C.; Jaramillo, J.; Gomperts, R.; Stratmann, R. E.; Yazyev, O.; Austin, A. J.; Cammi, R.; Pomelli, C.; Ochterski, J. W.; Ayala, P. Y.; Morokuma, K.; Voth, G. A.; Salvador, P.; Dannenberg, J. J.; Zakrzewski, V. G.; Dapprich, S.; Daniels, A. D.; Strain, M. C.; Farkas, O.; Malick, D. K.; Rabuck, A. D.; Raghavachari, K.; Foresman, J. B.; Ortiz, J. V.; Cui, Q.; Baboul, A. G.;

Clifford, S.; Cioslowski, J.; Stefanov, B. B.; Liu, G.; Liashenko, A.; Piskorz, P.; Komaromi, I.; Martin, R. L.; Fox, D. J.; Keith, T.; Al-Laham, M. A.; Peng, C. Y.; Nanayakkara, A.; Challacombe, M.; Gill, P. M. W.; Johnson, B.; Chen, W.; Wong, M. W.; Gonzalez, C.; Pople, J. A. GAUSSIAN 03, Revision C.02; Gaussian, Inc: Wallingford, CT, 2004.

(60)   Sohnlein, B. R.; Li, S.; Yang, D. S. *J. Chem. Phys.* **2005**, *123*, 214306.

(61)   Sohnlein, B. R.; Lei, Y. X.; Yang, D. S. *J. Chem. Phys.* **2007**, *127*, 114302.

(62)   Hay, P. J.; Wadt, W. R. *J. Chem. Phys.* **1985**, *82*, 270.

(63)   Hay, P. J.; Wadt, W. R. *J. Chem. Phys.* **1985**, *82*, 299.

(64)   Wadt, W. R.; Hay, P. J. *J. Chem. Phys.* **1985**, *82*, 284.

(65)   Berces, A.; Zgierski, M. Z.; Yang, D.-S. *Computational Molecular Spectroscopy*; Wiley: New York, 2000.

(66)   Bastiansen, O.; Hedberg, L.; Hedberg, K. *J. Chem. Phys.* **1957**, *27*, 1311.

(67)   Traettebm, M. *Acta. Chem. Scand.* **1966**, *20*, 1724.

(68)   Claus, K. H.; Kruger, C. *Acta Crystallogr. C* **1988**, *44*, 1632.

(69)   Fray, G. I.; Saxton, R. G. *The Chemistry of Cyclooctatetraene and Its Derivatives*; Cambridge University Press: New York, 1978.

(70)   Wenthold, P. G.; Hrovat, D. A.; Borden, W. T.; Lineberger, W. C. *Science* **1996**, *272*, 1456.

(71)   Miller, T. M.; Viggiano, A. A.; Miller, A. E. S. *J. Phys. Chem. A* **2002**, *106*, 10200.

(72)   Hammons, J. H.; Hrovat, D. A.; Borden, W. T. *J. Am. Chem. Soc.* **1991**, *113*, 4500.

(73)   Karadakov, P. B. *J. Phys. Chem. A* **2008**, *112*, 12707.

(74)   Andres, J. L.; Castano, O.; Morreale, A.; Palmeiro, R.; Gomperts, R. *J. Chem. Phys.* **1998**, *108*, 203.

(75)   Baik, M. H.; Schauer, C. K.; Ziegler, T. *J. Am. Chem. Soc.* **2002**, *124*, 11167.

(76)   Frutos, L. M.; Castano, O.; Merchan, M. *J. Phys. Chem. A* **2003**, *107*, 5472.

(77)   Streitwieser, A.; Dempf, D.; Lamar, G. N.; Karraker, D. G.; Edelstein, N. *J. Am. Chem. Soc.* **1971**, *93*, 7343.

(78)   Streitwieser, A.; Muller-Westerhoff, U. *J. Am. Chem. Soc.* **1968**, *90*, 7364.

(79)   Streitwieser, A.; Muller-Westerhoff, U.; Sonnichsen, G.; Mares, F.; Morrell, D. G.; Hodgson, K. O.; Harmon, C. A. *J. Am. Chem. Soc.* **1973**, *95*, 8644.

(80)   Avdeef, A.; Zalkin, A.; Raymond, K. N.; Hodgson, K. O. *Inorg. Chem.* **1972**, *11*, 1083.

(81)   Karraker, D. G.; Stone, J. A.; Jones, E. R.; Edelstein, N. *J. Am. Chem. Soc.* **1970**, *92*, 4841.

(82)   Hodgson, K. O.; Mares, F.; Starks, D. F.; Streitwieser, A. *J. Am. Chem. Soc.* **1973**, *95*, 8650.

(83)   Hodgson, K. O.; Raymond, K. N. *Inorg. Chem.* **1972**, *11*, 171.

(84)   Hodgson, K. O.; Raymond, K. N. *Inorg. Chem.* **1972**, *11*, 3030.

(85)   Rogers, D. M.; Wilson, S. R.; Girolami, G. S. *Organometallics* **1991**, *10*, 2419.

(86)   Brauer, D. J.; Kruer, C. *J. Organomet. Chem.* **1972**, *42*, 129.

(87)   Dietrich, H.; Soltwisch, M. *Angew. Chem. Int. Edit.* **1969**, *8*, 765.

(88)   Hosang, A.; Englert, U.; Lorenz, A.; Ruppli, U.; Salzer, A. *J. Organomet. Chem.* **1999**, *583*, 47.

(89)   Bachmann, B.; Heck, J.; Meyer, G.; Pebler, J.; Schleid, T. *Inorg. Chem.* **1992**, *31*, 607.

(90)   Bach, I.; Porschke, K. R.; Proft, B.; Goddard, R.; Kopiske, C.; Kruger, C.; Rufinska, A.; Seevogel, K. *J. Am. Chem. Soc.* **1997**, *119*, 3773.

(91)   Salcedo, R.; Martinez, A.; Sansores, L. E.; Gasque, L.; Garcia-Cruz, I. *J. Mol. Struc-Theochem* **2005**, *732*, 113.

(92)   Paquette, L. A. *Tetrahedron* **1975**, *31*, 2855.

(93)   Clark, J. P.; Green, J. C. *J. Chem. Soc. Dalton* **1977**, 505.

(94)   Nakajima, A.; Kaya, K. *J. Phys. Chem. A* **2000**, *104*, 176.

(95)   Miyajima, K.; Kurikawa, T.; Hashimoto, M.; Nakajima, A.; Kaya, K. *Chem. Phys. Lett.* **1999**, *306*, 256.

(96)   Kurikawa, T.; Negishi, Y.; Hayakawa, F.; Nagao, S.; Miyajima, K.; Nakajima, A.; Kaya, K. *Eur. Phys. J. D* **1999**, *9*, 283.

(97)   Kurikawa, T.; Negishi, Y.; Hayakawa, F.; Nagao, S.; Miyajima, K.; Nakajima, A.; Kaya, K. *J. Am. Chem. Soc.* **1998**, *120*, 11766.

(98)   Takegami, R.; Hosoya, N.; Suzumura, J.; Yada, K.; Nakajima, A.; Yabushita, S. *Chem. Phys. Lett.* **2005**, *403*, 169.

(99)   Takegami, R.; Hosoya, N.; Suzumura, J.; Nakajima, A.; Yabushita, S. *J. Phys. Chem. A* **2005**, *109*, 2476.

(100)   Hosoya, N.; Takegami, R.; Suzumura, J.; Yada, K.; Koyasu, K.; Miyajima, K.; Mitsui, M.; Knickelbein, M. B.; Yabushita, S.; Nakajima, A. *J. Phys. Chem. A* **2005**, *109*, 9.

(101)   Scott, A. C.; Foster, N. R.; Grieves, G. A.; Duncan, M. A. *Int. J. Mass Spectrom.* **2007**, *263*, 171.

(102)   Miyajima, K.; Knickelbein, M. B.; Nakajima, A. *J. Phys. Chem. A* **2008**, *112*, 366.

(103)   Jaeger, T. D.; Duncan, M. A. *J. Phys. Chem. A* **2004**, *108*, 11296.

(104)   Li, X.; Eustis, S. N.; Bowen, K. H.; Kandalam, A. *J. Chem. Phys.* **2008**, *129*, 124312.

(105)   Vass, G.; Sztaray, B.; Szepes, L. *J. Organomet. Chem.* **1998**, *560*, 7.

(106)   Liu, W. J.; Dolg, M.; Fulde, P. *Inorg. Chem.* **1998**, *37*, 1067.

(107)   Dolg, M.; Fulde, P.; Stoll, H.; Preuss, H.; Chang, A.; Pitzer, R. M. *Chem. Phys.* **1995**, *195*, 71.

(108)   Dolg, M.; Fulde, P.; Kuchle, W.; Neumann, C. S.; Stoll, H. *J. Chem. Phys.* **1991**, *94*, 3011.

(109)   Gong, Z.; Shen, H. Y.; Zhu, W. L.; Luo, X. M.; Chen, K. X.; Jiang, H. L. *Chem. Phys. Lett.* **2006**, *423*, 339.

(110)   He, L. Y.; Cheng, J. G.; Wang, T.; Li, C. M.; Gong, Z.; Liu, H.; Zeng, B. B.; Jiang, H. L.; Zhu, W. L. *Chem. Phys. Lett.* **2008**, *462*, 45.

(111)   Duncan, M. A.; Dietz, T. G.; Smalley, R. E. *J. Chem. Phys.* **1981**, *75*, 2118.

(112)   Krasnokutski, S. A.; Lei, Y. X.; Lee, J. S.; Yang, D. S. *J. Chem. Phys.* **2008**, *129*, 124309.

(113)   Fuller, J. F.; Li, S. G.; Sohnlein, B. R.; Rothschopf, G. K.; Yang, D. S. *Chem. Phys. Lett.* **2002**, *366*, 141.

(114)   Wang, X.; Lee, J. S.; Yang, D.-S. *J. Phys. Chem. A* **2006**, *110*, 12777.

(115)   Wang, X.; Lee, J. S.; Yang, D.-S. *J. Chem. Phys.* **2006**, *125*, 14309.

(116)   Krasnokutski, S. A.; Yang, D. S. *J. Chem. Phys.* **2009**, *130*, 134313.

(117)   Lide, D. R. *CRC Handbook of Chemistry and Physics*, 88 ed.; CRC Press: Boca Raton, 2008.

(118)   Batich, C.; Bischof, P.; Heilbronner, E. *J. Electron Spectrosc. Relat. Phenom.* **1972**, *1*, 333.

(119)   Cotton, F. A. *Chemical Applications of Group Theory*, 3rd ed.Wiley, New York, 1990.

(120)   Evans, S.; Green, J. C.; Jackson, S. E.; Higginson, B. *J. Chem. Soc. Dalton* **1974**, 304.

(121)   Frost, A. A.; Musulin, B. *J. Chem. Phys.* **1953**, *21*, 572.

(122)   Jun, C.-H. *Chem. Soc. Rev.* **2004**, *33*, 610.

(123)   Jones, W. D.; Feher, F. J. *J. Am. Chem. Soc* **1982**, *104*, 4240.

(124)   Jones, W. D.; Feher, F. J. *J. Am. Chem. Soc* **1984**, *104*, 4240.

(125)   Muetterties, E. L.; Bleeke, J. R. *Acc. Chem. Res.* **1979**, *12*, 324.

(126)   Bleeke, J. R.; Muetterties, E. L. *J. Am. Chem. Soc* **1981**, *103*, 556.

(127)   Steffey, B. D.; Chesnut, R. W.; Kerschner, J. L.; Pellechia, P. J.; Fanwick, P. E.; Rothwell, I. P. *J. Am. Chem. Soc* **1989**, *111*, 378.

(128)   Duncan, M. A. *Int. J. Mass Spectrom.* **2008**, *272*, 99.

(129)   Lyon, J. T.; Andrews, L. *J. Phys. Chem. A* **2005**, *109*, 431.

(130)   Miller, S. R.; Marcy, T. P.; Millam, E. L.; Leopold, D. G. *J. Am. Chem. Soc.* **2007**, *129*, 3482.

(131)   Lyon, J. T.; Andrews, L. *J. Phys. Chem. A.* **2006**, *110*, 7806.

(132)   Jaeger, T. D.; van Heijnsbergen, D.; Klippenstein, S. J.; von Helden, G.; Meijer, G.; Duncan, M. A. *J. Am. Chem. Soc.* **2004**, *126*, 10981.

(133)   Kambalapalli, S.; Ortiz, J. V. *J. Phys. Chem. A* **2004**, *108*, 2988.

(134)   Domenicano, A.; Schultz, G.; Kolonits, M.; Hargittai, I. *J. Mol. Struct.* **1979**, *53*, 179.

(135)   Almenningen, A.; Hargittai, I.; Samdal, S.; Brunvoll, J.; Domenicano, A.; Lowrey, A. *J. Mol. Struct.* **1983**, *96*, 373.

(136)   Hamilton, W. C.; Edmonds, J. W.; Tippe, A.; Rush, J. J. *Discuss. Faraday. Soc.* **1969**, 192.

(137)   Maverick, E.; Trueblood, K. N.; Bekoe, D. A. *Acta Crystallogr. B* **1978**, *34*, 2777.

(138)   Melissas, V.; Faegri, K.; Almlof, J. *J. Am. Chem. Soc.* **1985**, *107*, 4640.

(139)   Ibberson, R. M.; David, W. I. F.; Parsons, S.; Prager, M.; Shankland, K. *J. Mol. Struct.* **2000**, *524*, 121.

(140)   Rothmana, L. S.; Jacquemarta, D.; Barbeb, A.; Bennerc, C. D.; Birkd, M.; Browne, L. R.; Carleerf, M. R.; Chackerian, J., C. ; Chancea, G. K.; Couderth, L. H.; Danai, V.; Devic, V. M.; Flaudh, J.-M.; Gamachej, R. R.; Goldmank, A.; Hartmannh, J.-M.; Jucksl, K. W.; Makim, A. G.; Mandini, J.-Y.; Massien, S. T.; Orphalh, J.; Perrinh, A.; Rinslando, C. P.; Smitho, M. A. H.; Tennysonp, J.; Tolchenovp, R. N.; Tothe, R. A.;

Auweraf, J. V.; Varanasiq, P.; Wagnerd, G. *J. Quant. Spectrosc. Radiat. Transfer* **2005**, *96*, 139.

(141) Arney, D. J.; Wexler, P. A.; Wigley, D. E. *Organometallics* **1990**, *9*, 1282.

(142) Oberhammer, H.; Bauer, S. H. *J. Am. Chem. Soc.* **1969**, *91*, 10.

(143) Dallinga, G.; Toneman, L. H. *J. Mol. Struct.* **1967**, *1*, 117.

(144) Jeffrey, G. A.; Buschmann, J.; Lehmann, C. W.; Luger, P. *J. Am. Chem. Soc.* **1988**, *110*, 7218.

(145) Zhang, C. H.; Krasnokutski, S. A.; Zhang, B.; Yang, D. S. *J. Chem. Phys.* **2009**, *131*, 054303.

(146) Ebata, T.; Suzuki, Y.; Mikami, N.; Miyashi, T.; Ito, M. *Chem. Phys. Lett.* **1984**, *110*, 597.

(147) Blease, T. G.; Donovan, R. J.; Langridgesmith, P. R. R.; Ridley, T. *Laser Chem.* **1988**, *9*, 241.

(148) Walter, K.; Scherm, K.; Boesl, U. *Chem. Phys. Lett.* **1989**, *161*, 473.

(149) Held, A.; Selzle, H. L.; Schlag, E. W. *J. Phys. Chem. A* **1998**, *102*, 9625.

(150) Gunzer, F.; Grotemeyer, J. *Phys. Chem. Chem. Phys.* **2002**, *4*, 5966.

(151) Gunzer, F.; Grotemeyer, J. *Int. J. Mass Spectrom.* **2003**, *228*, 921.

(152) NIST Standard Reference Database 69 In *NIST Standard Reference Database 69*; http://webbook.nist.gov/chemistry/, 2009.

(153) Jaeger, T. D.; Pillai, E. D.; Duncan, M. A. *J. Phys. Chem. A* **2004**, *108*, 6605.

(154) Jaeger, J. B.; Pillai, E. D.; Jaeger, T. D.; Duncan, M. A. *J. Phys. Chem. A* **2005**, *109*, 2801.

(155) Jaeger, T. D.; Duncan, M. A. *J. Phys. Chem. A* **2005**, *109*, 3311.

(156) Imura, K.; Ohoyama, H.; Kasai, T. *Chem. Phys. Lett.* **2003**, *369*, 55.

(157) Lyon, J. T.; Andrews, L. *J. Phys. Chem. A* **2006**, *110*, 7806.

(158) Andrews, M. P.; Huber, H. X.; Mattar, S. M.; Mcintosh, D. F.; Ozin, G. A. *J. Am. Chem. Soc.* **1983**, *105*, 6170.

(159) Andrews, M. P.; Mattar, S. M.; Ozin, G. A. *J. Phys. Chem.* **1986**, *90*, 744.

(160) van Heijnsbergen, D.; von Helden, G.; Meijer, G.; Maitre, P.; Duncan, M. A. *J. Am. Chem. Soc.* **2002**, *124*, 1562.

(161) Li, H. Y.; Li, C. P.; Fan, H. W.; Yang, J. C. *J. Mol. Struc-Theochem* **2010**, *952*, 67.

(162) Pandey, R.; Rao, B. K.; Jena, P.; Blanco, M. A. *J. Am. Chem. Soc.* **2001**, *123*, 3799.

(163) Bauschlicher, C. W.; Partridge, H.; Langhoff, S. R. *J. Phys. Chem.* **1992**, *96*, 3273.

(164) Ouhlal, A.; Selmani, A.; Yelon, A. *Chem. Phys. Lett.* **1995**, *243*, 269.

(165) Yang, C. N.; Klippenstein, S. J. *J. Phys. Chem. A* **1999**, *103*, 1094.

(166) Klippenstein, S. J.; Yang, C. N. *Int. J. Mass Spectrom.* **2000**, *201*, 253.

(167) Kandalam, A. K.; Rao, B. K.; Jena, P.; Pandey, R. *J. Chem. Phys.* **2004**, *120*, 10414.

(168) Zhang, X. Y.; Wang, J. L. *J. Phys. Chem. A* **2008**, *112*, 296.

(169) Fischer, E. O.; Elschenbroich, C. *Chem Ber-Recl* **1970**, *103*, 162.

(170) Huttner, G.; Lang, S.; Fischer, E. O. *Angew. Chem. Int. Edit.* **1971**, *10*, 556.

(171) Huttner, G.; Lange, S. *Acta Crystall. B-Stru* **1972**, *B 28*, 2049.

(172) Bruck, M. A.; Copenhaver, A. S.; Wigley, D. E. *J. Am. Chem. Soc.* **1987**, *109*, 6525.

(173) Churchill, M. R.; Chang, S. W. Y. *J. Chem. Soc. Chem. Comm.* **1974**, 248.

(174) Goldberg, S. Z.; Stanley, G.; Spivack, B.; Eisenberg, R.; Braitsch, D. M.; Miller, J. S. *Abstr Pap Am Chem S* **1977**, *174*, 14.

(175) Albano, P.; Aresta, M.; Manassero, M. *Inorg. Chem.* **1980**, *19*, 1069.

(176) Schmid, H.; Ziegler, M. L. *Chem Ber-Recl* **1976**, *109*, 132.

(177) Solari, E.; Floriani, C.; Chiesivilla, A.; Guastini, C. *J. Chem. Soc. Chem. Comm.* **1989**, 1747.

(178) Fischer, E. O.; Lindner, H. H. *J. Organomet. Chem.* **1964**, *2*, 222.

(179) Fischer, E. O.; Lindner, H. H. *J. Organomet. Chem.* **1963**, *1*, 307.

(180) Ohare, D.; Raichaudhuri, A.; Murphy, V. *J. Chem. Soc. Dalton* **1993**, 3071.

(181) Thompson, M. R.; Day, C. S.; Day, V. W.; Mink, R. I.; Muetterties, E. L. *J. Am. Chem. Soc.* **1980**, *102*, 2979.

(182) Anderson, S. E.; Drago, R. S. *J. Am. Chem. Soc.* **1970**, *92*, 4244.

(183) NIST Standard Reference Database 69. http://webbook.nist.gov/chemistry/ (accessed 2009).

(184) Kruszewski, J.; Krygowski, T. M. *Tetrahedron Lett* **1972**, 3839.

(185) Krygowski, T. M. *J. Chem. Inf. Comput. Sci.* **1993**, *33*, 70.

(186) Krygowski, T. M.; Cyranski, M. K. *Chem. Rev.* **2001**, *101*, 1385.

(187) Schleyer, P. v. R. *Chem. Rev.* **2001**, *101*, 1115.

(188) Lide, D. R.; Frederikse, H. P. R. *CRC Handbook of Chemistry and Physics*, 78th ed.; CRC: New York, 1997.

(189) Sawka-Dobrowolska, W.; Bator, G.; Sobczyk, L.; Pawlukojc, A.; Ptasiewicz-Bak, H.; Rundlof, H.; Krawczyk, J.; Nowina-Konopka, M.; Jagielski, P.; Janik, J. A.; Prager, M.; Steinsvoll, O.; Grech, E.; Nowicka-Scheibe, J. *J. Chem. Phys.* **2005**, *123*.

(190) NIST Atomic Spectra Database. http://physics.nist.gov/PhysRefData/ASD/ (accessed 2010).

(191) Sohnlein, B. R. PFI-ZEKE Spectroscopy and Theoretical Calculations of Transition Metal-Aromatic Hydrocarbon Complexes, University of Kentucky, 2007.

(192) Eller, K.; Schwarz, H. *Chem. Rev.* **1991**, *91*, 1121.

(193) Pignataro, S.; Lossing, F. P. *J. Organomet. Chem.* **1967**, *10*, 531.

(194) Mueller, J.; Goeser, P. *J. Organomet. Chem.* **1968**, *12*, 163.

(195) Herberich, G. E.; Mueller, J. *J. Organomet. Chem.* **1969**, *16*, 111.

(196) Evans, S.; Green, J. C.; Jackson, S. E. *J. Chem. Soc., Faraday Trans. 2: Mol. Chem. Phys.* **1972**, *68*, 249.

(197) Guest, M. F.; Hillier, I. H.; Higginson, B. R.; Lloyd, D. R. *Mol. Phys.* **1975**, *29*, 113.

(198) Cabelli, D. E.; Cowley, A. H.; Lagowski, J. J. *Inorg. Chim. Acta* **1982**, *57*, 195.

(199) Chizhov, Y. V.; Timoshenko, M. M.; Yur'eva, L. P.; Zaitseva, N. N.; Uralets, I. A.; Kravtsov, D. N.; Asfandiarov, N. L. *J. Organomet. Chem.* **1989**, *361*, 79.

(200) Ryan, M. F.; Richardson, D. E.; Lichtenberger, D. L.; Gruhn, N. E. *Organometallics* **1994**, *13*, 1190.

(201)   Evans, S.; Green, J. C.; Jackson, S. E.; Higginson, B. *J. Chem. Soc., Chem. Commun., Dalton Trans: Inorg. Chem.* **1974**, 304.

(202)   Cloke, F. G. N.; Dix, A. N.; Green, J. C.; Perutz, R. N.; Seddon, E. A. *Organometallics* **1983**, *2*, 1150.

(203)   Meyer, F.; Khan, F. A.; Armentrout, P. B. *J. Am. Chem. Soc.* **1995**, *117*, 9740.

(204)   Lin, C.-Y.; Dunbar, R. C. *Organometallics* **1997**, *16*, 2691.

(205)   Penner, A.; Amirav, A.; Tasaki, S.; Bersohn, R. *J. Chem. Phys.* **1993**, *99*, 176.

(206)   Even, U.; Levine, R. D.; Bersohn, R. *J. Phys. Chem.* **1994**, *98*, 3472.

(207)   Ketkov, S. Y.; Mehnert, C.; Green, J. C. *Chem. Phys.* **1996**, *203*, 245.

(208)   Ketkov, S. Y.; Green, J. C.; Mehnert, C. P. *J. Chem. Soc., Faraday. Trans.* **1997**, *93*, 2461.

(209)   Kurikawa, T.; Takeda, H.; Hirano, M.; Judai, K.; Arita, T.; Nagao, S.; Nakajima, A.; Kaya, K. *Organometallics* **1999**, *18*, 1430.

(210)   Ketkov, S. Y.; Selzle, H. L.; Schlag, E. W.; Domrachev, G. A. *Chem. Phys. Lett.* **2003**, *373*, 486.

(211)   Ketkov, S. Y.; Selzle, H. L.; Schlag, E. W. *J. Chem. Phys.* **2004**, *121*, 149.

(212)   Li, Y.; Baer, T. *J. Phys. Chem. A* **2002**, *106*, 9820.

(213)   Choi, K.-W.; Kim, S. K.; Ahn, D.-S.; Lee, S. *J. Phys. Chem. A* **2004**, *108*, 11292.

(214)   Ketkov, S. Y.; Selzle, H. L.; Schlag, E. W. *Isr. J. Chem.* **2004**, *44*, 65.

(215)   Choi, K. W.; Choi, S.; Baek, S. J.; Kim, S. K. *J. Chem. Phys.* **2007**, *126*, 034308.

(216)   Choi, K. W.; Choi, S.; Ahn, D. S.; Han, S.; Kang, T. Y.; Baek, S. J.; Kim, S. K. *J. Phys. Chem. A* **2008**, *112*, 7125.

(217)   Judai, K.; Nakamura, Y.; Tachibana, M.; Negishi, Y.; Nakajima, A.; Kaya, K. *Chemistry Letters* **2001**, *30*, 114.

(218)   Smith, M. B.; March, J. *March's Advanced Organic Chemistry: Reactions, Mechanisms, and Structures*, 5th ed.; Wiley: New York, 2001.

(219)   Mazurek, U.; Schwarz, H. *Chem. Commun.* **2003**, 1321.

(220)   Caraiman, D.; Koyanagi, G. K.; Bohme, D. K. *J. Phys. Chem. A* **2004**, *108*, 978.

(221)   Forest, H.; Dailley, B. P. *J. Chem. Phys.* **1966**, *45*, 1736.

(222)   Pedersen, T.; Larsen, N. W.; Nygaard, L. *J. Mol. Struct.* **1969**, *4*, 59.

(223)   Mathier, E.; Welti, D.; Bauder, A.; Gunthard, H. H. *J. Mol. Spectry.* **1971**, *37*, 63.

(224)   Larsen, N. W.; Nicolaisen, F. M. *J. Mol. Struct.* **1974**, *22*, 29.

(225)   Gloriozov, I. P.; Vasil'kov, A. Y.; Ustynyuk, Y. A. *Russ. J. Phys. Ch.* **2006**, *80*, 394.

(226)   Ketkov, S. Y.; Domrachev, G. A.; Mehnert, C. P.; Green, J. C. *Russ. Chem. Bull.* **1998**, *47*, 868.

(227)   Ketkov, S. Y.; Sezle, H. L.; Cloke, F. G. N. *Angew. Chem. Int. Edit.* **2007**, *46*, 7072.

(228)   Calucci, L.; Englert, U.; Grigiotti, E.; Laschi, F.; Pampaloni, G.; Pinzino, C.; Volpe, M.; Zanello, P. *J. Organomet. Chem.* **2006**, *691*, 829.

(229)   Braga, D.; Costa, A. L.; Grepioni, F.; Scaccianoce, L.; Tagliavini, E. *Organometallics* **1997**, *16*, 2070.

(230)   Kohn, R. D.; Smith, D.; Mahon, M. F.; Prinz, M.; Mihan, S.; Kociok-Kohn, G. *J. Organomet. Chem.* **2003**, *683*, 200.

(231)   Benetollo, F.; Grigiotti, E.; Laschi, F.; Pampaloni, G.; Volpe, M.; Zanello, P. *J Solid State Electr* **2005**, *9*, 732.

(232)   Calderazzo, F.; Englert, U.; Pampaloni, G.; Volpe, M. *J. Organomet. Chem.* **2005**, *690*, 3321.

(233)   Pophristic, V.; Goodman, L. *Nature* **2001**, *411*, 565.

(234)   Weinhold, F. *Nature* **2001**, *411*, 539.

(235)   Schreiner, P. R. *Angew. Chem. Int. Ed. Engl.* **2002**, *41*, 3579.

(236)   Ruoff, R. S.; Klots, T. D.; Emilsson, T.; Gutowsky, H. S. *J. Chem. Phys.* **1990**, *93*, 3142.

(237)   Godfrey, P. D.; Brown, R. D. *J. Am. Chem. Soc.* **1998**, *120*, 10724.

(238)   Potts, A. R.; Baer, T. *J. Chem. Phys.* **1998**, *108*, 869.

(239)   Pitts, J. D.; Knee, J. L.; Wategaonkar, S. *J. Chem. Phys.* **1999**, *110*, 3378.

(240)   Kim, D.; Baer, T. *Chem. Phys.* **2000**, *256*, 251.

(241)   Florio, G. M.; Christie, R. A.; Jordan, K. D.; Zwier, T. S. *J. Am. Chem. Soc.* **2002**, *124*, 10236.

(242)   Zwier, T. S. *J. Phys. Chem. A* **2006**, *110,* 4133.

(243)   Ross, R. B.; Powers, J. M.; Atashroo, T.; Ermler, W. C.; LaJohn, L. A.; Christiansen, P. A. *J. Chem. Phys.* **1990**, *93*, 6654.

(244)   Connor, J. A.; Elsaied, N. I.; Martinhosimoes, J. A.; Skinner, H. A. *J. Organomet. Chem.* **1981**, *212*, 405.

(245)   Lin, C. Y.; Dunbar, R. C. *Organometallics* **1997**, *16*, 2691.

(246)   Almenningen, A.; Bastiansen, O.; Fernholt, L.; Cyvin, B. N.; Cyvin, S. J.; Samdal, S. *J. Mol. Struct. (THOCHEM)* **1985**, *128*, 59.

(247)   Tsuzuki, S.; Tanabe, K. *J. Phys. Chem.* **1991**, *95*, 139.

(248)   Karpfen, A.; Choi, C. H.; Kertesz, M. *J. Phys. Chem. A* **1997**, *101*, 7426.

(249)   Rubio, M.; Merchan, M.; Orti, E. *Theoretica Chimica Acta* **1995**, *91*, 17.

(250)   Arulmozhiraja, S.; Fujii, T. *J. Chem. Phys.* **2001**, *115*, 10589.

(251)   Tsuzuki, S.; Uchimaru, T.; Matsumura, K.; Mikami, M.; Tanabe, K. *J. Chem. Phys.* **1999**, *110*, 2858.

(252)   Grein, F. *J. Phys. Chem. A* **2002**, *106*, 3823.

(253)   Goller, A.; Grummt, U. W. *Chem. Phys. Lett.* **2000**, *321*, 399.

(254)   Charbonneau, G. P.; Delugeard, Y. *Acta Crystallogr. B* **1976**, *32*, 1420.

(255)   Hochstrasser, R. M.; McAlpine, R. D.; Whiteman, J. D. *J. Chem. Phys.* **1973**, *58*, 5078.

(256)   Charbonneau, G. P.; Delugeard, Y. *Acta Crystallogr. B* **1977**, *33*, 1586.

(257)   Ecolivet, C.; Sanquer, M.; Pellegrin, J.; Dewitte, J. *J. Chem. Phys.* **1983**, *78*, 6317.

(258)   Launois, P.; Moussa, F.; Lemeecailleau, M. H.; Cailleau, H. *Phys. Rev. B* **1989**, *40*, 5042.

(259)   Veron, A.; Emery, J.; Lariguillet, F. *J. Phys. C: Solid State* **1995**, *56*, 51.

(260)   Lemeecailleau, M. H.; Girard, A.; Cailleau, H.; Delugeard, Y. *Phys. Rev. B* **1992**, *45*, 12682.

(261)   Barrett, R. M.; Steele, D. *J. Mol. Struct.* **1972**, *11*, 105.

(262)   Bastiansen, O.; Samdal, S. *J. Mol. Struct.* **1985**, *128*, 115.

(263)   Suzuki, H. *Bull. Chem. Soc. Jpn.* **1959**, *32*, 1340.

(264)   Porter, L. C.; Bodige, S.; Selnau, H. E.; Murray, H. H. I.; McConnachie, J. M. *Organometallics* **1995**, *14*, 4222.

(265)   Elschenbroich, C.; Heck, J. *J. Am. Chem. Soc.* **1979**, *101*, 6773.

(266)   Philpott, M. R.; Kawazoe, Y. *J. Phys. Chem. A* **2008**, *112*, 2034.

(267)   Becke, A. D. *Phys. Rev. A* **1988**, *38*, 3098.

(268)   Perdew, J. P.; Wang, Y. *Phys. Rev. B* **1992**, *45*, 13244.

(269)   GAUSSIAN 03, Revision C. 02; Gaussian, Inc.: Pittsburgh, 2004.

(270)   King, W. A.; DiBella, S.; Lanza, G.; Khan, K.; Duncalf, D. J.; Cloke, F. G. N.; Fragala, I. L.; Marks, T. J. *J. Am. Chem. Soc.* **1996**, *118*, 627.

(271)   Sohnlein, B. R.; Li, S. G.; Fuller, J. F.; Yang, D. S. *J. Chem. Phys.* **2005**, *123*, 014318.

(272)   Yang, D. S.; Zgierski, M. Z.; Hackett, P. A. *J. Chem. Phys.* **1998**, *108*, 3591.

(273)   Yang, D. S.; Zgierski, M. Z.; Berces, A.; Hackett, P. A.; Roy, P. N.; Martinez, A.; Carrington, T.; Salahub, D. R.; Fournier, R.; Pang, T.; Chen, C. F. *J. Chem. Phys.* **1996**, *105*, 10663.

(274)   Kaskhedikar, N. A.; Maier, J. *Adv. Mater.* **2009**, *21*, 2664.

(275)   Ayalon, A.; Sygula, A.; Cheng, P. C.; Rabinovitz, M.; Rabideau, P. W.; Scott, L. T. *Science* **1994**, *265*, 1065.

(276)   Sato, K.; Noguchi, M.; Demachi, A.; Oki, N.; Endo, M. *Science* **1994**, *264*, 556.

(277)   Dahn, J. R.; Zheng, T.; Liu, Y. H.; Xue, J. S. *Science* **1995**, *270*, 590.

(278)   Papanek, P.; Radosavljevic, M.; Fischer, J. E. *Chem. Mater.* **1996**, *8*, 1519.

(279)   Ago, H.; Kato, M.; Yahara, K.; Yoshizawa, K.; Tanaka, K.; Yamabe, T. *J. Electrochem. Soc.* **1999**, *146*, 1262.

(280)   Ishikawa, S.; Madjarova, G.; Yamabe, T. *J. Phys. Chem. B* **2001**, *105*, 11986.

(281)   Zhu, Z. H.; Lu, G. Q. *Langmuir* **2004**, *20*, 10751.

(282)   Martinez, J. I.; Cabria, I.; Lopez, M. J.; Alonso, J. A. *J. Phys. Chem. C* **2009**, *113*, 939.

(283)   Baker, T. A.; Head-Gordon, M. *J. Phys. Chem. A* **2010**, *10.1021/jp105864v*.

(284)   Gal, J.-F.; Maria, P.-C.; Decouzon, M.; Mo, O.; Yanez, M.; Abboud, J. L. M. *J. Am. Chem. Soc.* **2003**, *125*, 10394.

(285)   Guell, M.; Poater, J.; Luis, J. M.; Mo, O.; Yanez, M.; Sola, M. *Chemphyschem* **2005**, *6*, 2552.

(286)   Ago, H.; Nagata, K.; Yoshizawa, K.; Tanaka, K.; Yamabe, T. *Bull. Chem. Soc. Jpn.* **1997**, *70*, 1717.

(287)   Morton-Blake, D. A.; Corish, J.; Beniere, F. *Theoretica Chimica Acta* **1985**, *68*, 389.

(288)   Bahn, C. S.; Lauderdale, W. J.; Carlin, R. T. *Int. J. Quantum Chem* **1995**, 533.

(289)   Frash, M. V.; Hopkinson, A. C.; Bohme, D. K. *J. Am. Chem. Soc.* **2001**, *123*, 6687.

(290)   Kang, H. S. *J. Phys. Chem. A* **2005**, *109*, 478.

(291)   Valencia, F.; Romero, A. H.; Ancilotto, F.; Silvestrelli, P. L. *J. Phys. Chem. B* **2006**, *110*, 14832.

(292)   Ferre-Vilaplana, A. *J. Phys. Chem. C* **2008**, *112*, 3998.

(293)   Amunugama, R.; Rodgers, M. T. *Int. J. Mass spectrom.* **2003**, *227*, 1.

(294)   Yang, D.-S.; Zgierski, M. Z.; Rayner, D. M.; Hackett, P. A.; Martinez, A.; Salahub, D. R.; Roy, P.-N.; Carrington, T., Jr. *J. Chem. Phys.* **1995**, *103*, 5335.

(295)   Zhang, K.; Guo, B.; Colarusso, P.; Bernath, P. F. *Science* **1996**, *274*, 582.

(296)   Szczepanski, J.; Vala, M. *Astrophys. J.* **1993**, *414*, 646.

(297)   Beck, S. M.; Powers, D. E.; Hopkins, J. B.; Smalley, R. E. *J. Chem. Phys.* **1980**, *73*, 2019.

(298)   Stockburger, M.; Gattermann, H.; Klusmann, W. *J. Chem. Phys.* **1975**, *63*, 4519.

(299)   Szczepanski, J.; Wang, H. Y.; Vala, M.; Tielens, A. G. G. M.; Eyler, J. R.; Oomens, J. *Astrophys. J.* **2006**, *646*, 666.

(300)   Balaban, A. T.; Durdevic, J.; Gutman, I.; Jeremic, S.; Radenkovic, S. *J. Phys. Chem. A* **2010**, *114*, 5870.

(301)   Randic, M. *Chem. Rev.* **2003**, *103*, 3449.

(302)   Balaban, A. T.; Randic, M. *New J. Chem.* **2004**, *28*, 800.

(303)   Schleyer, P. v. R. *Chem. Rev.* **2001**, *101*, 1115.

(304)   Amicangelo, J. C.; Armentrout, P. B. *J. Phys. Chem. A* **2000**, *104*, 11420.

(305)   Ma, J. C.; Dougherty, D. A. *Chem. Rev.* **1997**, *97*, 1303.

(306)   Cubero, E.; Luque, F. J.; Orozco, M. *Proc. Natl. Acad. Sci. U.S.A.* **1998**, *95*, 5976.

(307)   Kim, K. S.; Tarakeshwar, P.; Lee, J. Y. *Chem. Rev.* **2000**, *100*, 4145.

(308)   Battaglia, M. R.; Buckingham, A. D.; Williams, J. H. *Chem. Phys. Lett.* **1981**, *78*, 420.

(309)   Calvert, R. L.; Ritchie, G. L. D. *J. Chem. Soc., Faraday Trans. 2* **1980**, *76*, 1249.

(310)   Kamisuki, T.; Moriyama, I.; Igarashi, R.; Adachi, Y.; Maeda, S. *J. Chem. Phys.* **1980**, *73*, 3500.

(311)   Vala, M.; Szczepanski, J.; Pauzat, F.; Parisel, O.; Talbi, D.; Ellinger, Y. *J. Phys. Chem.* **1994**, *98*, 9187.

(312)   Joblin, C.; Dhendecourt, L.; Leger, A.; Defourneau, D. *Astron. Astrophys.* **1994**, *281*, 923.

(313)   Fourmann, B.; Jouvet, C.; Tramer, A.; Lebars, J. M.; Millie, P. *Chem. Phys.* **1985**, *92*, 25.

(314)   Tan, X.; Salama, F. *J. Chem. Phys.* **2005**, *122*, 084318.

(315)   Yoshizawa, K.; Okahara, K.; Sato, T.; Tanaka, K.; Yamabe, T. *Carbon* **1994**, *32*, 1517.

(316)   Babkov, L. M.; Glyadkovskii, V. I.; Davydova, N. I.; Karpova, V. A.; Klimova, L. A.; Kovner, M. A.; Sushchinskii, M. M.; Terekhov, A. A.; Shpolskii, E. V. *Opt Spektrosk.* **1973**, *34*, 70.

(317)   Babkov, L. M.; Kovner, M. A. *Opt Spektrosk.* **1973**, *35*, 370.

(318) Martin, J. M. L. *Chem. Phys. Lett.* **1996**, *262*, 97.

(319) Bermudez, G.; Chan, I. Y. *J. Phys. Chem.* **1986**, *90*, 5029.

(320) Sackmann, E.; Mohwald, H. *Chem. Phys. Lett.* **1972**, *12*, 467.

(321) Ha, T. K. *Chem. Phys. Lett.* **1981**, *79*, 313.

VITA

Personal:

Date of Birth: September 3, 1980

Place of Birth: Seoul, Republic of Korea

Education:

B.S., Chemistry, University of Auckland, Auckland, New Zealand, 2003

Publications:

1. Lee, Jung Sup.; Lei, Yuxiu.; Yang, Dong-Sheng. "Pulsed-Field Ionization Electron Spectroscopy of Titanium, Vanadium, and Cobalt Hexamethylbenzene Complexes," in preparation.

2. Lee, Jung Sup.; Krasnokutski, Serge. A.; Yang, Dong-Sheng. "High-resolution electron spectra, preferential metal-binding sites, and thermochemistry of lithium complexes of polycyclic aromatic hydrocarbons," accepted in *J. Chem. Phys.* **2010**

3. Lee, Jung Sup.; Kumari, Sudesh.; Yang, Dong-Sheng. "Conformational isomers and isomerization of group 6 (Cr, Mo, and W) metal-bis(toluene) sandwich complexes probed by variable-temperature electron spectroscopy," *J. Phys. Chem. A* **2010**, *114*, 11277.

4. Lee, Jung Sup.; Lei, Yuxiu.; Kumari, Sudesh.; Yang, Dong-Sheng. "Ring deformation and π-electron redistribution of methylbenzenes induced by metal coordination," *J. Phys. Chem. A* **2010**, *114*, 9136.

5. Krasnokutski, Serge. A.; Lee, Jung Sup.; Yang, Dong-Sheng. "High-resolution electron spectroscopy and structures of lithium-nucleobase (adenine, uracil, and thymine) complexes," *J. Chem. Phys.* **2010**, *132*.

6. Lee, Jung Sup.; Lei, Yuxiu.; Kumari, Sudesh.; Yang, Dong-Sheng. "Metal coordination converts the tub-shaped cyclo-octatetraene into an aromatic molecule: Electronic states and half-sandwich structures of group III metal-cyclo-octatetraene complexes," *J. Chem. Phys.* **2009**, *131*, 104304.

7. Krasnokutski, Serge. A.; Lei, Yuxiu.; Lee, Jung Sup.; Yang, Dong-Sheng. "Pulsed-field ionization photoelectron and IR-UV resonant photoionization spectroscopy of Al-thymine," *J. Chem. Phys.* **2008**, *129*, 124309.

8. Wang, Xu.; Lee, Jung Sup.; Yang, Dong-Sheng. "Electron spectroscopy, molecular structures, and binding energies of Al- and Cu-imidazole," *J. Phys. Chem. A* **2006**, *110*, 12777.

9. Wang, Xu.; Lee, Jung Sup.; Yang, Dong-Sheng. "Pulsed-field ionization electron spectroscopy and *ab initio* calculations of copper-diazine complexes," *J. Chem. Phys.* **2006**, *125*, 014309.